Multi-Source Inverter for Electrified Vehicles: Concept, Analytical Design, Efficiency Analysis, and Implementation

MULTI-SOURCE INVERTER FOR ELECTRIFIED VEHICLES: CONCEPT, ANALYTICAL DESIGN, EFFICIENCY ANALYSIS, AND IMPLEMENTATION

BY

LEA DORN-GOMBA,

A THESIS

SUBMITTED TO THE DEPARTMENT OF ELECTRICAL & COMPUTER ENGINEERING

AND THE SCHOOL OF GRADUATE STUDIES

OF MCMASTER UNIVERSITY

IN PARTIAL FULFILMENT OF THE REQUIREMENTS

FOR THE DEGREE OF

DOCTOR OF PHILOSOPHY

Doctor of Philosophy (2018) McMaster University

(Electrical & Computer Engineering) Hamilton, Ontario, Canada

TITLE:	Multi-Source Inverter for Electrified Vehicles: Concept, Analytical Design, Efficiency Analysis, and Implementation
AUTHOR:	Lea Dorn-Gomba Diplome d'ingenieur (Engineering degree) Ecole Nationale Superieure d'Electricite et de Mecanique (ENSEM), Nancy, France
SUPERVISOR:	Dr. Ali Emadi Ph. D. IEEE Fellow Canada Excellence Research Chair in Hybrid Powertrain
NUMBER OF PAGES:	xx, 207

To Jérôme

Abstract

This thesis focuses on the concept, analytical design, efficiency analysis, and implementation of the multi-source inverter (MSI) for electrified vehicles (EVs).

The fundamentals of power electronics in EVs, including the main powertain architectures and the characteristics of power electronic converters, are discussed. Vehicle-level modeling methods and simulation tools for power electronics are also analyzed.

Located at the heart of the propulsion system, traction inverters play a major role in the performance and competitiveness of a vehicle. Standard industry solutions are reviewed, and a comparison of alternative candidates is presented. The main modulation strategies are also reviewed. For any topology to be seriously considered by the automotive industry, it must be able to compete on cost, reliability, efficiency, and power density. These driving factors are discussed, and the design trade-offs are explained.

In view of the continuous power increase in modern EVs, current industry configurations show some limitations. As an alternative solution, the MSI is suggested to be used as a traction inverter. The fundamental purpose of this power converter is to connect two independent DC sources to the same AC output using a single conversion stage. The concept of the MSI is presented and two circuits are considered. The operating modes during both DC/AC and AC/DC conversions are detailed and new control strategies are proposed. Closed-loop control simulations are performed to verify the MSI operation in each operating mode. A scale-down prototype is experimentally tested with an electric

machine and a load to validate the effectiveness of the proposed topology and concept.

A comprehensive analytical design analysis of the switch configuration is presented, and analytical calculations of the capacitor requirements are suggested to select the proper capacitor banks for the MSI. An efficiency model based on the average and RMS currents of the switches is also proposed to evaluate the performance of the inverter. Experiments with the prototypes of both MSI circuits and an R-L load are carried out to validate the theoretical efficiency analysis. Design and efficiency comparisons of the MSI with the voltage source inverter are conducted as well.

The control and simulation of a new power-split powertrain with the MSI is discussed. As one of the most popular EVs on a sales-weighted basis, the Toyota Prius is analyzed as a case study. The suggested powertrain with the MSI aims to reduce the use of the DC/DC converter by offering an additional commutation path between the battery and the MSI. Another advantage of the MSI is the possibility to extend the battery charging opportunities. A vehicle-level simulation model of the traction drive system with the MSI is developed to estimate the potential benefits of the proposed powertrain. Simulations of the conventional and suggested powertrains are performed by applying the same voltage command of the DC/DC converter and power distribution between the battery and the electric machines.

Besides the hybrid power-split powertrains, the MSI can also be integrated into an active hybrid energy storage system. This new configuration aims to interconnect a battery and an ultracapacitor, without the use of any additional power electronic converters. A new control strategy is developed to manage the current distribution between the two sources and aims to take advantage of the high energy density of the batteries and the large specific power of the ultracapacitors, while minimizing battery degradation. Closed-loop control simulations are carried out to verify the operating principle of this novel configuration. The influence of the additional control parameters on the source currents is further investigated through simulations and validated with experiments on an R-L load.

Acknowledgments

I would like to express my sincere gratitude to my supervisor, Dr. Ali Emadi, who provided me precious guidance and insightful advice throughout my graduate studies. I cannot thank him enough for involving me in exciting projects. His inspirational leadership with a passion for excellence motivated me to push myself and accomplish my goals.

I am truly thankful to Dr. Pierre Magne and Dr. Babak Nahid-Mobarakeh for taking the time to share their valuable comments and helpful suggestions over the years.

I would like to thank all my colleagues at the McMaster Automotive Resource Center (MARC) for their assistance and enthusiasm. I particularly enjoyed the exchange of innovative ideas and the stimulating discussions with such a thoughtful research group. Special thanks to Romina Rodriguez, Alan Dorneles Callegaro, and Silvio Rotilli Filho for the great moments we shared. I am also very thankful to Dr. Jing Guo for her relevant feedback and her contribution to the experiments.

I would like to thank my family and friends for their endless support. I will be forever grateful to my parents and my sister who never stopped encouraging me. Despite the distance, they helped me go through the ups and downs that come with graduate studies. I would like to also express my deepest love and gratitude to Jerome Pommier for believing in me. His dedication and encouragements mean more to me than he can ever imagine.

Finally, I would like to acknowledge the Canada Excellence Research Chairs Program for funding, in part, this research.

Contents

List of Figures

List of Tables

Notation

Abbreviations

AEV	All Electric Vehicle
APM	Auxiliary Power Module
BEV	Battery Electric Vehicle
DOE	Department of Energy
EM	Electric Machine
ETDS	Electric Traction Drive System
EV	Electrified Vehicle
HESS	Hybrid Energy Storage System
HEV	Hybrid Electric Vehicle
HV	High Voltage
HWFET	Highway Fuel Economy Test cycle
ICE	Internal Combustion Engine
IGBT	Insulated Gate Bipolar Transistor
IM	Induction Motor
LV	Low Voltage

MSI	Multi-Source Inverter
NEDC	New European Driving Cycle
NPC	Neutral Point Clamped
OEM	Original Equipment Manufacturer
PCU	Power Control Unit
PHEV	Plug-in Hybrid Electric Vehicle
PI	Proportional Integral
PWM	Pulse Width Modulation
SPWM	Sinusoidal PWM
SVPWM	Space Vector PWM
UC	Ultracapacitor
UDDS	Urban Dynamometer Driving Schedule
VSI	Voltage Source Inverter

Symbols

$\cos(\phi)$	Power factor
$\Delta i_{C1,rms,j}$, $\Delta i_{C2,rms,j}$	RMS capacitor ripple currents in C_1 and C_2
$\hat{V}_{LN,0}$	Amplitude of the fundamental harmonic of the phase voltage
$\langle i_{in} \rangle$	Average input current that supplies the load
ω_r, ω_r^*	Measured and reference rotor speeds
C_1, C_2	Capacitors of V_{dc1} and V_{dc2}
d_c	Discharge duty cycle
EM_1, EM_2	Electric Machine 1 or 2

f_c	Control frequency
f_{sw}	Switching frequency
I_1, I_2, I_3	Inverter modes of the MSI
i_a, i_b, i_c	Phase currents
i_{bat}, $\langle i_{bat} \rangle$, Δi_{bat}	Battery current, average value, and ripple
i_{boost}	Output current of the DC/DC converter
i_{C1}, i_{C2}	Capacitors currents
i_{cmd}	DC current transferred through the DC/DC converter
$i_{d,msi}$, $i^*_{d,msi}$	Measured and reference d-axis currents of the MSI
$i_{d,vsi}$, $i^*_{d,vsi}$	Measured and reference d-axis currents of the VSI
$i_{dc,EM1}$, $i_{dc,EM2}$	DC currents of the inverters for EM_1 and EM_2
i_{dc1}, i_{dc2}	DC source currents of the MSI
i_{in1}, i_{in2}	Input currents of the MSI
$I_{pk,j}$	Peak amplitude of the output phase current
$i_{q,msi}$, $i^*_{q,msi}$	Measured and reference q-axis currents of the MSI
$i_{q,vsi}$, $i^*_{q,vsi}$	Measured and reference q-axis currents of the VSI
i_{ref}, $\langle i_{ref} \rangle$, Δi_{ref}	Reference current, average value, and ripple
i_{uc}, $\langle i_{uc} \rangle$	UC current and average value
M_j	Modulation index
MSI_1, MSI_2	MSI topologies
${P_{bat}}^*$	Reference battery power
P_{boost}	Power transferred through the DC/DC converter
${P_{EM1}}^*$, ${P_{EM2}}^*$	Reference powers of EM_1 and $EM2$

R_1, R_2	Rectifier modes of the MSI
$R_{\Delta I}$	Ratio of the battery current ripple
R_{ave}	Ratio of the time-average values between $\langle i_{bat} \rangle$ and $\langle i_{ref} \rangle$
$S_{T1,k}$ to $S_{T4,k}$	Switching functions of $T_{1,k}$ to $T_{4,k}$
T_{load}	Torque load
T_{sw}	Switching period
$v^*_{j,k}$	Reference voltage functions in the adapted SPWM
V_{AB}, V_{BC}, V_{CA}	Three-phase line-to-line voltages
V_{bat}	Battery voltage
V_{boost}	Output voltage of the DC/DC converter
V_{cmd}	Voltage command for the DC/DC converter
$V_{D5,k}$, $V_{D6,k}$	Voltage across $D_{5,k}$ and $D_{6,k}$ in the MSI_1
$V_{dc,j}$	Input voltage applied to the load (i.e. V_{dc2}, $V_{dc1} - V_{dc2}$, or V_{dc1})
V_{dc1}, V_{dc2}	DC source voltages of the MSI
V_{EM2}	DC voltage applied to EM_2

Chapter 1

Introduction

1.1 Motivation

Internal combustion engine (ICE) vehicles propelled by fossil fuels largely dominate the automotive market with more than 86.1 million vehicles sold worldwide in 2017. This mature technology offers high power along with fast refueling capability, which makes fuel-based vehicles cost-effective, robust, and functional for the consumers. However, major concerns have been raised regarding the sustainability of the non-renewable energies and their adverse impact on the environment and human health.

Over the past decades, the energy demand substantially increased due to the global population growth, the emergence of developing countries, and the high availability of new powered technologies. In 2016, the world devoured more than 13.3 trillion tonnes of energy of which the oil consumption accounted for 33%, as shown in Fig. 1.1a [1]. The transport sector consumed about 20% of the total energy demand and oil is its primary fuel source with 94% (Fig. 1.1b). Assuming than government policies and technologies evolve in a similar manner as the recent years, energy forecasting shows that the world oil consumption in transportation will rise by 28.7% by 2040. In addition, the growing scarcity of fuel-based resources leads to political and economic conflicts all over the world. Hence, energy

diversification is essential to reduce fossil fuel usage and avoid dependence on a sole energy source.

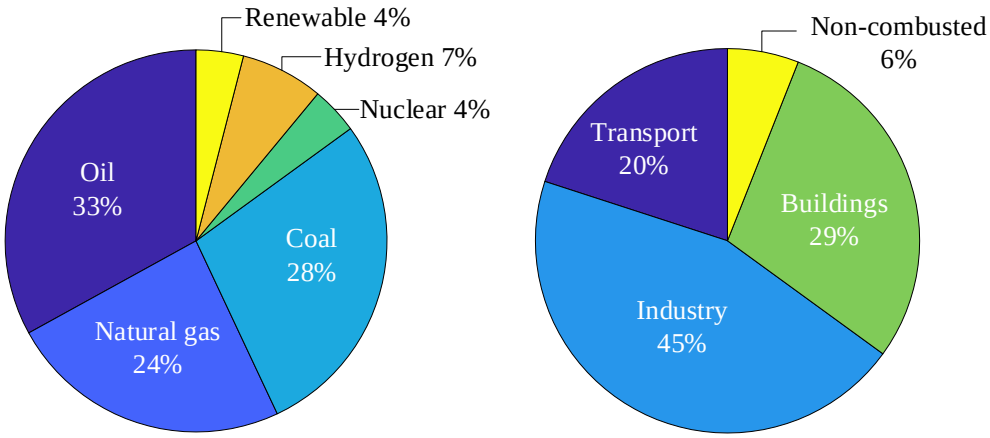

(a) By fuel type. (b) By sector.

Figure 1.1: World energy consumption in 2016.

Fuel consumption has also been put in the spotlight for environmental and health reasons. Indeed, oil combustion generates harmful gas emissions and atmospheric pollution that heavily contribute to global warming and impact on human health [2]. Governments have established multiple long-term plans for the automotive industry to promote the development and uptake of low carbon technologies [3, 4]. However, although automobile manufacturers reduced the average CO_2 emissions and oil consumption of fuel-based vehicles, improving the ICE technology might not be sufficient to meet the challenging regulations [5]. In view to further reduce the oil consumption, several countries announced their plan to ban fuel-based vehicles in the near future [6]. Therefore, transportation is more than ever challenged to offer alternative solutions relying on clean and renewable energy sources that can compete with ICE vehicles.

For the past few decades, electrified transportation gradually gain acceptance as they achieve promising performance [7]. A record volume of 1.1 million electrified vehicles (EVs) sold worldwide has been recently reached in 2017, which represents a sale increase of more

than 50% from the previous year [4]. Depending on their degree of electrification, EVs can reduce or eliminate the oil dependency by using other energy sources. Moreover, electrified powertrains achieve more than 90% efficiency, compared to only 30% for fuel-based vehicles, which allows for better fuel economy even in the presence of an ICE. Extensive research is undertaken by laboratories, suppliers, and original equipment manufacturers (OEMs) to develop cutting-edge technologies that address the barriers of every powertrain component. Governments have also set up new policies and objectives to further accelerate the market integration of EVs. For example, the U.S. Department of Energy (DOE) defined aggressive targets to develop powertrains at low cost, high efficiency, and high power density [8].

Located at the heart of the propulsion system, traction inverters draw attention to improve the vehicle performance since they ensure the power transfer between the energy sources and the electric machines (EMs). Most commercialized vehicles use traditional voltage source inverters (VSI) as traction inverters as they feature low cost, high power density, and simple control. Nevertheless, this topology shows some limitations due to the wide operating range of EMs and the high power requirements. Indeed, the VSI achieves low efficiency at light load and the EM performance is limited by the constant battery voltage. As an alternative solution, some OEMs integrate a DC/DC converter to provide a variable input voltage to the VSI. By doing so, the performance of the EMs can be improved along with the efficiency of both the inverter and the EM. However, this configuration also shows some drawbacks in terms of cost and power density. Moreover, the DC/DC converter power rating should be equal to that of the battery pack as they are connected in series. Hence, extending the electric driving range by increasing the power rating of the battery pack requires more trade-offs compared to the simple architecture. Numerous innovative inverter circuits for high voltage applications have been suggested in the literature and will be further discussed in Chapter 3. However, their competitiveness is adversely affected by either larger volume of the passive components or higher part counts compared to the VSI, while achieving similar performance. Thus, the complexity of their control and their cost

hold them back from commercialization in traction drive systems.

For the past few years, performance requirements for powertrain components in EVs, including traction inverters, have substantially increased in respond to the consumer demand, whereas cost reductions and power density improvement must be achieved. Overall, there is a need for innovative solutions that keep the advantages of current industry configurations while limiting the downsides. In view of exploring an alternative approach to address the challenges that traction inverters are facing, this thesis focuses on an inverter topology named the multi-source inverter (MSI) [9]. Its fundamental purpose is to connect two constant DC sources to the same AC output using a single conversion stage. Applied in conjunction with a DC/DC converter in a hybrid electrified powertrain, the MSI can provide a flexible voltage to the EM thanks to its dual DC input and aims to dissociate the DC/DC converter from the traction system in some driving conditions. By doing so, using the MSI as a traction inverter intends to enable high efficiency operation for both the inverter and the EM and aims extending the EM performance, while reducing the power rating of the DC/DC converter to improve the cost and power density of the overall electric traction system. On the other hand, when two distinct DC energy sources are available in the EV, such as in a hybrid energy storage system (HESS), the MSI can drive an EM with a flexible voltage without the use of an additional DC/DC converter. As a result, the MSI aims to keep the advantages of an active HESS while improving the cost and power density of the powertrain. As the MSI is a topology recently developed, very little work has been done so far. Therefore, the objective of this thesis is to validate the concept, assess its performance and design requirements, and estimate the potential benefits of its use as a traction inverter in an electrified powertrain.

1.2 Contributions

The author has contributed to several technical advances in analytical design, efficiency analysis, and implementation of the MSI for EVs. These contributions are briefly described below.

- Review of the main powertrain architectures in EVs and analysis of the modeling methods and simulation tools for power electronic converters at vehicle-level; published in [10] and to be submitted in [11].
- Review of the current traction inverter status in the automotive industry and practical design considerations; accepted for publication with minor revisions in [12].
- Introduction to the concept of the multi-source inverter for hybrid electric powertrains; published in [13, 14].
- Comprehensive design analysis and efficiency comparison of the multi-source inverter and the voltage source inverter; to be submitted in [15].
- Multi-source inverter for power-split hybrid electric powertrains; submitted in [16].
- Active hybrid energy storage system using the multi-source inverter; published in [17, 18].

1.3 Thesis outline

This thesis is organized into eight chapters. It focuses on the concept of the MSI for EVs, analytical design, efficiency analysis, and implementation.

Chapter 1 has given the motivation for inverter research applied to EVs, as well as the thesis contributions.

Chapter 2 presents the fundamentals of power electronics in EVs. The main powertain architectures, sorted by degree of electrification, are first outlined. Then, the power electronic converters and their current characteristics are discussed. The Toyota Prius is also reviewed as a case study. Finally, modeling methods and simulation tools for power electronics at vehicle-level are analyzed, as they gain interest to assess the impact of the powertrain architectures, the component sizing, and the control strategies on the performance of the vehicle.

Chapter 3 presents the standard traction inverters implemented in the automotive industry. Alternative solutions, suggested to outweigh the downsides of the traditional inverters, are also reviewed. The main modulation techniques are compared and practical design considerations including cost, reliability, efficiency, and packaging are discussed.

Chapter 4 introduces the concept of the MSI. The converter topology can be modeled by two different circuits by replacing ideal switches with power semiconductors. The theoretical behavior of the MSI is analyzed during both DC/AC and AC/DC operations. Due to the uniqueness of the circuits, standard pulse width modulation (PWM) methods cannot be applied. Hence, new adapted PWM techniques are suggested and the operating modes of the MSI are verified through simulations. Finally, a scale-down prototype has been built and tested on an experimental setup composed of an induction motor and a load. Closed-loop control experiments with several speed and torque references have been carried out to validate the concept of the proposed topology.

Chapter 5 analyzes the design and the efficiency of the MSI. The switch configuration is first discussed based on voltage and current requirements. The VA ratings of both MSI circuits and the VSI are compared. Due to the two DC sources and the multiple operating modes, new analytical equations of the RMS capacitor ripple current and capacitance are suggested to select the proper capacitor banks of the MSI. The requirements and the overall volume of the capacitor bank in the MSI and the VSI are compared. At last, an analytical efficiency model based on the average and RMS currents in the switches is developed for

both MSI topologies. By considering a constant R-L load and under the same power requirements, the efficiency varies regarding the mode in which the MSI operates. As a result, depending on the operating conditions, the most efficient mode can be selected, ensuring the MSI to operate at high efficiency over a wide output voltage range. Experiments were performed with the prototypes of both MSI circuits and an R-L load to validate the analytical efficiency models. An efficiency comparison between both MSI topologies and the VSI is also conducted.

Chapter 6 discusses the implementation of the MSI in a power-split powertrain. Control strategies of a conventional power-split architecture, similar to the Toyota Prius, are first analyzed. The powertrain operating modes are classified by analyzing the status of the ICE, the charge or discharge of the battery, and the motoring or generating operations of the EMs. Vehicle-level simulation models of the battery and the electric traction drive system, developed in Autonomie, are also detailed. Then, control strategies of the new powertrain with the MSI are proposed by combining the operating modes of the inverter with the power distribution applied in the conventional architecture. Due to the DC dual input of the MSI, simulations in Autonomie raises several barriers. As an alternative solution, a vehicle-level simulation model is developed in Matlab/Simulink. Finally, several drive cycles are tested, and the performance of the conventional and suggested powertrains are compared. By doing so, the potential benefits of using the MSI in a power-split architecture are highlighted.

Chapter 7 introduces a new active HESS topology that directly pairs Li-ion batteries with ultracapacitors through the MSI to drive an EM without the use of any additional power electronic converters. Because of the specific current distribution in the MSI, an innovative control scheme has been developed to regain current sharing between the sources. Two variables can be adjusted to smooth the input source currents and bias the use of one energy storage device over another, which allows controlling the discharge rate of the two sources. Closed-loop control simulations for a drive cycle have been performed to verify the operating principle of this novel HESS topology. The influence of the additional control

parameters on the input currents and states of charge of the sources has been further investigated through simulations. Furthermore, experiments with an R-L load have been carried out and validated the theoretical influence of the new control on the input DC currents.

Chapter 8 is dedicated to conclusions and future work.

Chapter 2

Fundamentals of power electronics in electrified vehicles

For the past decades, EVs are continuing to show promise as more manufacturers announce plans to develop hybrid (HEVs), plug-in hybrid (PHEVs) and all electric vehicles (AEVs). In 2012, the U.S DOE initiated a long-term project called the 'EV Everywhere Grand Challenge' with the goal of developing cost-effective, powerful and reliable EVs that can compete with conventional fuel-based technologies [19]. At the heart of all electrified powertrains is one or more EMs which operate either in conjunction with an ICE or replace it entirely. To drive them, a traction inverter is required to convert the DC power available from the battery pack to variable frequency AC power. Additional power electronics are used to ensure the proper operations of the vehicle, such as providing power to the accessory loads and charging the battery. Even though multiple powertrain configurations are available, most of them are composed of the same power electronics whose power rating varies depending on the OEM strategy. Vehicle-level modeling and simulation tools gain interest as EVs become more complex. These methods aim to assess the impact of the powertrain architectures, the component sizing, and the control strategies on the performance of the vehicle.

In this chapter, fundamentals of power electronics in EVs are discussed. First, the main powertrain architectures, sorted by degree of electrification, are summarized. Then, the characteristics of the power electronics are reviewed, and the Toyota Prius is taken as a case study. At last, modeling methods and simulation tools for power electronic converters at vehicle-level are discussed.

2.1 Main powertrain architectures

In a conventional fuel-based powertrain, the wheels are driven by an ICE and the electrical accessories are powered by a low voltage (LV) 12V battery. The control is moderately simple since the mechanical, thermal, and electrical systems have limited interactions between each other. On the other hand, EVs reduce the exhaust emissions and the fuel consumption by using energy storage systems either in combination with the ICE or by themselves to propel the vehicle [7, 20]. Several powertrain architectures are currently implemented in commercialized EVs and their performance differ regarding the strategy of the OEMs. They can be sorted in three groups based on their degree of electrification, namely Micro and Mild HEV, HEVs and PHEVs, and AEVs.

2.1.1 Micro and Mild HEVs

Micro HEVs are the first levels of electrification as they require simple and cheap engineering adjustments of the conventional ICE powertrain. Indeed, the architecture is slightly modified by integrating a small EM of about 5 kW to perform the start-stop function when the ICE idles [21]. The powertrain can achieve up to 5-10% fuel consumption reduction in urban driving while keeping the usual 12V battery [22]. However, improvement opportunities are quite limited due to the modest enhancements.

In Mild HEVs, an EM of usually 5-20 kW is used as a starter/generator. Various means of coupling with the ICE have been developed such as the well-known configurations

belt starter/generator and integrated starter/generator (BSG and ISG) [23, 24]. Due to the increasing power demand from the accessory loads, several OEMs add a larger battery pack to the powertrain with a voltage up to 130V. The 48V BSG/ISG architectures draw particular attention as they do not require extra safety protections due to a voltage below 60V [25, 26]. In the meanwhile, increasing the battery voltage to about 100V allows the EM to further assist the ICE during accelerations, which leads to 15-20% fuel economy improvement. General Motors upgraded its eAssist system with a 86V Li-ion battery pack in the third generation and Honda used a 130V battery in the Accord and Compact Sedan models [27–29]. In Mild HEVs, the additional battery is only charged through regenerative braking; thus, no battery charger is required. Hence, this architecture remains simple while ensuring the stop-start function, assisting in vehicle propulsion, and supplying the accessory loads in combination with the 12V battery. However, regardless the voltage level of the additional battery, this configuration requires an auxiliary power module (APM) consisting of a DC/DC buck converter connected between the 12V battery and the additional one. Hence, even though Mild HEVs achieve higher fuel economy compared to Micro HEVs, they are also more expensive.

2.1.2 HEVs and PHEVs

HEV and PHEV powertrains further reduce the gas emissions and fuel consumption by integrating a larger battery pack with a high voltage (HV) varying from 200V to 400V [30]. One or more EMs are used to assist the propulsion or run the vehicle in electric-only mode when the ICE is turned off. Similar powertrain architectures can be used in both HEVs and PHEVs and the differences between these two types of EVs are due to the battery power rating. Averaged HEVs integrate 20-60 kW EMs powered by a 1-2 kWh battery pack that can be charged through regenerative braking when the vehicle is coasting [31]. Up to 40% fuel economy is achievable but the ICE remains the main source of power, as the battery can only drive the vehicle by itself for less than 10 km. On the other hand, PHEVs have

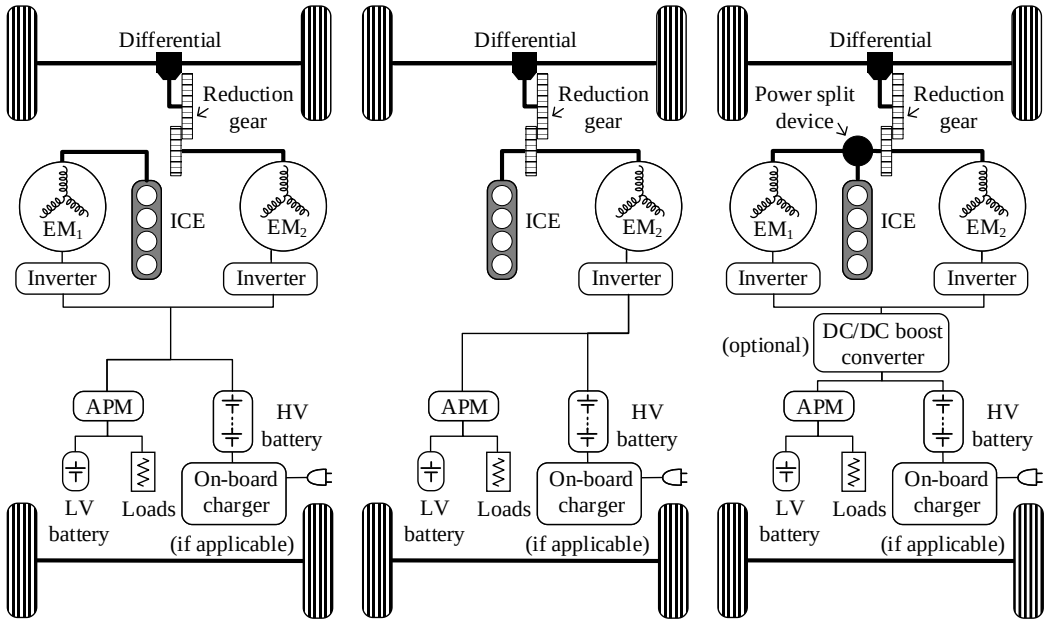

(a) Series configuration. (b) Parallel configuration. (c) Power-split configuration.

Figure 2.1: HEV and PHEV powertrain architectures.

enlarged the battery pack from 5 kWh, for the mass market PEHVs, to 15-20 kWh for the high performance vehicles [31–33]. Hence, the EM power rating is increased to 60-150 kW and the battery can propel the vehicle without the ICE for an electric driving range of 20-60 km. Even though regenerative braking is also available to charge the battery, it is not sufficient to ensure the full charge. Thus, an additional on-board charger is required in PHEVs to charge the battery with the grid.

A wide array of HEVs and PHEVs is currently available on the market and they can be categorized in three main architectures, namely the series, parallel, and power-split configurations, as shown in Fig. 2.1 [34]. All of them include an APM for a 12V battery and the accessory loads. An on-board charger is only integrated in PHEVs. The architectures mainly differ from each other regarding the mechanical and electrical connections between the ICE and the EMs.

Series architecture

In a series powertrain configuration, the ICE is decoupled from the wheels and its mechanical power is converted into electricity through a generator EM_1 (Fig. 2.1a). As a result, only EM_2 is connected to the final drive and the speed of the ICE is independent from the vehicle speed. This enables the ICE to operate at its optimum torque and speed to maximize its efficiency. The HV battery can be charged at any time with regenerative braking or by the ICE even when the vehicle idles. Finally, the powertrain is powered by either the HV battery, the ICE or the combination of both sources depending on the optimal power distribution that would achieve the highest fuel economy. Overall, this configuration is mechanically simple and offers a good control flexibility.

The series architecture shows some demerits regarding the power density. Each system needs to be sized according to either the HV battery or the ICE power ratings to fully take advantage of the power available by the sources. Hence, this architecture is more popular for vehicles where the volume of the components is not the most critical factor. Furthermore, although the ICE can operate efficiently over a wide range of operating points, the overall efficiency of the powertrain drops due to the multiple power conversion steps from the ICE to the wheels. Indeed, the mechanical power from the ICE is first converted into electricity through EM_1, then transferred by the inverters, and finally converted back into mechanical power with EM_2. A few PHEVs uses the series configuration, such as the BMW i3 REx and the Honda Accord where a two-motor series powertrain achieve almost 60% fuel consumption reduction [33, 35].

Parallel architecture

Unlike the series configuration, a parallel architecture enables the ICE to directly drive the wheels by mechanically coupling it to the reduction gear (Fig. 2.1b). Only EM_2 is necessary and can provide power to the wheels either alone or in conjunction with the ICE.

This control flexibility allows for power sharing at full load, so the ICE and the EM only need to be sized to transfer half of the maximum load demand. Thus, significant power density improvement can be achieved while accomplishing similar performances compared to the series powertrain. Moreover, the efficiency of the powertrain is improved when the ICE is used since its power does not need to be converted multiple times, as it is the case in a series architecture. On the other hand, the efficiency of the ICE itself cannot be optimized due to its mechanical coupling with the wheels.

In conclusion, a parallel architecture is an attractive solution for light-duty vehicles due to its simplicity, cost-effectiveness, and power density. This configuration is widely used in HEVs and PHEVs by most European manufacturers such as the Volkswagen group, BMW, and Mercedes but also by other OEMs like Hyundai and Honda [23, 36].

Power-split architectures

Power-split architectures combine the advantages of the series and the parallel configurations while minimizing their drawbacks. Although the control is more complex, and the powertrains are more expensive than the two previous architectures, they achieve better performance and are the most common configurations on a sales-weighted basis.

The Prius was the first mass-production HEV introduced to the market and Toyota still uses this architecture in its latest models [36, 37]. Fig. 2.1c shows the architecture of the Toyota Prius MY2010 where both EMs are mechanically coupled with the ICE through a planetary gear system and a reduction gear. When the ICE is used, its power can be shared between EM_1 and the wheels. By doing so, the ICE speed and torque are controlled so that the efficiency is optimized under several driving conditions. In case of high power demands, EM_2 assists the ICE in the propulsion. Hence, the ICE and the EMs can be downsized accordingly based on the gear ratio since they do not have to carry the peak power of the powertrain. An additional DC/DC boost converter is used to step up the HV battery, which improves the efficiency of the inverters and the EMs and extends the torque-speed

characteristic. Other OEMs do not necessarily use this optional DC/DC converter as it increases the cost and volume of the powertrain.

General Motors developed an alternative power-split configuration, called the Voltec, that combines two EMs and the ICE though a planetary gear and three clutches in the first generation [38]. The vehicle can run either in electric-only mode with one EM, or in electric-only mode with two EMs, or as a series architecture, or finally in power-split mode like the Toyota Prius. Lately, General Motors introduced the second generation composed of two planetary gears and three clutches [39,40]. By doing so, the powertrain can operate in more operating modes, which increases the all-electric driving range and the fuel economy, while reducing the volume and weight of the traction drive components.

2.1.3 AEVs

In view of the aggressive targets regarding fuel consumption and gas emission reductions, AEVs are very good solutions since the ICE is removed from the powertrain and they exclusively use energy sources to propel the vehicle [8]. Hence, they achieve high efficiency, zero gas emissions, and are independent from oil. The power is provided by either one type of energy source or a combination of several sources to form a commonly called HESS [41,42]. For example, a HESS technology can combine the high energy density of a battery pack with the high power density of an ultracapacitor (UC) to extend the vehicle driving range while improving its dynamic performance. Numerous HESS configurations including one or more power electronics converters have been investigated in the literature and will be reviewed in Chapter 7. In the following, two principal AEV architectures are discussed due to their superior performance and integration in the automotive market.

Battery EVs (BEVs) are the most popular AEVs today where General Motors, Nissan, and Tesla currently dominate the market [43]. This is mainly due to the enhancements of the electric driving range and the vehicle performance. Indeed, the power rating of the battery varies from 20 kWh to 40 kWh for most BEVs which enables driving the vehicle

for 100-150 km in one charge [33, 44]. The high-performance Tesla Model S integrates a massive battery pack of 60-100 kWh and pushes the boundaries with an impressive 300-400 km driving range. The BEV powertrain is simple compared to HEVs and PHEVs since it uses a single battery pack that supplies one or more EMs mechanically coupled to the differential of the vehicle through diverse gears and clutches [34]. However, BEVs still face several challenges that prevent them from being fully adopted by the consumers. One can cite the limited charging station availability, the charging time that remains relatively inconvenient and the higher cost compared to fuel-based vehicles.

Fuel cells are open systems that generate electricity from the electrochemical reaction between hydrogen gas, stored in an external tank, and oxygen, delivered to the fuel cell stack from outside [45]. Hence, instead of using petroleum like ICE vehicles, fuel cell vehicles are refilled with hydrogen and simply exhaust water since no combustion is involved. Three vehicle models are available on the U.S. market today, namely Honda Clarity, Hyundai Tucson, and Toyota Mirai [46–49]. They all have the same architecture composed of a fuel cell stack and a single EM of about 100 kW. The powertrain also integrates a small battery pack of less than 1 kWh to assist the propulsion during high power demands. No on-board charger is required since it is charged through regenerative braking. The battery voltage varies between 250V to 350V and an additional DC/DC boost converter is used in the Toyota Mirai to step up the voltage level to 650V, similarly to the Toyota Prius previously mentioned. In theory, the fuel cell technology is a good solution in respond to the restricted driving range of BEVs and their slow charging time. Indeed, commercialized fuel cell vehicles offer 480-580 km cruising range and refueling the tank takes less than five minutes. Nevertheless, the limited availability of refueling infrastructures and the cost slow down the market penetration of fuel cell vehicles [50].

2.2 Power electronics in electrified powertrains

Depending on the powertrain architecture, various power electronics are used to control and transfer the power between the battery, the EMs, and the rest of the electrical components. The electric traction drive system (ETDS) includes the EMs, the traction inverters, that can also operate as rectifiers, and an optional DC-DC boost converter to step up the battery voltage. Although they are not part of the propulsion system, other power electronic converters are integrated in the powertrain to ensure the proper operation of the vehicle. An APM, consisting of a DC-DC buck converter, is connected between the HV and LV batteries to run the accessory loads. Moreover, BEVs and PHEVs integrate large battery packs that cannot be solely charged with regenerative braking. Hence, an on-board charger is added to the powertrain to charge the battery with the grid.

Although the market has been dominated by HEVs since the last decade, the current sale status tends to move towards PHEVs and BEVs. In response to the high power demand, on-going research works on new technologies to achieve higher performance, longer electric driving range, and improved fuel economy. The U.S DOE also set up new objectives for 2025 where the peak power of the propulsion system has been raised from 55 kW to 100 kW [8]. Indeed, development of cost-effective and powerful electrified powertrains is the key to compete with ICE vehicles and accelerate the market penetration of EVs. Hence, every powertrain component is submitted to aggressive targets and the power electronics are no exception.

In the following, the main characteristics of power electronics in EVs, except for Micro and Mild HEVs, are briefly reviewed.

2.2.1 Power electronics in the ETDS

In the new targets defined by the U.S DOE for 2025, the power electronics in the ETDS refer to a single 100 kW inverter and a DC/DC boost converter if applicable. Currently,

the average on-road converters achieve 18 kW/L at a cost of 10 $/kW, while it is expected to reach 100 kW/L at 2.7 $/kW for 2025 [8]. Hence, substantial improvements regarding the cost and the power density are necessary.

DC/AC converter

Most modern electrified powertrains use EM requiring AC power while the energy source provides DC power [51]. As a result, DC/AC converters, also known as inverters, are necessary to transfer power in the ETDS. When the EM is generating, the inverter operates as a rectifier and returns the power back to the battery to charge it. Detailed analysis of standard traction inverters and alternative candidates are provided in Chapter 3. The modulation techniques and the practical design considerations are also discussed. The VSI is currently used in commercialized EVs and can be either directly connected between the battery and the EM or it can be used in combination with a DC/DC boost converter.

DC/DC boost converter

One solution applied in some HEVs and PHEVs consists of using a DC-DC boost converter between the battery and the DC-link of the traction inverter. By doing so, the voltage of the battery is stepped up according to the driving conditions, which enables the operation of the inverter and the EM at high efficiency [52]. This configuration presents several additional advantages such as extending the constant torque characteristic, reducing the current rating on the switches, and having a higher inverter power supply voltage without increasing the battery voltage. However, a high power DC/DC converter has also some demerits since its power rating must match that of the battery pack to avoid derating the battery system. Indeed, as the battery and the DC/DC converter are in series, the power rating of the two is limited by the lowest one. As a result, a high power battery pack and, hence, a high power DC/DC converter, will adversely impact on the power density and cost of the powertrain due to the inductor which is usually bulky and expensive. Furthermore, this configuration

directly affects the overall efficiency of the powertrain during both traction and regenerative braking mode due to the additional conversion stage.

2.2.2 Other power electronic systems

In addition to the ETDS, the on-board charger and APM are subjected to their own targets for 2025 and face different barriers.

On-board charger

Chargers play a crucial role in the mass adoption of PHEVs and BEVs due to their impact on the charging time and the battery life [53]. Three levels of charging speed are commonly reported depending on the power delivered. The first level is considered slow and the power is limited to 2 kW. The second level is more popular and can be implemented in private or public infrastructures. The charging speed is twice faster than the previous level and a power of 4-20 kW is expected. Finally, facilities operating in the third level are also known as superchargers and can charge a vehicle in less than one hour by delivering 50-100 kW. Unlike off-board systems, on-board chargers are limited in power due to size, weight, and cost constraints. As a result, they only operate in the first two levels and are rated at 3-10 kW in most commercialized vehicles.

Various on-board topologies have been developed over the years. Commercialized vehicles have unidirectional chargers that only allow the grid to transfer power to the battery. On the other hand, bidirectional systems are emerging concepts and under extensive investigation. They aim for a flexible power transfer with both grid-to-vehicle and vehicle-to-grid operations [54]. Although they seem to offer interesting features such as grid stabilization and optimized energy distribution, their practical application raises some safety concerns and require tremendous changes of the actual infrastructures. Hence, they are not ready for mass production yet due to their high cost and complex integration. Integrated chargers are innovative solutions to optimize the power density of the powertrain. By using the motor

windings and the power electronics, integrated systems achieve good performance despite their complexity. Several configurations have been developed with one or more EMs and are reviewed in [53]. Besides the well-known conductive technique that consists of plug in a cord to the vehicle, inductive charging, also known as wireless, gains interest due to its potential convenience for the consumers. Indeed, they magnetically transfer power so that no physical connection is needed between the vehicle and the charging infrastructure.

APM

Apart from Micro and Mild HEVs, electrified powertrains use the HV battery pack to power the LV accessory loads such as air conditioning, wipers, lighting, and radio. Thus, an APM consisting of a DC/DC buck converter, is necessary to step down the nominal 325V battery voltage to 12V [22]. Due to safety reasons, galvanic isolation is required to protect the passengers and the rest of the vehicle in case of failure from either the HV or LV side. Although the APM is not part of the propulsion system, its design and control have a major impact on the vehicle performance. Indeed, high efficiency is crucial to maximize the use of the HV battery for the propulsion system while optimizing the power draw for the accessory loads. The 2025 targets require the APM to provide 5 kW at 98% efficiency with a power density of 4.6kW/L [8]. Several isolated converters have been deeply studied in the literature such as flyback, forward, push-pull, half-bridge, and full-bridge. However, alternative solutions should be considered due to the high power requirements [55].

Multifunctional converters are single systems that serve several purposes. For example, a bidirectional APM can be used in buck mode to transfer power to the loads and in boost mode to pre-charge the capacitor bank of the traction inverter [10]. Indeed, the sizable capacitor bank connected to the DC-link needs to be pre-charged to avoid the damage caused by initial inrush currents. One conventional method is the use of a pre-charge circuit composed of a bypass relay and a resistor. This circuit can be eliminated by using a bidirectional APM, which also enables the control of the pre-charging time. Integrated systems have also

been investigated to further reduce the cost while achieving high performance. In [56], an APM integrates an active filter to reduce the second-order harmonics generated during the charge of the battery. By doing so, the conventional bulk DC-link capacitor connected to the battery is replaced by the integrated system, which allows for 70% cost reduction.

2.2.3 Case study: HEV Toyota Prius

Since the introduction of the Prius in 1997, Toyota has continued to lead the HEV market and still implements the power-split architecture in most of its vehicles. In 2004, the OEM introduced the second generation with a power control unit (PCU) composed of a dual inverter, a DC/DC boost converter, and an APM [57]. All components are integrated into a single enclosure and share the same cooling system to optimize the packaging. Since 2004, Toyota has improved its transmission system to achieve higher performance while keeping the same PCU composition. The third generation, developed in 2010, used a high speed reduction gear in series with a planetary gear to drive the differential, as shown in Fig. 2.1c [37]. In 2016, the fourth generation was introduced, and the planetary gear has been replaced by parallel gears, which reduces the mechanical losses by 20% [23].

Although the latest generation is composed of the same PCU components than the Prius MY2004, significant improvements can be noticed. In Table 2.1, the specifications of the propulsion system in the Toyota Prius MY2010 and MY2016 are compared [36, 58]. The volume and weight have been decreased by 33% and 12% respectively by using half-bridge semiconductor modules with double-sided cooling and integrated packaging for the DC-link capacitors. The double sided cooling technique is an emerging concept that has also been implemented in the high performance inverters from Hitachi and General Motors [59, 60]. This method removes heat from both the top and bottom sides of the module, which reduces the footprint up to 45% compared to the conventional single-sided cooling technology [61]. Hence, thermal management is improved along with the power density by extending the heat dissipation area of the module. Instead of using single semiconductors, Toyota developed

Table 2.1: Propulsion system specifications of the Toyota Prius MY2010 and MY2016.

Components	Specifications	MY2010	MY2016
ICE	Peak power rating	73 kW	73 kW
EM_1		42 kW	22 kW
EM_2		60 kW	53 kW
DC/DC converter	Output voltage	200V-650V	200V-600V
PCU	Weight	13.5 kg	11.9 kg
	Volume	11.2 L	6.8 L

its own half-bridge modules for the dual inverter and the DC/DC boost converter. By doing so, the footprint has been reduced by 22% and the stray inductance decreased by 55% due to the shorter distance between the chips. Besides the power semiconductors, the DC-link capacitors are also under the spotlight as they are the heaviest and most voluminous components in a traction inverter. A better integration of the capacitor with the DC side bus bar enables power density and efficiency improvements [62–64]. Indeed, by minimizing the series inductance in the DC side, the voltage overshoot across the switches can be reduced. Hence, the power modules do not need to be over designed to ensure a voltage safety margin and the inverter power density can be optimized. Increasing the operating voltage that is traditionally lowered due to the safety requirements also improves the efficiency of the inverter. Toyota applied this technique for its PCU and reported a series inductance reduction of 58%. Furthermore, the snubber circuits, usually added to reduce the surge voltages across the switches, have been removed.

Overall, the Toyota Prius is a competitive HEV even if the PCU is composed of more power electronics than other powertrains. However, increasing the power rating in respond to the high power demand raises new challenges, specifically for the DC/DC converter, in terms of power density and cost.

2.3 Vehicle-level modeling and simulations tools

2.3.1 Motivation

While device- and system-level models provide detailed analysis of the chip and converter operations, vehicle-level modeling offers a global overview of the powertrain and its control by considering the interactions between the power electronic converters and the other components in the vehicle, such as the ICE, the battery, and the EMs. Hence, this method aims to assess the impact of the powertrain architectures, the component sizing, and the control strategies on the performance of the vehicle. Furthermore, simulation tools are suitable solutions since they offer accurate results for distinct configurations, while keeping a low cost and short computational time despite multiple iterations, unlike building hardware.

It has been seen in Section 2.1 that several powertrain architectures are available and are composed of many power electronic converters whose requirements vary depending on the configuration selected by the OEM. In view of the large array of possible technologies, optimization design problems based on vehicle-level models can be defined to select the most suitable size of the systems regarding the vehicle performance targets. Although the plant and the control used to be optimized separately, there is a trend to couple them into multi-objective functions [65–67]. For example in [68], a convex algorithm is used to minimize the cost of the powertrain while considering the component size, the energy management, and the charge of the battery from the grid. As a result, powerful and cost-effective systems are selected, which leads to further improvements regarding the efficiency of the vehicle, the fuel consumption, the cost, and the exhaust emissions. Operational boundaries with voltage, current, and temperature ratings also need to be considered [69]. By simulating the powertrain with the safety considerations and fault diagnosis of the converters, the proper operation of the systems and the vehicle are verified [70, 71].

Advanced control strategies can be tested at vehicle-level where local controls of the

components are combined with a global supervisory control of the vehicle [72, 73]. Depending on the drive cycle, the power demand is regulated and shared between the systems to ensure satisfactory driving conditions for the driver while maximizing the performance of the vehicle. Optimization algorithms aim to further improve the power energy management between the components [74–76]. Offline methods, such as dynamic programing, are simple to implement in real-time controllers due to their short computational time [77, 78]. However, the optimal solutions are limited to the tested operating points, leading to lower performance for unpredictable drive patterns. Although online algorithms generate optimal solutions in real-time and are, thus, more flexible to various driving conditions, they require higher computational performance and are more challenging to implement. One solution commonly used to optimize the energy management with fast computational time is to combine the complementary characteristics of the offline and online methods [79, 80].

Overall, vehicle-level modeling is a powerful tool that offers comprehensive results to analyze the performance and the control of the vehicle under several driving conditions. Thus, it is crucial to develop accurate models for the power electronics converters as they stand at the heart of the ETDS and ensure the power transfer between the electrical components.

2.3.2 Modeling methods

Power electronic converters are often overlooked in vehicle-level models at the expense of other systems, such as the vehicle dynamics, the EMs, the battery, and the ICE [81–83]. However, there is a recent growing interest for modeling these components due to the aggressive power requirements under which electrified powertrains are subjected [8]. Indeed, breakthrough technologies are intensively researched in view of expanding the market adoption of EVs and these advances need to be accurately captured to evaluate their potential impact on the vehicle performance, control, efficiency, and cost.

One major concern in vehicle-level simulations is the need for extensive computing

power. In device- and system-level simulations, dynamic models are widely used to acquire the transient behavior of the converters and the time-step is usually chosen in the range of nanoseconds to microseconds. Hence, short-term analyses are preferred to provide accurate results in an acceptable time. On the other hand, vehicle-level modeling assesses the powertrain performance over a large timeframe of several minutes due to the slow dynamics of components such as the battery and the mechanical systems. Thus, simulating the fast behavior of power electronics converters raises challenges as the computational time needs to be limited with simplification assumptions while ensuring satisfactory accuracy.

In the following, two modeling methods for power electronic converters integrated in large-scale systems such as electrified powertrains are presented [84].

Averaged models

As previously mentioned, dynamic models are not suitable for vehicle-level simulations since they would require highly computational performance and long simulation time. As alternative solutions, averaged models extract the essential low-frequency behavior of the converters while neglecting the high-frequency transients. As a result, the time-step can be enlarged which improves the simulation capability. Several averaging methods can be found in the literature [85]. The state-space averaged model is based on mathematical equations derived from the instantaneous model where the state variables are replaced by their averaged values [86–88]. By doing so, the model becomes time-invariant while the non-linearities are preserved, which sustains the converter dynamics. This model is particularly efficient for transients lower than one-tenth the switching frequency and is widely used in the control design. Instead of using equations, circuit averaged models approximate the waveforms of the components by replacing the non-linear devices, such as the switches, by controlled voltage or current sources [89,90]. In [91], general methods to develop state-space and circuit averaged models for DC/DC and DC/AC converters are presented. The averaged models of the VSI and the DC/DC boost converter for hybrid powertrain applications are

also expressed in [92]. Moreover, the simulation times of detailed dynamic models and averaged models are compared, and the impact of the time-step is discussed. The power losses in DC/DC converters can be derived from the averaged models, as shown in [93] for hybrid powertrains composed of fuel cells, batteries, and ultracapacitors. In [94], the power losses of an inverter are averaged from the state-space equations.

Steady-state modeling

Steady-state modeling for power electronic converters is the most straightforward method since it fully neglects the transients and is based on look-up tables or maps filled with empirical data. For example, Oak Ridge National Laboratory experimentally measured the power losses of the inverters and DC/DC converters in several vehicles at different operating points [37,57,95,96]. The efficiency maps can be implemented in the vehicle-level models of the power electronic converters, which reduces the computational time and power compared to averaged models. Steady-state models are preferred for slow dynamic analysis such as supervisory control strategies, powertrain efficiency, fuel economy, and exhaust emissions. However, this method shows some limitations in optimization problems since the data are not based on dynamic equations. Indeed, the spikes and overshoots generated during transient events are overlooked in steady-state models, which makes the design of local control and component sizing often inadequate.

In conclusion, averaged methods are more suitable to model the fast behavior of power electronic converters and optimized their control, while steady-state models achieve satisfactory results for slow dynamic analysis in high-level simulations.

2.3.3 Simulation tools

Vehicle-level simulation tools are becoming increasingly accessible as computing capability improves. They tend to include every component of the powertrain at different levels of modeling details with a view of design comparison, performance assessment, and control

optimization. As previously mentioned, either averaged methods or steady-state look-up tables are commonly used to model power electronic converters in large-scale systems. The main simulations tools are reviewed in the following.

Mathworks tools are popular solutions to model electrified powertrains from the battery to the wheels [97, 98]. Matlab, Simulink, and Stateflow are commonly used since they allow for modeling at vehicle- and at system-levels, which simplifies the transition between these two analyses. Optimization tools are also widely available and can be easily parametrized. Overall, the flexibility of this framework is particularly interesting as the modeling methods are directly chosen by the user. For example, power electronics can be partly implemented with averaged models to emphasize the dynamic behavior and the control, while other converter characteristics, such as the efficiency, can be modeled with look-up tables. By doing so, the simulation offers accurate results in an acceptable computational time. Moreover, the integration of innovative power electronics and the development of new control strategies are not limited to commercialized vehicles. On the other hand, using Mathworks raises some challenges. Indeed, prior knowledge in electrified powertrain is necessary to ensure the proper operation of the vehicle model. Hence, setting up a simulation model is a time-consuming task and requires substantial expertise. Moreover, as each model is unique, an unified worldwide nomenclature is essential to improve the exchange of the models in the industry and accelerate the time-to-market process.

Driven by the need for a common platform gathering a large array of EVs, many vehicle-level software programs have emerged. Among the most popular tools, one can cite ADVISOR developed by National Renewable Energy Laboratory [99]. This vehicle simulator was composed of steady-state models and allowed for fuel economy and performance assessments. Since 2004, ADVISOR has been phased out and other simulation tools are used to characterize the effects of new technologies on the vehicle operation and cost [100]. Another famous vehicle model, called PSAT, was developed in Matlab/Simulink by Argonne National Laboratory and offered more accurate results than ADVISOR by modeling the

powertrain components as combinations of averaged models and look-up tables [99]. In 2010, PSAT is replaced by a state-of-the-art simulation tool called Autonomie, which is today considered as the primary reference by the U.S DOE [101, 102]. This Matlab-based environment features standard architectures on a plug-and-play basis where components can be quickly integrated and replaced [103]. Vehicle models are developed with extensive test validation realized on several commercialized vehicles with different degree of electrification. Thus, Autonomie enables performance analysis and vehicle energy consumption with a large database of components, powertrain configurations and drive cycles. Although this simulation tool allows for customizable plant and controllers, its predefined graphical user interface makes the integration of new power converters challenging. Indeed, every subsystem needs to have the same number of inputs and outputs to ensure the proper operation of the software. Hence, simulating new components or powertrain configurations that have not been commercialized yet is rather limited.

In conclusion, numerous simulation tools have been developed over the past few years and there is a clear trend for flexible, accurate, and automated platforms to evaluate the component performance in electrified powertrains. Mathworks tools offer detailed analysis for a specific powertrain where new technologies and controls can also be implemented in the model. However, in-depth expertise is required due to the restricted support for modeling the whole powertrain. On the other hand, Autonomie enables rapid architecture comparisons and high-level performance assessment such as supervisory control, fuel economy, and cost. Detailed models and control can also be integrated if they follow the same format than the one defined in the graphical interface. However, this simulation tool shows some limitations regarding the customization of powertrains with unconventional architectures and components.

Chapter 3

Traction inverters in electrified vehicles

National laboratories, OEMs, and suppliers have been working together to improve the ETDS including the traction inverter. Regarding the previous inverter objectives defined by the U.S DOE for 2020, a 30 kW continuous (55 kW peak) design is expected to achieve a power density of 13.4 kW/L and a specific density of 14.1 kW/kg at a cost of $3.3/kW for 100,000 units. Several OEMs and Tier 1 suppliers have already overcome some of the barriers. For example, Delphi disclosed a 55 kW peak traction inverter with 15 kW/L and 17 kW/kg [104]. However, the cost remains the biggest challenge as the inverter reached $5/kW. As previously mentioned, the U.S DOE recently updated the objectives to accelerate the market integration of EVs and suggested new targets for 2025 [8]. For the inverter power module composed of an inverter and, if applicable, a DC/DC boost converter, a 100 kW integrated design with 100 kW/L at $2.7/kW is expected. This represents respectively 18% and 87% cost and volume reductions compared to the 2020 goals.

In the following, the standard traction inverters implemented in commercialized vehicles are reviewed and alternative candidates are discussed. Then, typical control strategies are

compared. Finally, practical inverter design considerations including a review of the inverter components and the design driving factors are presented.

3.1 Standard industry solutions

Due to their high efficiency and low cost, the clear majority of production EVs today utilize three phase VSI based on insulated gate bipolar transistors (IGBTs). As shown in Fig. 3.1, the battery pack can be either directly connected to the inverter DC input (Fig. 3.1a), or a DC/DC boost converter can be used to step up the battery voltage and supply the inverter with a controlled DC voltage (Fig. 3.1b). In both circuits, a large DC-link capacitor C_{dc} smooths the ripple current and voltage generated by the switching action of the active devices. This ensures that the DC-link voltage is nearly constant and reduces the high frequency current harmonics. The VSI topology requires six switches which are modulated to generate a three-phase sinusoidal output current to the EM [105].

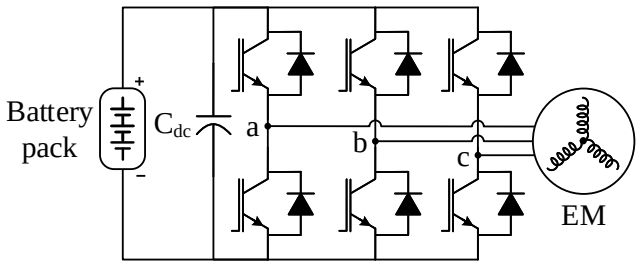

(a) VSI.

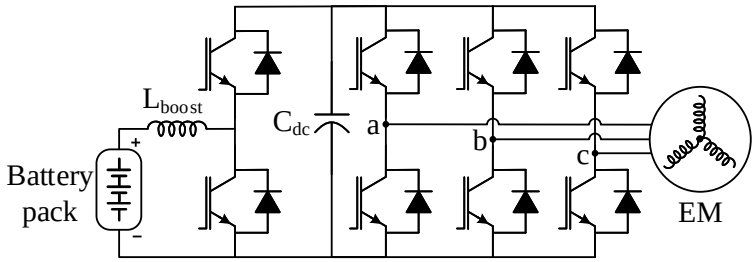

(b) VSI combined with a DC/DC boost converter.

Figure 3.1: Standard inverter topologies used in the automotive industry.

Thanks to its single conversion stage, the architecture shown in Fig. 3.1a is cheap, easy to manufacture, and requires simple control of the switching devices. Moreover, the VSI has been intensively studied and widely used in the industry over the past decades, which makes this topology mature, robust, and reliable. In motor drive applications, the phase currents are nearly sinusoidal since they are filtered by the leakage inductance of the EM, minimizing the machine losses. The output voltage harmonics can be reduced by selecting the appropriate modulation technique and will be further discussed in Section 3.3.

On the other hand, the VSI does have some drawbacks when applied to electrified powertrains. Primarily, the VSI acts as a buck type topology which means that the peak line-to-line AC output voltage is always lower than the DC bus voltage. As a result, the torque-speed characteristic of the EM is limited by the battery voltage which would need to be increased in order to improve the EM performance, particularly at high speeds. To do so, a larger battery pack is required, increasing the weight, size, and cost of the overall powertrain. One can also note that both the VSI and the EM achieve low efficiency in the low speed and light load area because of the fixed DC voltage imposed by the battery pack. Due to the switching actions of the devices, a large DC-link capacitor is necessary to filter the voltage on the DC side and protect the battery, adding significant cost and size to the inverter [106]. Additional considerations must be taken to prevent a short-circuit condition from occurring in the VSI, in which the top and bottom switches in a phase leg are both turned on simultaneously. This is achieved through adding a dead-time between turning off one switch and the turning on of the next. However, this dead-time adds a nonlinearity to the modulation resulting in distortion of the AC output current which translates to harmonics in the torque output of the EM and generates additional losses.

By stepping up the battery voltage with a DC/DC converter as shown in Fig. 3.1b, the torque-speed characteristic of the EM can be extended. The current rating of the switching devices is also reduced while keeping a battery pack voltage fairly low. Another advantage of using a DC/DC converter is the capability to supply the inverter with an adaptable DC

voltage that varies regarding the driving requirements. By doing so, the high efficiency areas of the inverter and EM can be enlarged, and the inverter output voltage distortions can be reduced [52, 107]. While the combination of the VSI with a DC/DC boost converter overcomes many gaps of the VSI, adding a power converter also shows some demerits. Due to the series connection between the battery pack and the DC/DC converter, they both need to have similar power ratings in order to fully utilize the battery power. Hence, a large battery pack implies a sizable DC/DC converter where the inductor L_{boost} is usually heavy and expensive. Additional control is also necessary to adjust the variable voltage accordingly which increases the complexity of the system.

Overall, either used by itself or in combination with an additional DC/DC boost converter, the VSI is still the most widely used topology as it offers a good trade-off between performance, control complexity, cost, and size of the electrified powertrain.

3.2 Alternative candidates

Many alternative topologies have been proposed including soft switching inverters and multi-level inverters. Most circuits require additional power switches and passive elements beyond the standard VSI, which increases not only the cost, but also the control complexity, volume, and weight of the system. For any topology to be seriously considered by the automotive industry, it must be able to compete on cost regardless of what other benefits it may present. In the following, three inverter topologies with potential value for the industry, namely the current source inverter, the Z-source inverter, and three-level inverters, are reviewed and their competitiveness for electrified powertrains is analyzed.

3.2.1 Current source inverter

The current source inverter is a traditional inverter that converts power from a DC current source to an AC output [105]. A DC voltage source, such as a battery pack, can also be

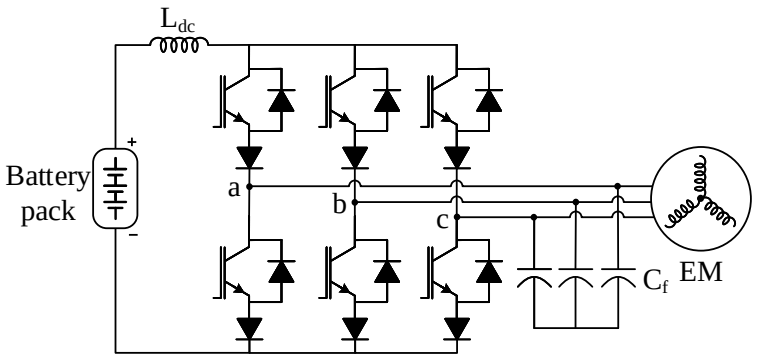

Figure 3.2: Current source inverter circuit with IGBTs in series with diodes.

used if it is connected in series with a large inductor L_{dc}, as shown in Fig. 3.2. Unlike the VSI, the output AC voltages are almost sinusoidal, which makes this topology suitable for applications where high-voltage quality is a major concern. The circuit is composed of six switching devices that need to withstand bidirectional voltage and ensure unidirectional current flow. Symmetric thyristors or IGBTs in series with diodes are common solutions implemented in the industry. For motor drive applications, capacitor banks C_f are required on the AC output due to the high distortion of the phase currents caused by the switching action.

Among the advantages of using the current source inverter, one can cite its capability of boosting the input voltage to produce an AC output peak voltage higher than the DC input voltage. This eliminates the need for a separate DC/DC boost converter and extends the constant power range of the EM by providing sufficient output voltage [108]. Regarding the control of the switching devices, it can be noted that only one top switch and one bottom switch must be turned on at the same time since the capacitors on the AC side should not be short-circuited and the current source cannot be opened. As a result, a short circuit through the switches in the same phase leg is not an issue in the current source inverter, unlike in the VSI as previously mentioned.

Nevertheless, the current source inverter has downsides that restrain its use in electrified powertrain. In order to avoid an open circuit on the DC side that would destroy the

devices, an overlap time should be implemented in the control of the switches, which also causes current and voltage distortions. Furthermore, while the significant reduction of the capacitive filter can improve the power density of the inverter, there is still a need for a DC-link inductor that is usually bulky and heavy in high power applications. Practically, the lower efficiency and higher cost compared to the VSI have prevented the adoption of the current source inverter in automotive traction applications [109].

3.2.2 Z-source inverter

The Z-source inverter combines some characteristics of the VSI and current source inverter where either a voltage or current source can be directly connected to its input terminals [110]. For example in Fig. 3.3, a battery pack supplies power to the AC load and the circuit uses six semiconductor devices that require unidirectional voltage blocking capability and bidirectional current flow. The uniqueness of the topology lies in its DC-link filters that are composed of two capacitor banks, C_1 and C_2, connected in X shape and two inductors L_1 and L_2. With an appropriate control of the switches, the Z-source inverter can operate as a buck-boost inverter since it is capable of producing an AC output voltage either higher or lower than the DC input source. When a buck operation is required by the load, similar modulation strategies as for the VSI are applied. If boost operation is necessary, an adapted control that uses the shoot-through zero states is implemented to step up the voltage.

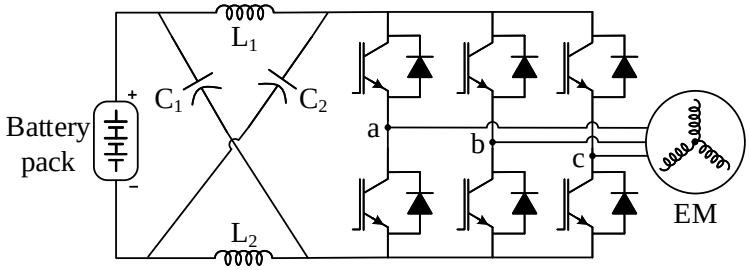

Figure 3.3: Z-source inverter circuit.

The Z-source inverter could be a suitable alternative solution for electrified powertrains

due to its buck-boost feature since DC sources, such as batteries, have a wide voltage range [111, 112]. Moreover, unlike VSI and current source inverter topologies, shoot-through and open circuit are not destructive status for the switches in the Z-source inverter, enhancing the reliability of the inverter. Compared to the standard topologies mentioned in Section 3.1, this inverter provides higher or similar efficiency than respectively the VSI and the combination of the VSI with a DC/DC boost converter [113]. However, even though the number of active devices is low, the passive component requirements are higher in the Z-source inverter. Hence, the cost and volume still held this topology back from the automotive industry.

3.2.3 Three-level inverters

Over the past few years, three-level inverters have gained interest in the industry as alternative solutions to the standard VSI. Among the many topologies that have been developed, the Neutral Point Clamped (NPC) and the T-type NPC (TNPC) are the most competitive solutions for medium to high voltage applications [114–117]. Fig. 3.4a and Fig. 3.4b show the power circuits of the NPC and TNPC inverters respectively. The NPC topology consists of four power semiconductors and two clamping diodes per phase leg, while the TNPC topology is similar to the VSI with an additional center leg composed of a bidirectional switch for each phase leg. In both circuits, the input capacitor bank is split into two capacitors C_{dc} that have a voltage rating equal to half the DC-link voltage.

Advanced studies have highlighted several benefits of three-level inverters [118, 119]. An efficiency analysis for a wide range of switching frequencies has been conducted to compare the VSI, the NPC, and the TNPC inverters. Results show that the efficiency of the VSI is higher only for low frequencies and drops significantly above 10 kHz. On the other hand, the TNPC is more efficient for medium frequencies between 10 kHz to 30 kHz, while the NPC becomes slightly more efficient for frequencies above 30 kHz. Thanks to the neutral point (N) connected between the two capacitors in Fig. 3.4, three-level inverters provide output

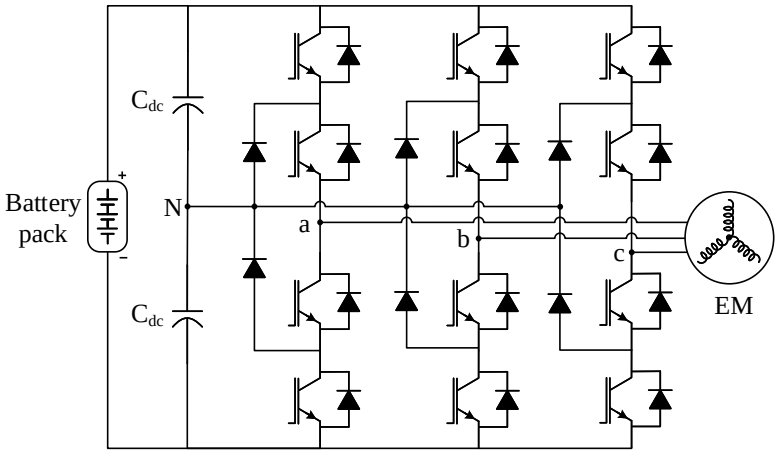

(a) NPC topology.

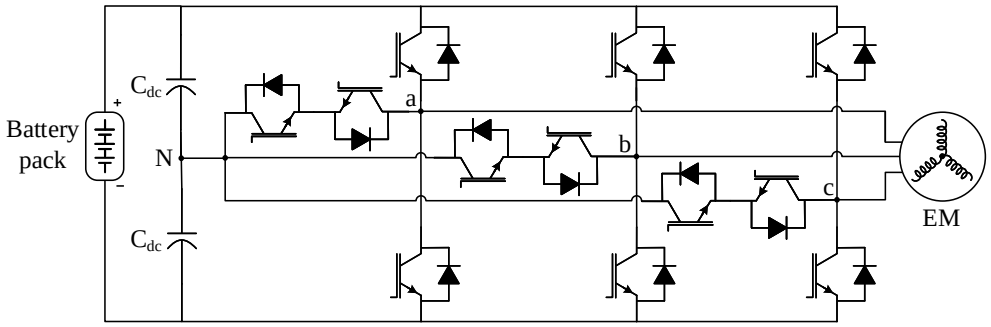

(b) TNPC topology.

Figure 3.4: Three-level inverter configurations.

voltages with lower harmonic distortion than the VSI, reducing the filter requirements and improving the efficiency of the motor. Nevertheless, the volume of the capacitor banks for three-level inverters is twice that of the VSI and additional control is required to ensure DC-link voltage balancing. Moreover, both topologies suffer from high cost and increased control complexity due to a high part count.

3.3 Modulation techniques

The AC output voltages produced by the inverter and feeding the EM are generated thanks to the use of PWM techniques that switch the power semiconductors in a desired pattern.

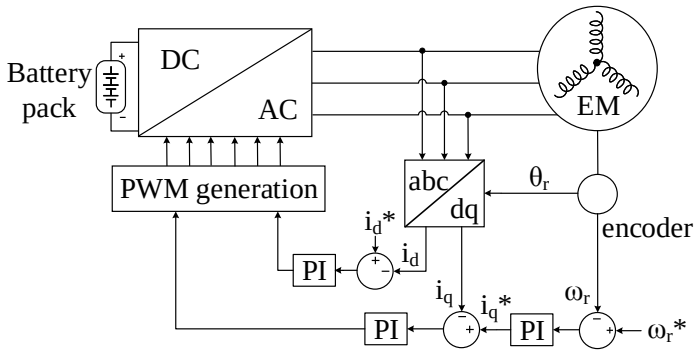

Figure 3.5: Closed loop control scheme of an EM.

Fig. 3.5 shows the speed-torque control scheme of an EM. Closed-loop control is achieved by the inverter through phase current and rotor position feedback, thus requiring at least two phase current sensors in the inverter and a suitable interface for a resolver or encoder from the EM.

It has been shown in the previous sections that, despite the many topologies suggested in the literature, only the VSI and its combination with a DC/DC boost converter are used in electrified powertrains today. Hence, this section focuses on the modulation strategies for the standard VSI and will discuss the most popular techniques, namely the sinusoidal PWM (SPWM) and space vector PWM (SVPWM). Due to the switching action of the devices, the AC output voltages and currents are not purely sinusoidal but a combination of a sinusoidal fundamental component with several harmonics. This is an issue since the current harmonics contribute to the copper losses in the motor windings and have an impact on the torque ripple. Indeed, the harmonic losses in the load are proportional to the RMS value of the ripple current [120]. The harmonic spectrum also influences the acoustic noise emissions in motor drives [121, 122]. Hence, the proper PWM technique must be selected based on the trade-off between control complexity, efficiency, acoustic quality, and electromagnetic interference emissions.

3.3.1 SPWM

The SPWM is one of the most classic techniques used in the industry due to its simplicity [120]. It was first developed with analog circuits, but digital implementation is now a standard procedure. The switching pattern is obtained by comparing a triangular carrier signal operating at a desired switching frequency, with three modular sinusoidal waveforms out-of-phase by 120° and operating at a fundamental frequency much lower than the switching frequency. The fundamental output voltage amplitude is linearly controlled by the modulation index which varies between 0 to 1. One drawback of this modulation scheme is its limited use of the DC-link voltage V_{dc} since the maximum amplitude of the fundamental output phase voltage is $V_{dc}/2$. Moreover, this method generates relatively high total harmonic distortion in the line voltages compared to other techniques, causing higher harmonic losses.

3.3.2 SVPWM

Despite its intensive computational requirements, SVPWM has gained popularity as the widespread adoption of digital signal processors and microcontrollers enabled low cost implementations [120,123]. Its fundamental purpose is to synthesize the output line voltage by applying three switching state vectors during a specific switching time. Since two switches of the same phase leg cannot be simultaneously turned-on, the VSI can operate in eight switching states defined by space vectors. Two of them are called zero vectors since they produce zero AC line voltage, as their name suggest. As a result, the AC line voltage is defined as a combination of the two adjacent state vectors and one zero vector.

Although the SVPWM technique is more complex than the SPWM, it achieves better performance by generating output voltages and currents with reduced harmonic distortion, improving the efficiency of the inverter as well as the EM. Furthermore, the maximum fundamental amplitude of the phase voltage is equal to $V_{dc}/\sqrt{3}$, which is about 15% higher

than the SPWM method in linear region [124, 125]. Hence, the SVPWM enables a better DC link utilization, which can be even further extended through six-step operation in the over modulation region.

Though it is challenging to confirm which modulation strategy is used for the traction inverters in every electrified vehicle, it is believed that the SVPWM is preferred due to its performance superiority. For example, it has been reported in [126, 127] that General Motors employs the SVPWM for the linear region.

3.4 Practical inverter design considerations

As one of the essential systems of the powertrain, traction inverters play a major role in the performance and competitiveness of the vehicle. At mass production scale, there are many design considerations which can ultimately be traced back to four primary objectives: cost, reliability, efficiency, and power density. Each inverter component affects these parameters, requiring trade-offs in order to provide the most suitable product given the vehicle requirements.

3.4.1 Inverter components

Power semiconductor sales continue to grow as the EV market expands. IGBTs have always been the predominant choice for inverters compared to other switching devices due to the maturity of the technology, its wide availability, low cost, and sufficient power capability. IGBTs with a blocking voltage of 650V to 1200V can easily handle today's battery pack voltages which vary from 200V to 450V in most EVs. Furthermore, power modules with high current capability or discrete devices connected in parallel have emerged as solutions in response to high power demands.

Gate drivers are greatly responsible for the efficiency of the inverter as they influence the dynamic behavior of the IGBTs and the freewheeling diodes. They are composed

of integrated circuits that transmit isolated control signals to switch the device and provide protective feedback. For high voltage applications, such as traction inverters, most integrated circuits use optocouplers or pulse transformers due to their high isolation capabilities [128]. The gate driver design needs to consider the factors influencing the switching performance. Several approaches have been developed, from passive circuits using external gate-emitter capacitors and gate resistors to closed-loop control that adjust the signal based on the IGBT operation [129].

The DC-link capacitor is a crucial component of the inverter as it protects both the input source and the power devices from hazardous current and voltage spikes. The proper selection is based on the ripple current and the capacitance calculated from ripple voltage requirements [130, 131]. Compared to electrolytic capacitors, film capacitors have shown many benefits for inverter applications where high current ripple capability is a concern while high capacitance is less a priority. Indeed, a more power-dense, efficient, and low-cost design can be achieved with film capacitors, as shown in [106]. Moreover, while temperature variations affect both technologies, electrolytic capacitors are particularly sensitive, with every 10 °C rise reducing the lifetime of the capacitor by approximately half [132].

Due to the continuous power requirement increase, heat dissipation has become a critical concern in inverter design. In fact, high temperatures have been identified as the primary sources of failure and overheating dramatically reduces the reliability of the power converters and shortens their lifetime [133, 134]. Hence, thermal management systems, such as heat sinks, have become staple components and optimizing their design is a challenging task as they require advanced loss and thermal models [135–138]. Many cooling techniques have been studied over the years [139]. Liquid cooling is commonly preferred in high power inverters since they efficiently dissipate more heat in a limited space compared to forced air cooling. They also operate better regardless of the ambient environmental conditions.

Bus bars are commonly used in high power inverters due to their superior current capability compared to printed circuit boards (PCBs) and higher power density compared to

wires. Their design is a complex procedure that requires many considerations such as the shapes of the DC-link capacitor and power devices, the thermal management system, the current density, and the operating environment [140]. Particular attention must be paid to minimize any parasitic inductance introduced by the bus bar connections which can have a significant effect on surge voltages during switching.

3.4.2 Cost

For true mass market adoption of EVs to occur, there must be a compelling economic case in addition to the environmental one. The traction inverter in a production BEV today can make up approximately 5% of the powertrain cost [141]. Cost reductions from all aspects of the electrified powertrain must be achieved to reach parity with ICE counterparts and the inverter is no exception.

Even though the power rating and, thus, the cost of an inverter varies with the vehicle requirements, the component cost share stays roughly similar. For example, Fig. 3.6 shows the cost breakdown of the 75 kW inverter module of the Audi A3 e-Tron 2016 [36]. In order to maximize the packaging, the enclosure integrates a single traction inverter, an APM, a control board, and a liquid cooling system shared by the converters. The control board enables interfacing with the vehicle supervisory system and ensures the communication between both power converters. The inverter accounts for 46.3 % of the total cost. Regarding the component cost breakdown of the inverter itself, the power semiconductors and their control are significant contributors with respectively 25.3% and 36%. The DC-link capacitor banks also highly effect the cost with 18.9%.

Multiple approaches are undertaken to lower the cost of power electronics systems. For the 55 kW inverter project, Delphi focused on developing new 'Viper' IGBT modules and high temperature capacitors [104, 142]. The cost breakdowns of this inverter and the potential future inverter meeting the 2025 targets are provided in [8]. Integrated technologies combining mechanical, electrical, and thermal properties seem to be the key to optimize

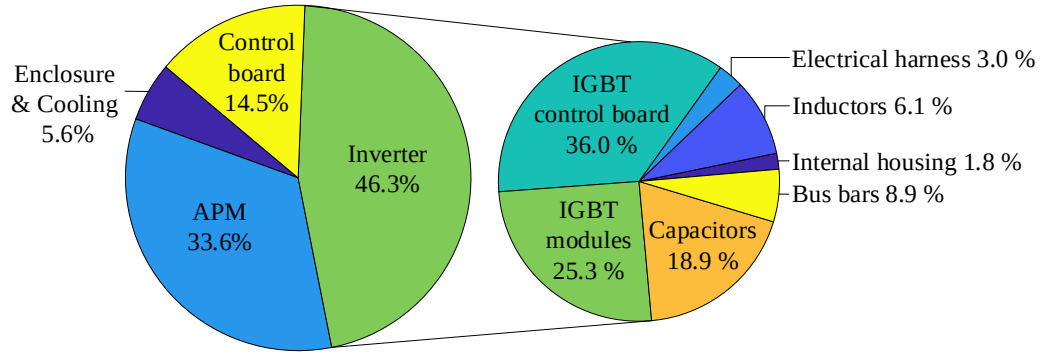

Figure 3.6: Component cost shares of the inverter module in the Audi A3 e-Tron.

system designs for volume production and provide affordable products.

3.4.3 Reliability

Reliability is of critical interest due to the extreme sensitivity to fault occurrences in the automotive market. Methods to detect failures at an early stage and estimate the component failure rate have greatly improved [143, 144]. System transients, heavy loads, and environmental conditions, such as extreme temperatures, mechanical vibrations, and humidity, are the most common causes of failure regardless of the application sector. In Fig. 3.7, the fault distribution in power converters is presented. Capacitors, power devices, and PCBs are the most vulnerable components with 30%, 26%, and 21% failure rate respectively [145].

Semiconductor devices are particularly sensitive to short- and open-circuit events depending on the converter. When a fault occurs, wire bond connections and solder joints are the weakest points of the modules. Advanced models have been developed by taking into account the thermal, electrical and mechanical stresses [146–148]. By doing so, a lifetime prediction can be achieved considering the application of the devices. Moreover, such models can be used to improve fault detection methods [149]. Analysis of failures modes in DC-link capacitors and lifetime models can be found in [150]. Ceramic, aluminum, and film capacitors are compared, and a reliability-oriented design procedure is suggested based

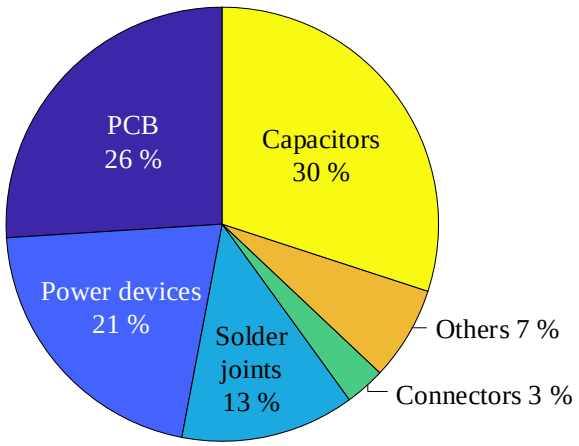

Figure 3.7: Fault distribution in power converters.

on the application.

Since traction inverters are mainly composed of switching devices and DC-link capacitors, they are particularly subjected to failure events. Based on the failure rate of each component, the global reliability, and the lifetime can be estimated [151, 152]. In the VSI topology, short-circuit of the devices is the most destructive event and special control methods, such as the implementation of a dead-time and device desaturation detection are required to improve the reliability of the converter. Fault tolerant inverter topologies have also been studied to replace the traditional VSI [153]. For example, switch-redundant topologies and cascaded inverters have shown significant reliability improvement, at the expense of cost increase. Reducing the thermal stress with larger heat sinks and better coolant is another solution to improve the reliability, which can adversely impact on the power density of the system. Overall, reliability is a driving factor in inverter design as it requires many trade-offs to provide a cheap but safe product.

3.4.4 Efficiency

Operating at high efficiency reduces fuel consumption and extends the vehicle driving range by saving energy from the battery pack. It also allows for smaller thermal management

systems, which enables lower cost, higher power density, and improved reliability.

As previously mentioned, the combination of the VSI with a DC/DC converter achieves higher efficiency compared to the simple use of the VSI under several operating conditions [52, 107]. This is due to the variable input voltage that feeds the inverter. Indeed, adapting the voltage regarding the power requirements enables the inverter to operate at high modulation index which reduces the losses.

Regarding the loss breakdown in a VSI, most losses are generated by the power semiconductors. The conduction losses vary quadratically with the load current and the switching losses are linearly dependent on the switching frequency and the load current. As a result, the conduction losses are dominant in case of heavy load and low switching frequencies. On the other hand, the switching losses prevail at high switching frequencies, regardless of the current load [109, 118, 136]. In [106], the power losses in aluminum and film capacitors are calculated for different power factors, ambient temperatures, and modulation strategies. They both generate negligible losses compared to the operating power of the inverter. The other components such as the gate drivers, the bus bars, and the PCBs have also limited impact on the efficiency of high power inverters. Thus, they will not be further discussed.

3.4.5 Power density and specific power

By convention, the power density refers to the power-to-volume ratio, measured in W/L, while the specific power represents the power-to-weight ratio, expressed in W/kg. They are both of interest since a compact design allows for easier integration in the powertrain and larger passenger space in the car. Furthermore, light systems lead to lower energy consumption to carry them in the vehicle.

As mentioned earlier, traction inverters are composed of multiple components and their selection depends on the OEM strategy. Hence, the total volume and weight greatly varies between the brands. In Table 3.1, the power density and specific power of the inverter modules for different OEMs are compared. It should be kept in mind that these figures

Table 3.1: Comparison of inverter modules in recent EVs.

Model	DOE targets EV (2025) [8]	Toyota Prius HEV (2016) [58]	Audi A3 e-Tron PHEV (2016) [36]	Nissan LEAF BEV (2012) [154]
Components	Inverter[a]	PCU	Inverter and APM	Inverter
Peak power rating (kW)	100	55	75	80
Power density (kW/L)	100	7.8	9.4	7.1
Specific power (kW/kg)	-[b]	4.5	7.4	4.8

[a] including a DC/DC boost converter if applicable.
[b] value not reported.

do not refer to the traction inverter itself but to the integrated module. Indeed, most modules are composed of the traction inverter and other converters such an APM, a DC/DC boost converter, and the heat sink to maximize the packaging. More details regarding the composition of the modules are given in [12].

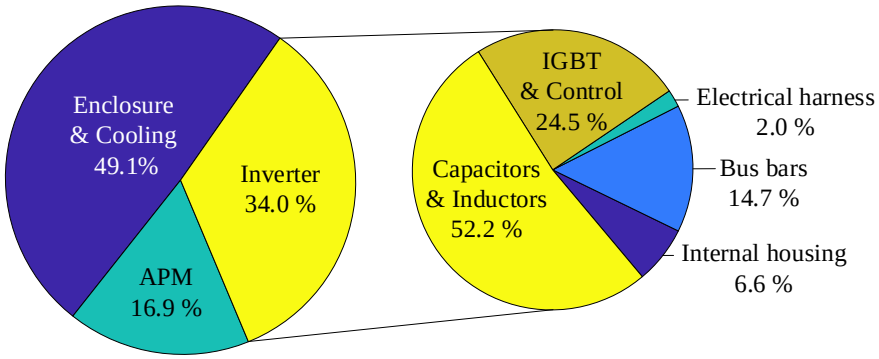

Figure 3.8: Component weight breakdown of the inverter module in the Audi A3 e-Tron.

Calculating the volume breakdown of each component is challenging due to their complex shape. However, the weight breakdown is more accessible, and Fig. 3.8 shows the weight share of the inverter module in the Audi A3 e-Tron [36]. It can be seen that the enclosure and the heat sink are the heaviest component of the module. This is due to the fact that they are both plain die cast aluminum components. In the inverter, the weight share is

dominated by the capacitor and inductors that account for 52.2%. As a result, the specific power could be greatly increased by improving the packaging of the cooling system and the passive components.

Some OEMs and Tier 1 suppliers achieved significant improvements by using IGBT modules with double sided cooling. By improving the heat transfer from the semiconductors to the cooling plate, the system can operate at high current ratings while keeping a DC voltage between 400V to 700V. The 55 kW inverter from Delphi reached 15 kW/L and 17 kW/kg by using the Viper IGBT modules [155]. Hitachi also achieved an impressive power density of 35 kW/L for its integrated inverter module composed of an inverter and an APM [59].

Chapter 4

On the concept of the multi-source inverter

4.1 Introduction

Despite the wide array of inverter topologies, nearly all contemporary EVs integrate only one kind of inverter: the renowned VSI. In a simple electrified powertrain architecture, this converter directly connects the battery pack to the EM without the use of any additional power electronics. Although this configuration is affordable and power-dense, it also achieves low efficiency at light load due to the use of a fixed DC-link voltage. Furthermore, the EM performance is limited by the constant battery voltage. Some electrified powertrains, such as in the Toyota Prius presented in Section 2.2.3, use a DC/DC boost converter in conjunction with the VSI, as shown in Fig. 4.1a. By doing so, the battery voltage can be stepped up regarding the driving requirements. One major benefit of this adaptable voltage is the extension of the high efficiency areas for both the inverters and the EMs. The constant torque-speed characteristic of the EMs can also be enlarged without the need for a higher battery voltage. However, the power density of DC/DC converters are mostly affected by the sizable inductor. Due to the continuous increase of the power requirements in modern

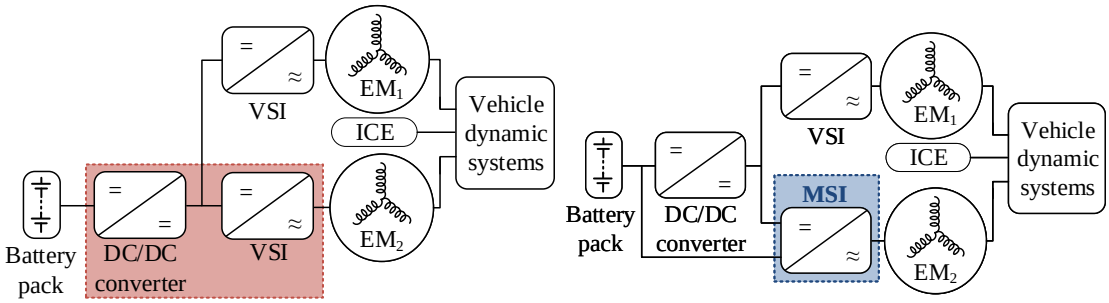

(a) Conventional power-split powertrain. (b) Suggested powertrain with the MSI.

Figure 4.1: Hybrid powertrain comparison.

electrified powertrains, the volume and weight of the DC/DC converter might undermine the benefits of using this configuration. Moreover, this converter limits the battery pack power rating since they are connected in series. Hence, extending the electric driving range requires more trade-offs between performance, cost, and power density, compared to the simple architecture. Overall, there is a need for innovative solutions that keep the advantages of current industry configurations while limiting the downsides.

This chapter presents an inverter topology named the multi-source inverter (MSI) [9]. Its fundamental purpose is to connect two distinct DC sources to the same AC output using a single conversion stage. Due to its dual DC source, this power converter can be implemented in power-split architectures, such as those used in the Toyota Prius. Compared to the conventional configuration that integrates a DC/DC converter connected in series with the battery pack, the suggested powertrain with the MSI connects the battery to one DC input, while the other source is provided by the high DC-link voltage shared between the two inverters, as displayed in Fig. 4.1b. By a simple control of the switches, it will be shown in the following that either one source or a combination of both can drive the wheels, depending on the power requested by the driver. This means that the MSI can operate in three distinct operating modes during the DC/AC conversion and can supply power to the EM with a variable DC voltage. In a specific mode, the battery directly provides power to the EM without using the DC/DC converter. Thus, the high power DC/DC converter

can be dissociated from the traction system in some driving conditions. The efficiency of the electrified traction drive is also expected to improve due to the single conversion stage between the battery and the EM. On the other hand, traction inverters applied in electrified powertrains are bidirectional as they need to transfer power when the EM operates as a motor and a generator. By using IGBT/diode modules, it will be shown that the MSI can also act as a rectifier and two operating modes are available. In each rectifier mode, the power generated by the EM is provided to one DC input, while no power is transferred to the other. In other terms, one operating mode allows for the charge of the battery directly by the EM and the DC/DC converter is bypassed. Overall, the use of the additional DC/DC converter can be limited when the MSI operates as an inverter and a rectifier. This aims to reduce the power rating of the DC/DC converter.

In the following sections, the MSI topology and the operating modes in both DC/AC and AC/DC conversions are first presented. Due to the uniqueness of the circuit, the conventional control strategies presented in Section 3.3 cannot be applied and new adapted PWM techniques are suggested. Then, the theoretical operations and the control are verified through simulations with Matlab/Simulink. Finally, a scale-down prototype has been built and experimentally tested in closed-loop control with an induction motor (IM) and a load. Experimental results validate the concept of the proposed topology.

4.2 Topologies

The MSI is a power converter which aims to connect several DC sources to the same AC output using a single conversion stage. For instance, Fig. 4.2 depicts the topology with two DC sources, namely V_{dc1} and V_{dc2}, connected between (P_1) and (O), and (P_2) and (O).

By replacing the ideal switches $Q_{1,k}$, $Q_{2,k}$, and $Q_{3,k}$, where k=a, b or c is the corresponding phase leg, by IGBTs and diodes, the MSI can be modeled with two different configurations as shown in Fig. 4.3. Fig. 4.3b shows the circuit of MSI_1 where each phase

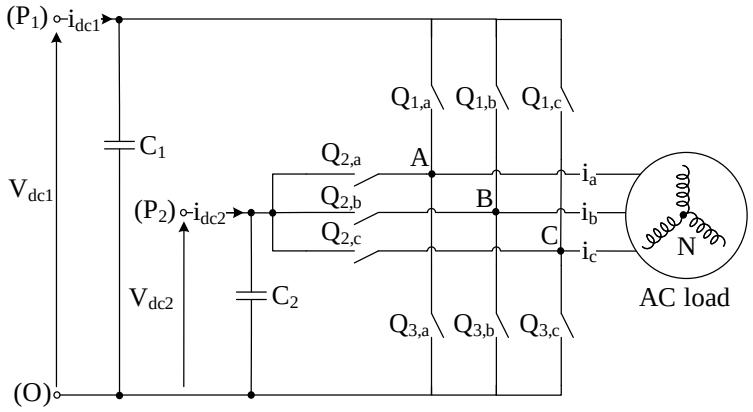

Figure 4.2: MSI topology with two DC sources.

leg is composed of four IGBTs and freewheeling diodes, namely $T_{1,k}/D_{1,k}$ to $T_{4,k}/D_{4,k}$, and two clamping diodes $D_{5,k}$ and $D_{6,k}$. On the other hand, Fig. 4.3c shows the MSI_2 circuit where $Q_{1,k}$ and $Q_{4,k}$ are replaced by simple IGBT/diode modules $T_{1,k}/D_{1,k}$ and $T_{4,k}/D_{4,k}$, while $Q_{2,k}$ consists of two devices $T_{2,k}/D_{2,k}$ and $T_{3,k}/D_{3,k}$ sharing a common emitter. This enables the active control of the current flow in both directions in the middle phase leg.

Although the MSI_1 and MSI_2 topologies seem similar to the NPC and TNPC circuits introduced in Section 3.2.3, the connections on the DC side greatly differ from the three-level inverters. Indeed, in conventional three-level inverters, a single input DC source is connected between (P_1) and (O) while the upper devices (formed by the switches between (P_1) and (P_2)) and lower devices (composed of the switches between (P_2) and (O)) are connected to a neutral point (P_2). By doing so, an additional DC voltage level equal to zero is generated, reducing the harmonic distortion of the output voltages and currents. Moreover, the voltage across the input series-connected capacitors is one half of the DC input voltage. On the contrary, the MSI does not have a neutral point and the upper and lower devices are not connected to each other by (P_2). As a result, two independent DC sources can be applied with distinct input capacitor banks C_1 and C_2. This leads to asymmetrical voltage ratings and current waveforms, impacting on the design requirements and the efficiency. More details will be provided in Chapter 5. Furthermore, the control

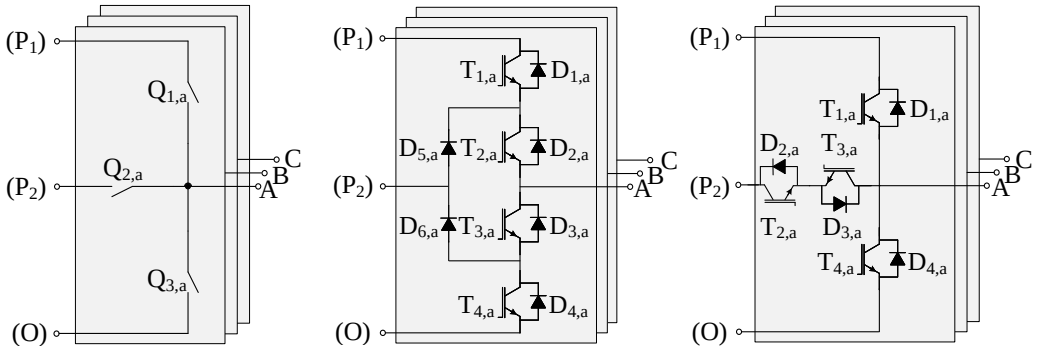

(a) Ideal switches. (b) MSI_1 circuit. (c) MSI_2 circuit.

Figure 4.3: MSI topologies.

methods for the MSI clearly differ from those used for three-level inverters, which will be further discussed in Section 4.4.

4.3 Operating modes

4.3.1 DC/AC conversion

Depending on the state of the switches in Fig. 4.2, it can be seen that the MSI is composed of three standard VSI. Hence, during the DC/AC conversion, the MSI can operate in three distinct operating modes where three different DC voltages are applied to the output line-to-line voltages:

- Mode I_1: The source V_{dc2} supplies the load by using the switches $Q_{2,k}$ and $Q_{3,k}$. The upper switches $Q_{1,k}$ are always turned off and V_{dc1} is not used;
- Mode I_2: The source V_{dc1} supplies the load while charging V_{dc2}. The switches $Q_{1,k}$ and $Q_{2,k}$ are used and the voltage applied to the output is equal to V_{dc1}-V_{dc2}. The lower switches $Q_{3,k}$ are always turned off;
- Mode I_3: Only V_{dc1} supplies the load by using the switches $Q_{1,k}$ and $Q_{3,k}$. The switches $Q_{2,k}$ in the middle phase leg are always turned off and V_{dc2} is not used.

The line-to-line voltages [V_{AB},V_{BC},V_{CA}] and phase voltages [V_{AN},V_{BN},V_{CN}] are calculated with the well-known formulas as in (4.1) and (4.2).

$$\begin{aligned} V_{AB} &= V_{AN} - V_{BN} \\ V_{BC} &= V_{BN} - V_{CN} \\ V_{CA} &= V_{CN} - V_{AN} \end{aligned} \tag{4.1}$$

$$\begin{bmatrix} V_{AN} \\ V_{BN} \\ V_{CN} \end{bmatrix} = \frac{1}{3} \begin{bmatrix} 2 & -1 & -1 \\ -1 & 2 & -1 \\ -1 & -1 & 2 \end{bmatrix} \times \begin{bmatrix} V_{AO} \\ V_{BO} \\ V_{CO} \end{bmatrix} \tag{4.2}$$

From Fig. 4.2, the voltages [V_{AO}, V_{BO}, V_{CO}] can be derived as functions of the gate signal of the switches and the DC-bus voltages. They are expressed as in (4.3).

$$\begin{aligned} V_{AO} &= S_{Q1,a}V_{dc1} + S_{Q2,a}V_{dc2} - Z_a i_a \\ V_{BO} &= S_{Q1,b}V_{dc1} + S_{Q2,b}V_{dc2} - Z_b i_b \\ V_{CO} &= S_{Q1,c}V_{dc1} + S_{Q2,c}V_{dc2} - Z_c i_c \end{aligned} \tag{4.3}$$

where Z_k is the phase impedance of the load, and $S_{Q1,k}$ and $S_{Q2,k}$ are the switching functions of $Q_{1,k}$ and $Q_{2,k}$. By convention, it is considered that the switching function is equal to 0 if the switch is turned off and is equal to 1 if the switch is turned on. To prevent the topology from short-circuit events, the switches $Q_{3,k}$ are complementary to $Q_{2,k}$ in Mode I_1, $Q_{1,k}$ are complementary to $Q_{2,k}$ in Mode I_2, and $Q_{3,k}$ are complementary to $Q_{1,k}$ in Mode I_3.

According to the state of the switches in (4.3), it can be seen that the combination of the two DC sources enables supplying the load with seven different line-to-line voltages. Table 4.1 summarizes the switching combinations with the ideal switches and neglects the voltages produced by the impedance Z_k in each phase shown in (4.3).

When the ideal switches are replaced by IGBT/diode modules, $S_{Q1,k}$ and $S_{Q2,k}$ are not applicable anymore and (4.3) needs to be updated. According to Fig. 4.3b, the voltages

Table 4.1: Switching combinations of the MSI with ideal switches.

Modes	States of switches									Line-to-line voltages		
	$Q_{1,a}$	$Q_{1,b}$	$Q_{1,c}$	$Q_{2,a}$	$Q_{2,b}$	$Q_{2,c}$	$Q_{3,a}$	$Q_{3,b}$	$Q_{3,c}$	V_{AB}	V_{BC}	V_{CA}
I_1	Turned off			1	0	0	0	1	1	V_{dc2}	0	$-V_{dc2}$
				1	1	0	0	0	1	0	V_{dc2}	$-V_{dc2}$
				0	1	0	1	0	1	$-V_{dc2}$	V_{dc2}	0
				0	1	1	1	0	0	$-V_{dc2}$	0	V_{dc2}
				0	0	1	1	1	0	0	$-V_{dc2}$	V_{dc2}
				1	0	1	0	1	0	V_{dc2}	$-V_{dc2}$	0
I_2	1	0	0	0	1	1	Turned off			$V_{dc1} - V_{dc2}$	0	$-(V_{dc1} - V_{dc2})$
	1	1	0	0	0	1				0	$V_{dc1} - V_{dc2}$	$-(V_{dc1} - V_{dc2})$
	0	1	0	1	0	1				$-(V_{dc1} - V_{dc2})$	$V_{dc1} - V_{dc2}$	0
	0	1	1	1	0	0				$-(V_{dc1} - V_{dc2})$	0	$V_{dc1} - V_{dc2}$
	0	0	1	1	1	0				0	$-(V_{dc1} - V_{dc2})$	$V_{dc1} - V_{dc2}$
	1	0	1	0	1	0				$V_{dc1} - V_{dc2}$	$-(V_{dc1} - V_{dc2})$	0
I_3	1	0	0	Turned off			0	1	1	V_{dc1}	0	$-V_{dc1}$
	1	1	0				0	0	1	0	V_{dc1}	$-V_{dc1}$
	0	1	0				1	0	1	$-V_{dc1}$	V_{dc1}	0
	0	1	1				1	0	0	$-V_{dc1}$	0	V_{dc1}
	0	0	1				1	1	0	0	$-V_{dc1}$	V_{dc1}
	1	0	1				0	1	0	V_{dc1}	$-V_{dc1}$	0

$[V_{AO}, V_{BO}, V_{CO}]$ in the MSI_1 topology are given by (4.4).

$$\begin{aligned} V_{AO} &= F_{1,a}V_{dc1} + G_{1,a}V_{dc2} - Z_a i_a \\ V_{BO} &= F_{1,b}V_{dc1} + G_{1,b}V_{dc2} - Z_b i_b \\ V_{CO} &= F_{1,c}V_{dc1} + G_{1,c}V_{dc2} - Z_c i_c \end{aligned} \tag{4.4}$$

where $F_{1,k}$ and $G_{1,k}$ are defined by $F_{1,k} = S_{T1,k} \wedge S_{T2,k}$ and $G_{1,k} = S_{T1,k} \oplus S_{T2,k}$, with '$\wedge$' and '$\oplus$' the AND and XOR signs respectively in Boolean logic. Moreover, $S_{T1,k}$ and $S_{T2,k}$ are the switching functions of the switches $T_{1,k}$ and $T_{2,k}$. It should also be noted that the devices $T_{3,k}$ and $T_{4,k}$ are complementary to $T_{1,k}$ and $T_{2,k}$ respectively in the three operating modes.

In the MSI_2 presented in Fig. 4.3c, the voltages $[V_{AO}, V_{BO}, V_{CO}]$ are expressed as in (4.5).

$$\begin{aligned} V_{AO} &= F_{2,a}V_{dc1} + G_{2,a}V_{dc2} - Z_a i_a \\ V_{BO} &= F_{2,b}V_{dc1} + G_{2,b}V_{dc2} - Z_b i_b \\ V_{CO} &= F_{2,c}V_{dc1} + G_{2,c}V_{dc2} - Z_c i_c \end{aligned} \tag{4.5}$$

where $F_{2,k} = S_{T1,k}$ and $G_{2,k} = S_{T2,k} \wedge S_{T3,k}$. It can be noted that the switches $T_{3,k}$ and $T_{4,k}$ are complementary to $T_{1,k}$ and $T_{2,k}$ respectively in Modes I_1 and I_2. On the other hand, the switches $T_{4,k}$ are complementary to $T_{1,k}$ in Mode I_3.

Table 4.2 summarizes the device switching states and the input DC voltage applied to the load regarding the different operating modes of the MSI_1 and MSI_2. It can be noticed that the same control is used for Modes I_1 and I_2, while Mode I_3 is different.

One can also note that the DC source voltages should be selected as in (4.6). By doing so, the voltage $V_{dc1} - V_{dc2}$ applied to the load in Mode I_2 is positive and greater than V_{dc2}.

$$V_{dc1} > 2 \times V_{dc2} \tag{4.6}$$

Table 4.2: Device switching states of the MSI during DC/AC conversion.

Inverter modes	MSI topologies	Device switching states				Input DC voltages applied to the load
		$S_{T1,k}$	$S_{T2,k}$	$S_{T3,k}$	$S_{T4,k}$	
I_1	MSI_1 and MSI_2	0	0 or 1	1	1 or 0	V_{dc2}
I_2	MSI_1 and MSI_2	0 or 1	1	1 or 0	0	$V_{dc1} - V_{dc2}$
I_3	MSI_1	0 or 1	0 or 1	1 or 0	1 or 0	V_{dc1}
	MSI_2	0 or 1	0	0	1 or 0	

4.3.2 AC/DC conversion

Similarly to the VSI, both MSI topologies can ensure the AC/DC conversion due to the use of IGBT/diode devices. The DC current can be controlled while keeping the DC-link voltage constant [105, 156]. However, the control strategies developed for the VSI need to be adjusted since the MSI_1 and MSI_2 have more switches and two DC voltages.

In rectifier mode, it can be seen from Fig. 4.3a that the MSI consists of two standard VSI operating as rectifiers. Hence, two distinct operating modes can be considered:

- Mode R_1: The power is supplied to V_{dc1} by using $Q_{1,k}$ and $Q_{3,k}$. The switches $Q_{2,k}$ are always turned off and no power is transferred to V_{dc2};
- Mode R_2: The power is supplied to V_{dc2} by using $Q_{2,k}$ and $Q_{3,k}$. The switches $Q_{1,k}$ are always turned off and no power is transferred to V_{dc1}.

Compared to the DC/AC operations of the MSI, one can note that $Q_{2,k}$ and $Q_{3,k}$ are both used in Modes I_1 and R_2, while $Q_{1,k}$ and $Q_{3,k}$ are controlled in Modes I_3 and R_1. Hence, the switching combinations expressed in (4.4) and (4.5) are also applicable when the MSI_1 and MSI_2 operate as rectifiers. Table 4.3 describes the device switching states during the rectifier operations of the MSI. It can be noted that the control differs between the MSI_1 and MSI_2 in Mode R_1 and is similar in Mode R_2. During Mode R_1, the switches $T_{1,k}$ and $T_{2,k}$ in the MSI_1 simultaneously receive the same gate signal while $T_{3,k}$ and $T_{4,k}$ are

complementary. By doing so, the current i_{dc1} can be controlled to a reference value i^*_{dc} and the current i_{dc2} is equal to zero. On the other hand, the switches $T_{2,k}$ and $T_{3,k}$ are always turned off in the MSI_2 during Mode R_1, and the devices $T_{1,k}$ and $T_{4,k}$ are complementary. Finally, Mode R_2 is achieved by controlling the switches $T_{2,k}$ and $T_{4,k}$, while $T_{1,k}$ and $T_{3,k}$ are always turned off and on respectively for both the MSI_1 and the MSI_2. By doing so, the current i_{dc2} is controlled to i^*_{dc} and i_{dc1} is equal to zero.

Table 4.3: Device switching states of the MSI during AC/DC conversion.

Rectifier modes	MSI topologies	Device switching states				DC currents	
		$S_{T1,k}$	$S_{T2,k}$	$S_{T3,k}$	$S_{T4,k}$	i_{dc1}	i_{dc2}
R_1	MSI_1	0 or 1	0 or 1	1 or 0	1 or 0	i^*_{dc}	0
	MSI_2	1 or 0	0	0	0 or 1		
R_2	MSI_1 and MSI_2	0	0 or 1	1	1 or 0	0	i^*_{dc}

4.4 Adapted PWM strategies

Due to the uniqueness of the MSI topologies, conventional PWM strategies, discussed in Section 3.3, cannot be used to control the converter. Thus, new control strategies have been implemented and can be applied when the MSI operates either as an inverter or a rectifier. In the following, two PWM strategies are presented, namely the adapted SPWM and SVPWM.

4.4.1 Adapted SPWM

Similarly to the traditional SPWM technique for two-level inverters, the suggested control strategy compares a sinusoidal reference function $v^*_{j,k}(t)$ with a triangular carrier $v_{carrier}(t)$ to generate the pulse gate signals for the switches. However, in the adapted SPWM, the amplitude of $v_{carrier}(t)$ varies along with the input voltage defined by the operating mode of the MSI, unlike in the commonly used SPWM where it is equal to the fixed input DC voltage.

Indeed, in the adapted SPWM, the operating mode is selected based on the amplitude of $v^*_{j,k}(t)$ which then defines the amplitude of $v_{carrier}(t)$. As a result, the three-phase reference functions, shown in Fig. 4.4a, can be expressed as in (4.7) and (4.8).

$$\begin{aligned} v^*_{j,a}(t) &= M_j \sin(\omega t) \\ v^*_{j,b}(t) &= M_j \sin(\omega t + \tfrac{2\pi}{3}) \\ v^*_{j,c}(t) &= M_j \sin(\omega t - \tfrac{2\pi}{3}) \end{aligned} \tag{4.7}$$

$$M_j = 2\hat{V}_{LN,0}/V_{dc,j} \tag{4.8}$$

where M_j is the modulation index lying between [0;1], j=1, 2 or 3 denotes the inverter mode in which the MSI operates, $\hat{V}_{LN,0}$ is the amplitude of the fundamental harmonic of the phase voltage and $V_{dc,j}$ is the input voltage applied to the load in the corresponding operating mode (i.e. V_{dc2}, $V_{dc1} - V_{dc2}$ or V_{dc1}). Due to the variability of $V_{dc,j}$, it can be seen in Fig. 4.4b that the range of $\hat{V}_{LN,0}$ is related to the operating mode. Indeed, for a fixed $\hat{V}_{LN,0}$ and with a constant load, a higher modulation index is necessary in Mode I_1 compared to Modes I_2 or I_3. This is particularly interesting in terms of efficiency since a high modulation index leads to low currents and, hence, low conduction losses in the switches, when a constant load and power are considered. This characteristic will be further discussed in Chapter 5.

4.4.2 Adapted SVPWM

The SVPWM technique is usually preferred in motor drive applications because it offers better controllability at high speed in comparison to the SPWM technique. Also, it presents better performance in terms of harmonic distortion in control of AC motor and DC bus utilization. As previously mentioned, the phase legs in the MSI topologies are similar to the NPC and TNPC inverter circuits. Thus, an adapted SVPWM strategy was developed to control the switches in the MSI based on its similarities with these three-level inverters.

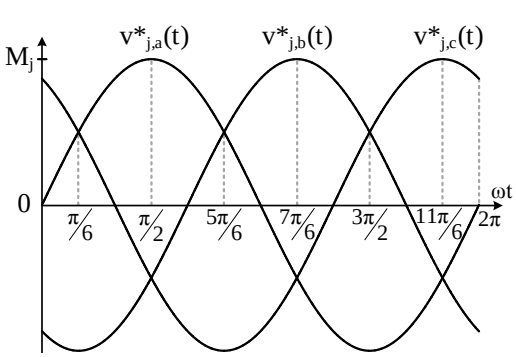

(a) Reference functions over one cycle.

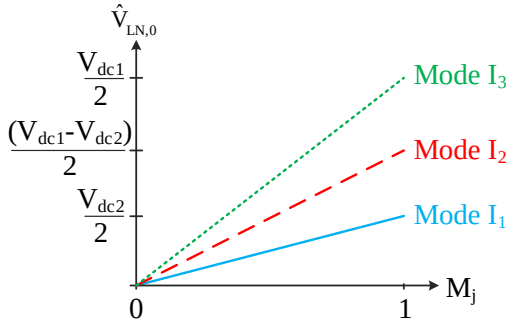

(b) Voltage range of $\hat{V}_{LN,0}$ over M_j in each operating modes.

Figure 4.4: Operating principle of the adapted SPWM.

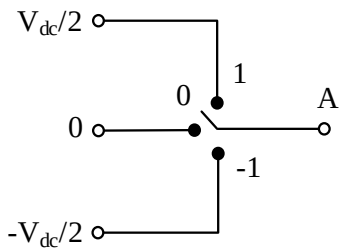

(a) In a three-level inverter.

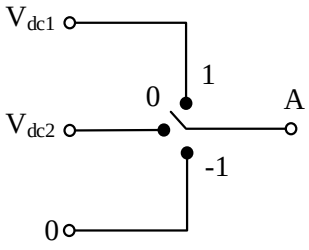

(b) In the MSI.

Figure 4.5: Output voltage levels.

As the widely used SVPWM, the new strategy consists of applying the reference voltage as a combination of the two nearest vectors and one zero vector in the alpha-beta reference plane. The main difference between the adapted SVPWM and the typical one is related to the voltage states. For three-level inverters, three voltage states -1, 0, and 1 represent the achievable phase voltage levels of each phase leg (respectively -V_{dc}/2, 0, V_{dc}/2), as shown in Fig. 4.5a. However, the DC source voltage in the MSI can be equal to either V_{dc1} or V_{dc2}. Hence, the output voltage in each operating mode is reachable by only two of the three voltage states, as displayed in Fig. 4.5b. Table 4.4 summarizes the accessible voltage states per operating mode for both the MSI_1 and MSI_2 circuits.

In Fig. 4.6, the spatial vector representation in alpha-beta diagram of the new SVPWM strategy is composed of three hexagons, whose size varies depending on the voltage applied

Table 4.4: Voltage states of the MSI_1 and MSI_2.

Operating modes	Voltage states	Output voltage
I_1	-1 and 0	V_{dc2} or 0
I_2	0 and 1	V_{dc1} or V_{dc2}
I_3	-1 and 1	V_{dc1} or 0

to the load. The radius of the inner circle of each hexagon represents the maximum voltage V_{lim1}, V_{lim2} or V_{lim3} achievable in Mode I_1, I_2 or I_3 and is equal to $V_{dc2}/\sqrt{3}$, $(V_{dc1}-V_{dc2})/\sqrt{3}$ or $V_{dc1}/\sqrt{3}$ respectively. Each hexagon is composed of six sectors. Compared to the control for three-level inverters, only 21 vectors are used instead of 27 vectors and no region selection is needed. As a result, the control of the MSI remains simple and easy to implement. After the mode and sector identification, the switching duration of each vector is calculated in a similar way as in a typical SVPWM control scheme. Finally, symmetric switching sequences were chosen in order to reduce the harmonic distortion and the number of switching, allowing power loss reductions.

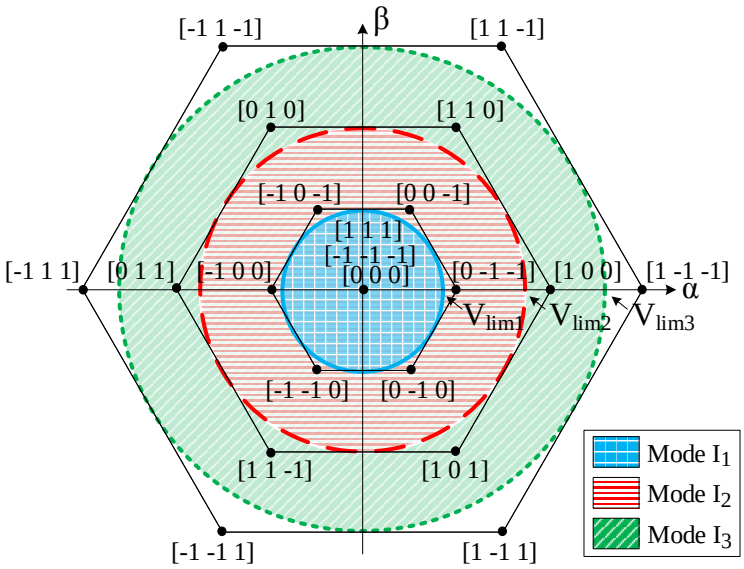

Figure 4.6: Space vector representation of the adapted SVPWM.

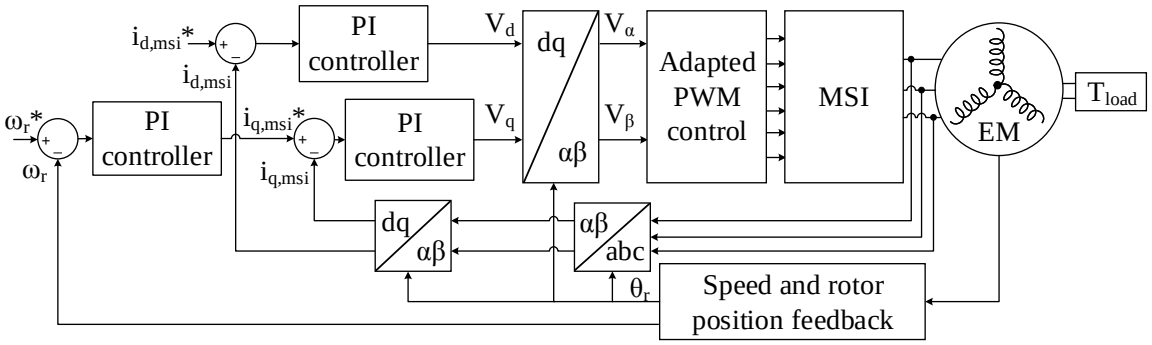

Figure 4.7: New control scheme with the MSI.

4.5 Simulation results

A dedicated control strategy using a conventional field oriented control, also called vector control, was implemented in simulations to verify the MSI operations [157]. The closed-loop control scheme is presented in Fig. 4.7. Based on speed and current references (ω_r^* and $i_{d,msi}^*$), proportional integral (PI) controllers generate a reference voltage in alpha-beta axis whose module $|V_{ref}|$ is compared to the maximum voltages achievable in each operating mode. If the adapted SPWM strategy is implemented, the voltage limits of Modes I_1, I_2 and I_3 are equal to respectively $V_{dc2}/2$, $(V_{dc1} - V_{dc2})/2$ and $V_{dc1}/2$, as shown in Fig. 4.4b. On the other hand, if the adapted SVPWM is chosen, $|V_{ref}|$ is compared to V_{lim1}, V_{lim2}, and V_{lim3} from Fig. 4.6. Once the operating mode is selected, the gate signals are generated as described in Section 4.4.

The closed-loop control model was developed in Matlab/Simulink with an IM and parameters are listed in Table 4.5. The MSI operates as an inverter and drives the IM as a motor when the power is positive, which implies both speed and torque references in the same direction. If the speed and torque have opposite signs, the IM generates power and the MSI operates as a rectifier. Hence, the same simulation model presented in Fig. 4.7 can be used to simulate both DC/AC and AC/DC operations.

Simulations in inverter operations were performed at three different speed references, 250

rpm, 500 rpm, and 900 rpm, a constant reference current $i^*_{d,msi}$ of 15 A, and a constant load torque T_{load} of 14 N.m. These values were selected with a view to show the MSI operating in the three modes I_1, I_2, and I_3. Moreover, the adapted SVPWM was implemented in this simulation model.

Table 4.5: Parameters with an IM and a load.

Component	Parameter	Value
DC source voltages	V_{dc1}	150 V
	V_{dc2}	50 V
Multi-source inverter	Switching frequency	10 kHz
Induction motor	Power	10 HP
	Voltage	208 V to 230 V
	Current	27.6 A to 24.4 A
	Number of poles	2
	Stator resistance	0.135 Ω
	Rotor resistance	0.18 Ω
	Stator inductance	0.064 H
	Rotor inductance	0.064 H
	Inertia	0.1 $kg.m^2$
	Rated speed	3500 rpm
Battery pack	Energy	5.9 kWh
	Voltage (nominal)	50 V
	Capacity	116 Ah

Simulation waveforms in inverter mode for the MSI_1 are displayed in Fig. 4.8. Similar outcomes were obtained with the MSI_2 and will not be presented to avoid redundancy. As shown in Fig. 4.8a, the rotor speed converges to the three reference values. From Figs. 4.8b and 4.8c, it can be seen that the MSI switches between the operating modes as expected. Indeed, when the reference voltage module $|V_{ref}|$ is lower than $V_{lim,1}$, the MSI operates in Mode I_1. On the other hand, if $|V_{ref}|$ stays between $V_{lim,1}$ and $V_{lim,2}$, or between $V_{lim,2}$ and $V_{lim,3}$, the MSI is in Mode I_2 or I_3 respectively. The input DC current waveforms, shown in

Fig. 4.8d, are also in line with the theory. In Mode I_1, i_{dc2} is positive while the current i_{dc1} remains null. This confirms that V_{dc2} supplies the motor whereas V_{dc1} is not being used. In Mode I_2, the positive value of i_{dc1} and negative value of i_{dc2} validates the charge of V_{dc2} from V_{dc1} while the motor is running. One can also note that i_{dc2} is equal to the negative of i_{dc1} (losses neglected). This is because, in Mode I_2, the two input sources are in series and the negative pole of V_{dc2} is connected to the negative pole of V_{dc1}. Hence, the current driving the load is the same as the one charging V_{dc2}. In Mode I_3, i_{dc2} is equal to zero, which confirms that V_{dc2} is not being used. In this mode the motor is driven by V_{dc1}, as verified by a positive i_{dc1}. In Fig. 4.8e, the line voltage V_{AB} varies along with the operating modes, as stated in Tables 4.1. From Fig. 4.8f, one can note that the amplitudes of the stator currents i_a, i_b, and i_c are constant even if the MSI operates in different modes. This is due to the fact that the current $i^*_{d,msi}$ and the load torque T_{load}, which is proportional to $i_{q,msi}$, were kept constant. On the other hand, the frequency increases as the rotor speeds faster, which is consistent with the theory. At last, one can note that the MSI operates in Mode I_3 for a very short period of time at $t = 2sec$, during the step increase of the reference speed. This is due to a voltage spike on the signal $|V_{ref}|$ that exceeds $V_{lim,3}$. To prevent this effect, $|V_{ref}|$ can be filtered in order to reduce the noise of the signal and the parameters of the PI controllers can also be adjusted to limit the overshoot during the transition. For real-time applications, a state machine with hysteresis control would be a better method to manage the mode transition. Indeed, this would ensure a smooth transition and improve the stability of the system since it prevents the MSI from switching between two modes at high frequency.

Simulation in rectifier operations were carried out with the same Matlab/Simulink model presented in Fig. 4.7 and the parameters shown in Table 4.5. Unlike in inverter operations, a negative speed reference was given while T_{load} was kept positive. By doing so, the speed and torque have opposite signs and the power is negative. This means that the IM acts as a generator and the MSI becomes a rectifier. Two different speed references $\omega_r{}^* = -1150$

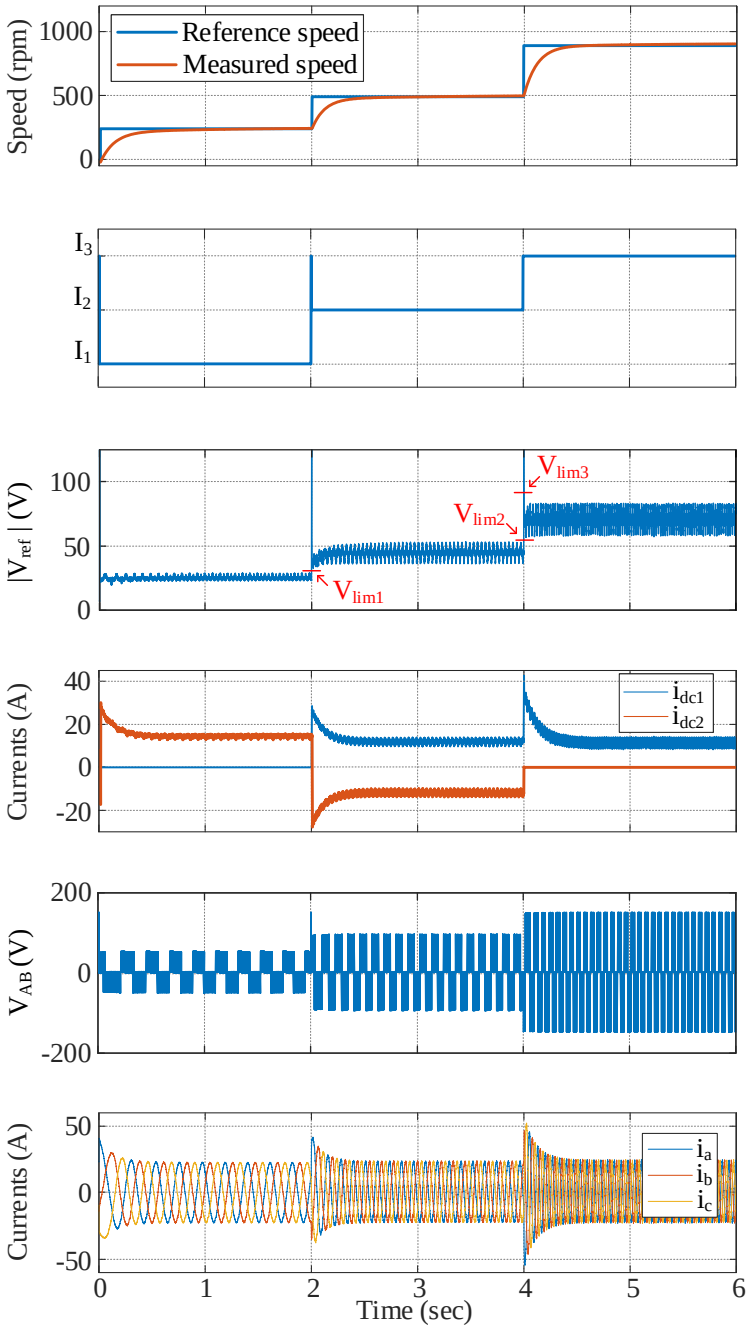

(a) Rotor speed.

(b) Operating mode.

(c) Voltage module $|V_{ref}|$.

(d) Input currents i_{dc1} and i_{dc2}.

(e) Line voltage V_{AB}.

(f) Phase currents i_a, i_b and i_c.

Figure 4.8: Simulation waveforms with the MSI_1 in inverter modes I_1, I_2, and I_3.

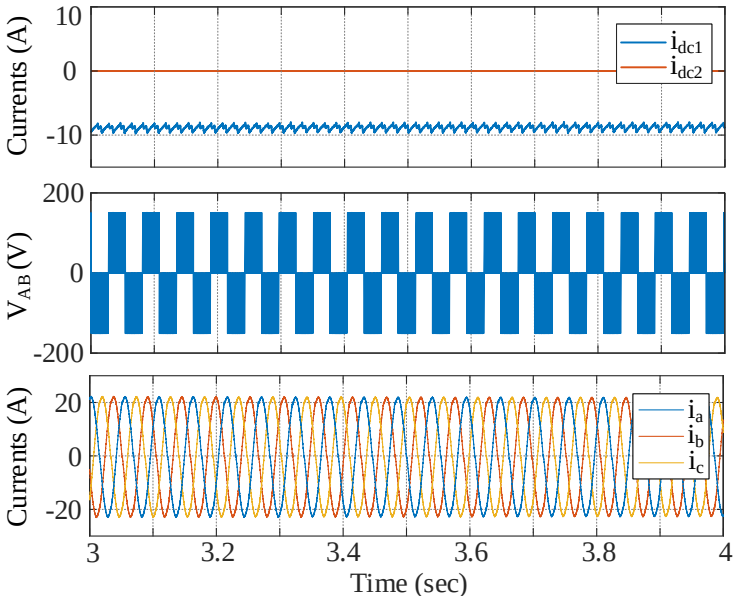

Figure 4.9: Simulation results in Mode R_1 at ${\omega_r}^* = -1150$ rpm.

rpm and ${\omega_r}^* = -500$ rpm were chosen to simulate the two rectifier modes presented in Section 4.3.2. The current $i^*_{d,msi}$ is fixed at 15A and T_{load} is constant and equal to 14 N.m. Results are shown in Figs. 4.9 and 4.10 for respectively Modes R_1 and R_2.

From Fig. 4.9, it can be seen that i_{dc1} is negative while i_{dc2} is equal to zero. This confirms that the power is only transferred to V_{dc1} in Mode R_1. Fig. 4.10 shows the MSI operating in Mode R_2, which is verified by the negative value of i_{dc2} and i_{dc1} is null. In both modes, one can note that the waveforms of V_{AB} and the phase currents i_a, i_b and i_c are also consistent with the theory. Indeed, the amplitude of the line voltage matches with the DC voltage receiving power. Moreover, the amplitudes of the phase currents stay constant regardless the speed since T_{load} was kept constant and only the frequency changes.

In conclusion, the simulation results verify the theoretical operation principles of the MSI in inverter and rectifier operations.

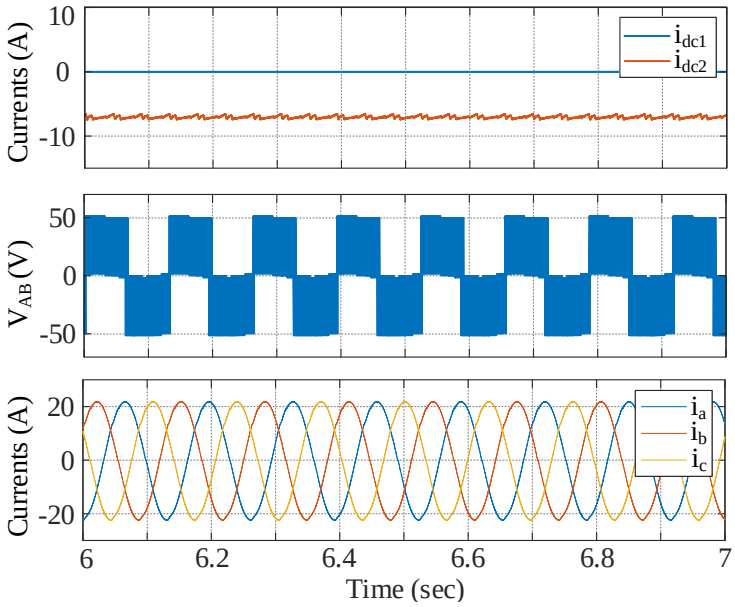

Figure 4.10: Simulation results in Mode R_2 at ${\omega_r}^* = -500$ rpm.

4.6 Experimental validation with an EM

A scaled-down prototype of the MSI_1 was built to validate the effectiveness of the inverter and is shown in Fig.4.11. The circuit is composed of three IGBT modules type F3L50R06W1E3-B11. The DC source V_{dc2} is supplied by a battery pack and V_{dc1} is provided by a power supply. The MSI drives a motor IM_A with the closed-loop control scheme presented in Fig. 4.7. A second machine IM_B is shafted connected to IM_A and driven by a standard VSI, as presented in Fig. 4.12. The torque load is controlled with the currents of the VSI on the dq-axis, namely $i_{d,vsi}$ and $i_{q,vsi}$. Several safety precautions have been integrated to the experimental setup, including fuses, emergency-stop button, pre-charge circuits and inrush current detection. Fig. 4.13 shows the complete experimental setup where the protective enclosure has been removed for the picture. The control of the whole setup including the gate signals of the MSI and the VSI, the safety features, the sensors, and the speed encoder are managed by a real-time system MicroAutoBox II and the software dSPACE. Experiments were performed with the parameters from Table 4.5 and both IMs

have the same characteristics.

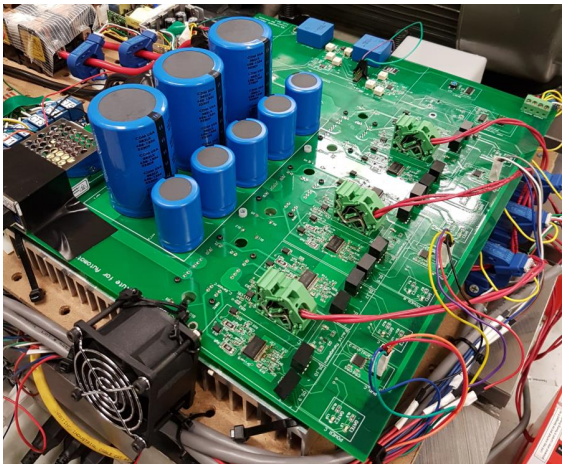

Figure 4.11: Prototype of the MSI_1.

Experiments were carried out under the same driving conditions as in the simulations to provide a one-to-one comparison. The MSI is controlled with $i^*_{d,msi} = 15$ A and $T_{load} = 14$ N.m, corresponding to $i^*_{d,vsi} = 15$ A and $i^*_{q,vsi} = 25$ A for the control of the VSI. Results in inverter modes are presented in Figs. 4.14 to 4.16 with a speed reference of 250 rpm, 500 rpm, and 900 rpm respectively. The phase current i_a, the DC currents i_{dc1} and i_{dc2}, and the line voltage V_{AB} are shown in each case. The magnified view of the simulated waveforms of the DC currents, line voltage, and phase currents from Fig. 4.8 are also displayed along with the experimental results in each operating mode.

In Fig. 4.14, the MSI_1 operates in Mode I_1 where only the battery supplies the load. This is confirmed by the positive value of i_{dc2} while i_{dc1} is almost null. The amplitude of the line voltage V_{AB} is equal to V_{dc2}, as expected from Table 4.2. Fig. 4.15 displays a positive current i_{dc1} and the maximum amplitude of V_{AB} is equal to 100 V. This is consistent with the theory of Mode I_2 where V_{dc1} supplies the load, but the voltage is equal to $V_{dc1} - V_{dc2}$ because of the series connection of the two DC sources. One can also note that the battery is charged with i_{dc2} almost equal to the negative of i_{dc1}. The difference in magnitude is due

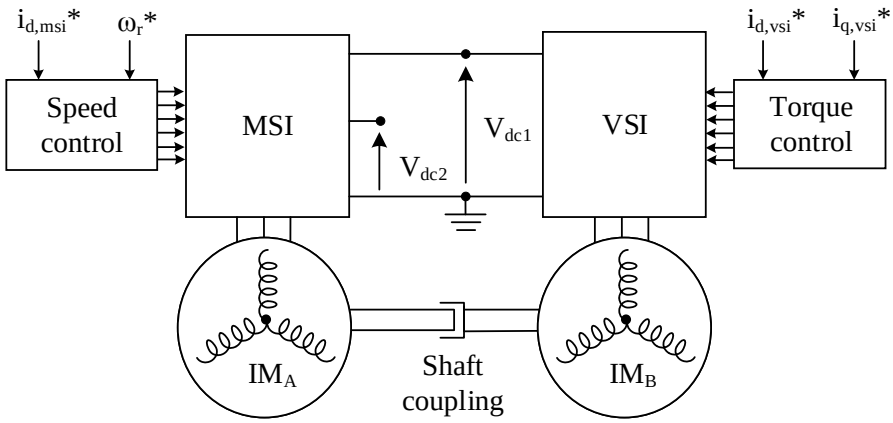

Figure 4.12: Scheme of the experimental setup.

to the losses generated in the inverter. At last, Mode I_3 is shown in Fig. 4.16. Although the DC currents are noisier than expected in Fig. 4.16b, it is clear that the average value of i_{dc1} is positive and the average value of i_{dc2} is equal to zero. This validates the theory where V_{dc1} supplies the load and the battery is not used.

Several hypotheses were investigated regarding the oscillations of i_{dc2} in Mode I_3. It was found that they are caused by the clamping diodes $D_{5,k}$ and $D_{6,k}$ that conduct a small portion of the battery current. Indeed, when $T_{1,k}$ and $T_{2,k}$ are turned on, $D_{6,k}$ is reverse biased by applying Kirchoff's voltage law. Moreover, $D_{5,k}$ is forward biased and a positive value of i_{dc2} can flow. On the other hand, $D_{5,k}$ is reverse biased when $T_{3,k}$ and $T_{4,k}$ are switched on, while $D_{6,k}$ conducts and i_{dc2} is negative. Experiments have been carried out to verify this theory. Although it is challenging to measure the currents in the chips due to the use of IGBT modules, the voltage across each device is accessible. Fig. 4.17 displays the experimental waveforms of the voltage V_{D5} across $D_{5,a}$, V_{D6} across $D_{6,a}$, the current i_{dc2} and the phase current i_a. From Fig. 4.17a, the non-filtered voltages clearly vary between zero to $V_{dc1} - V_{dc2}$ for $D_{5,a}$ and zero to V_{dc2} for $D_{6,a}$, which is consistent with Kirchoff's voltage law. In Fig. 4.17b, the signals have been filtered and it can be seen that i_{dc2} is positive when $D_{6,a}$ conducts, while it is negative when $D_{5,a}$ is forward biased. This confirms the

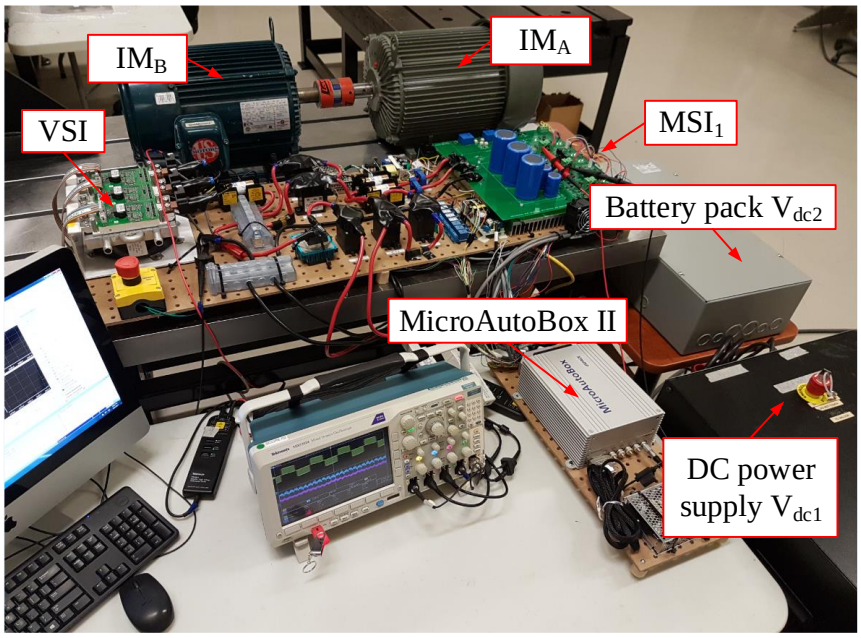

Figure 4.13: Experimental test setup with the MSI_1.

assumption that both clamping diodes are responsible for the fluctuations of i_{dc2}. Although the relationship between the amplitude of the current ripple of i_{dc2} and the load is still unsure, it can be noticed that the oscillations are negligible compared to i_{dc1}. Hence, in the following of the thesis, the clamping diodes will be assumed reverse biased in Mode I_3.

The experimental setup presented in Fig. 4.13 can also be used to test the rectifier modes of the MSI_1. Indeed, by controlling the speed and torque with opposite signs, IM_B will act as a motor and IM_A becomes a generator. Experiments were performed with the same parameters from Table 4.5. The MSI is controlled with $i^*_{d,msi} = 15$ A and $T_{load} = 14$ N.m, corresponding to $i^*_{d,vsi} = 15$ A and $i^*_{q,vsi} = 25$ A for the control of the VSI. Two negative speed references of -500 rpm and -1150 rpm were tested and results are presented in Figs. 4.18 and 4.19 respectively. These operating points have been chosen to show the MSI operation in both Modes R_1 and R_2. The stator current i_a, the DC currents i_{dc1} and i_{dc2}, and the line voltage V_{AB} are displayed in each case.

Fig. 4.18a shows the waveforms of the MSI_1 in Mode R_1 where the maximum amplitude

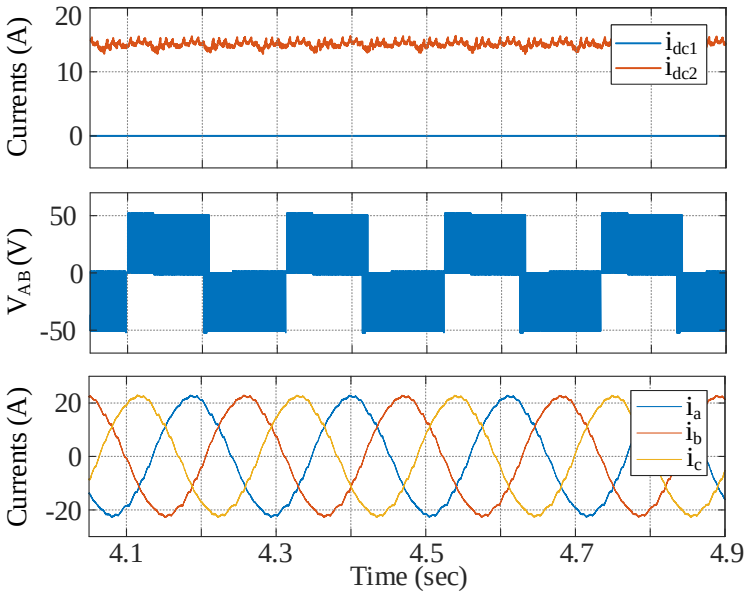

(a) Magnified view of the simulation waveforms.

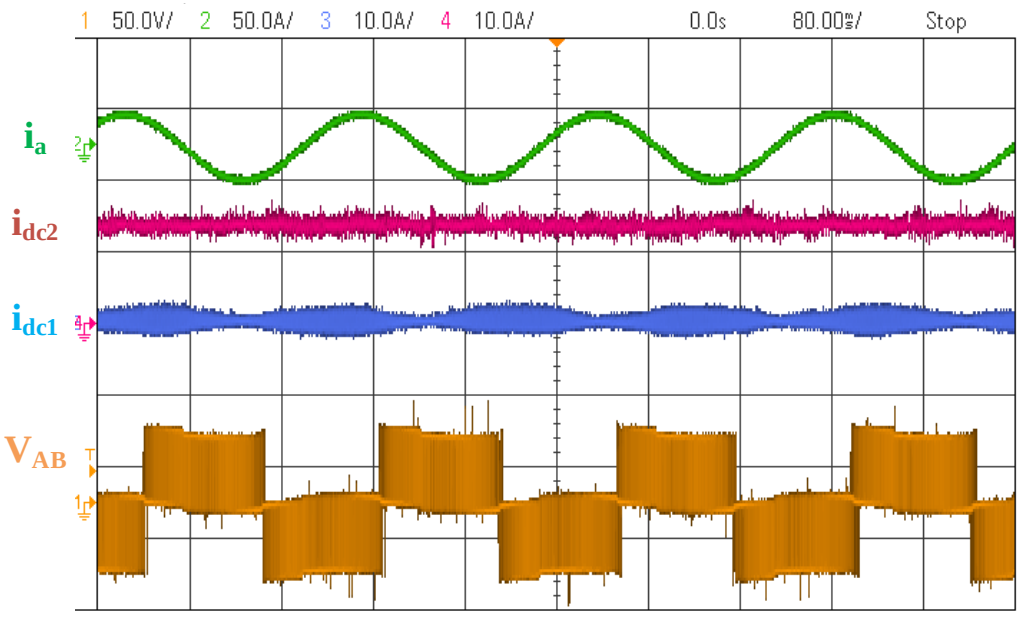

(b) Experimental waveforms.

Figure 4.14: Results in Mode I_1 at $\omega_r{}^* = 250$ rpm.

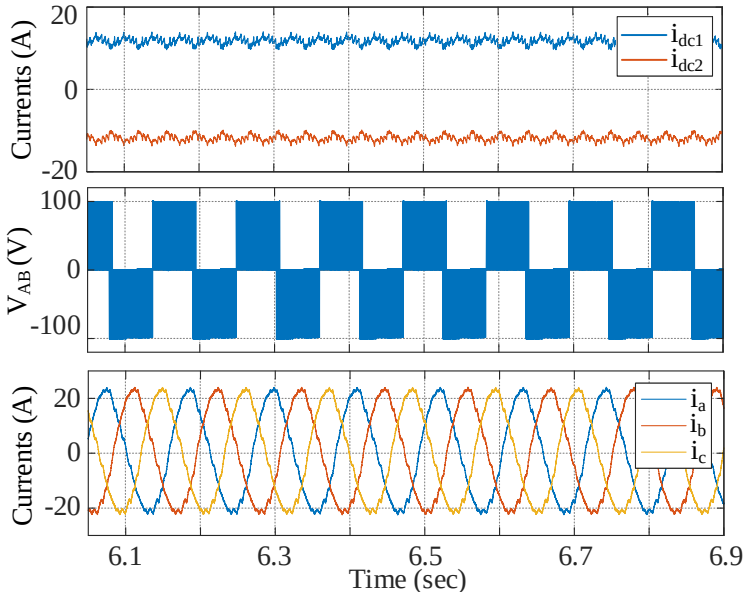

(a) Magnified view of the simulation waveforms.

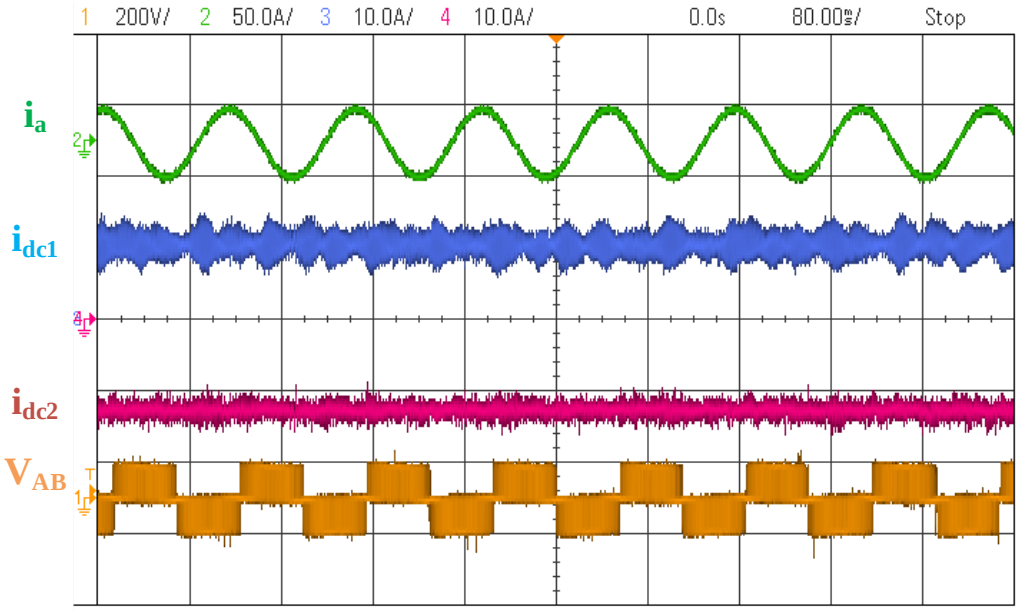

(b) Experimental waveforms.

Figure 4.15: Results in Mode I_2 at $\omega_r^* = 500$ rpm.

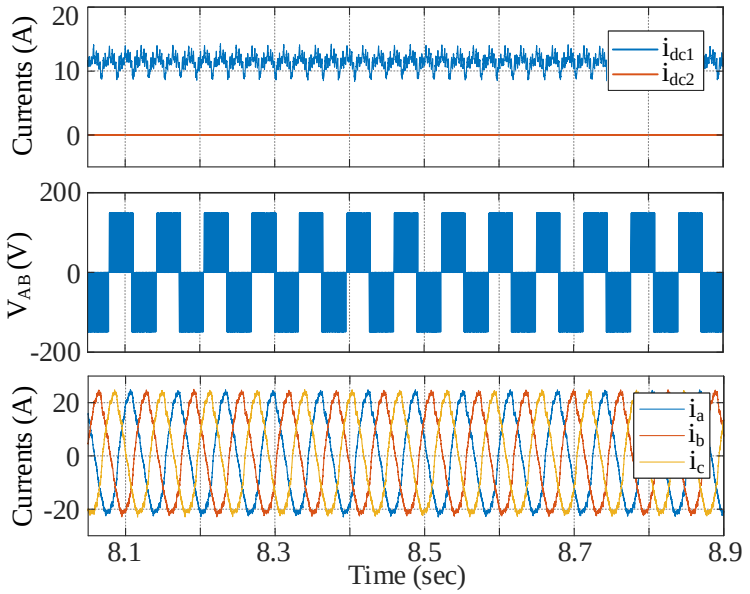

(a) Magnified view of the simulation waveforms.

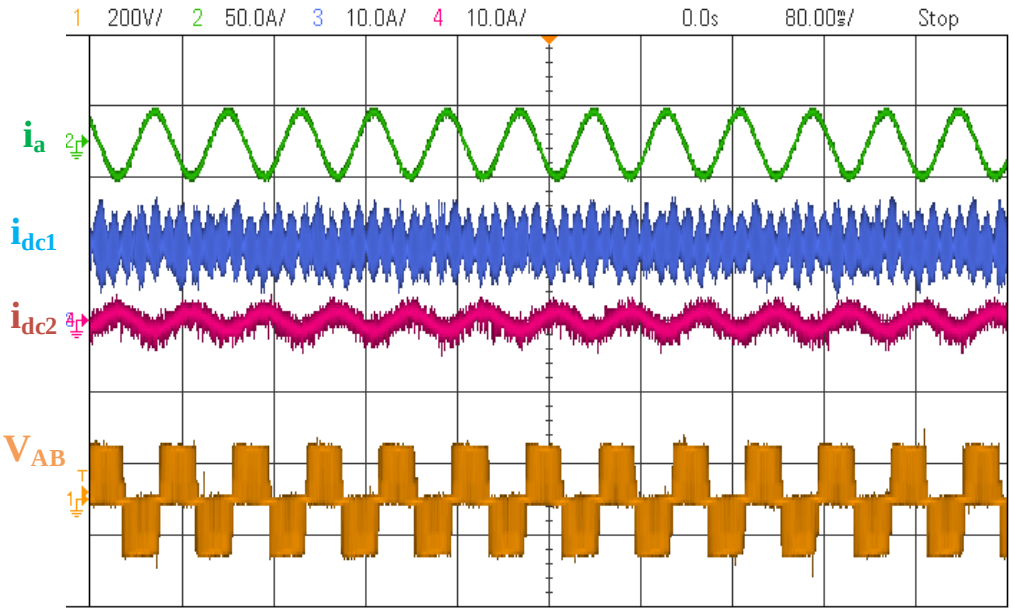

(b) Experimental waveforms.

Figure 4.16: Results in Mode I_3 at $\omega_r^* = 900$ rpm.

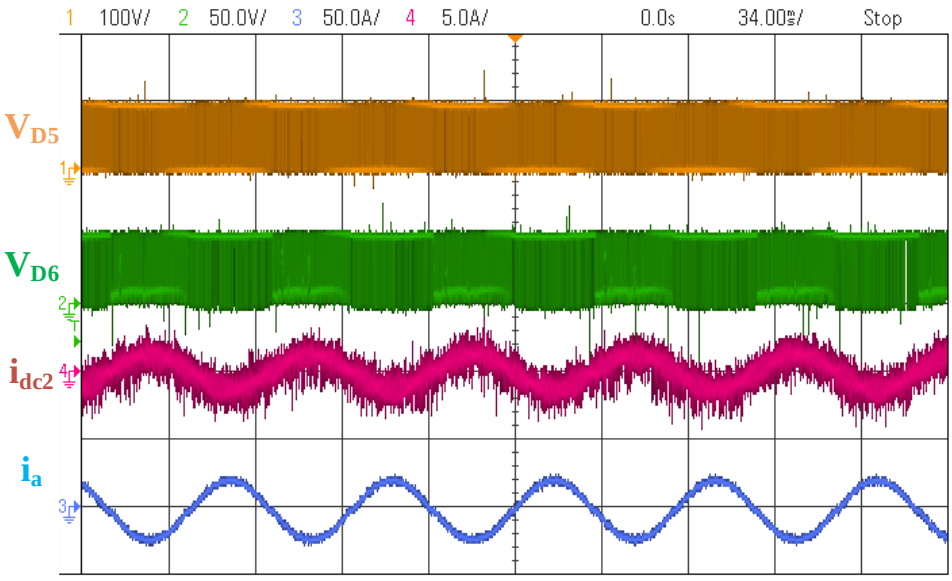

(a) Normal signals.

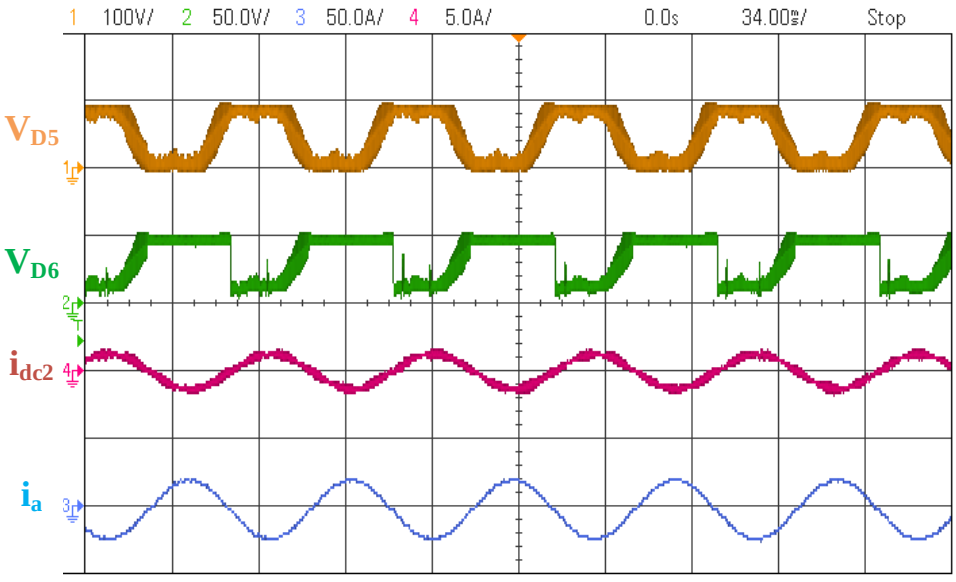

(b) Filtered signals.

Figure 4.17: Experimental verification of the clamping diode conduction in Mode I_3.

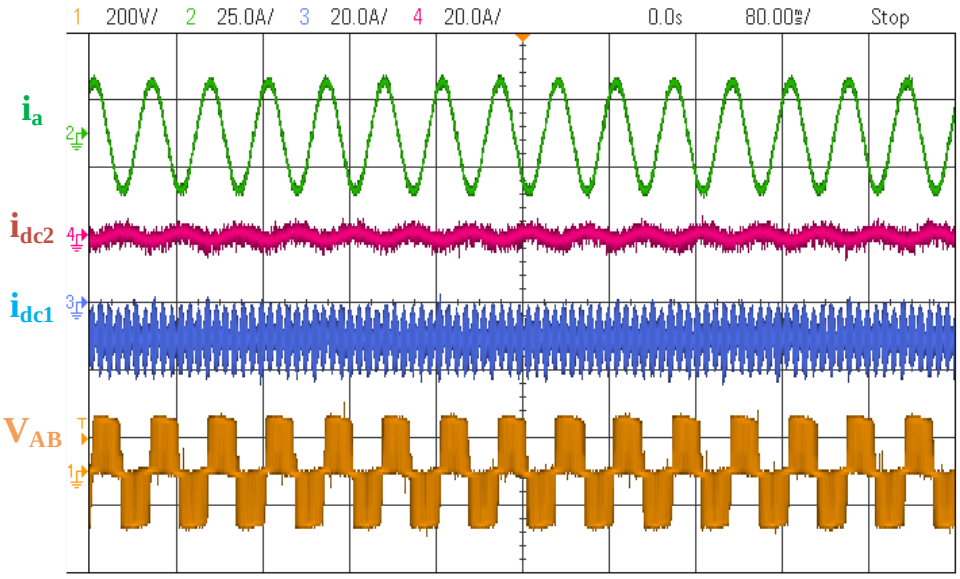

(a) Normal signals.

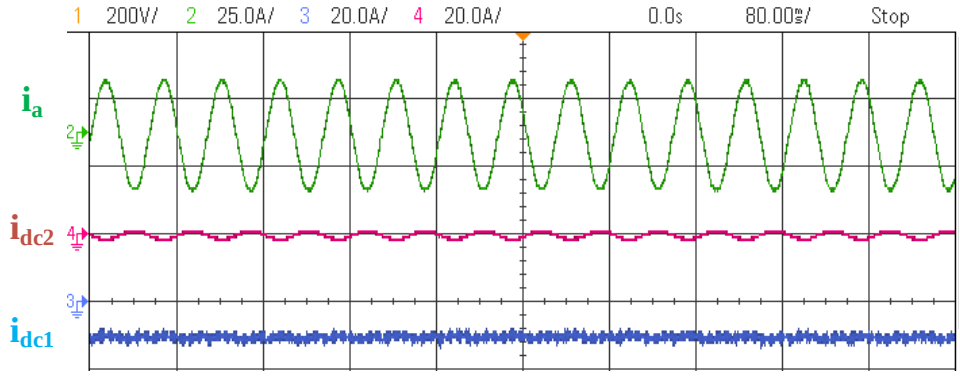

(b) Filtered signals.

Figure 4.18: Experimental waveforms in Mode R_1 at $\omega_r^* = -1150$ rpm.

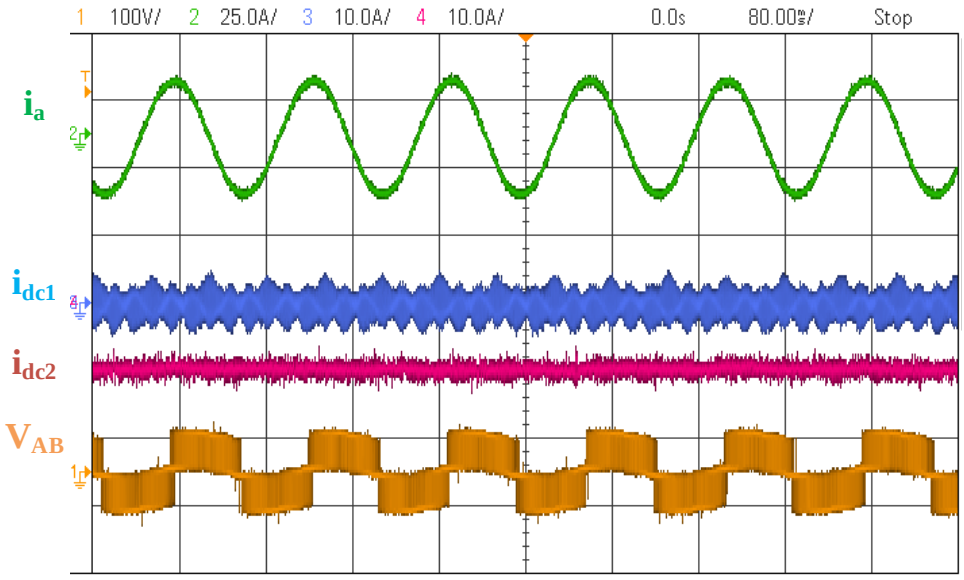

(a) Normal signals.

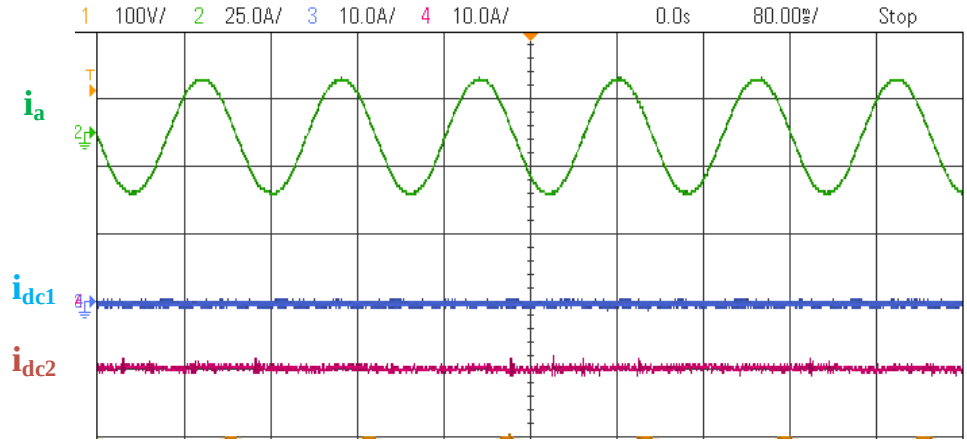

(b) Filtered signals.

Figure 4.19: Experimental waveforms in Mode R_2 at $\omega_r^* = -500$ rpm.

of V_{AB} is equal to V_{dc1}. Similarly to Mode I_3, the DC currents in Mode R_1 are noisy due to the clamping diodes $D_{5,k}$ and $D_{6,k}$ that alternatively conduct, as previously explained. In Fig. 4.18b, the filtered signals clearly show that the current i_{dc1} is negative and i_{dc2} is equal to zero. This confirms that the power generated by IM_A is provided to V_{dc1} while no power is transferred to V_{dc2}. Fig. 4.19a shows a negative i_{dc2} and i_{dc1} is almost null. Furthermore, the maximum amplitude of V_{AB} is equal to V_{dc2}. This validates that the MSI_1 operates in Mode R_2 where the power is supplied to V_{dc2} and no power is transferred to V_{dc1}.

Overall, the experiments in both inverter and rectifier modes are consistent with the theory and the simulation results.

4.7 Conclusion

In this chapter, the concept of the MSI was introduced. This inverter enables independent DC sources to drive the propulsion EM while using a single conversion stage. Two circuits, MSI_1 and MSI_2, are considered and both can operate in three operating modes during the DC/AC conversion, allowing for an adaptable voltage to supply the EM. In Mode I_1, the battery pack V_{dc2} directly provides power to the load. Mode I_2 enables extending the charging opportunities of the battery while the EM is running. The voltage applied to the load is equal to $V_{dc1} - V_{dc2}$. Finally, in Mode I_3, the high DC voltage V_{dc1} supplies the load and the battery is not used. New PWM control strategies, namely the adapted SPWM and SVPWM, have been presented for both the MSI_1 and MSI_2. By using IGBTs, the MSI is bidirectional and can also ensure the AC/DC conversion. Both the MSI_1 and MSI_2 can operate in Modes R_1 and R_2 where the power is supplied to one DC input or another. Simulations were performed in closed-loop control with multiple speed references and a constant torque to verify the MSI operation in inverter and rectifier modes. During the DC/AC conversion, three positive speed references and a positive torque were given to run the EM as a motor and verify the MSI in the three inverter modes. By providing

a negative speed and positive torque, the EM generates power and the MSI operates as a rectifier. Simulations results are consistent with the theory. A scale-down prototype of the MSI_1 was built and experimentally tested with an IM. The experimental setup includes a second IM controlled as a load and several safety features. Experiments were carried out under the same operating conditions as in simulations. By controlling the speed and torque, both inverter and rectifier operations can be verified, and results validated the theoretical operation principles of the MSI.

Chapter 5

Design and efficiency analysis

5.1 Introduction

As previously mentioned in Section 3.4, the competitiveness of a new topology is often evaluated in terms of cost, reliability, power density, and efficiency. In Fig. 3.6, it has been seen that the power devices account for more than 20% of the total inverter cost. The VA rating, that considers the peak current and voltage of the switches, is a criterion commonly used to compare topologies [113]. Thus, applying this method to the MSI provides a comprehensive understanding of the switch configuration. As one of the most sizable component, the input DC-link capacitor bank plays a major role in the power density, weight, and cost of an inverter. The appropriate selection requires the calculation of the RMS capacitor current and voltage ripples to prevent the capacitor from overheating, while ensuring an acceptable ripple voltage on the DC side. In the MSI, each source V_{dc1} and V_{dc2} needs its own capacitor bank. Various methods have been developed to design the most suitable capacitor depending on the inverter topology and the modulation strategy [131, 158–160]. However, none of them have been applied to the MSI yet. As two-level and three-level inverters are commonly used in the industry, numerous approaches have been suggested in the literature to evaluate the efficiency [161–163]. Through the analysis of the current in the switches

and the datasheet parameters, the power losses can be fairly estimated [164, 165]. However, the commutation paths in the MSI significantly differ from standard inverters. Thus, the previously mentioned methods cannot be directly applied to the MSI and further analysis needs to be carried out to estimate its efficiency.

In this chapter, a comprehensive design and efficiency analysis of the MSI is provided. As the primary function of the MSI is to ensure the DC/AC conversion, the following analysis will not consider the rectifier operations. The switch configuration is analyzed based on the voltage and current requirements for both MSI topologies. Due to the uniqueness of the circuits, the selection of the capacitor banks requires the analysis of the capacitor current and voltage in each operating mode of the MSI. From these analytical equations, the size of the capacitor bank can be then carefully selected in the worst-case scenario. At last, the efficiency analysis, derived from analytical calculation of the currents in the switches, is presented. By considering a constant R-L load and under the same power requirements, the efficiency varies regarding the mode in which the MSI operates. As a result, depending on the operating conditions, the most efficient mode can be selected, ensuring the MSI to operate at high efficiency over a wide output voltage range.

In the following sections, the switch configuration is first discussed. Then, a comprehensive study of the RMS capacitor ripple current and capacitance is suggested to select the proper capacitor banks of the MSI. Finally, an efficiency model based on the analytical calculations of the average and RMS currents in the switches is developed. Experiments with an R-L load have been carried out to validate the efficiency model. Furthermore, comparisons of the MSI_1 and the MSI_2 with the VSI are provided along with the switch, capacitor, and efficiency analyses.

5.2 Switch configuration

The total VA rating is a factor commonly used to compare inverter topologies in terms of switch configuration. The switch VA rating is defined as the product of the maximum peak current flowing through the device with the maximum voltage across the terminals. Then, the total VA rating is the sum of the VA ratings of all devices in the inverter. In Section 4.3, it has been seen that both MSI circuits can operate in the same operating modes where a variable voltage is applied to the load. However, the control of the switches and, thus, the commutation paths greatly differ. Hence, the VA ratings are expected to be different and the current and voltage stresses in each MSI topology have to be considered in detail.

5.2.1 Maximum peak current

The three-phase output currents $i_a(t)$, $i_b(t)$ and $i_c(t)$ are assumed sinusoidal and phase-shifted by $2\pi/3$ between each other. They can be expressed as in (5.1) and (5.2).

$$\begin{aligned} i_a(t) &= I_{pk,j}\sin(\omega t - \phi) \\ i_b(t) &= I_{pk,j}\sin(\omega t + \tfrac{2\pi}{3} - \phi) \\ i_c(t) &= I_{pk,j}\sin(\omega t - \tfrac{2\pi}{3} - \phi) \end{aligned} \tag{5.1}$$

$$I_{pk,j} = \hat{V}_{LN,0}/Z_k \tag{5.2}$$

where $I_{pk,j}$ is the peak amplitude of the output phase current in the corresponding operating mode and ϕ is the phase shift angle between the fundamental harmonics of the line voltage and the phase current.

Substituting (4.8) into (5.2) and by considering a constant R-L load, one can note that the peak current is proportional to the DC voltage $V_{dc,j}$, that varies depending on the operating mode (i.e. V_{dc2}, $V_{dc1} - V_{dc2}$ or V_{dc1}). Moreover, the maximum value is obtained for a modulation index M_j equal to unity. Hence, $I_{pk,3}$ in Mode I_3 is higher than in Modes

I_1 and I_2 since V_{dc1} is higher than V_{dc2} and $V_{dc1} - V_{dc2}$.

From Table 4.2, the maximum current stress in each switch and for every operating mode can be derived for both MSI topologies. The results are shown in Fig. 5.1. In Modes I_1 and I_2, the switches are controlled in a similar way in both the MSI_1 and MSI_2. In Mode I_1, the switches $T_{1,k}/D_{1,k}$ are always turned off while the other devices conduct. Hence, the maximum current stress of every switch in the circuits is equal to $I_{pk,1}$, except for $T_{1,k}/D_{1,k}$ where it is equal to zero. In Mode I_2, the peak current of $T_{4,k}/D_{4,k}$ is equal to zero since they are always turned off and it is equal to $I_{pk,2}$ for the other switches. On the other hand, the control in MSI_1 and MSI_2 differs from each other in Mode I_3. In the MSI_1, the switches are controlled by pair where $T_{1,k}/D_{1,k}$ and $T_2, k/D_{2,k}$ receive the same gate signal and $T_{3,k}/D_{3,k}$ and $T_{4,k}/D_{3,k}$ are complementary. It has been seen in Fig. 4.17 that a small portion of the phase current is conducted by the clamping diodes $D_{5,k}$ and $D_{6,k}$. However, this current is negligible compared to the peak current and the clamping diodes can be considered reverse biased. Hence, the MSI_1 topology is equivalent to a VSI where each top and bottom switch per phase leg consists of two devices in series. As a result, the maximum current stress in every device, except the clamping diodes, is equal to $I_{pk,3}$. In the MSI_2, the switches $T_{2,k}/D_{2,k}$ and $T_{3,k}/D_{3,k}$ are both always turned off and the topology is similar to the VSI. Hence, the current flows only through $T_{1,k}/D_{1,k}$ and $T_{4,k}/D_{4,k}$.

5.2.2 Maximum blocking voltage

The voltage stress across each switch can be determined from Table 4.2 and by applying Kirchoff's voltage law in each phase leg. The results are shown in Fig. 5.2 and depend on the operating modes.

In the VA rating calculations, the maximum peak current and maximum voltage are considered over the three operating modes. For the MSI_1, it can be seen that the maximum voltage of the inner switches $T_{2,k}/D_{2,k}$ and $T_{3,k}/D_{3,k}$ is equal to V_{dc1}. On the other hand,

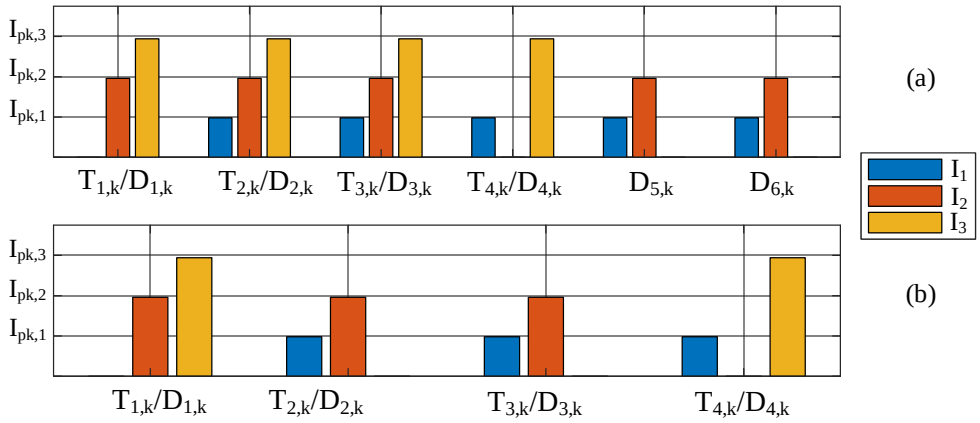

Figure 5.1: Maximum peak current in: (a) MSI_1. (b) MSI_2.

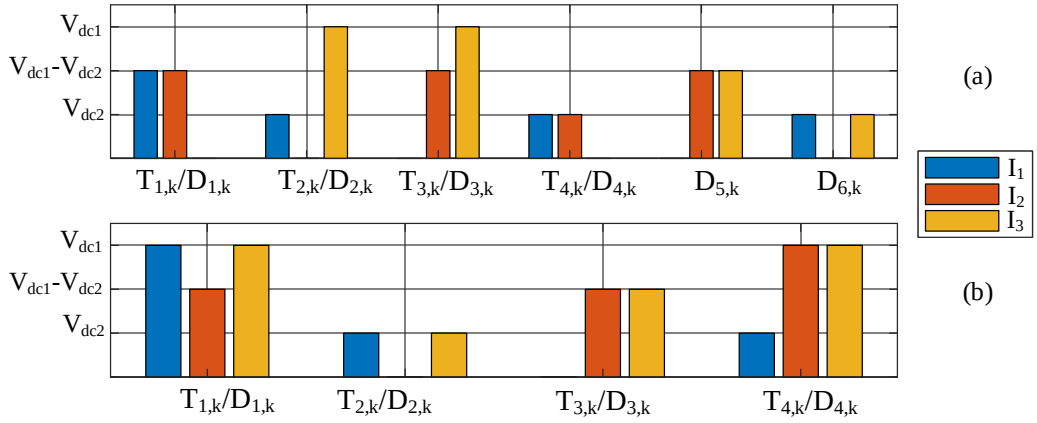

Figure 5.2: Maximum voltage stress in: (a) MSI_1 (b) MSI_2.

a voltage of $V_{dc1} - V_{dc2}$ has to be blocked by $T_{1,k}/D_{1,k}$ and $D_{5,k}$. Furthermore, the highest voltage stress on the switches $T_{4,k}/D_{4,k}$ and $D_{6,k}$ is equal to V_{dc2}. In the MSI_2, the maximum voltage across the devices greatly differ from the MSI_1. Indeed, $T_{1,k}/D_{1,k}$ and $T_{4,k}/D_{4,k}$ have a blocking voltage of V_{dc1} while the voltage stress of $T_{3,k}/D_{3,k}$ and $T_{2,k}/D_{2,k}$ is equal to $V_{dc1} - V_{dc2}$ and V_{dc2} respectively.

5.2.3 VA rating comparison

In the following, the VA ratings of the MSI_1, MSI_2 and VSI are compared. In order to provide a fair comparison, the VA rating of the VSI has been calculated for three DC source levels, V_{dc2}, $V_{dc1} - V_{dc2}$, and V_{dc1}, corresponding to the DC voltage applied to the load in each operating mode of the MSI. Due to the symmetry of the circuit, each switch conducts the phase current alternatively and the voltage stress is equal to the DC-link voltage. Hence, the maximum peak current in every switch of the VSI is equal to $I_{pk,3}$ and the blocking voltage is equal to V_{dc1}. In Fig. 5.3, the VA ratings of one phase leg in three topologies have been normalized over the VA rating of the VSI and are compared. The parameters are presented in Table 5.1 and the voltages were chosen in the same range than those used in commercialized vehicles. As expected, the VSI has the lowest VA rating due to a lower part count. However, even if the MSI_2 has twice more switches than the VSI, its VA rating only increases by 27.8%. On the other hand, the MSI_1 suffers from the two additional switches and clamping diodes per phase leg, which leads to a VA rating 55.6% higher than the VSI.

Table 5.1: Comparison parameters with an R-L load.

Parameters	Values
V_{dc1}	600 V
V_{dc2}	200 V
Switching frequency	10 kHz
Fundamental frequency	10 Hz
Three-phase R-L load	5.1 Ω and 256 μH

In conclusion, although the MSI topologies have twice or three times more devices than the VSI, their competitiveness in terms of switch configuration is moderately impacted.

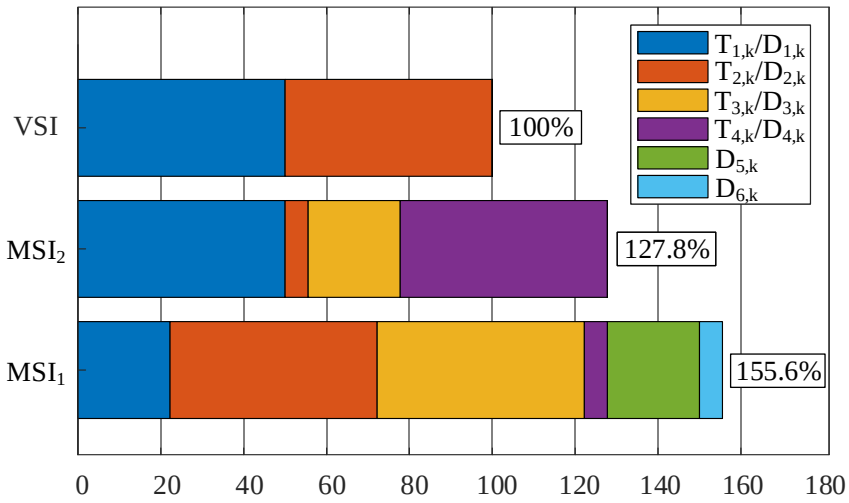

Figure 5.3: Normalized VA rating of one phase leg in the VSI and both MSI topologies.

5.3 DC-link capacitor banks

The RMS value of the capacitor ripple currents $\Delta i_{C1,rms,j}$ and $\Delta i_{C2,rms,j}$ and the capacitances $C_{1,j}$ and $C_{2,j}$ are the main factors to select the appropriate DC-link capacitor banks. However, their values depend on the operating modes of the MSI, and the proper selection of the capacitor banks needs to be considered in the worst-case scenario. In the following, the capacitor analysis will be detailed for both the MSI_1 and the MSI_2.

5.3.1 Commutation paths

From Fig. 5.4 and considering a Wye (Y) connection of the load, the input currents are expressed as in (5.3) for the MSI_1 and in (5.4) for the MSI_2.

$$\begin{aligned} i_{in1,MSI_1}(t) &= F_{1,a} i_a(t) + F_{1,b} i_b(t) + F_{1,c} i_c(t) \\ i_{in2,MSI_1}(t) &= G_{1,a} i_a(t) + G_{1,b} i_b(t) + G_{1,c} i_c(t) \end{aligned} \tag{5.3}$$

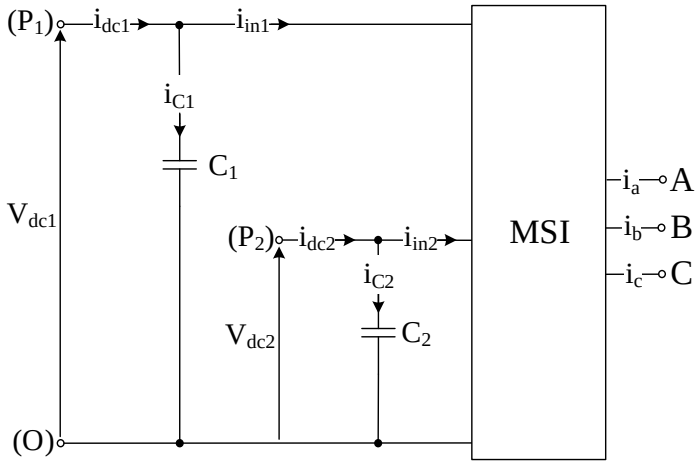

Figure 5.4: Capacitor banks of the MSI.

$$\begin{aligned} i_{in1,MSI_2}(t) &= F_{2,a}i_a(t) + F_{2,b}i_b(t) + F_{2,c}i_c(t) \\ i_{in2,MSI_2}(t) &= G_{2,a}i_a(t) + G_{2,b}i_b(t) + G_{2,c}i_c(t) \end{aligned} \tag{5.4}$$

where the switching functions $F_{1,k}$, $G_{1,k}$, $F_{2,k}$, and $G_{2,k}$ were defined in Section 4.3. Although $i_{in1,MSI_1}(t)$ and $i_{in1,MSI_2}(t)$, as well as $i_{in2,MSI_1}(t)$ and $i_{in2,MSI_2}(t)$, are given by different equations depending on the MSI topology, the same results can be found by replacing the switching functions. Hence, in the following, the input currents will be denoted by $i_{in1}(t)$ and $i_{in2}(t)$ for both the MSI_1 and MSI_2.

From (5.3), (5.4) and Table 4.2, $i_{in1}(t)$ and $i_{in2}(t)$ can be found for each of the three operating modes of both MSI topologies and the six intervals shown in Fig. 4.4a. For example, Fig. 5.5 presents the simplified switching states $S_{T1,k}$ and $S_{T2,k}$, and the waveforms of $i_{in1}(t)$ and $i_{in2}(t)$ over one switching period during the interval $[\frac{\pi}{6};\frac{\pi}{2}]$ of Fig. 4.4a for the three operating modes. One can note that $v^*_{j.k}(t)$, expressed in (4.7), can be supposed constant over one switching period T_{sw} as the switching frequency of $v_{carrier}(t)$ is considered much larger than the reference function frequency. Moreover, the switching waveforms of $S_{T1,k}$ are not shown in Fig. 5.5a since the devices $T_{1,k}$ are always turned off in Mode I_1.

In a similar manner, the switching patterns of $S_{T2,k}$ are not shown in Fig. 5.5b since $T_{2,k}$ remain turned on in Mode I_2, as mentioned in Table 4.2. In Mode I_3 the control differs for the MSI_1 and MSI_2 and different switching pattern for $S_{T1,k}$ and $S_{T2,k}$ are shown in Figs. 5.5c and 5.5d. One can note that the switching waveforms of $S_{T2,k}$ are not shown in Fig, 5.5d since $T_{2,k}$ are always turned off in the MSI_2 operating in Mode I_3.

From Fig. 5.5a, the input current $i_{in2}(t)$ can be divided into four operating areas, namely I to IV during the time intervals T_1 to T_4 respectively. The commutation paths are detailed in Fig. 5.6 when the MSI_1 operate in Mode I_1 during the interval $[\frac{\pi}{6};\frac{\pi}{2}]$ shown in Fig. 4.4a. It is assumed that the phase currents $i_a(t)$ and $i_c(t)$ are positive while $i_b(t)$ is negative. In this operating mode, the DC-link voltage V_{dc2} is supplied through (P_2) and (O). From Fig. 5.6a, it can be seen that $i_a(t)$ and $i_c(t)$ flows through the freewheeling diodes $D_{3,a}/D_{4,a}$ and $D_{3,c}/D_{4,c}$ while $i_b(t)$ flows over $T_{3,b}$ and $T_{4,b}$ since $T_{2,k}$ is switched off during the operating area I. Hence, the current $i_{in2}(t)$ remains null. In Fig. 5.6b, $T_{2,a}$ is switched on, $i_a(t)$ flows from (P_2) to the AC side and the commutation paths for $i_b(t)$ and $i_c(t)$ remains similar than previously. The current $i_{in2}(t)$ is now equal to $i_a(t)$ during the operating area II. In Fig. 5.6c, $T_{2,c}$ is switched on and $i_{in2}(t)$ is equal to the sum of $i_a(t)$ and $i_c(t)$ during the operating area III. Finally, Fig. 5.6d shows the commutation paths during the operating area IV, where the devices $T_{2,k}$ in every phase leg are switched on and their complementary $T_{4,k}$ are switched off. Hence, the phase currents $i_a(t)$ and $i_c(t)$ flow respectively through $T_{2,a}/D_{5,a}$ and $T_{2,c}/D_{5,c}$. However, since $i_b(t)$ is negative, the current flows from the AC side to (P_2) through $T_{3,b}$ and $D_{6,b}$ as $T_{4,b}$ is switched off and the current $i_{in2}(t)$ is equal to zero.

From Fig. 5.5b, it can be seen that $i_{in1}(t)$ and $i_{in2}(t)$ can also be divided into four operating areas when the MSI_1 operates in Mode I_2. Furthermore, $i_{in2}(t)$ is equal to the opposite of $i_{in1}(t)$ since the sources are connected in series and the negative pole of V_{dc2} is connected to the negative pole of V_{dc1}. When the MSI_1 and the MSI_2 is in Mode I_3, as shown in Figs. 5.5c and 5.5d, $i_{in2}(t)$ is equal to zero and $i_{in1}(t)$ follows the same pattern

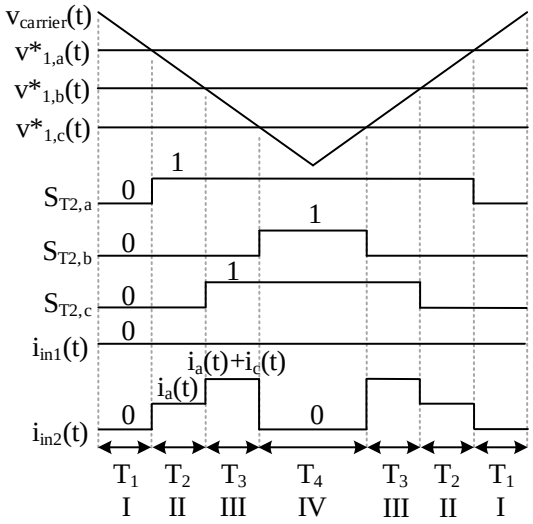

(a) Mode I_1 for the MSI_1 and MSI_2.

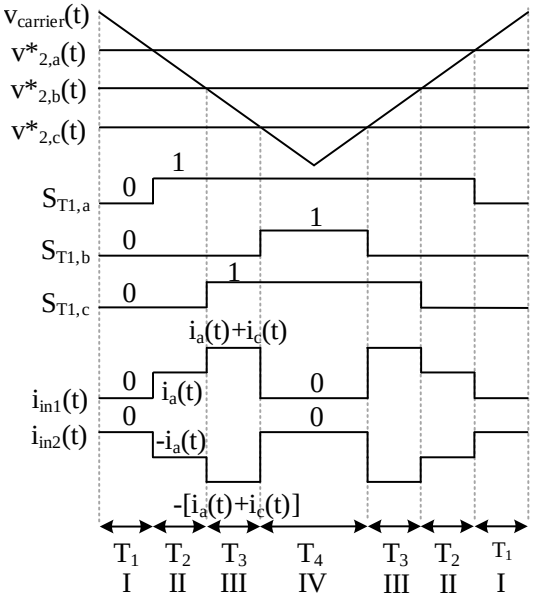

(b) Mode I_2 for the MSI_1 and MSI_2.

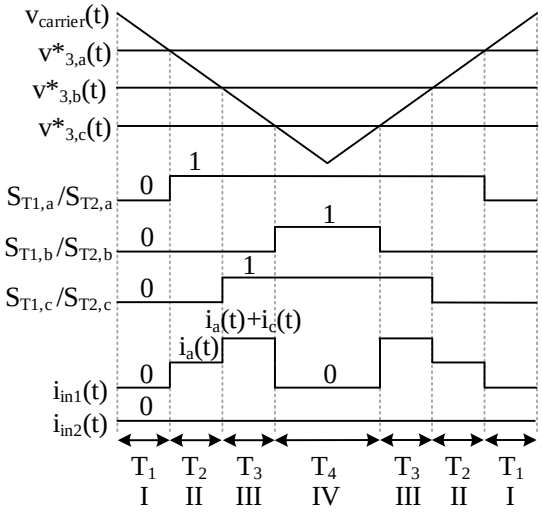

(c) Mode I_3 for the MSI_1.

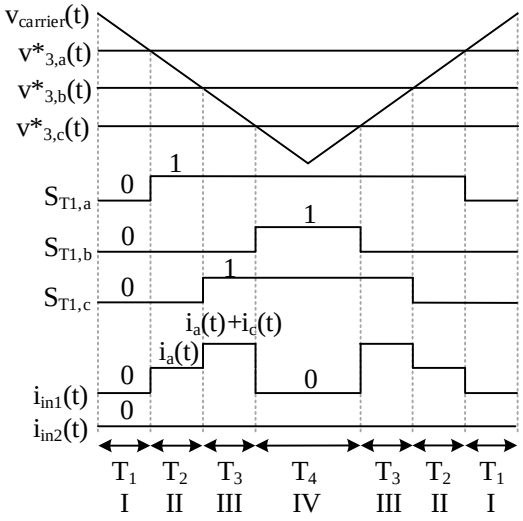

(d) Mode I_3 for the MSI_2.

Figure 5.5: PWM waveforms over one switching period for the MSI_1 and MSI_2.

than in Mode I_2. The commutation paths of the operating areas during the interval $[\frac{\pi}{6}; \frac{\pi}{2}]$ of Fig. 4.4a when the MSI_1 operates in Modes I_2 or I_3, and the commutation paths in MSI_2 for the three operating modes are shown in the Appendices A.1 and A.2.

5.3.2 RMS capacitor ripple currents

From Fig. 4.2, both capacitor currents $i_{C1}(t)$ and $i_{C2}(t)$ can be calculated by (5.5) for the MSI_1 and MSI_2.

$$i_{C,s}(t) = i_{dc,s}(t) - i_{in,s}(t) \tag{5.5}$$

where $i_{dc,s}(t)$ is the DC source current, $i_{in,s}(t)$ is the input current of the MSI and s=1 or 2 denotes the number of the DC source.

Moreover, each current from (5.5) can be divided into the average I_{avg} representing the DC component, and the ripple Δi corresponding to the AC component, as given in (5.6).

$$\begin{aligned} i_{C,s}(t) &= I_{C,s,avg} + \Delta i_{C,s}(t) \\ i_{in,s}(t) &= I_{in,s,avg} + \Delta i_{in,s}(t) \\ i_{dc,s}(t) &= I_{dc,s,avg} + \Delta i_{dc,s}(t) \end{aligned} \tag{5.6}$$

Substituting (5.6) into (5.5), the AC and DC parts can be separated and are expressed in (5.7).

$$\begin{aligned} I_{C,s,avg} &= I_{dc,s,avg} - I_{in,s,avg} \\ \Delta i_{C,s}(t) &= \Delta i_{dc,s}(t) - \Delta i_{in,s}(t) \end{aligned} \tag{5.7}$$

Since the average current of a capacitor is equal to zero and assuming that the ripple of the DC source current is negligible compared to the ripple of the input current of the

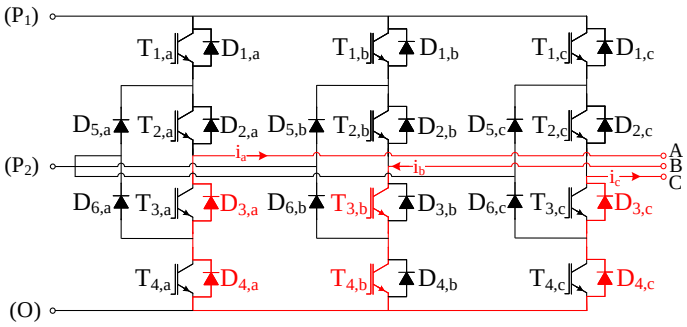

(a) Operating area I.

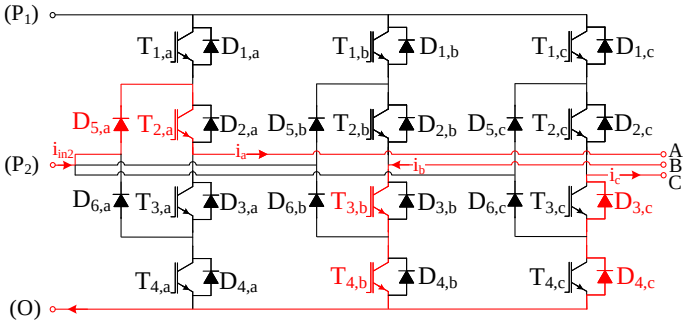

(b) Operating area II.

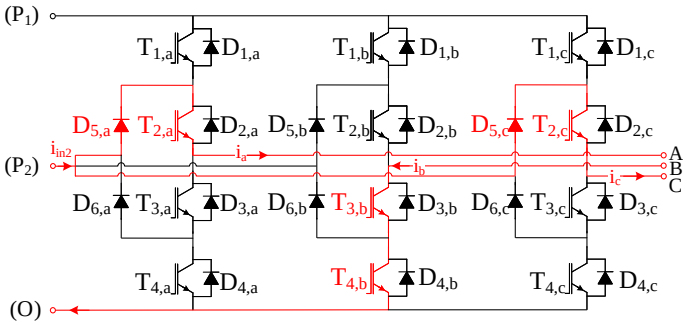

(c) Operating area III.

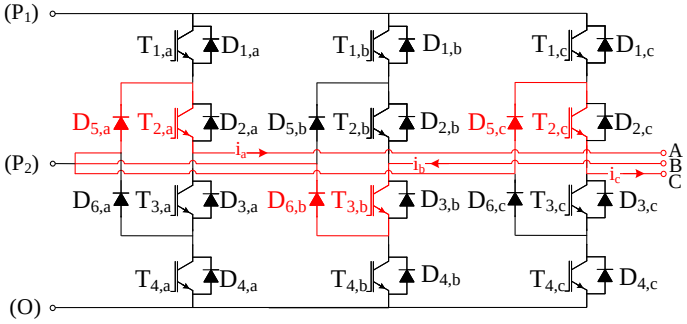

(d) Operating area IV.

Figure 5.6: Commutation paths of the MSI_1 operating in Mode I_1.

inverter, (5.7) can be approximated to (5.8).

$$\Delta i_{C,s}(t) \quad = \quad I_{in,s,avg} - i_{in,s}(t) \tag{5.8}$$

The RMS value of the capacitor current is defined as in (5.9).

$$\Delta i_{C,s,rms} \quad = \quad \frac{1}{T_{sw}} \int_0^{T_{sw}} \Delta i_{C,s}(t)^2 \, \mathrm{d}t \tag{5.9}$$

where T_{sw} is the switching period.

By substituting (5.8) into (5.9), the RMS value of the capacitor ripple current $\Delta i_{C,s,rms}$ can be expressed as a function of $i_{in,s,rms}$ and $I_{in,s,avg}$ and is given in (5.10).

$$\Delta i_{C,s,rms} \quad = \quad \sqrt{i_{in,s,rms}^2 - I_{in,s,avg}^2} \tag{5.10}$$

$$\begin{aligned} i_{in,s,rms}^2 \quad &= \quad \frac{3}{\pi} \int_{\frac{\pi}{6}}^{\frac{\pi}{2}} \left(\frac{1}{T_{sw}} \int_0^{T_{sw}} i_{in,s}(t)^2 \, \mathrm{d}t \right) \mathrm{d}\omega t \\ i_{in,s,avg} \quad &= \quad \frac{3}{\pi} \int_{\frac{\pi}{6}}^{\frac{\pi}{2}} \left(\frac{1}{T_w} \int_0^{T_{sw}} i_{in,s}(t) \, \mathrm{d}t \right) \mathrm{d}\omega t \end{aligned} \tag{5.11}$$

In (5.11), the currents $i_{in,s}^2$ and $i_{in,s}$ are first integrated over one switching period. Then, they only need to be calculated over one of the six intervals presented in Fig. 4.4a. Indeed, due to the symmetrical operation of the inverter under a balanced load, the result will be the same for the five other intervals [130, 158].

From Fig. 5.5, the currents $i_{in1}(t)$ and $i_{in2}(t)$ can be expressed as functions of the three-phase output currents $i_a(t)$, $i_b(t)$ and $i_c(t)$ in each operating area. For example, when the MSI_1 operates in Mode I_1 and $t \in [\frac{\pi}{6}; \frac{\pi}{2}]$, the input currents are expressed as in (5.12) and

(5.13).

$$i_{in1}(t) = 0 \tag{5.12}$$

$$i_{in2}(t) = \begin{cases} 0 & t \in T_1, T_4 \\ i_a(t) & t \in T_2 \\ i_a(t) + i_c(t) & t \in T_3 \end{cases} \tag{5.13}$$

By substituting (5.12) into (5.11), it is clear that $i_{in1,rms}$ and $I_{in1,avg}$ remain null. As a result, the RMS capacitor ripple current $\Delta i_{C1,rms}$ is equal to zero in Mode I_1. On the other hand, by neglecting the deadtimes between the switches and the reverse recovery current in the freewheeling diodes, , $i_{in2,rms}$ and $I_{in2,avg}$ can be calculated by substituting (5.13) and (5.1) into (5.11) [131]. Finally, $\Delta i_{C2,rms}$ in Mode I_1 is given by (5.14).

$$\begin{aligned} \Delta i_{C2,rms} &= A_1(M_1, \phi).\frac{I_{pk,1}}{\sqrt{2}} \\ A_j(M_j, \phi) &= \sqrt{\frac{\sqrt{3}M_j}{2\pi} + (\frac{2\sqrt{3}M_j}{\pi} - \frac{9}{8}M_j^2)cos^2(\phi)} \end{aligned} \tag{5.14}$$

The same procedure can be applied to calculate the analytical expressions of $i_{in1}(t)$ and $i_{in2}(t)$ in Modes I_2 and I_3 from Figs. 5.5b and 5.5c. The final expressions of $\Delta i_{C1,rms}$ and $\Delta i_{C2,rms}$ in each operating mode are provided in Table 5.2.

Fig. 5.7 shows $\Delta i_{C1,rms}$ and $\Delta i_{C2,rms}$ as functions of the modulation index M_j and the power factor $cos(\phi)$ in each operating mode of both MSI topologies. One can note that $\Delta i_{C1,rms}$ in Mode I_1 and $\Delta i_{C2,rms}$ in Mode I_3 are not displayed since they are equal to zero. Moreover, $\Delta i_{C1,rms}$ and $\Delta i_{C2,rms}$ are equal in Mode I_2. Indeed, as shown in Fig. 5.5b, the current $i_{in2}(t)$ is equal to $-i_{in1}(t)$, hence, the RMS values are equal. From Fig. 5.7a, it can be seen that $\Delta i_{C1,rms}$ reaches its maximum in Mode I_3 while the highest value

Table 5.2: $\Delta i_{C1,rms}$ and $\Delta i_{C2,rms}$ in every operating mode of both MSI topologies.

Operating modes	$\Delta i_{C1,rms}$	$\Delta i_{C2,rms}$
I_1	0	$A_1(M_1,\phi).\frac{I_{pk,1}}{\sqrt{2}}$
I_2	$A_2(M_2,\phi).\frac{I_{pk,2}}{\sqrt{2}}$	$A_2(M_2,\phi).\frac{I_{pk,2}}{\sqrt{2}}$
I_3	$A_3(M_3,\phi).\frac{I_{pk,3}}{\sqrt{2}}$	0

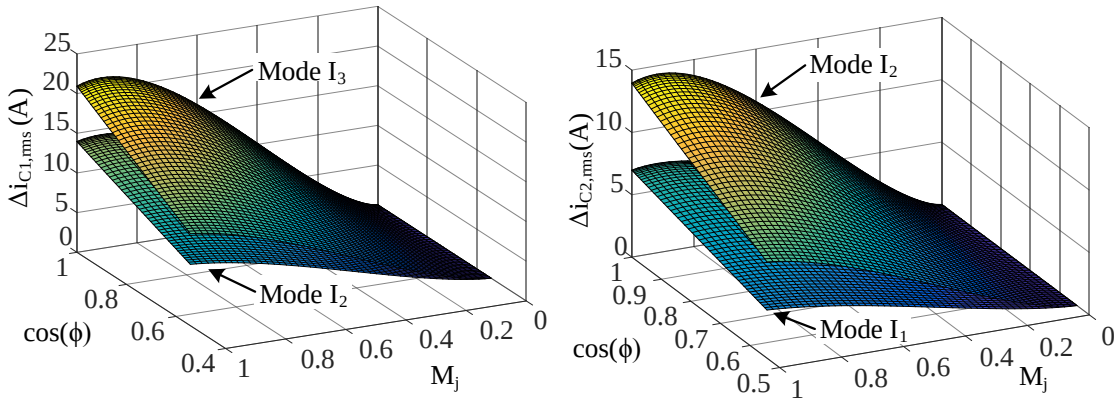

(a) $\Delta i_{C1,rms}$ in C_1.

(b) $\Delta i_{C2,rms}$ in C_2.

Figure 5.7: RMS capacitor ripple currents for every operating mode of the MSI topologies.

of $\Delta i_{C2,rms}$ is achieved in Mode I_2 (see Fig. 5.7b). This is due to the assumption that the R-L load is constant in all three operating modes of the MSI. Thus, for a similar power factor and modulation index, the output voltage and, hence, the peak current in Mode I_3, are greater than in Modes I_1 and I_2. As a result, the current capability of C_1 and C_2 should be selected based on the maximum output current required by the load in each operating mode to prevent the capacitor banks from overheating.

5.3.3 Capacitances

The capacitances C_1 and C_2 also depend on the mode in which the MSI operates and are calculated from the RMS value of the capacitor ripple voltage $\Delta V_{C1,rms}$ and $\Delta V_{C2,rms}$.

These values only need to be calculated over one switching period in one of the six intervals defined in Fig. 4.4a since the load is considered balanced. They can be defined by (5.15).

$$\Delta V_{C,s,rms}^2 = \frac{3}{\pi}\int_{\frac{\pi}{6}}^{\frac{\pi}{2}}\left(\frac{1}{T_{sw}C_s}\int_0^{T_{sw}}\Delta i_{C,s}(t)^2\,\mathrm{d}t\right)\mathrm{d}\omega t \tag{5.15}$$

For example, when the MSI operates in Mode I_1, $\Delta i_{C,s}(t)$ can be expressed as in (5.16) and (5.17) from (5.8), (5.12) and (5.13).

$$\Delta i_{C1}(t) = 0 \tag{5.16}$$

$$\Delta i_{C2}(t) = \begin{cases} I_{in2,avg} & t \in T_1, T_4 \\ I_{in2,avg} - i_a(t) & t \in T_2 \\ I_{in2,avg} - (i_a(t) + i_c(t)) & t \in T_3 \end{cases} \tag{5.17}$$

Finally, by substituting (5.16) into (5.15), it is clear that $\Delta V_{C1,rms}$ is equal to zero in Mode I_1. Furthermore, substituting (5.17) into (5.15) gives the final expressions of $\Delta V_{C2,rms}$ in Mode I_1 as shown in (5.18) [131, 158].

$$\begin{aligned} \Delta V_{C2,rms} &= B_1(M_1,\phi).\frac{I_{pk,1}M_1}{16C_2 f_{sw}\sqrt{2}} \\ B_j(M_j,\phi) &= \sqrt{(6 - \tfrac{96M_j\sqrt{3}}{5\pi} + \tfrac{9M_j^2}{2})cos^2(\phi) + \tfrac{8M_j\sqrt{3}}{5\pi}} \end{aligned} \tag{5.18}$$

where f_{sw} is the switching frequency of the MSI.

Similar calculations can be applied in Modes I_2 and I_3 but will not be presented to avoid redundancy. The RMS capacitor ripple voltages $\Delta V_{C1,rms}$ and $\Delta V_{C2,rms}$ are commonly fixed to 5% to 10% of the corresponding DC input source voltage and the appropriate capacitance for each operating mode of the MSI are given in Table 5.3.

Table 5.3: C_1 and C_2 in every operating mode of both MSI topologies.

Operating modes	C_1	C_2
I_1	0	$B_1(M_1,\phi).\dfrac{I_{pk,1}.M_1}{16\Delta V_{C2,rms}.f_{sw}\sqrt{2}}$
I_2	$B_2(M_2,\phi).\dfrac{I_{pk,2}.M_2}{16\Delta V_{C1,rms}.f_{sw}\sqrt{2}}$	$B_2(M_2,\phi).\dfrac{I_{pk,2}.M_2}{16\Delta V_{C2,rms}.f_{sw}\sqrt{2}}$
I_3	$B_3(M_3,\phi).\dfrac{I_{pk,3}.M_3}{16\Delta V_{C1,rms}.f_{sw}\sqrt{2}}$	0

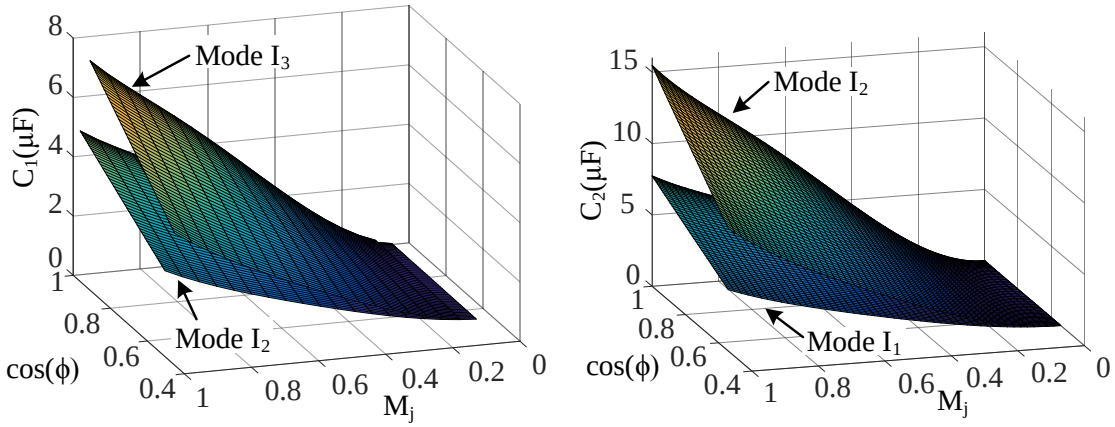

(a) C_1. (b) C_2.

Figure 5.8: Capacitances for every operating mode of the MSI.

In Fig. 5.8, the capacitances C_1 and C_2 are shown for every operating mode as functions of M_j and $cos(\phi)$ for the same parameters presented in Table 5.1. Similarly to Fig. 5.7, the capacitances C_1 in Mode I_1 and C_2 in Mode I_3 are not presented. Moreover, from Fig. 5.8a it is clear that the highest value of C_1 is reached in Mode I_3 while the maximum value of C_2 is obtained in Mode I_2 (see Fig. 5.8b). Hence, for the same reasons previously mentioned, both capacitances should be selected based on the maximum output current required by the load in each operating mode to ensure satisfying filtering of the DC input sources.

5.3.4 Capacitor comparison

The total volume of the capacitor bank in the MSI is expected to be larger than that of the VSI. Indeed, the MSI has two DC-link capacitors for its sources instead of one, as it is the case in the VSI. In the following, the capacitor requirements for the MSI and VSI are compared to estimate this volume increase. In order to provide a fair comparison, the capacitance C_{vsi} and the RMS capacitor ripple current $\Delta i_{C,rms}$ of the VSI were calculated for three DC source levels, V_{dc2}, $V_{dc1} - V_{dc2}$ and V_{dc1}, corresponding to the DC voltage applied to the load in each operating mode of the MSI. The analytical equations are given in [158, 159]. It has been found that the maximum values of C_{vsi} and $\Delta i_{C,rms}$ are reached for a DC voltage equal to V_{dc1}. As a result, the capacitor requirements for C_1 in the MSI are similar to those for C_{vsi}. This means that the volume increase of the capacitor bank in the MSI is only due to C_2. Table 5.4 summarizes the capacitor specifications for the MSI and the VSI considering the parameters listed in Table 5.1. One can note that the voltage and current ratings for C_2 are much lower than for C_1 and C_{vsi}.

Table 5.4: Capacitor requirement comparison.

Inverter topology	Capacitor bank	Voltage breakdown (V)	Capacitance (μF)	RMS current ripple (Arms)
VSI	C_{vsi}	650	7.73	21.50
MSI	C_1	650	7.73	21.50
	C_2	250	15.46	14.33

From the specifications of Table 5.4, two industrial capacitor models have been selected to compare the capacitor volume of the MSI and the VSI [166]. For example, the model C4AEGBW5500A3JK from KEMET is chosen for C_2 since it features a capacitance of $50\mu F$, a blocking voltage of 450V, and $\Delta i_{C2,rms}$ is equal to 16A. On the other hand, the model C4AEJBW5200A3JJ is selected for C_1 and C_{vsi} due to a capacitance of $20\mu F$, a blocking voltage of 700V, and $\Delta i_{C1,rms}$ equal to 12.5A. However, in view of the low RMS

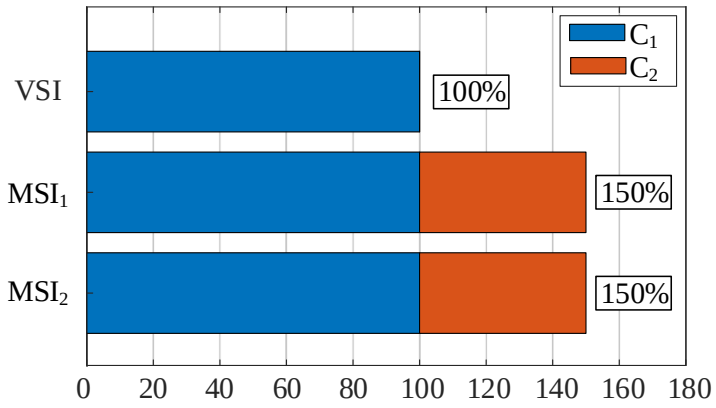

Figure 5.9: Normalized capacitor volume of the VSI and both MSI topologies.

current capability compared to the requirements, two capacitors in parallel must be used to filter V_{dc1}. From the datasheet, one can also note that both models have the same dimensions and, thus, the same volume. As a result, C_1 has a total volume twice larger than C_2. Fig. 5.9 displays the normalized capacitor volume in both MSI topologies and the VSI. The values have been normalized by taking the VSI as the reference. It can be seen that the total volume of the capacitor bank in the MSI_1 and MSI_2 increases by 50% compared to the VSI. In conclusion, although the MSI has twice more capacitors than the VSI, its capacitor volume does not double but increases by one half.

5.4 Efficiency analysis

In this section, the efficiency of both MSI topologies is analyzed by estimating the conduction and the switching losses of the switches. To do so, the power losses are calculated from the averaged and RMS currents in the switches and the datasheet parameters.

5.4.1 Average and RMS currents in the switches

Due to the discontinuity of the current in the devices, the average and RMS values are approximated by applying the mid-ordinate rule [160]. This method consists of splitting

the device current curve into rectangles with a width equal to the conduction time of the switch and the height is assumed to be the value of the phase current at the instant t. As a result, the average current $I_{avg,device}$ and RMS current $I_{rms,device}$ of each device are given as in (5.19).

$$\begin{aligned} I_{avg,device} &= \frac{1}{2\pi}\int_{\alpha_1}^{\alpha_2} i_a(t) F_{device,j}(t)\,\mathrm{d}t \\ I^2_{rms,device} &= \frac{1}{2\pi}\int_{\alpha_1}^{\alpha_2} i_a(t)^2 F_{device,j}(t)\,\mathrm{d}t \end{aligned} \tag{5.19}$$

where α_1 and α_2 are respectively the lower and upper limits of the interval during which the device conducts over one fundamental period. The function $F_{device,j}(t)$ is the conduction duty cycle function that varies over time and depends on the operating mode. It represents the duration over a switching period during which the switch conducts the phase current [167].

For the sake of brevity, only the calculations of the function $F_{device,j}(t)$ in Mode I_1 will be presented for both MSI_1 and MSI_2. A similar procedure can be applied for Modes I_2 and I_3. Moreover, the analysis will only be detailed for the phase leg A as the load is considered balanced, implying identical results for the switches in the two other phase legs.

Average and RMS currents in MSI_1

Fig. 5.10 shows the phase current $i_a(t)$, the fundamental harmonic of the line voltage $V_{AN,0}(t)$ and the current waveforms in the devices of leg A when the MSI_1 operates in Mode I_1 over one fundamental period. From a detailed analysis of the waveforms presented in Fig. 5.10, the function $F_{device,1}(t)$ for each device can be developed as follows.

- The devices $T_{1,a}$, $D_{1,a}$ and $D_{2,a}$ never conduct. Hence, the functions $F_{T1a,1}(t)$, $F_{D1a,1}(t)$ and $F_{D2a,1}(t)$ are equal to zero over the fundamental period;
- In Mode I_1, it has been seen that the switch $T_{3,a}$ is always turned on, as seen in

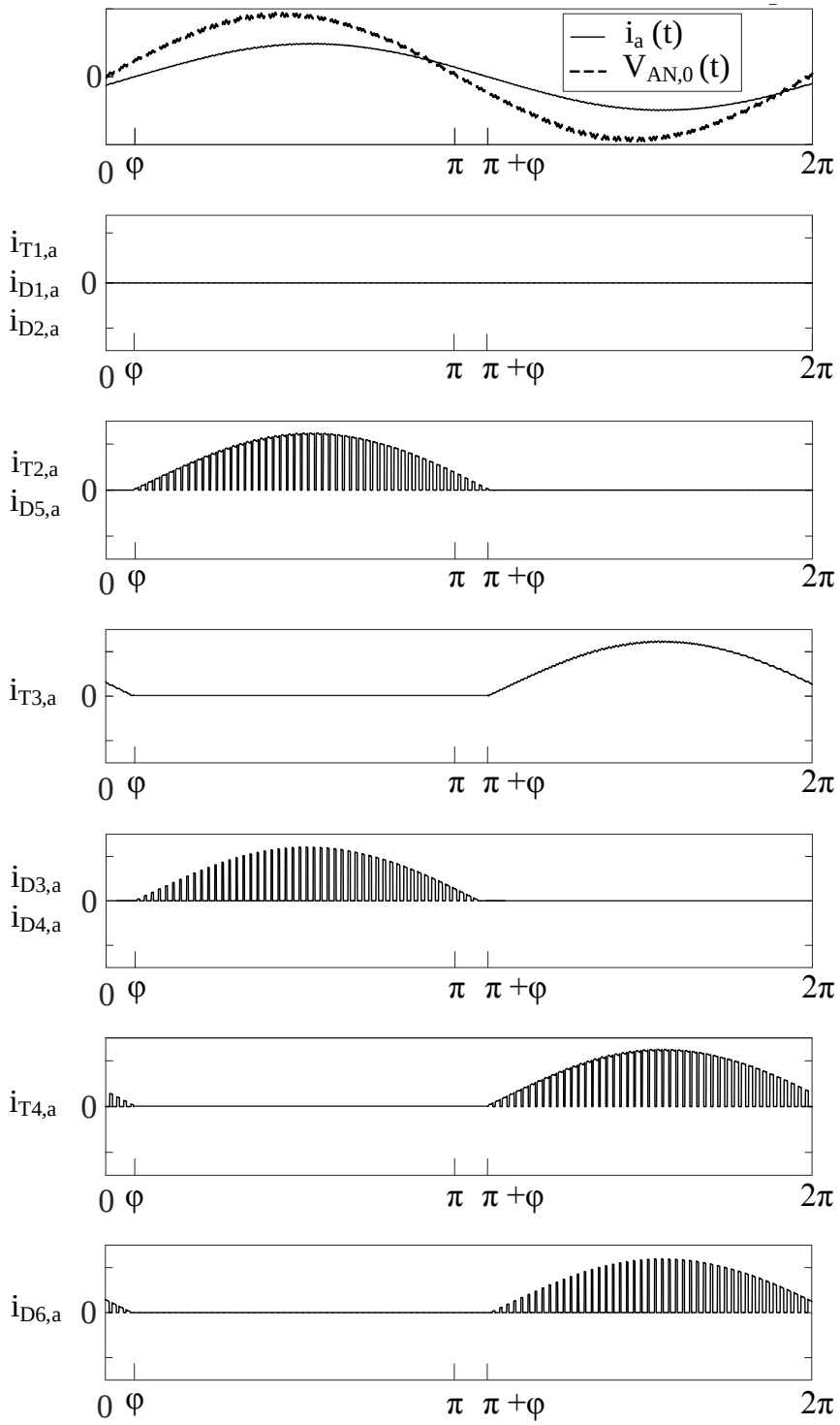

Figure 5.10: Waveforms of $i_a(t)$, $V_{AN,0}(t)$ and the current in the devices of the phase leg A when the MSI_1 operates in Mode I_1.

Table 4.2. As a result, the switch conducts during the interval $[0;\phi] \cup [\pi+\phi; 2\pi]$ and $F_{T3a,1}(t)$ is equal to 1;

- Both $T_{2,a}$ and $D_{5,a}$ conduct during the interval $[\phi; \pi+\phi]$ and $T_{4,a}$ conducts during the interval $[0;\phi] \cup [\pi+\phi; 2\pi]$. However, unlike $T_{3,a}$ that is always turned on, these three devices periodically switch and their conduction duty cycle functions $F_{T2a,1}(t)$, $F_{D5a,1}(t)$ and $F_{T4a,1}(t)$ depend on the intersection between the carrier function $v_{carrier}(t)$ and the reference voltage $v^*_{1,a}(t)$. In Fig. 5.11a, the functions $v_{carrier}(t)$ and $v^*_{1,a}(t)$ have been shifted up by one to simplify the calculations and Fig. 5.11b is a zoom of the area surrounded by a red rectangle in Fig. 5.11a. For similar reasons announced in Section 5.3.1, $v^*_{1,a}(t)$ is considered constant over one carrier period. From Fig. 5.11b, the equality given in (5.20) can be derived based on geometric considerations.

$$\begin{aligned} \frac{T_{sw}F_{T2a,1}(t)}{T_{sw}} &= \frac{v^*_{1,a}(t)+1}{2} \\ F_{T2a,1}(t) &= \frac{1}{2}(1+M_1\sin(\omega t)) \end{aligned} \tag{5.20}$$

As a result, $F_{T2a,1}(t)$, $F_{D5a,1}(t)$ and $F_{T4a,1}(t)$ are expressed as in (5.20) and the average and RMS currents are given by (5.21) and (5.22).

$$I_{avg,(T_{2,a}/D_{5,a}/T_{4,a})} = I_{pk,1}(\frac{1}{2\pi}+\frac{M_1\cos\phi}{8}) \tag{5.21}$$

$$I^2_{rms,(T_{2,a}/D_{5,a}/T_{4,a})} = I_{pk,1}(\frac{1}{8}+\frac{M_1\cos\phi}{3\pi}) \tag{5.22}$$

- Finally, $D_{3,a}$ and $D_{4,a}$ complement $T_{2,a}$ and $D_{5,a}$ during the interval $[\phi; \pi+\phi]$ while $D_{6,a}$ complements $T_{4,a}$ during $[0;\phi] \cup [\pi+\phi; 2\pi]$. Hence, their conduction duty cycle functions are identical and can be expressed as in (5.23). The average and RMS

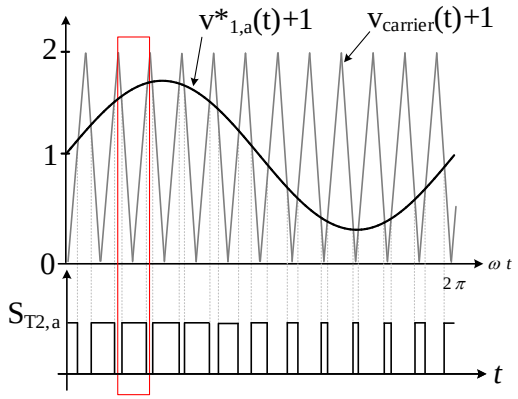

(a) Functions $v_{carrier}(t)$ and $v^*_{1,a}(t)$ shifted up by one and PWM signal $S_{T2,a}$.

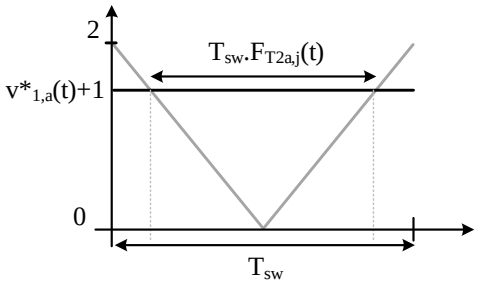

(b) Zoom of the red rectangle.

Figure 5.11: Geometric considerations to calculate $F_{T2a,1}(t)$.

currents are given by (5.24) and (5.25).

$$\begin{aligned} F_{D3a,1}(t) &= F_{D4a,1}(t) = F_{D6a,1}(t) \\ F_{D3a,1}(t) &= 1 - F_{T2a,1}(t) \\ &= \frac{1}{2}(1 - M_1 \sin(\omega t)) \end{aligned} \tag{5.23}$$

$$I_{avg,(D_{3,a}/D_{4,a}/D_{6,a})} = I_{pk,1}(\frac{1}{2\pi} - \frac{M_1 \cos\phi}{8}) \tag{5.24}$$

$$I^2_{rms,(D_{3,a}/D_{4,a}/D_{6,a})} = I_{pk,1}(\frac{1}{8} - \frac{M_1 \cos\phi}{3\pi}) \tag{5.25}$$

From the aforementioned analysis, the conduction duty cycle function and the average and RMS currents for each device are summarized in Table 5.5a when the MSI_1 operates in Mode I_1.

Table 5.5: Average and RMS currents, and power losses of each device in Mode I_1.

(a) In the MSI_1.

Devices	$F_{device,1}(t)$	$I_{avg,device}$	$I^2_{rms,device}$	$P_{cond,device}$	$P_{sw,device}$
$T_{1,k}/D_{1,k}/D_{2,k}$	0	0	0	0	0
$T_{2,k}/D_{5,k}$ $T_{4,k}$	(5.20)	(5.21)	(5.22)	(5.27)	(5.29)
$T_{3,k}$	1	$\frac{I_{pk}}{\pi}$	$\frac{I_{pk}}{2}$	(5.27)	0
$D_{3,k}/D_{4,k}$ $D_{6,k}$	(5.23)	(5.24)	(5.25)	(5.27)	(5.29)

(b) In the MSI_2.

Devices	$F_{device,1}(t)$	$I_{avg,device}$	$I^2_{rms,device}$	$P_{cond,device}$	$P_{sw,device}$
$T_{1,k}/D_{1,k}$	0	0	0	0	0
$T_{2,k}/D_{3,k}$ $T_{4,k}$	(5.20)	(5.21)	(5.22)	(5.27)	(5.29)
$T_{3,k}/D_{2,k}$ $D_{4,k}$	(5.23)	(5.24)	(5.25)	(5.27)	(5.29)

Average and RMS currents in MSI_2

Fig. 5.12 shows the phase current $i_a(t)$, the fundamental harmonic of the line voltage $V_{AN,0}(t)$ and the current waveforms in the switches of phase leg A when the MSI_2 operates in Mode I_1 over one fundamental period.

From a detailed analysis of the waveforms presented in Fig. 5.12, the function $F_{device,1}(t)$ for each device can be developed as follows.

- The functions $F_{T1a,1}(t)$ and $F_{D1a,1}(t)$ are equal to zero over the fundamental period since the devices $T_{1,a}$ and $D_{1,a}$ never conduct;
- The devices $T_{2,a}$ and $D_{3,a}$ periodically switch during $[\phi; \pi + \phi]$ and $T_{4,a}$ conducts during the interval $[0; \phi] \cup [\pi + \phi; 2\pi]$. Hence, their conduction duty cycle functions

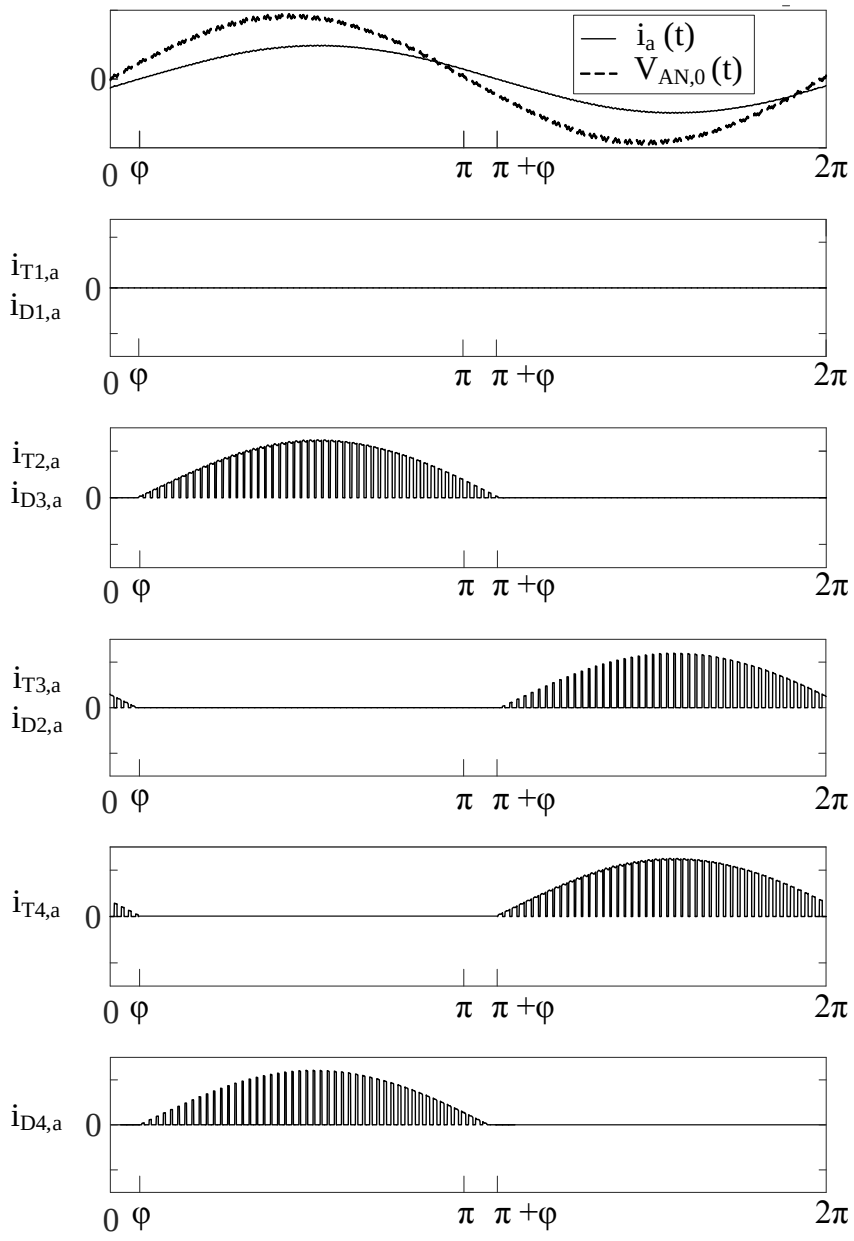

Figure 5.12: Waveforms of $i_a(t)$, $V_{AN,0}(t)$ and the current waveforms in the devices of the phase leg A when the MSI_2 operates in Mode I_1.

are calculated as in (5.20) and the average and RMS currents are given by (5.21) and (5.22).

- Finally, $T_{3,a}$ and $D_{2,a}$ complement $D_{3,a}$ and $T_{2,a}$ during the interval $[\phi; \pi + \phi]$ while $D_{4,a}$ complements $T_{4,a}$ during $[0; \phi] \cup [\pi + \phi; 2\pi]$. Hence, their conduction duty cycle functions are identical and can be expressed as in (5.23). The average and RMS currents are given by (5.24) and (5.25).

From the aforementioned analysis, the conduction duty cycle function and the average and RMS currents for each device are summarized in Table 5.5b when the MSI_2 operates in Mode I_1.

5.4.2 Power loss calculation

The average conduction losses $P_{cond,device}$ for both IGBTs and diodes can be calculated as in (5.26) [163, 165].

$$\begin{aligned} P_{cond,device} &= \frac{1}{2\pi}\int_{\alpha_1}^{\alpha_2} V_{device}(t).i_a(t).F_{device,j}(t)\,\mathrm{d}t \\ V_{device}(t) &= V_{device,0} + R_{device}.i_a(t) \end{aligned} \tag{5.26}$$

where $V_{device}(t)$ is either $V_{CE}(t)$ or $V_F(t)$ the voltage across the IGBTs or the diodes according to the static characteristic, $V_{device,0}(t)$ is either V_{CE0} or V_{F0} the zero-current voltages and R_{device} is either R_{CE} or R_F the on-sate resistances from the datasheet of the IGBTs or diodes respectively.

From (5.19) and (5.26), the average conduction losses are expressed as in (5.27) and are summarized in Table 5.5 when both MSI topologies operate in Mode I_1.

$$P_{cond,device} = V_{device,0}.I_{avg,device} + R_{device}.I^2_{rms,device} \tag{5.27}$$

On the other hand, the average switching losses $P_{sw,device}$ can be estimated for both the

IGBTs and diodes by (5.28).

$$\begin{aligned} P_{sw,device} &= f_{sw}.\frac{1}{2\pi}\int_{\beta_1}^{\beta_2} E_{sw,device}(i(t))\,\mathrm{d}t \\ E_{sw,device}(i(t)) &= E_{sw,nom}.\frac{i(t)}{I_{nom}}.\frac{V_{dc,j}}{V_{nom}} \end{aligned} \tag{5.28}$$

where β_1 and β_2 are respectively the lower and upper limits of the switching interval over one fundamental period. The energy dissipation $E_{sw,nom}$ is given in the datasheet at nominal current I_{nom} and nominal voltage V_{nom}. For IGBTs, $E_{sw,nom}$ can be defined as the sum of the turn-on $E_{on,nom}$ and the turn-off $E_{off,nom}$ energies while it is equal to the reverse recovery energy $E_{rec,nom}$ for diodes. The current $i(t)$ represents the current flowing through the device when it switches. For example, from Fig. 5.10 when the MSI_1 operates in Mode I_1, it can be seen that every device switching during the interval $[\phi;\pi+\phi]$ conducts the current $i_a(t)$ while a current $-i_a(t)$ flows through the devices switching during the interval $[0;\phi]\cup[\pi+\phi;2\pi]$. By integrating (5.28), the switching power losses are identical for both switching intervals and can be expressed as in (5.29).

$$P_{sw,device} = f_{sw}.\frac{1}{\pi}.E_{sw,nom}.\frac{I_{pk,1}}{I_{nom}}.\frac{V_{dc,1}}{V_{nom}} \tag{5.29}$$

One can note that $T_{3,a}$ is always turned on in Mode I_1 which means that it does not generate switching losses. The switching losses for every device in Mode I_1 are summarized in Table 5.5.

Finally, from Table 5.5 and by considering the load balanced, the total losses P_{tot} of the MSI can be directly calculated as the sum of the conduction and switching losses of every device in the three legs of the inverter and are expressed as in (5.30).

$$P_{tot} = 3\sum_{device}(P_{cond,device}+P_{sw,device}) \tag{5.30}$$

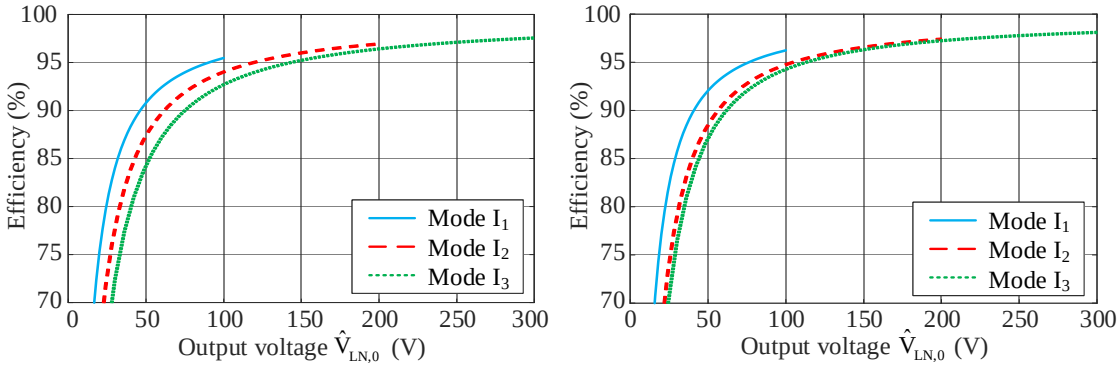

(a) MSI_1. (b) MSI_2.

Figure 5.13: Theoretical efficiencies of the MSI.

The theoretical efficiencies of the MSI_1 and the MSI_2 have been calculated with the parameters presented in Table 5.1 and the IGBT modules type F3L50R06W1E3-B11 and F3L100R12W2H3-B11 respectively. Results are shown in Fig. 5.13 for a power factor close to unity. At low output voltage, both topologies can operate in the three modes and the efficiency in Mode I_1 is higher than in Modes I_2 and I_3. Indeed, for the same amplitude $\hat{V}_{LN,0}$, the modulation index in Mode I_1 is higher than for Modes I_2 and I_3 since V_{dc2} is smaller than $V_{dc1} - V_{dc2}$ and V_{dc1}. Similarly, the MSI achieves higher efficiency in Mode I_2 compared to Mode I_3. As a result, by actively controlling the mode in which the MSI operates and keeping a high modulation index, high efficiency can be achieved over a wide power range. One can also note that the peak efficiency obtained in Mode I_1 is lower than those obtained in Modes I_2 and I_3. This is due to the DC input voltage applied to the inverter that is equal to V_{dc2} in Mode I_1 and is lower than the DC voltages applied in Modes I_2 and I_3 (i.e. $V_{dc1} - V_{dc2}$ and V_{dc1} respectively). This characteristic brings new opportunities in terms of design optimization where the DC voltage levels could be selected to maximize the efficiency of the inverter depending on its application.

Table 5.6: Experimental parameters with an R-L load.

Parameters	Values
V_{dc1}	150 V
V_{dc2}	50 V
Switching frequency	10 kHz
Fundamental frequency	10 Hz
Three-phase R-L load	5.1 Ω and 256 μH

5.4.3 Experimental validation with the MSI_1

Experiments were performed with the prototype presented in Fig. 4.11 and the parameters in Table 5.6 where a battery pack supplies V_{dc2}, and a power supply provides V_{dc1}. The experimental setup is shown in Fig. 5.14 and the adapted SPWM technique was used to control the switches. In every mode, the efficiency has been measured with a Yokogawa WT1800 precision power analyzer and the modulation index was increased in steps by varying the amplitude of the output voltage $\hat{V}_{LN,0}$ while the power factor was kept constant and close to unity.

Fig. 5.15 shows the current waveforms of $i_{dc1}(t)$, $i_{dc2}(t)$ and the three-phase load $i_a(t)$, $i_b(t)$, $i_c(t)$ for a modulation index M_j equal to 1 in each operating mode. The experimental results with the adapted SPWM control are consistent with the analysis of the inverter modes detailed Chapter 4. Indeed, in Mode I_1, V_{dc2} provides power to the load while V_{dc1} is not used. This can be seen from Fig. 5.15a where $i_{dc2}(t)$ is positive and $i_{dc1}(t)$ remains null. Moreover, in Mode I_2, V_{dc1} supplies the load and charges V_{dc2} at the same time, as it is shown in Fig. 5.15b where $i_{dc1}(t)$ is positive and $i_{dc2}(t)$ is the inverse. Finally in Fig. 5.15c, V_{dc1} supplies the load in Mode I_3 and V_{dc2} is not used. This results in a positive $i_{dc1}(t)$ while $i_{dc2}(t)$ is equal to zero.

In Fig. 5.16, the measured efficiencies are compared to the calculated values over the output voltage range depending on the operating mode. It can be noticed that, when

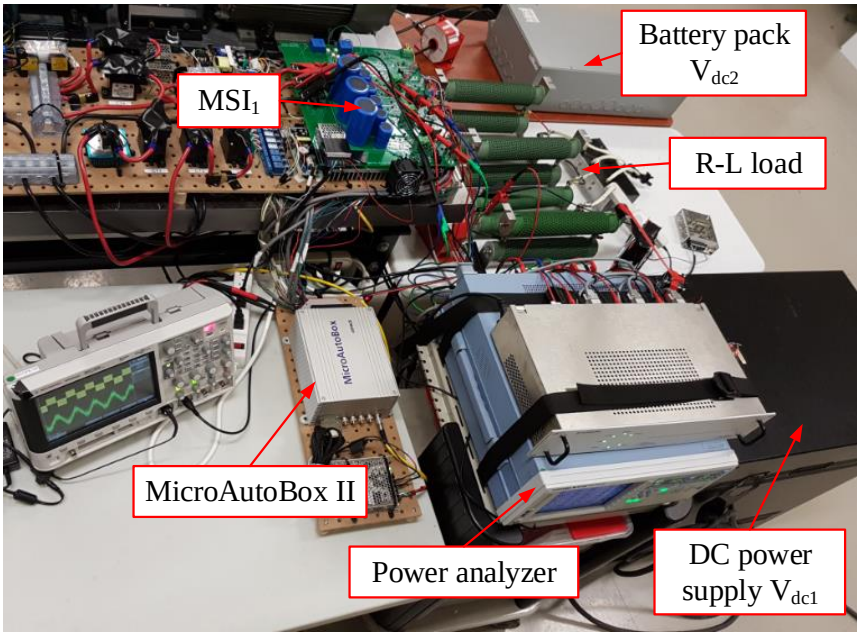

Figure 5.14: Experimental test setup of the MSI_1 with an R-L load.

the modulation index is low, the measured efficiency is slightly higher than the calculated one in Modes I_1 and I_2. These discrepancies are due to the datasheet parameters used in the averaged equations (5.27) and (5.29). Indeed, these parameters where considered constant and were extracted from the datasheet for a fixed temperature equal to $T_j = 125°C$. However, during the experiments, the IGBT modules operate at a temperature much lower than $T_j = 125°C$ which also implies lower values for the parameters. Hence, at a low modulation index, the power losses were overestimated. On the other hand, as the modulation index and, thus, the power increases, the devices heat up and the parameters used in the averaged model are closer from the experimental values. As a result, the error between the calculated and measured efficiencies at high modulation index is reduced. As a future work, the accuracy of the model can be improved by considering the temperature as a variable in the average equations and the temperature of the IGBT modules should be experimentally measured.

Table 5.7 summarizes the maximum calculated and measured efficiencies achieved and

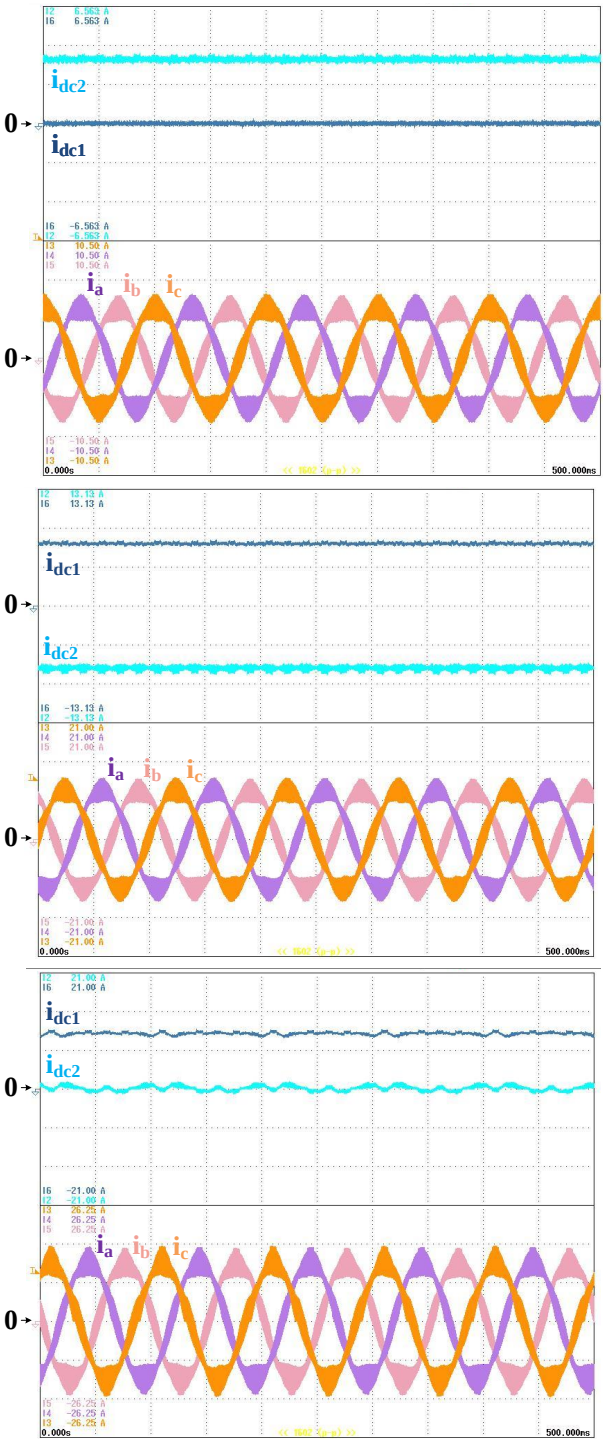

(a) Mode I_1.

(b) Mode I_2.

(c) Mode I_3.

Figure 5.15: Experimental current waveforms of the MSI_1 with the adapted SPWM.

the error between them for each operating mode. It can be noticed that the maximum calculated efficiency matches the measured one with an error of less than 2% in every operating mode. Hence, these results validate the analytical efficiency analysis of the MSI_1 previously presented.

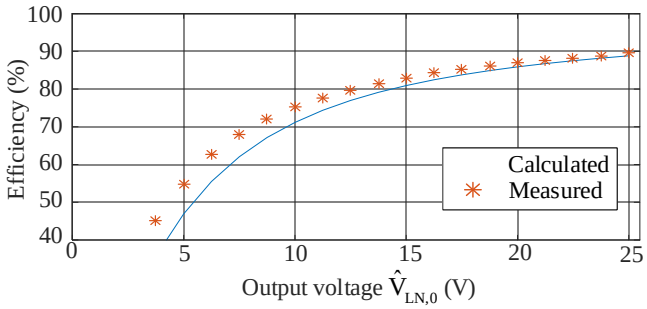

(a) Mode I_1.

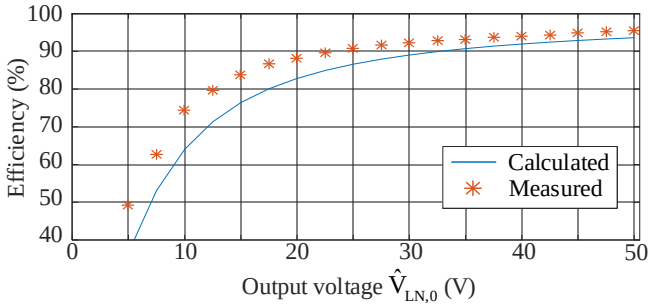

(b) Mode I_2.

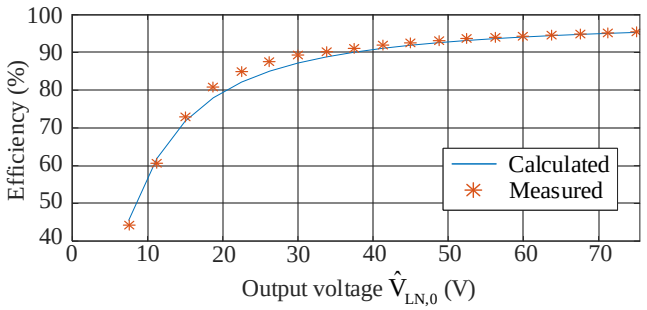

(c) Mode I_3.

Figure 5.16: Calculated and measured efficiencies of the MSI_1.

5.4.4 Experimental validation with the MSI_2

A scaled-down prototype of the MSI_2 was built and is shown in Fig.5.17. The circuit is composed of three IGBT modules type F3L100R12W2H3-B11. Experiments were carried

Table 5.7: Experimental efficiency comparison for the MSI_1.

Operating modes	1	2	3
$\hat{V}_{LN,0}$	25 V	50 V	75 V
Maximum measured efficiency (%)	88.74	95.00	94.72
Corresponding calculated efficiency (%)	89.06	93.64	95.36
Error (%)	-0.36	1.45	-0.67

out with an R-L load and the parameters are presented in Table 5.6. The DC source V_{dc2} is supplied by a battery pack and V_{dc1} is provided by a power supply. The experimental waveforms of the phase current i_a, the DC currents i_{dc1} and i_{dc2}, and the line voltage V_{AB} are presented in Figs. 5.18 with the adapted SPWM control. The output voltage $\hat{V}_{LN,0}$ was set to 25V, 50V, and 75V to show the operation of the MSI_2 in respectively Modes I_1, I_2, and I_3. It can be seen that each mode is in line with the theory detailed in Chapter 4. When the MSI_2 operates in Mode I_3, one can also note in Fig. 5.18c that the current i_{dc2} is equal to zero with no oscillations, unlike the waveforms shown in Fig. 4.16b for the MSI_1. This is because the MSI_2 does not have clamping diodes and the switches $T_{2,k}$ and $T_{3,k}$ are turned off in Mode I_3, which prevents the current i_{dc2} from flowing.

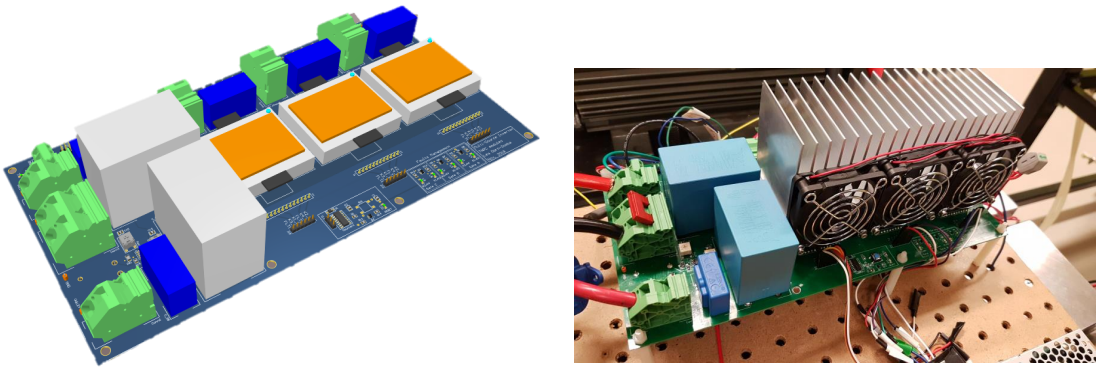

(a) Model in Altium Designer. (b) Experimental prototype.

Figure 5.17: Prototype of the MSI_2.

In every mode, the efficiency has been measured with a Yokogawa WT1800 precision

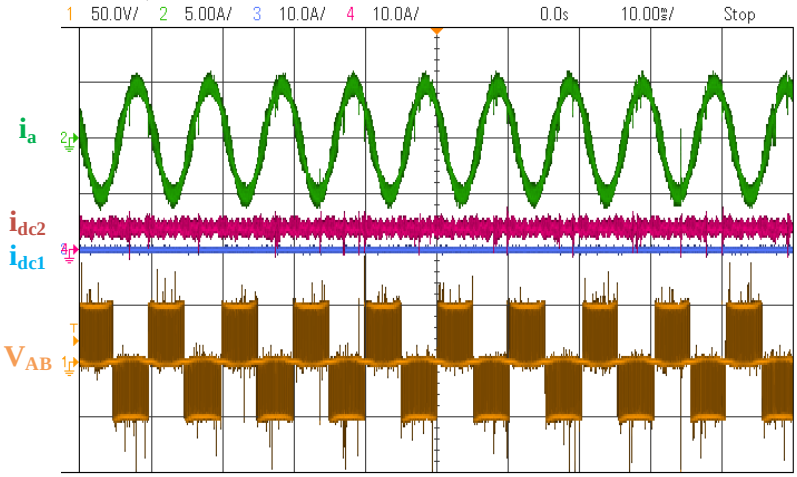

(a) Mode I_1.

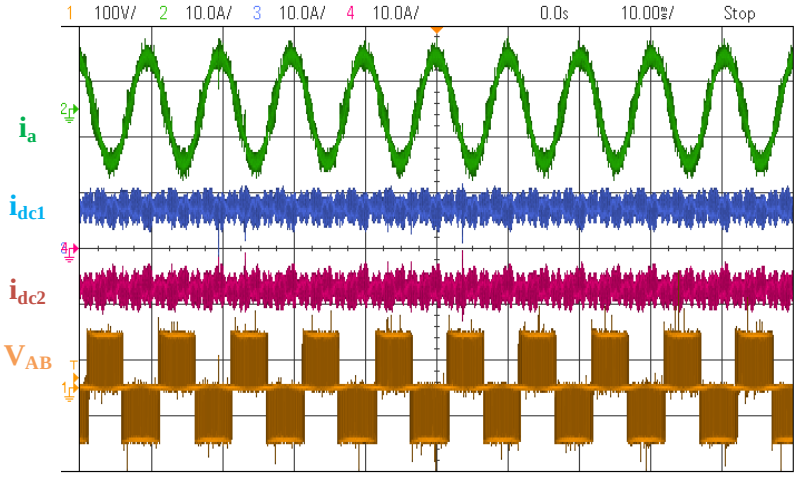

(b) Mode I_2.

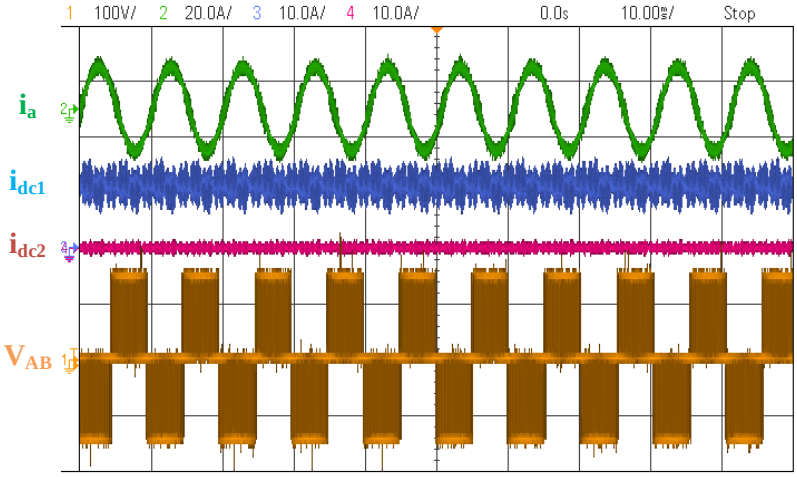

(c) Mode I_3.

Figure 5.18: Experimental waveforms of the MSI_2 with an R-L load.

Table 5.8: Experimental efficiency comparison for the MSI_2.

Operating modes	1	2	3
$\hat{V}_{LN,0}$	25 V	50 V	75 V
Maximum measured efficiency (%)	92.37	96.62	96.83
Corresponding calculated efficiency (%)	91.74	95.22	97.25
Error (%)	-0.68	1.47	-0.43

power analyzer and the modulation index was increased in steps by varying the amplitude of the output voltage $\hat{V}_{LN,0}$ while the power factor was kept constant and close to unity. Results are shown in Fig. 5.19. It can be noticed that the error between the measured efficiencies and the calculated values is fairly small even at a low modulation index, unlike the results for the MSI_1. This is due to the experimental conditions where the IGBT modules were operating at high temperatures even in Mode I_1 when the efficiency measurements were taken. Hence, the parameters used in (5.27) and (5.29) for a temperature of $T_j = 125°C$ were closed from the experimental conditions.

Table 5.8 summarizes the maximum calculated and measured efficiencies achieved and the error between them for each operating mode. It can be noticed that the maximum calculated efficiency matches the measured one with an error of less than 2% in every operating mode. Hence, these results validate the analytical efficiency analysis of the MSI_2 previously presented.

5.4.5 Efficiency comparison

In this section, the efficiency of the MSI_1, MSI_2, and VSI are compared. The efficiency of the VSI has been calculated from equations detailed in [165] with three levels of DC voltage corresponding to the DC voltage applied to the load $V_{dc,j}$ in each inverter mode of the MSI (i.e. V_{dc2}, $V_{dc1} - V_{dc2}$, V_{dc1}). The parameters are listed in Table 5.1. As previously mentioned in Section 5.2, the current rating and the blocking voltage of the switches in the MSI depend on the operating modes and the inverter topology. Due to the high DC

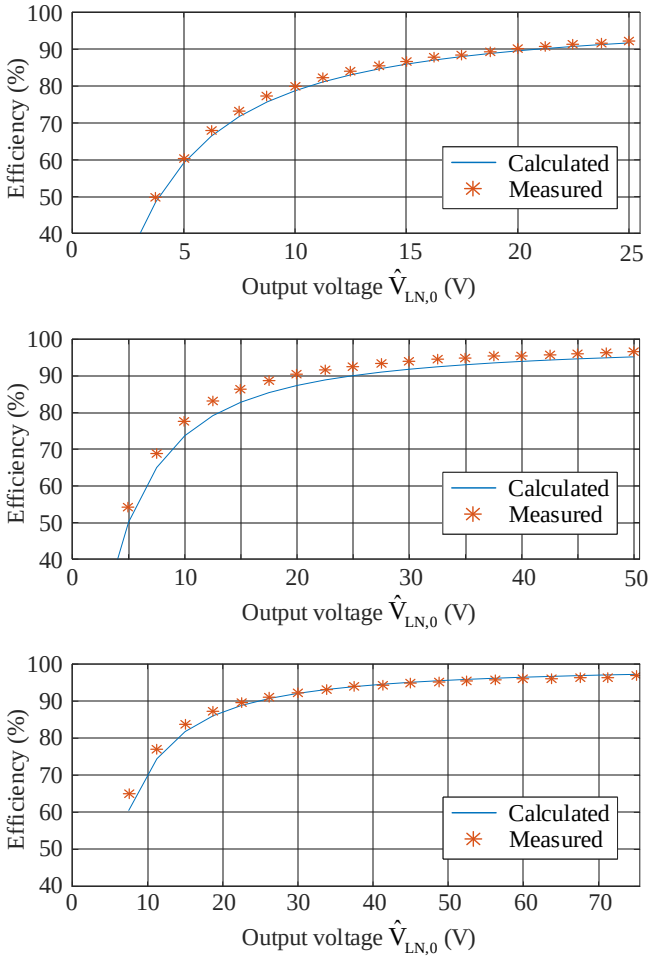

(a) Mode I_1.

(b) Mode I_2.

(c) Mode I_3.

Figure 5.19: Calculated and measured efficiencies of the MSI_2.

voltage requirements presented in Table 5.1, discrete IGBTs and diodes were selected with a blocking voltage of either 600V or 1200V and the same current rating. From Fig. 5.2 and Table 5.1, 1200V devices were chosen if the maximum voltage stress is equal to V_{dc1}, while 600V devices were selected for a maximum voltage stress of $V_{dc1} - V_{dc2}$ and V_{dc2}. Table 5.9 summarizes the blocking voltage for each component in every inverter topology.

The analysis presented in Section 5.4 was applied with the parameters of Table 5.1 and results are shown in Fig. 5.20. In Fig. 5.20a, $V_{dc,load}$ is equal to V_{dc2} which means that the MSI topologies operate in Mode I_1 and the DC voltage of the VSI is equal to V_{dc2}.

Table 5.9: Blocking voltage comparison.

Devices	VSI	MSI_1	MSI_2
$T_{1,k}/D_{1,k}$	1200 V	1200 V	1200 V
$T_{2,k}/D_{2,k}$	1200 V	600 V	600 V
$T_{3,k}/D_{3,k}$	-	600 V	600 V
$T_{4,k}/D_{4,k}$	-	1200 V	1200 V
$D_{5,k}$	-	600 V	-
$D_{6,k}$	-	600 V	-

The efficiency of the VSI is slightly higher than for the MSI_1 and the MSI_2 due to its lower part number. Indeed, in the VSI, the current flows through either the top or bottom switch in each phase leg. On the contrary, the current flows in one or two switches per phase leg in the MSI_2 and always two switches in the MSI_1, as shown in Figs. A.3 and 5.6. Hence more conduction and switching losses are generated in the MSI_1 and MSI_2 compared to the VSI, which is translated by lower efficiencies. Fig. 5.20b corresponds to the case where both MSI topologies operate in Mode I_2 and a voltage $V_{dc1} - V_{dc2}$ is applied to the DC side of the VSI. Similarly to the previous case, the VSI is more efficient due to the current flowing through more switches during the commutation paths of the MSI_1 and MSI_2, as displayed in Figs. A.1 and A.4. Finally, in Fig. 5.20c, the MSI circuits operate in Mode I_3 and V_{dc1} is applied to the VSI. One can note that the efficiency curves of the VSI and the MSI_2 overlap. This is due to the fact that the switches $T_{2,k}$ and $T_{3,k}$ in the MSI_2 are always turned off in Mode I_3, as mentioned in Table 4.2. As a result, the current flows either through the top switch $T_{1,k}/D_{1,k}$ or the bottom switch $T_{4,k}/D_{4,k}$, as shown in Fig. A.5. Hence, this commutation path is similar to the one in the VSI, leading to equal efficiencies. For the MSI_1, its efficiency is still adversely impacted by the current flowing through two switches, as displayed in Fig. A.2.

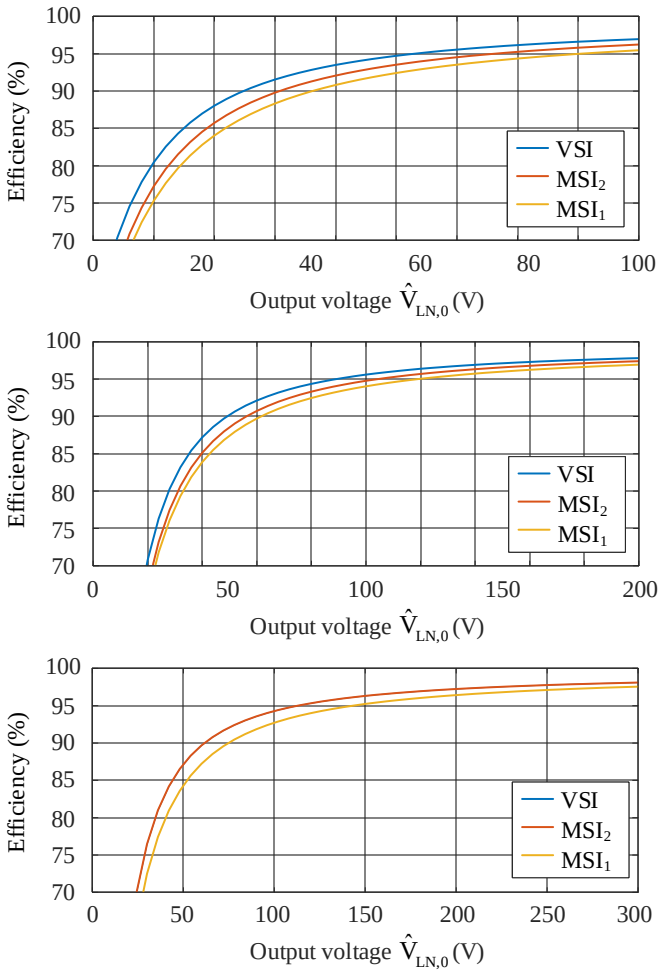

(a) $V_{dc,1}$=V_{dc2}.

(b) $V_{dc,2}$=$V_{dc1} - V_{dc2}$.

(c) $V_{dc,3}$=V_{dc1}.

Figure 5.20: Efficiency comparison between the MSI_1, MSI_2, and the VSI.

5.5 Conclusion

In this chapter, the switch configuration of the MSI was analyzed and the VA ratings of the MSI_1, MSI_2, and the VSI were compared. Although the MSI_1 and MSI_2 have respectively three and two times more switches than the VSI, their VA ratings are moderately impacted with an increase of 55.6% and 27.8% respectively. As the most sizable component in an inverter, the capacitor requirements were discussed and comprehensive analytical calculations of the RMS capacitor ripple current and capacitance were suggested to select the

proper capacitor banks for the MSI. Due to the additional DC input source, the overall volume of the capacitors is increased by 50% compared to the VSI. Finally, analytical efficiency analysis based on the average and RMS currents in the switches were developed for both the MSI_1 and MSI_2. Simulations showed that high efficiency can be achieved thanks to an active control of the mode in which the MSI operates. Indeed, by choosing the operating mode and, thus, the input DC voltage that provides power to the load, the MSI can enlarge its high efficiency areas by performing at a high modulation index. Experiments with the MSI_1 and MSI_2 prototypes, a 50V battery pack, and a 150V power supply were performed on an R-L load to validate the analytical efficiency models. A minimum error of less than 2% between the calculated and measured efficiencies in every operating mode of the MSI_1 and MSI_2 is achieved. A comparison between the MSI_1, the MSI_2, and the VSI was also carried out. The MSI_1 is less efficient than the MSI_2 due to the additional switches and the clamping diodes, regardless the operating modes. Furthermore, the MSI_2 is slightly less efficient than the VSI when a similar DC voltage of V_{dc2} or $V_{dc1} - V_{dc2}$ is applied to the load. If a high voltage of V_{dc1} is applied, the MSI_2 operates in Mode I_3 and is as efficient as the VSI.

Chapter 6

Multi-source inverter in hybrid electric powertrains

6.1 Introduction

System- and device-level models of the MSI have been developed in the previous chapters to provide a comprehensive analysis of the MSI_1 and MSI_2. In Chapter 4, the MSI was considered at system-level to validate the concept of the topology and its control through the theoretical analysis of the operating modes, simulations, and experiments in closed-loop control with an IM and a load. Chapter 5 discussed the design requirements and the efficiency of the MSI at device level. Throughout the analysis of the switch configuration, the VA rating has been estimated. Analytical calculations for the DC-link capacitor requirements have been developed based on detailed studies of the RMS capacitor current and voltage ripples. Finally, power losses were also calculated by analyzing the current waveforms in the switches and experiments were carried out to validate the theory. Overall, system- and device-level studies provided thorough results to validate the concept and estimate the performance of the MSI.

In this chapter, the implementation of the MSI in a power-split powertrain is discussed

and a vehicle-level simulation model is developed to estimate the potential benefits of the new powertrain. Power-split architectures, such as those developed in the Toyota Prius, integrate a DC/DC converter to provide a variable input voltage to the dual inverter. By doing so, the performance of the EMs can be improved along with the efficiency of the ETDS. For the past few years, OEMs tend to increase the power requirements of EVs in respond to the consumer demand. As a result, integrating this additional DC/DC converter adversely impacts on the power density and the cost due to the power inductor and the extra switches. Moreover, this converter and the battery pack should have the same power rating since they are connected in series. Hence, extending the electric driving range by increasing the power rating of the battery pack requires more trade-offs between performance, cost, and power density, compared to the simple architecture. With a view to overcome these issues, a new powertrain is suggested where the principal traction inverter is replaced by the MSI. When applied in power-split powertrains, the terminal inputs of the topology are connected to the battery pack V_{dc2} and the high DC-link voltage V_{dc1} shared with the other inverter, as shown in Fig. 4.1b. Depending on the operating mode, the battery can be either connected in series with the DC/DC converter or provides power separately. Indeed, by applying the control previously presented in Chapter 4, the battery pack can directly transfer power to the EM due to the additional connection on the DC side. Hence, the DC/DC converter can be bypassed in some driving conditions and a reduction of its power rating is expected without derating the battery system. Moreover, the overall efficiency of the propulsion system can be improved due to the variable voltage and the single conversion stage between the battery and the EM. When the DC/DC converter is connected in series with the battery, the powertrain can operate in two distinct operating modes. One mode enables extending the charging opportunities of the battery pack and the other mode allows for high power demands. In total, three operating modes are achievable with the MSI when a DC/AC conversion is required. On the other hand, the MSI can act as a rectifier in case of regenerative braking or when the ICE provides extra power to charge the battery. Two

operating modes are available, and the EM generates power to either V_{dc1} or V_{dc2}. Hence, the power can be transferred to the battery either through the DC/DC converter or directly to its terminals thanks to the additional DC connection. As a result, the DC/DC converter can be bypassed during some battery charging events.

In the following sections, the control and simulation model of a conventional power-split powertrain, similar to the MY2010 Toyota Prius, are first analyzed. Then, control strategies of the new powertrain with the MSI are proposed by considering all operating modes of the topology and a vehicle-level simulation model is developed in Matlab/Simulink. Finally, simulations were performed for several drive cycles and the performance of the conventional and suggested powertrains are compared.

6.2 Conventional powertrain control and model

The following analysis focuses on the MY2010 HEV Toyota Prius as a case study. Control strategies of this power-split powertrain have been substantially studied by multiple laboratories, such as the Argonne National Laboratory and the Idaho National Laboratory. Furthermore, a vehicle model was developed in the software Autonomie, presented in Section 2.3.3, and validated with intensive performance testing [168]. Hence, throughout extensive literature review and simulations with Autonomie, the fundamentals of powertrain control and simulation modeling for this specific architecture are analyzed.

In this section, the control strategies of the power split device composed of the ICE and both EMs are first reviewed. Then, the powertrain operating modes are discussed. Finally, the simulation model of the ETDS, developed in Autonomie and available in Matlab/Simulink, is analyzed.

6.2.1 Control strategies of the power split device

Control systems in contemporary HEVs are subject to continuous improvements to ensure the operation of the powertrain at its best performance. They are not only influenced by the vehicle speed but also by other factors such as accelerations, braking demands, and the state of charge (SOC) of the battery. Hence, they use elaborated control strategies based on optimization algorithms to manage the power distribution between the EMs, the ICE, and the battery pack. The primary purpose of these multi-objective functions is to maximize the efficiency of the ICE, while maintaining the battery SOC at an acceptable rate. By doing so, the driving performance are optimized, which leads to further fuel consumption reductions and gas emission minimization.

In the Toyota Prius powertrain, the ICE can be turned on or off and its power can be shared between the EMs and the differential of the vehicle. Both EMs can operate as motors or generators and the control of the speed and torque depends on the wheel power requirements, the ICE operations, and the battery. In view of the numerous variables, the control of this architecture is complex, and the model is summarized in Fig. 6.1. The battery SOC is estimated by advanced algorithms and the driver power demand is calculated from the vehicle speed and acceleration or braking requests. First, the controller decides to turn on or off the ICE based on the power required by the driver and the SOC rate. Then, the power demands for the ICE and the battery are calculated and two cases are achievable. If the SOC is high and the battery can provide sufficient power to drive the wheels, the ICE is turned off and the vehicle operates in electric-only mode. On the other hand, when the SOC is low or the power demand is too high for the battery, the ICE is turned on. Under these driving conditions, the battery assists the propulsion or is charged through either regenerative braking or by the ICE that shares its power to drive the wheels while regulating the battery SOC. The optimal speed and torque operating points of the ICE are calculated from the power requirements to maximize its efficiency. Finally, the speeds

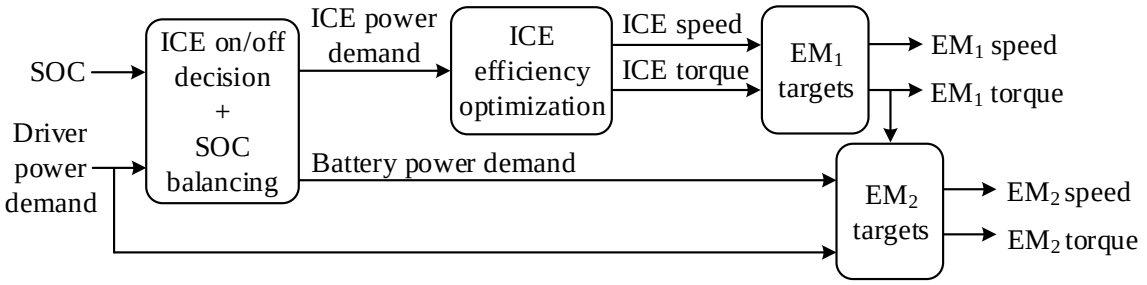

Figure 6.1: Control model of the Toyota Prius power split device.

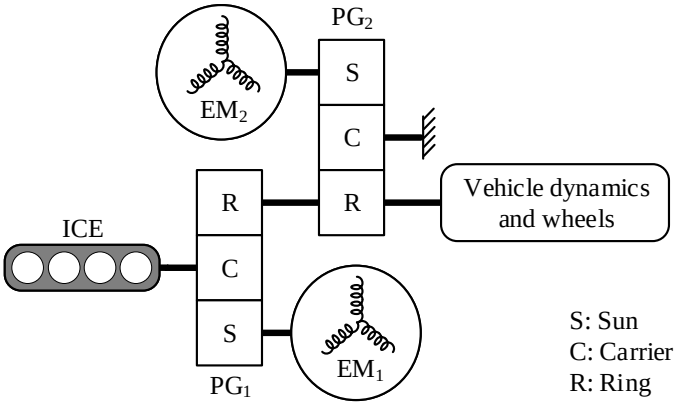

Figure 6.2: Mechanical diagram of the Toyota Prius power split device.

and torques of the EMs are determined based on the mechanical coupling with the ICE in a power split device. Fig. 6.2 shows the mechanical diagram of the Toyota Prius gear system [37]. The power split device uses two planetary gears, namely PG_1 and PG_2, where both ring gears share the same rotational shaft linked to the wheels. The carrier of PG_1 is connected to the ICE that transmits mechanical power to EM_1 through the sun gear. The rotational shaft of EM_2 is linked with the sun gear of PG_2 and the speed and torque are proportional to those of the wheels since the carrier gear is fixed. Thus, the speed and torque of EM_1 are regulated based on the ICE optimal operation, as shown in Fig. 6.1. Furthermore, the mechanical power of EM_2 is defined by the power demands of the driver, the battery, and the torque of EM_1.

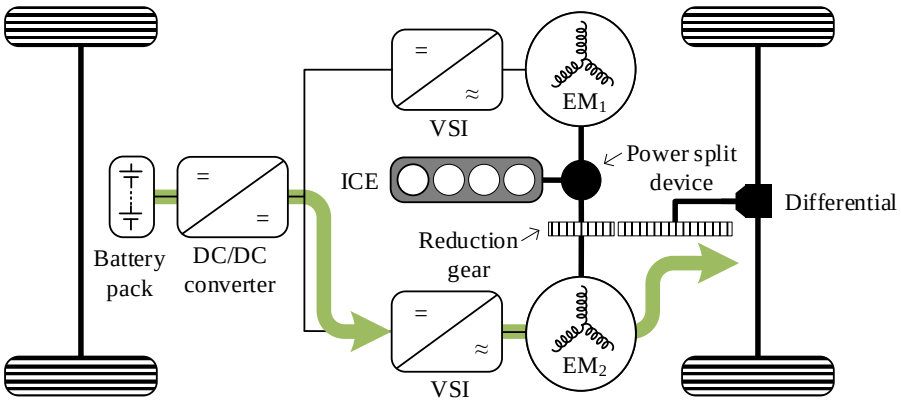

Figure 6.3: Power flow during the eletric-only mode.

6.2.2 Powertrain operating modes

The operating modes of power-split powertrains can be classified by analyzing the status of the ICE, the charge or discharge of the battery, and the motoring or generating operations of the EMs. In total, four modes can be distinguished, namely the electric-only, the combined driving, the combined driving and charging, and the regenerative braking modes.

Electric-only mode

The vehicle operates in electric-only mode when the battery is the sole source to drive the wheels. In this case, the HEV acts as a BEV since the ICE is turned off. Thus, it is the most suitable operation for a vehicle as it enables zero fuel consumption and no exhaust emissions. Fig. 6.3 shows the power flow in the powertrain. The battery power is transferred through the DC/DC converter that can either step up the voltage or simply leave it at the battery level. Then, the power is supplied to EM_2 to drive the wheels thanks to its mechanical connection, as previously shown in Fig. 6.2. In the meantime, no power is provided to EM_1 since the ICE is turned off.

The electric-only mode is achievable under specific driving conditions. Indeed, the ICE is turned off if the power requested by the wheels is lower than the battery power rating

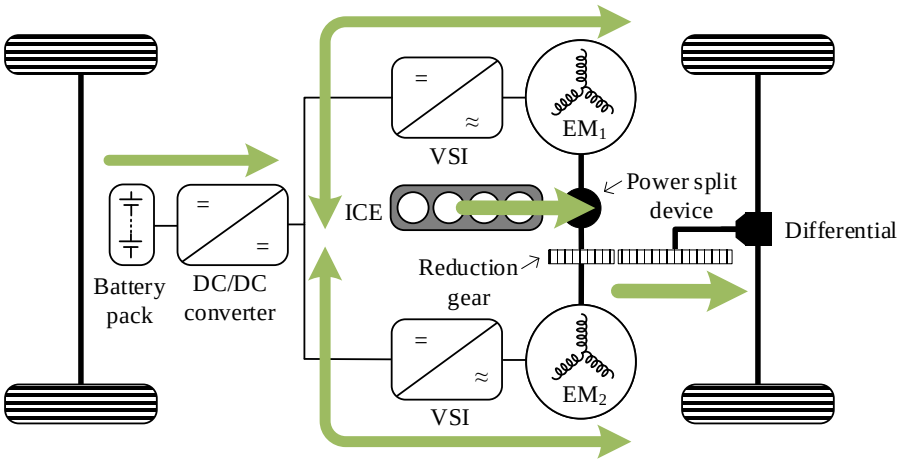

Figure 6.4: Power flow during the combined mode.

and if the SOC is within an acceptable range. Hence, the powertrain is usually controlled in electric-only mode during light accelerations and low to middle speeds. If the driver power demand is above the maximum battery power or if the SOC rate is lower than the limit allowed by the system, the battery is not sufficient anymore to drive the wheels. As a result, within a short period of time, the battery provides power to both EMs, and EM_1 is used to start the ICE.

Combined driving mode

When the power requested by the driver is beyond the battery capability, the ICE is turned on. Hence, the combined driving mode corresponds to the case where the ICE is the principal source of energy and the battery assists the propulsion. The power flow is shown in Fig. 6.4. The battery is discharging, and its power is transferred by the DC/DC converter to the EMs. Both EMs can operate as motors or generators, depending on the operation of the ICE. When one of the EMs operate in generating mode, the other EM necessarily acts as a motor to ensure a proper power flow in the powertrain. For similar reasons, whereas simultaneous motoring operation is allowed, both EMs cannot generate power at the same time.

As previously mentioned, the ICE operates at a specific speed and torque that maximize its efficiency. By doing so, the fuel consumption of the vehicle is reduced. Due to the gear connection between the ICE and EM_1, the power of EM_1 varies along with the ICE optimal operating point. The speed and torque of EM_2 is then adjusted considering the mechanical power provided by the power split device and the power requested by the wheels.

During the combined driving mode, the powers supplied by the battery and the ICE are added since the two sources are used in parallel. Hence, this mode is preferred for driving conditions with high power requirements, such as high speeds, heavy loads, and sudden accelerations. However, when the battery SOC drops below a specific threshold defined in the control system, the battery needs to be charged and the powertrain exits the combined driving mode.

Combined driving and charging mode

Battery packs in HEVs are not designed to be charged by the grid. Hence, if the SOC is lower than an acceptable rate, the battery is charged by the components within the powertrain. One charging technique uses the ICE to generate power back to the battery. The ICE is the sole source that drives the vehicle and provides more power than required by the wheels to charge the battery in the meantime. The powertrain is, thus, operating in combined driving and charging mode. Fig. 6.5 displays the power flow in the powertrain. Both EMs can act as motors or generators. Unlike in combined driving mode, they cannot simultaneously operate in motoring mode, but they can operate in generating mode. In other terms, if one EM acts as a motor, the other necessarily generates power back to the battery to guarantee an appropriate power flow between the powertrain components.

During this mode, the controller still optimizes the efficiency of the ICE and the same control described in Fig. 6.1 is applied. Compared to the other operating modes, the vehicle can operate in combined driving and charging mode under a wild array of driving conditions. Indeed, this mode mainly depends on the SOC rate, which is why it is reachable at high

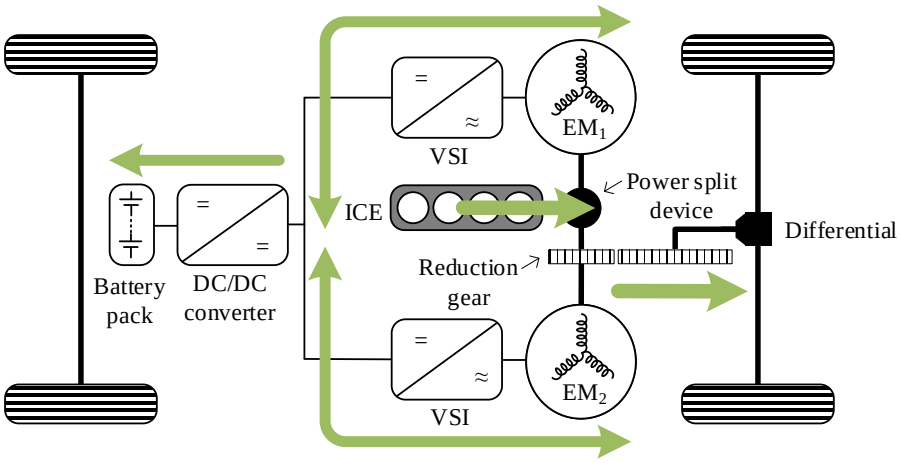

Figure 6.5: Power flow during the combined and charging mode.

or low speeds and for various load demands. However, the fuel consumption is higher than in other cases since the ICE needs to provide power to drive the wheels, while charging the battery at the same time. Thus, this operating mode is not suitable due to the extra fuel used to charge the battery. Another charging method using regenerative braking is usually preferred.

Regenerative braking

The regenerative braking technique is commonly used in contemporary EVs to charge the battery. This system is popular as it recovers the kinetic energy, usually dissipated as heat, during decelerations and braking events. Fig. 6.6 shows the power flow in the powertrain. The mechanical power is provided by the wheels and converted into electricity by EM_2 that acts as a generator. Then, the DC/DC converter transfers power to the battery while adjusting the voltage level. Since no propulsion energy is required by the driver, the ICE is turned off and no fuel is consumed. The controller regulates the speed and torque of EM_2 based on the power available from the regenerative braking system and the EM power capability. No power is converted by EM_1 as it stands still while the ICE is turned off.

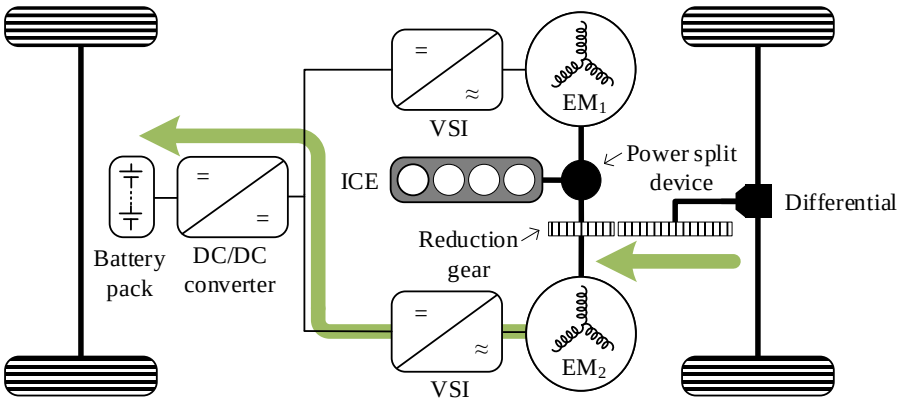

Figure 6.6: Power flow during the regenerative braking mode.

6.2.3 Simulation model

In this section, the analysis is focused on modeling the battery and the ETDS, composed of the DC/DC converter, both EMs, and the inverters. The APM, the mechanical dynamic system, and the ICE models will not be detailed.

In Autonomie, powertrain simulations are developed based on forward-looking models [168]. This simulation modeling technique is named after the direction of its calculations that start from the driver power demand to the component controllers. It is a popular method as it offers a close representation of actual controls implemented in commercialized EVs. More specifically, forward-looking powertrain simulations work as follows [169]. For a specific drive cycle, the wheel power demand, including propulsion and braking events, is sent to a driver model that controls the power distribution between the ICE and the EMs, as previously shown in Fig. 6.1. Then, the power profiles from the power split device are used to calculate the power requirements for each component in the rest of the vehicle model. Finally, the vehicle model calculates the actual speed of the vehicle and the driver model, that acts as a PI controller, compares the desired and actual vehicle speeds to minimize the error. Overall, a forward-looking model captures the component dynamics and enables developing real-world control strategies.

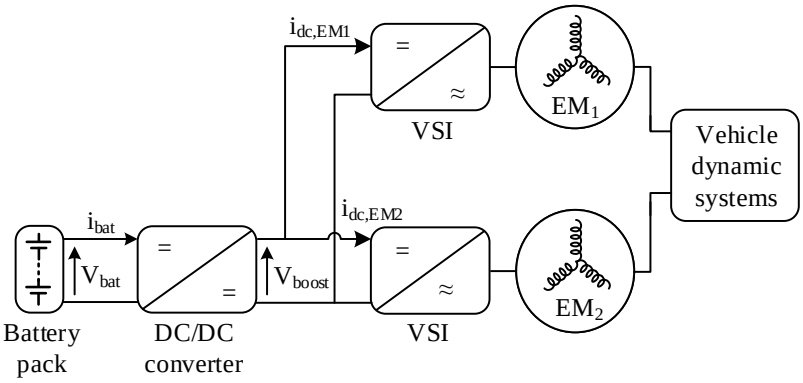

(a) Simplified powertrain schematic.

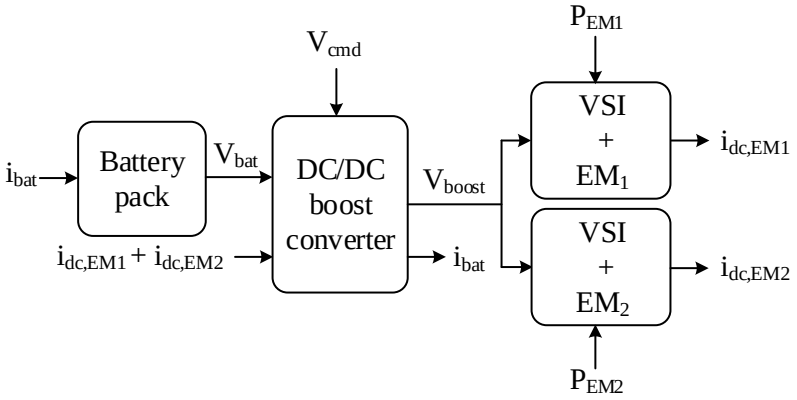

(b) Simulation model.

Figure 6.7: Conventional battery and ETDS models in the Toyota Prius.

Fig. 6.7a shows the simplified powertrain of the Toyota Prius with the variables used in the simulation model of the battery and the ETDS, displayed in Fig. 6.7b. Vehicle-level models vary depending on the objectives of the simulation, as discussed in Section 2.3. In this section, the simulations aim to verify the powertrain operating mode theory previously presented and extract the power profiles of the components in the vehicle model. Hence, averaged and steady-state modeling methods can be used since they provide results with an acceptable accuracy in a reasonable simulation time. Each component of Fig. 6.7b is modeled as a combination of a local controller and the plant system.

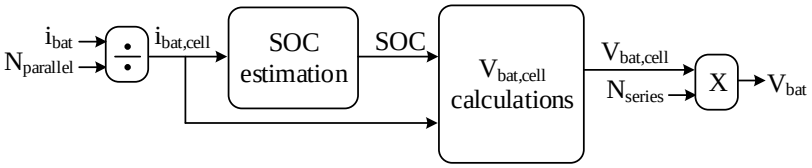

Figure 6.8: Simulation model of the battery.

Battery pack

In Fig. 6.7b, it can be seen that the battery model uses the battery current i_{bat} as input signal to generate the battery voltage V_{bat} in the output. Several battery models have been suggested in the literature [41]. For example, lumped parameters models use equations to calculate the cell voltage $V_{bat,cell}$ with parameters experimentally determined beforehand. Fig. 6.8 shows the battery model used in the simulation.

The cell current $i_{bat,cell}$ is calculated by dividing i_{bat} by the number of cells in parallel $N_{parallel}$ in the battery pack. It is then used for SOC estimation and to calculate the cell voltage $V_{bat,cell}$. Numerous algorithms have been developed to estimate the SOC but will not be further discussed as it is out of the scope of this thesis. The calculations of $V_{bat,cell}$, given by (6.1), are based on the open circuit voltage (OCV) and the charge or discharge resistance R_{bat}. These parameters depend on the cell chemistry and are experimentally obtained. Finally, V_{bat} is the product of $V_{bat,cell}$ and the number of cells in series N_{series} in the pack.

$$V_{bat,cell} = OCV - R_{bat}.i_{bat,cell} \tag{6.1}$$

DC/DC boost converter

An averaged model based on equations is used to represent the DC/DC boost converter. Depending on the speed of the vehicle and the power required by the wheels, the local controller sends a voltage command V_{cmd} to step up the battery voltage or not. The output

voltage V_{boost} varies between three values, namely V_{dc2}, V_{dc1}, and a voltage level close to $V_{dc1} - V_{dc2}$. The output signal of the model represents the battery current i_{bat} converted by the DC/DC converter. It is expressed as in (6.2) when the converter transfers power from the battery to the inverters, or as in (6.3) when the power is converted in the opposite direction.

$$i_{bat} = \frac{1}{\eta}\frac{V_{boost}(i_{dc,EM1} + i_{dc,EM2})}{V_{bat}} \tag{6.2}$$

$$i_{bat} = \eta\frac{V_{boost}(i_{dc,EM1} + i_{dc,EM2})}{V_{bat}} \tag{6.3}$$

where η is the efficiency of the converter considered constant, and $i_{dc,EM1}$ and $i_{dc,EM2}$ are the DC currents of the inverters for EM_1 and EM_2 respectively.

VSI and EMs

The VSI and the corresponding EM are combined into the same model where the inverter is considered as a simple DC voltage. The EM is modeled by a lookup table providing the electric power P_{elec} required by the speed and torque demands from the mechanical power P_{EM}, as shown in Fig. 6.9. These torque and speed signals are sent by the controller previously described in Fig. 6.1. Then, P_{elec} is divided by the input DC voltage of the inverter, corresponding to the output voltage V_{boost} of the DC/DC boost converter. This gives the input DC current $i_{dc,EM}$ that needs to be supplied by the DC/DC converter.

Although EM_1 and EM_2 do not have similar power ratings and characteristics, their inverters are both connected to the DC-link voltage V_{boost}. Hence, the same model in Fig. 6.9 can be used for both EMs and the lookup tables are adjusted based on each EM performance.

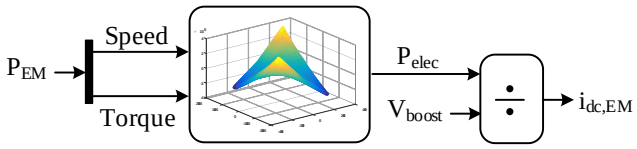

Figure 6.9: Simulation model of the EM and inverter.

6.3 Suggested powertrain with the MSI

Due to the uniqueness of the topology, the control methods and simulation models previously presented in Section 6.2 cannot be directly applied to the new powertrain with the MSI. Indeed, the additional DC-link connection between the battery and the inverter leads to significant changes regarding the power flow between the powertrain components. Furthermore, the MSI can operate in several operating modes, as presented in Chapter 4, that differ from those applied to a traditional VSI.

In this section, the control strategies of the suggested powertrain with the MSI are discussed. A vehicle-level simulation model of the battery and the ETDS has been developed in Matlab/Simulink and is also detailed.

6.3.1 Powertrain control

In the previous section, it has been shown that the powertrain driving modes of the Toyota Prius are characterized based on the status of the ICE, the battery, and the EMs. The output voltage of the DC/DC converter V_{boost} is not considered in the analysis since it does not impact on these powertrain control strategies. Indeed, it only affects the local control of the inverters and the DC/DC converter. For the suggested powertrain with the MSI, the control needs to consider the variable voltage capability of the MSI and the additional DC-link connection between the battery and the inverter. In other terms, the new control depends on the DC voltage applied to the EMs, and the status of the battery and EM_2. In order to provide a fair comparison between the conventional power-split architecture of

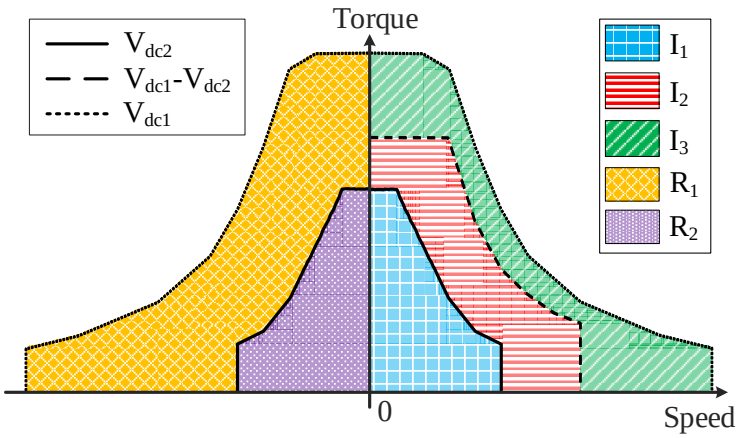

Figure 6.10: Torque-speed characteristic of EM_2 with the operating modes of the MSI.

the Toyota Prius and the suggested powertrain with the MSI, new control strategies are developed from the analysis of the DC voltage applied to EM_2, named V_{EM_2}, and the power profiles of the battery and the EMs. By doing so, the proposed control system aims to apply the same power distribution described in Section 6.2 between the ICE and the EMs, while considering the MSI features.

A combination of the torque-speed characteristic of EM_2 with the operating modes of the MSI is presented in Fig. 6.10. Five distinct regions can be identified, corresponding to the three inverter modes and two rectifier modes of the MSI. One can notice that different torque-speed envelopes are reached. This is due to the voltage applied to the EM. Indeed, a high DC voltage applied to the load enlarges the maximum torque and power contours. Furthermore, when the MSI operates in Modes I_1 and R_2, the load is supplied with a voltage V_{dc2}. On the other hand, a voltage $V_{dc1} - V_{dc2}$ is applied in Mode I_2, while a voltage equal to V_{dc1} is provided in Modes I_3 and R_1. Hence, the envelop in Modes R_1 and I_3 is larger than that of Modes I_1, I_2, and R_2.

The control modes of the suggested power-split powertrain are sorted based on the MSI operating modes. Fig. 6.11 shows the three operations when the MSI operates as an inverter and EM_2 acts as a motor. When EM_2 operates as a generator, two rectifier

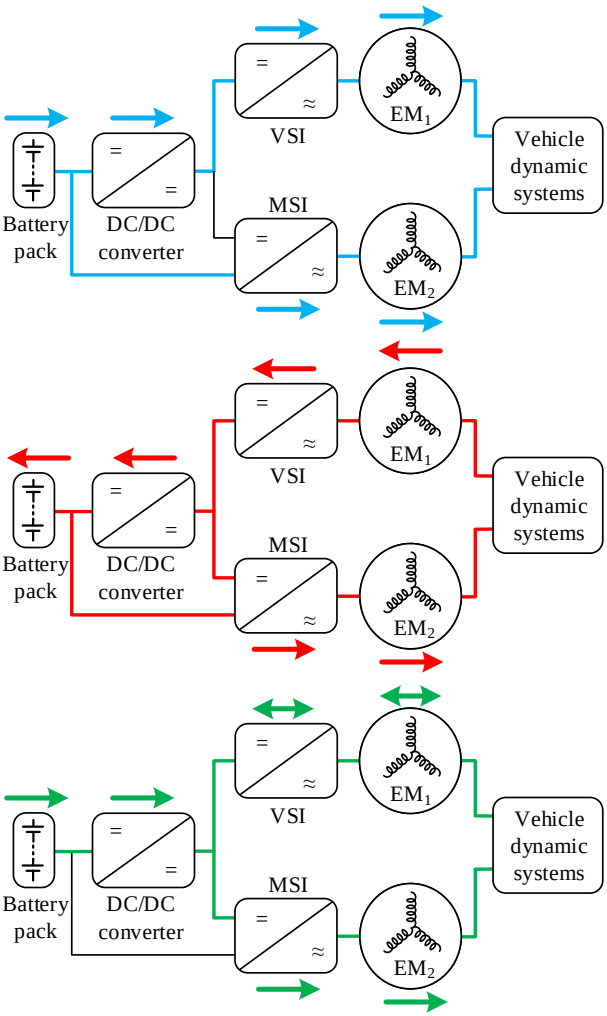

(a) Mode I_1 where $V_{EM2} = V_{dc2}$.

(b) Mode I_2 where $V_{EM2} = V_{dc1} - V_{dc2}$.

(c) Mode I_3 where $V_{EM2} = V_{dc1}$.

Figure 6.11: Power flow during the inverter modes of the MSI in the suggested powertrain.

modes are achieved by the MSI, as displayed in Fig. 6.12. The purpose of these sketches is to illustrate the power flow in each operating mode. One can notice that the ICE is not displayed in the figures since its status does not interfere with the MSI operating modes. Indeed, the ICE follows the same control as described in Fig. 6.1 and can be either turned on or off.

Fig. 6.11a shows the power flow in the suggested powertrain when the MSI operates in Mode I_1. The battery provides power to the wheels and both EMs operate as motors. By

analogy with the driving modes previously presented, the suggested powertrain operates either in electric-only mode if the ICE is turned off, or in combined driving mode when the ICE is turned on to assist the propulsion. Unlike in the conventional powertrain, it can be seen that the battery power is not entirely transferred by the DC/DC converter. Indeed, it is shared between the DC/DC converter and the MSI, due to the inverter operation in Mode I_1. Hence, this mode enables the battery to directly provide the power requested by EM_2 thanks to the additional DC connection, and the DC/DC converter only transfers the power required by EM_1. This feature is particularly interesting since only a portion of the battery power is converted by the DC/DC converter, which allows for power rating reductions of the converter. Furthermore, the voltage provided to EM_2 is equal to V_{dc2}. Thus, a variable voltage is still supplied to the EM, as it is the case in the Toyota Prius.

In Fig. 6.11b, the MSI operates in Mode I_2 where the power from V_{dc1} is used to drive EM_2 and to charge the battery in the meantime. By analyzing the status of the EMs, one can note that the ICE is necessarily turned on and the powertrain operates in combined driving and charging mode. This is due to the fact that the battery is charging and EM_2 is in motoring mode, which prevents the system from operating in regenerative braking mode or any other driving operations. As a result, the ICE supplies EM_1 and its power is then shared between the DC/DC converter and the terminals V_{dc1} of the MSI. This powertrain control mode also differs from the conventional operation since the additional DC connection between the battery and the MSI is used to charge the battery. By doing so, the charging opportunities are extended, while similar power is transferred through the DC/DC converter, compared to the conventional operation.

When the MSI operates in Mode I_3, V_{dc2} is not used and V_{dc1} provides power to EM_2, as shown in Fig. 6.11c. The battery is discharging and the DC/DC converter transfers entirely the battery power to both inverters. The power flow during this driving mode is similar to the one in the conventional power-split powertrain since the additional DC-link between the battery and the MSI is not used. Overall, this powertrain control mode does not differ from

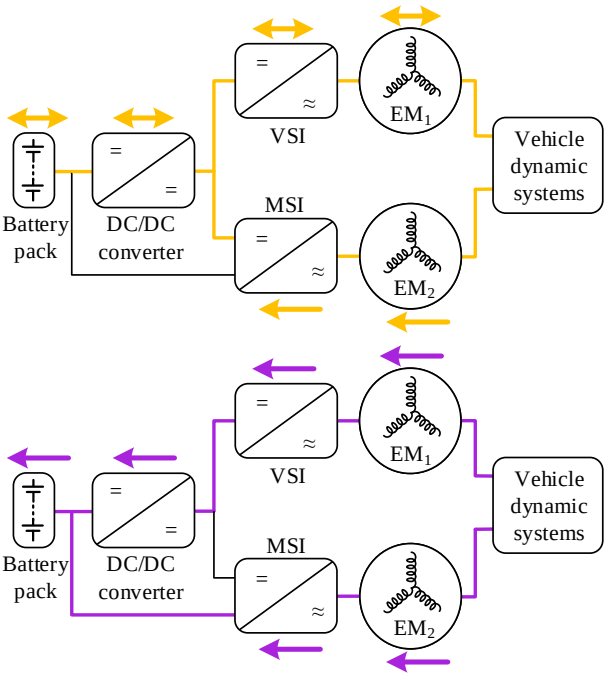

(a) Mode R_1 where $V_{EM2} = V_{dc1}$.

(b) Mode R_2 where $V_{EM2} = V_{dc2}$.

Figure 6.12: Power flow during the rectifier modes of the MSI in the suggested powertrain.

the conventional control and similar power rating of the DC/DC converter is requested. If the ICE is turned on, the powertrain operates in combined driving mode. Depending on the optimal operation of the ICE, EM_1 operates in either motoring or generating mode. On the other hand, electric-only mode is reached if the ICE is turned off and EM_1 does not convert any power.

In Fig. 6.12a, the MSI operates in Mode R_1 and the power generated by EM_2 is solely supplied to V_{dc1}. By analogy with the driving modes from Section 6.2.2, several cases can be considered due to the status of the battery, the ICE, and EM_1. If the battery is charged, the vehicle operates either in regenerative braking mode or in combined driving and charging mode. When the battery is discharging, the powertrain can only operate in combined driving mode since EM_2 must work as a generator in Mode R_1. Moreover, EM_1 acts as a motor or a generator, depending on the ICE control. Despite the numerous driving mode possibilities, the DC connection between the battery and the MSI is not used.

Hence, similar operation of the DC/DC converter is expected compared to the conventional powertrain, and the powertrain control remains similar.

Finally, Fig. 6.12b shows the MSI operating in Mode R_2. The battery is charged by the ICE, if it is turned on, or by the regenerative braking system when the ICE is turned off. Hence, the suggested powertrain can operate either in combined driving and charging mode or in regenerative braking mode respectively. Unlike in the conventional powertrain, the DC/DC converter does not entirely transfer the power from the EMs. Indeed, the power from EM_2 is directly transferred to the battery thanks to the additional DC connection with the MSI. As a result, only the power from EM_1 goes through a double conversion stage due to the DC/DC converter. Overall, this mode enables new charging possibilities and the power rating of the DC/DC converter can be reduced compared to the conventional powertrain.

In conclusion, the above-mentioned analysis showed that three out of five control modes of the suggested powertrain with the MSI bring new opportunities in terms of battery charging or allows for power rating reduction of the DC/DC converter. In order to quantify the benefits of the proposed powertrain, a vehicle-level simulation model has been developed and tested with several drive cycles.

6.3.2 Vehicle-level simulation model

Simulating the suggested powertrain in Autonomie raises several barriers due to the dual DC input in the MSI circuit. Indeed, although the software enables updating the component models, a specific format is required and the additional DC connection between the MSI and the battery is challenging to model in the predefined interface of the software. Moreover, each component control of the ETDS, presented in Fig. 6.7b, needs to be updated to take into account the operating modes of the MSI. To overcome these limitations, the ETDS of the suggested powertrain with the MSI has been developed in Matlab/Simulink. Fig. 6.13a shows the proposed powertrain with the variables used in the simulation model displayed

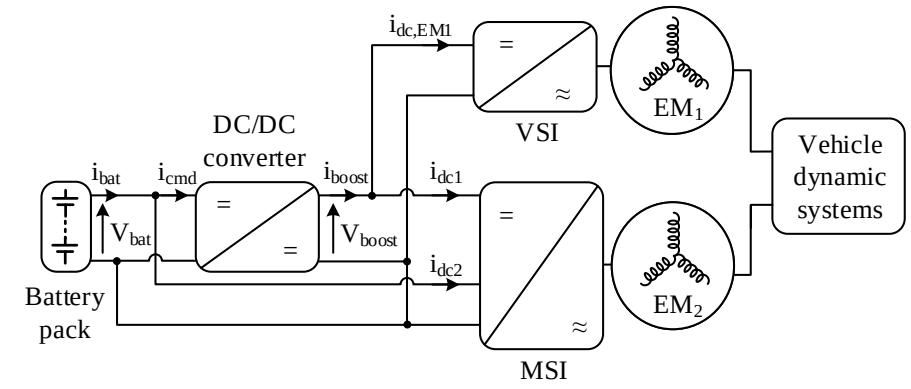

(a) Simplified powertrain schematic with the MSI.

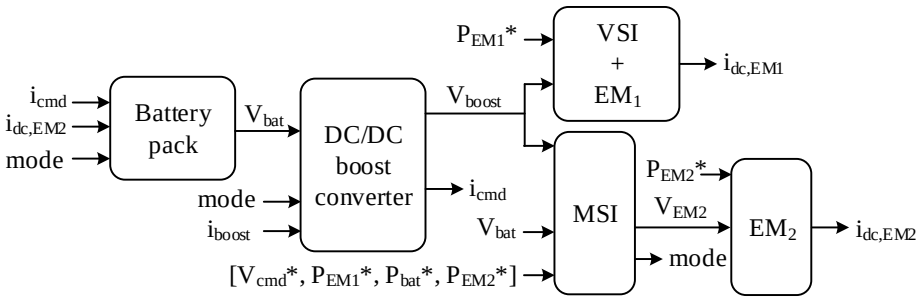

(b) Simulation model.

Figure 6.13: Battery and ETDS models with the MSI.

in Fig. 6.13b. One can notice that the current $i_{dc,EM2}$ does not appear in Fig. 6.13a. This is due to the fact that three cases can be distinguished depending on the operating mode. Indeed, i_{dc1} is equal to $i_{dc,EM2}$ in Modes I_3 and R_1, while i_{dc2} is null. In Mode I_2, i_{dc1} is equal to $i_{dc,EM2}$ and i_{dc2} is equal to $-i_{dc1}$. Finally, i_{dc2} is equal to $i_{dc,EM2}$ in Modes I_1 and R_2 and i_{dc1} is null.

MSI

Unlike the traditional VSI, the plant is modeled as a DC voltage that varies along with the operating modes and reaches three values (i.e. V_{dc2}, $V_{dc1} - V_{dc2}$, or V_{dc1}). On the other hand, the local controller needs to determine in which mode the MSI operates by applying the same voltage command of the DC/DC converter $V_{cmd}{}^*$, and the same power

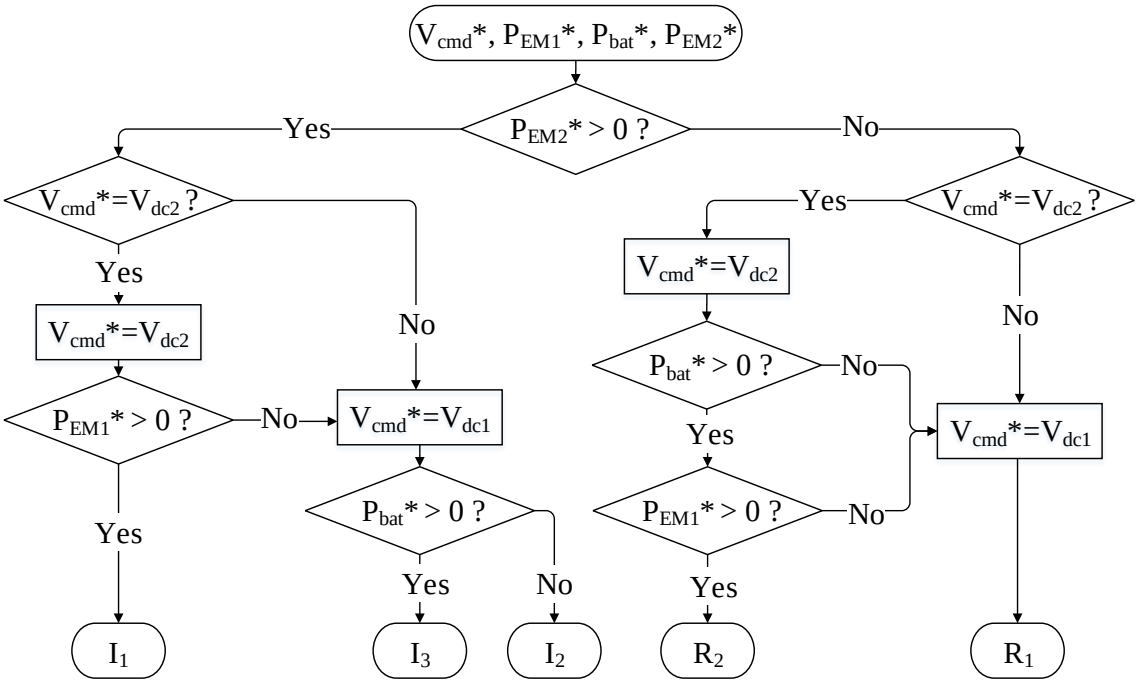

Figure 6.14: Flowchart for the operating mode determination.

profiles of the EMs and the battery that were applied in the Toyota Prius to ensure a fair comparison between the suggested and conventional powertrains. To do so, a flowchart is used to characterize the operating modes along with the powertrain driving conditions, as shown in Fig. 6.14. The variables denoted by * are the reference signals extracted from the simulations of the Toyota Prius powertrain. By convention, it is considered that an EM is motoring if its power is positive, and is generating when its power is negative. Furthermore, the battery is charging when $P_{bat}{}^*$ is negative and it discharges when $P_{bat}{}^*$ is positive.

The flowchart is composed of several conditions to sort the operating modes and define the driving requirements of the suggested traction drive system. First, the operation of EM_2 is identified to determine if the MSI operates as an inverter or a rectifier. If $P_{EM2}{}^*$ is positive, the MSI ensures a DC/AC conversion and three operating modes are available. On the contrary, the MSI acts as a rectifier if $P_{EM2}{}^*$ is negative and two operating modes are reachable. In both cases, the voltage command $V_{cmd}{}^*$ is then observed. In the conventional

powertrain model, the local controller of the DC/DC converter decides to step up the battery voltage in case of high power requirements from the EMs. By doing so, the current in the switches is reduced and the torque-speed envelope of the EM is enlarged. In order to keep a similar control in the suggested model, the MSI must operate in a mode that supplies EM_2 with a high voltage V_{dc1} if the same driving conditions as in the conventional powertrain are met. Hence, ${V_{cmd}}^*$ provides a second requirement in the operating mode determination since it specifies whether the DC/DC converter is used or not. Finally, supplementary conditions are required in each operating mode to ensure the proper power flow in the suggested powertrain. For example, the status of EM_1 needs to be observed when the MSI operates as an inverter and V^*_{cmd} is equal to V_{dc2}. Indeed, the MSI can operate in Mode I_1 only if EM_1 is in motoring mode, as shown in Fig. 6.11a. If EM_1 acts as a generator, the controller disregards ${V_{cmd}}^*$ and forces the MSI to operate in Mode I_2 or I_3, depending on the status of the battery. This enables ${P_{EM1}}^*$ to be transferred back to EM_2, which is not possible if the MSI operates in Mode I_1. During the AC/DC conversion and if V^*_{cmd} is equal to V_{dc2}, Mode R_2 is reachable only if two additional conditions are satisfied. Due to the DC connection between the battery and the MSI, the controller needs to verify that ${P_{bat}}^*$ and ${P_{EM1}}^*$ are both negative to ensure the charge of the battery, while the DC/DC converter only transferred ${P_{EM1}}^*$. In other circumstances, the controller overlooks V^*_{cmd} and forces the MSI to operate in Mode R_1.

Battery pack

Although the battery plant model, presented in Fig. 6.8, can remain similar in the suggested powertrain, the local controller needs to be updated. The battery current i_{bat} is calculated

by applying the control rules described in (6.4).

$$i_{bat} = \begin{cases} i_{cmd} & \text{if mode} \in I_3 \text{ or } R_1 \\ i_{cmd} + i_{dc,EM2} & \text{if mode} \in I_1 \text{ or } R_2 \\ i_{cmd} - i_{dc,EM2} & \text{if mode} \in I_2 \end{cases} \tag{6.4}$$

By applying Kirchoff's current law and considering the current direction defined as in Fig. 6.13a, it can be seen that i_{bat} is the sum of i_{cmd} and i_{dc2}. If Mode I_3 or R_1 is applied, the DC connection between the battery and the MSI is not used and i_{dc2} is equal to zero, as shown in Figs. 6.11c and 6.12a. Hence, the battery power is entirely transferred by the DC/DC converter and i_{bat} is equal to i_{cmd}. When the MSI operates in Mode I_1 or R_2, the battery is connected to both the MSI and the DC/DC converter, and i_{dc2} that is equal to $i_{dc,EM2}$. Hence, i_{bat} is the sum of i_{cmd} and $i_{dc,EM2}$. Finally, Fig. 6.11b shows the power flow in Mode I_2 where the battery is charged by EM_2 thanks to the direct connection with the MSI, and by i_{cmd} through the DC/DC converter. Due to the negative direction of $i_{dc,EM2}$ when it flows back to the battery, i_{bat} is equal to the difference of i_{cmd} by $i_{dc,EM2}$.

DC-DC boost converter

In the suggested powertrain with the MSI, the output voltage of the DC/DC converter V_{boost} is controlled differently compared to the conventional powertrain. In the Toyota Prius, V_{EM2} is equal to V_{boost} and varies between three levels, namely V_{dc2}, V_{dc1}, and a voltage level close to $V_{dc1} - V_{dc2}$ [37]. On the other hand, it has been shown in Section 4.3 that the MSI can supply the load with three different voltages, while the DC input sources are fixed to V_{dc1} and V_{dc2}. Hence, in the suggested powertrain, V_{boost} should be equal to V_{dc1} in Modes I_2, I_3, and R_1, while it should be equal to V_{dc2} in Modes I_1 and R_2 to ensure that the same DC voltage is supplied to both EM_1 and EM_2.

The output current i_{boost} of the DC/DC converter is expressed as in (6.5). In Modes I_2,

I_3, and R_1, the DC/DC converter transfers the current between the battery and both EMs. Thus, it is expressed as the sum of $i_{dc,EM1}$ and $i_{dc,EM2}$. On the contrary, only the current $i_{dc,EM1}$ is converted during Modes I_1 and R_2, since $i_{dc,EM2}$ is directly transferred through the additional DC connection between the battery and the MSI.

$$i_{boost} = \begin{cases} i_{dc,EM1} + i_{dc,EM2} & \text{if mode} \in I_2,\ I_3, \text{ or } R_1 \\ i_{dc,EM1} & \text{if mode} \in I_1 \text{ or } R_2 \end{cases} \tag{6.5}$$

The input current i_{cmd} of the DC/DC converter, can be expressed as in (6.6) when the power is converted from the battery to the inverters, or as in (6.7) when the converter transfers power in the opposite direction.

$$i_{cmd} = \frac{1}{\eta}\frac{V_{boost} i_{boost}}{V_{bat}} \tag{6.6}$$

$$i_{cmd} = \eta\frac{V_{boost} i_{boost}}{V_{bat}} \tag{6.7}$$

where η is the efficiency of the converter considered constant.

VSI and EMs

In the suggested powertrain with the MSI, the models of both EMs and the inverter of EM_1 are similar than those used in the conventional powertrain and were presented in Section 6.2.3.

6.4 Simulation results

The MY2010 Toyota Prius model was simulated in Autonomie with the same parameters detailed in Table 2.1. The reference signals $V_{cmd}{}^*$, $P_{EM1}{}^*$, $P_{EM2}{}^*$, and $P_{bat}{}^*$ were extracted for four standard drive cycles, namely the urban dynamometer driving schedule (UDDS),

the highway fuel economy test cycle (HWFET), the US06, and the new European driving cycle (NEDC). These reference waveforms were then used in the suggested powetrain model with the MSI, as described in Section 6.3.1. For example, Fig. 6.15 shows the simulation results of the suggested powertrain for an UDDS drive cycle. In Fig. 6.15a, the voltage command $V_{cmd}{}^*$ is equal to 1 if the DC/DC converter steps up the battery voltage or is equal to 0 if not. The power profiles of the EMs alternatively vary between positive and negative values since both EM_1 and EM_2 can operate as motors or generators, as shown in Figs. 6.15b and 6.15c. Similarly, the battery frequently charges or discharges, which is translated by respectively negative or positive values of the battery power, as displayed in Fig. 6.15d. Finally, Fig. 6.15e shows the MSI operating mode variation. Depending on the reference signals, the MSI operates in one of its five modes by following the control strategies previously presented in Fig. 6.14. The simulation model of the suggested powertrain has also been tested for the other drive cycles previously mentioned, and the MSI operating mode variation is consistent with the theory. Hence, the simulation model of the suggested powertrain with the MSI operates as expected.

6.4.1 DC/DC converter power comparison

Compared to the conventional powertrain of the Toyota Prius, the suggested powertrain with the MSI aims to reduce the use of the DC/DC converter in the traction system by offering an alternative commutation path between the battery and the MSI. By doing so, the battery is not always connected in series with the DC/DC converter, which allows for power rating reduction of the converter, while keeping a variable voltage to supply the EMs. Moreover, the power rating of the battery pack can be enlarged independently from that of the DC/DC converter.

In the previous section, the theoretical analysis of the powertrain operations showed that the power transferred by the DC/DC converter, named P_{boost}, can be reduced under several driving conditions. Indeed, during Mode I_1, the battery pack can directly drive EM_2

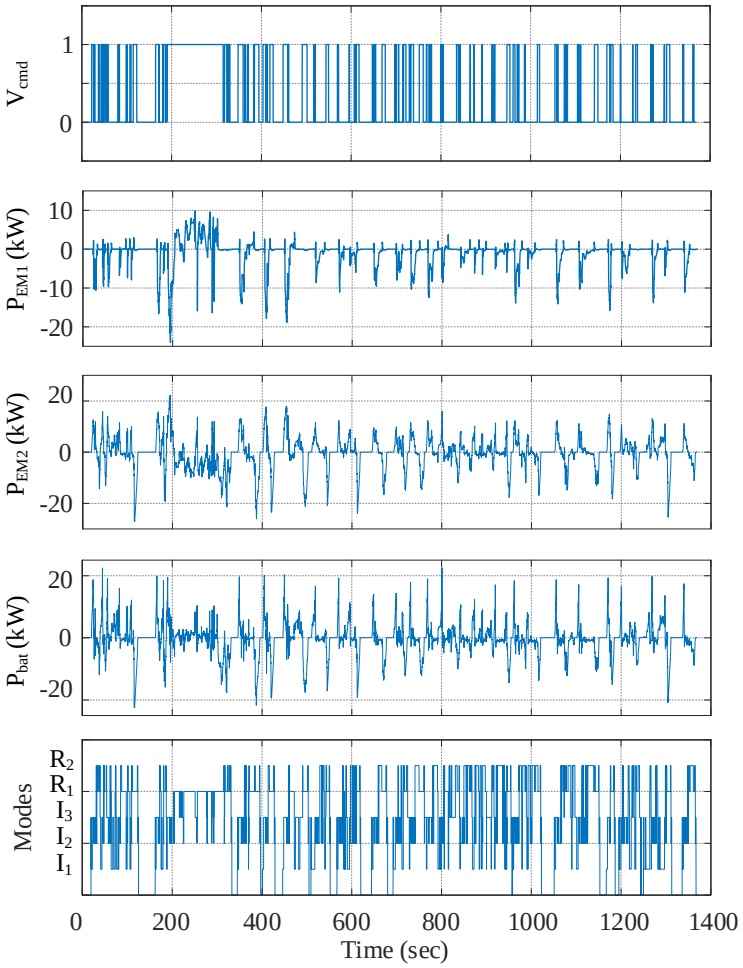

(a) $V_{cmd}{}^*$.

(b) $P_{EM1}{}^*$.

(c) $P_{EM2}{}^*$.

(d) $P_{bat}{}^*$.

(e) MSI operating mode variation.

Figure 6.15: Verification of the MSI operating mode variation during an UDDS cycle.

through the MSI thanks to the additional DC connection of the inverter. Furthermore, in Mode R_2, the power generated by EM_2 is transferred to the battery without using the DC/DC converter. On the other hand, similar operation of the DC/DC converter is expected in Modes I_2, I_3 and R_1, compared to the conventional powertrain. As a result, further analysis of P_{boost} is required to quantify the impact of the MSI on the DC/DC converter design.

In this section, the power transferred through the DC/DC converter in the conventional and suggested powertrains are compared. Simulations have been carried out to evaluate

the power reduction of the DC/DC converter that can be achieved in each operating mode. For example, Fig. 6.16 shows the waveforms of P_{boost} in the conventional and the suggested powertrains for each operating mode during an UDDS drive cycle. It is clear from Figs. 6.16b and 6.16f that significant power reductions are achieved in Modes I_1 and R_2. In the following, the average power transferred through the DC/DC converter and the peak power are compared in each operating mode for the four drive cycles.

Average power

The average power P_{ave} transferred by the DC/DC converter can be defined as the integral of the instantaneous power P_{boost} over the time period of the drive cycle T_{cycle}. It can be expressed as in (6.8).

$$P_{ave} = \frac{1}{T_{cycle}} \int_0^{T_{cycle}} P_{boost} \, \mathrm{d}t \tag{6.8}$$

Fig. 6.17 shows the distribution of P_{boost} between the control modes of the suggested powertrain with the MSI during each drive cycle. In an UDDS cycle, about 17.65% of the total power is transferred when the powertrain runs in Mode I_1, while 6.50% are converted during Mode R_2. This means that 75.85% of the total power is transferred by the DC/DC converter during either Modes I_2, I_3, or R_1. This power distribution can be explained by the fact that the control has been optimized for the Toyota Prius powertrain and frequently uses the DC/DC converter to step up the battery voltage during fast accelerations and middle speeds. During the drive cycle HWFET, the power is mainly transferred when the powertrain operates in Mode I_3 due to the high speeds requirements from the wheels. However, short braking events and light accelerations occur, which gives a few opportunities for the powertrain to operate in Modes I_1 and R_2. Overall, 18.90% of the total power is transferred during these two modes. An US06 cycle depicts an aggressive driver with numerous high speed and fast acceleration events. Under these driving conditions, the

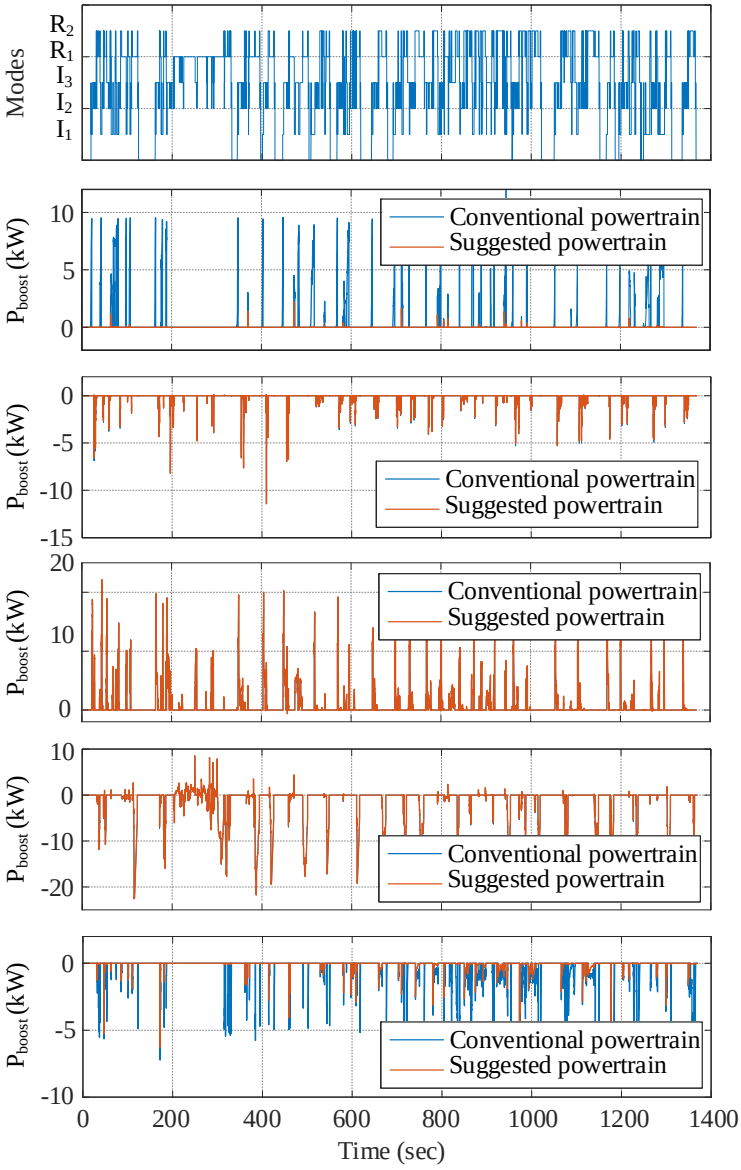

(a) MSI operating mode variation.

(b) Mode I_1.

(c) Mode I_2.

(d) Mode I_3.

(e) Mode R_1.

(f) Mode R_2.

Figure 6.16: Comparison of P_{boost} in each operating mode during an UDDS drive cycle.

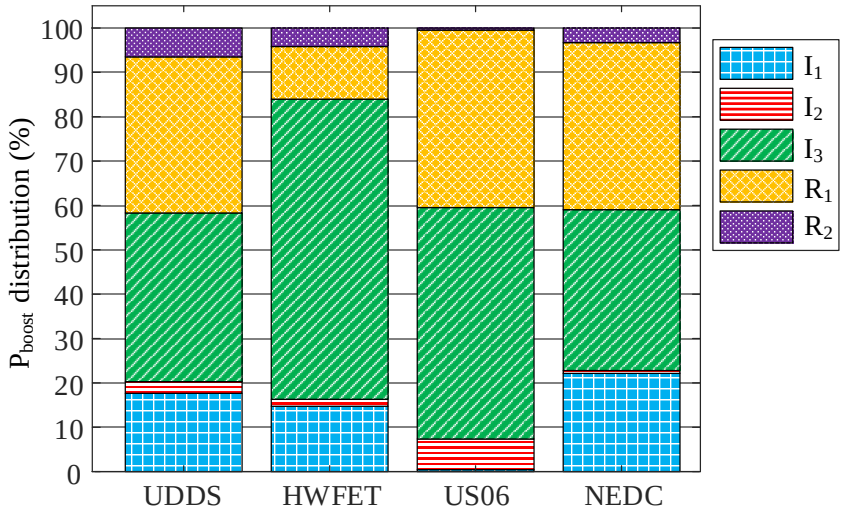

Figure 6.17: P_{boost} distribution between the operating modes.

battery pack can barely provide enough power to drive the wheels by itself. This is confirmed by the very low percentages of 0.44% in Mode I_1 and 0.47% in Mode R_2. Finally, results for the NEDC cycle show that 25.45% of the power is transferred during Modes I_1 and R_2. These results are similar to those obtained for an UDDS cycle since the NEDC also represents an urban route with several stops and light accelerations.

Table 6.1 shows the percentage of P_{boost} that is transferred through the additional connection between the battery and the MSI in the proposed powertrain and does not need to be converted by the DC/DC converter. For example, during Mode I_1 in an UDDS cycle, 97.53% of the power that usually goes through the DC/DC converter in the conventional powertrain is bypassed thanks to the use of the MSI. Indeed, only P_{EM1} is converted by the DC/DC converter in the suggested powertrain, while P_{EM2} is transferred between the battery and the MSI thanks to the additional DC connection. Significant power is also bypassed in the other drive cycles in both Modes I_1 and R_2. On the other hand, when the MSI operates in Modes I_2, I_3 and R_1, the additional connection between the battery and the MSI is not used. This means that the power is fully converted by the DC/DC converter and 0% is bypassed.

Table 6.1: Bypassed power P_{boost} compared to the conventional powertrain (in %).

Modes \ Drive cycles	UDDS	HWFET	US06	NEDC
I_1	97.53	88.44	99.58	98.27
R_2	84.11	97.56	87.04	95.80
I_2, I_3 and R_1	0	0	0	0

The total average power reductions achievable in Modes I_1 and R_2 during each drive cycle are calculated by multiplying the corresponding power ratio from Fig. 6.17 with the percentage of bypassed power reached with the suggested powertrain from Table 6.1. Results are displayed in Fig. 6.18. Among the four drive cycles studied, the NEDC and the UDDS provide the largest power reductions where the overall average power transferred through the DC/DC converter during each drive cycle is reduced by 24.93% and 22.68 % respectively. On the contrary, the lowest reduction is achieved for the US06 with 0.85%. This is consistent with the driving behaviors of these cycles since an urban track with low speed events and frequent stops increases the opportunities for the powertrain to operate in Modes I_1 and R_2, unlike an aggressive route composed of numerous fast accelerations at high speed. One can also note that 17.11 % reduction are accomplished for the HWFET cycle due to the main operation of the powertrain in Mode I_3. In conclusion, although the same mechanical power distribution optimized for the Toyota Prius was used in the suggested powertrain, up to 25% of the average power transferred though the DC/DC converter can be reduced by using the MSI in Modes I_1 and R_2. These are encouraging results since the control has not been optimized for the suggested powertrain. More power reduction could be potentially achieved by revising the powertrain control, including the mechanical power distribution of the EMs, to take advantage of the additional DC connection between the battery and the MSI.

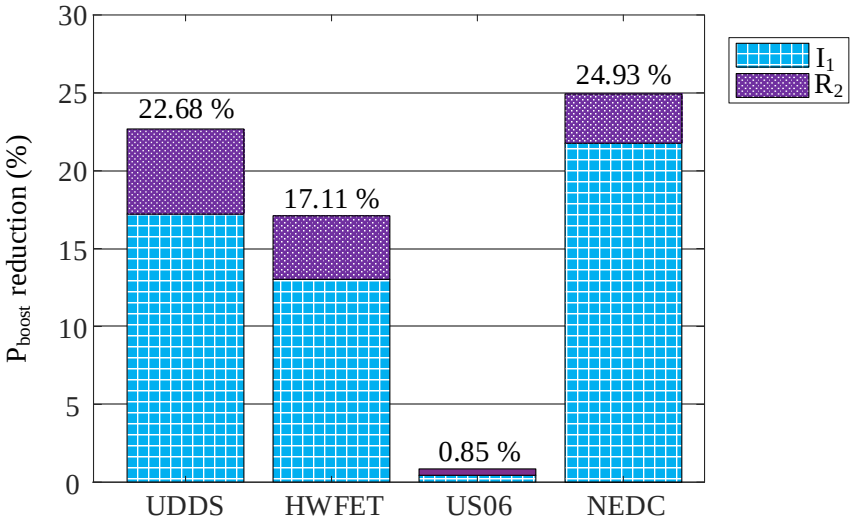

Figure 6.18: Total average power reduction of P_{boost}.

Peak power

The peak power should also be compared to evaluate the impact of the MSI on the DC/DC converter design. The power rating is defined by the maximum peak power achieved by the converter while considering every operating condition. In the previous paragraph, it has been seen that P_{boost} can be reduced in Modes I_1 and R_2 but not in the other modes. Hence, the peak power in each operating mode for the four drive cycles has been analyzed to determine if the power rating of the DC/DC converter can be reduced. Table 6.2 summarizes the peak power reduction achieved with the suggested powertrain compared to the conventional architecture. When the MSI operates in Modes I_1 and R_2, the peak power significantly reduces in each drive cycle. For instance, the peak power in Mode I_1 during the HWFET cycle is reduced by 44.90% and by 96.42% in Mode R_2. However, the power rating of the DC/DC converter can only be reduced if the maximum power is reached during either one of these two modes, while considering the other modes. Unfortunately, the maximum power is transferred in Mode I_3, where no power reduction is achievable despite the use of the MSI. Hence, using the MSI as a traction inverter, while keeping the same

Table 6.2: Peak power reduction of P_{boost} per operating mode (in %).

Modes \ Drive cycles	UDDS	HWFET	US06	NEDC
I_1	70	44.90	95.34	65.17
R_2	10.25	96.42	51.07	45.26
I_2, I_3 and R_1	0	0	0	0

control developed in the Toyota Prius with the reference signals $V_{cmd}{}^*$, $P_{EM1}{}^*$, $P_{EM2}{}^*$, and $P_{bat}{}^*$, does not allow for power rating reduction of the DC/DC converter. Nevertheless, it is believed that the power rating could be reduced if the control of the suggested powertrain, including the power distribution between the EMs, the ICE, and the battery pack, was optimized so that it predominately operates in the modes that use the additional DC connection between the battery and the MSI. By doing so, the maximum power over a drive cycle would be transferred during Modes I_1 and R_2, allowing for power rating reduction of the DC/DC converter.

In conclusion, the analysis of the average and peak powers showed the potential benefits of using the MSI if an appropriate power distribution between the EMs and the battery was applied to the suggested powertrain. Indeed, new powertrain control strategies should be developed by considering the operating modes of the MSI. More specifically, the powertrain should predominately operate in the modes that use the additional DC connection between the battery and the MSI. By doing so, the maximum power over a drive cycle would be transferred during Modes I_1 and R_2, allowing for power rating reduction of the DC/DC converter.

6.4.2 SOC comparison

When the MSI operates in Mode I_2, the current $i_{dc,EM2}$ is used to drive EM_2 while charging the battery without being converted by the DC/DC converter. Fig. 6.19 shows the influence of this unique feature on the battery SOC during an UDDS drive cycle. Due to higher values

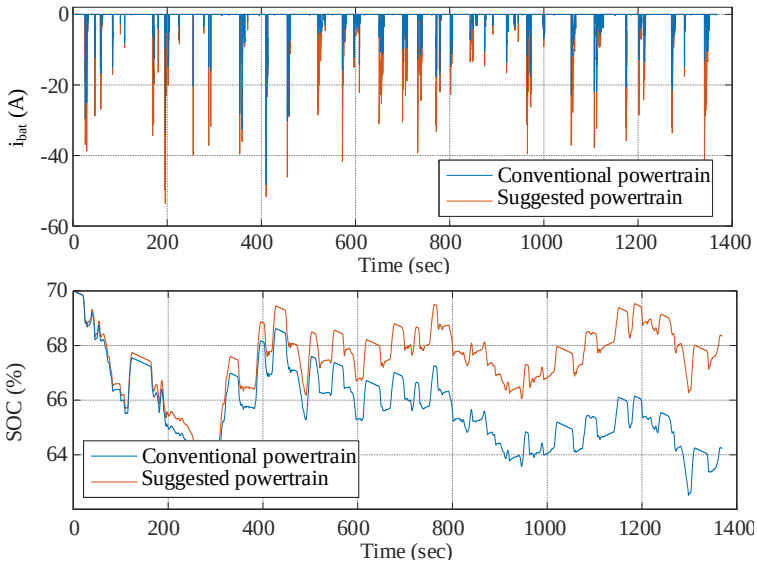

(a) Battery current i_{bat}.

(b) Battery SOC.

Figure 6.19: Charging opportunities during Mode I_2.

of i_{bat} flowing to the battery in the suggested powertrain, the final SOC rate is higher than in the Toyota Prius by 4%. It should be noted that this result was obtained while the same control, developed in the Toyota Prius with the reference signals $V_{cmd}{}^*$, $P_{EM1}{}^*$, $P_{EM2}{}^*$, and $P_{bat}{}^*$, was applied to both powertrains. Thus, the ICE in the suggested powertrain with the MSI does not produce more power to run the vehicle while charging the battery and the fuel consumption is similar to that of the Toyota Prius. As a result, another advantage of the MSI is the possibility to extend the battery charging opportunities. Moreover, it is believed that further improvements could be achieved by developing an optimized control for the suggested powertrain that mainly uses Mode I_2 to charge the battery.

6.5 Conclusion

In this chapter, the implementation of the MSI in a power-split powertrain was discussed. First, the MY2010 HEV Toyota Prius was analyzed as a case study. Control strategies of the power split device and powertrain operating modes were reviewed. The simulation

models of the battery and the ETDS have also been detailed and simulations were carried out with Autonomie. Then, the control and model of the powertrain with the MSI have been proposed. To provide a fair comparison between the conventional and the suggested powertrains, the same power distribution between the EMs and the battery was applied in the new control system, while considering the MSI operating modes. The control of the output voltage of the DC/DC converter was also kept similar. From a detailed analysis of the new powertrain control, it has been shown that three out of five driving conditions of the suggested powertrain with the MSI bring new opportunities in terms of battery charging and power rating reduction of the DC/DC converter. Finally, a vehicle-level simulation model of the battery and the ETDS has been developed in Matlab/Simulink to quantify the benefits of the proposed powertrain. Simulations were performed for four drive cycles and the power profile of the DC/DC converter and the battery SOC of the conventional and suggested powertrains are compared. Although the same control strategies developed for the Toyota Prius were applied to the suggested powertrain with the MSI, up to 25% of the power transferred by the DC/DC converter can be reduced in most drive cycles tested. Furthermore, the MSI allows extending the battery charging opportunities thanks to Mode I_2. However, the power rating of the DC/DC converter cannot be reduced by applying the same control of the Toyota Pius in the suggested powertrain. This is due to the fact that the power distribution was optimized for the Toyota Prius and, hence, the optimal control does not consider the additional connection between the battery and the MSI. Nonetheless, these results are encouraging and showed the potential of the suggested powertrain. It is believed that further power reduction of the DC/DC converter can be achieved by developing an optimized control specifically for the suggested powertrain with the MSI.

Chapter 7

Active hybrid energy storage system topology using the multi-source inverter

7.1 Introduction

Several contemporary BEVs utilize Li-ion batteries to meet the load demands of the EM. These energy sources have a high energy density allowing for large electric-only driving range, but they do not offer high power densities. Although their power rating might meet the peak load requirements of a vehicle, higher C-rates exhibited by the battery are found to reduce the battery lifetime [170]. As a result, requiring the battery to meet highly dynamic load profiles increases the rate of unwanted side reactions which, in turn, results in further plating of the solid-electrolyte interface [171–173]. This translates into an increase in the internal resistance which reduces its lifespan or can even lead to premature failure. In contrast to Li-ion batteries, ultracapacitors (UCs) offer larger power densities but at the cost of lower energy densities.

A HESS harnesses the benefits of both Li-ion batteries and UCs by pairing these two energy sources together [22,174–176]. Indeed, integrating an UC as a second source into an electric powertrain enables to alleviate the peak load demand which is otherwise requested from the battery bank. By doing so, the battery is left to provide most of the constant load demand while the power-dense UC bank supplies the peak power profile. In other terms, the battery wear is minimized, and the battery lifetime can be extended [177–179].

Numerous HESS topologies have been suggested in the literature [41]. In a passive parallel configuration, the battery and the UC are directly connected to the DC input of the inverter, without the use of any additional power electronics. The DC current supplying the load is the sum of the battery and the UC currents, and both source voltages are equal due to the parallel connection. Although this configuration is competitive in terms of cost and power density, its lack of control adversely affects the performance of the system. Indeed, the current distribution between the sources mainly depends on the internal resistances. Since the UC has an energy density much lower than that of the battery, it tends to discharge faster. To prevent the UC voltage from dropping, the battery needs to charge the UC to keep both voltages equal, while supplying the load. As a result, more energy is requested from the battery, affecting its lifetime and the performance of the system. Another solution is to connect a DC/DC converter between the battery pack and the UC, as shown in Fig. 7.1a. By doing so, the source currents can be controlled to use the battery for most of the constant power, while the UC meets dynamic load profiles [180–182]. Moreover, this additional power converter enables the control of the charge and discharge rates of the two sources. As a result, the battery lifetime can be extended, and the efficiency of the system is improved. However, even if active HESS topologies achieve promising performance and are more controllable compared to passive HESS structures, they are still held back from commercial applications. Indeed, their use in traction drive systems is mainly limited by the high cost, extra weight, and large volume of the DC/DC converter.

The fundamental concept of the MSI was introduced in Chapter 4. This topology was

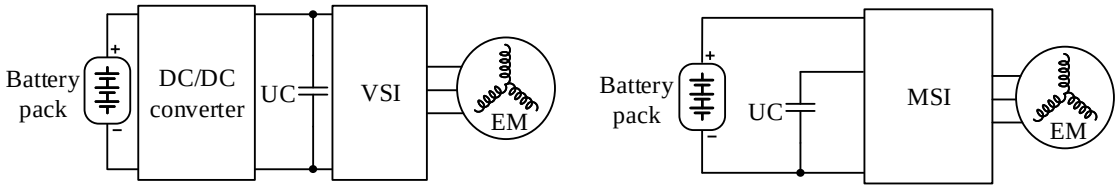

(a) Parallel active HESS topology. (b) Suggested HESS topology with the MSI.

Figure 7.1: HESS topology comparison.

first developed for HEVs and PHEVs with power-split powertrains where a battery pack and the ICE provide power to the wheels. Depending on the operating mode, it has been shown that the MSI can drive an EM with three DC voltage levels during the DC/AC conversion. Hence, this power converter aims to generate a variable voltage from two DC sources using a single conversion stage.

Besides hybrid power-split powertrains, the MSI can also be integrated in AEVs driven by a HESS. Fig. 7.1b shows the new suggested active HESS topology with the MSI where one DC-link voltage is provided by the battery while the other source is the UC. During DC/AC operations, it has been previously shown in Chapter 4 that the MSI supplies power from either one source or a series combination of both. Hence, the sources are never connected in parallel, as it is the case in a parallel HESS configuration. Because of the specific current distribution of the MSI, an innovative control scheme has been developed to regain current sharing between the sources, as it is traditionally done with active parallel HESS topologies. By doing so, an active control of the input sources and their current is achieved without the use of a DC/DC converter. Therefore, the combination of a HESS topology with the MSI intends to keep the advantages of an active parallel HESS without the drawbacks of a DC/DC converter.

In this chapter, the active HESS topology with the MSI is first presented and the novel control scheme managing the current distribution between the two sources is detailed. Then, simulations in closed-loop control with an interior permanent magnet (IPM) synchronous machine have been performed to verify the theoretical operations of the proposed topology.

Finally, the impact of the new control strategy on the DC sources is further investigated and validated through simulations and experiments.

7.2 Suggested topology using the MSI

Like every active HESS structure, the proposed topology with the MSI needs to efficiently control the source currents to take advantage of the high energy density of batteries and the large specific power and cycle life of UCs, while minimizing the battery degradation.

As previously mentioned in Chapter 4, the MSI has three distinct inverter modes that can be employed. When a closed-loop speed-torque control strategy is applied, the PI controllers generate a voltage reference that is used in the adapted PWM method to determine the operating mode and decide which source drives the wheels. As a result, the two sources never supply power to the motor simultaneously and the DC current provided to the load is equal to either the battery current or the UC current. This prevents the use of a similar control strategy than in a conventional parallel HESS where the DC input current of the inverter is equal to the sum of the currents from both sources. Thus, applying a speed-torque control to the EM without any additional control of the sources is not sufficient to obtain similar performance as with a conventional active HESS architecture.

A novel control scheme has been developed to manage the current distribution in the proposed active HESS topology with the MSI. Simulations in closed-loop control over an UDDS drive cycle will be presented in the following to verify its principle of operation.

7.2.1 System control

An active control of the operating modes can be combined with the speed-torque control scheme to effectively manage the current distribution between the two sources. This additional mode control has two degrees of freedom, namely, the control frequency f_c and the discharge duty cycle d_c, representing the conduction time during which the battery supplies

power to the load. The fundamental purpose of the mode control is to periodically switch the operating mode between Modes I_1 and I_3, regardless of the mode determined by the speed-torque control strategy. By doing so, the load demand will be regularly met by either the battery current or the UC current. Furthermore, with an appropriate choice of f_c, the input capacitor banks will filter the source currents to prevent them from being discontinuous. Thereby, over one control period ($1/f_c$), the average input current supplying the EM will be the sum of the source currents just like with a typical parallel HESS. Furthermore, since the discharge duty cycle biases the use of one energy source over another, it can control the average source currents and, hence, the discharge rate of the sources. Over one control period, the average battery current $\langle i_{bat} \rangle$ and the average UC current $\langle i_{uc} \rangle$ can be expressed as functions of the average input current $\langle i_{in} \rangle$ that supplies the load and the discharge duty cycle d_c. They are calculated as in (7.1).

$$\begin{aligned} \langle i_{bat} \rangle &= d_c.\langle i_{in} \rangle \\ \langle i_{uc} \rangle &= (1 - d_c).\langle i_{in} \rangle \end{aligned} \tag{7.1}$$

The control scheme of the active HESS topology using the MSI is shown in Fig. 7.2. The speed, torque and mode controls act simultaneously and aim to impact on the adapted PWM technique without impeding the performance of the overall system. As a result, this new control scheme regains current sharing between both sources and discharge rate regulation, as it is traditionally done with active HESS topologies. Moreover, it intends to achieve similar performance, with the additional benefit of not using a DC/DC converter.

7.2.2 Simulation results

The proposed active HESS topology with the MSI has been modeled in Matlab/Simulink. The Li-ion battery model used in this work is a first-order equivalent circuit model. The model has been parameterized using experimental cell test data for an SOC-OCV curve

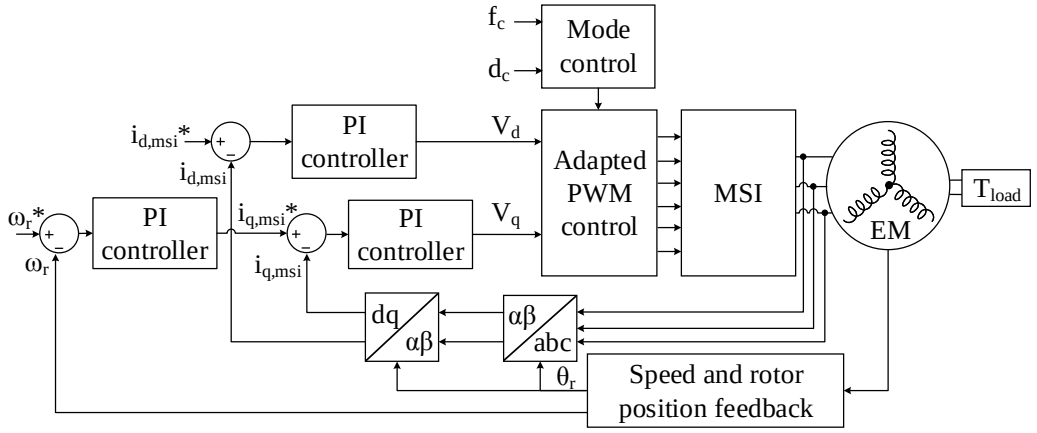

Figure 7.2: Control scheme of the active HESS topology using the MSI.

and a pulse discharge test for a Batterist lithium polymer battery cell (PF9744128). On the other hand, UCs have a shorter time constant compared to Li-ion batteries due to a lower internal resistance. The UC model used in this work includes leakage current and equivalent series resistance [183]. The SOC-OCV relationship is presumed to be linear as a result of the lack of faradaic reactions occurring in UC [183, 184]. The capacitance and the two resistance values are based on the Maxwell BCAP3400 ultracapacitor [185]. The SOC of the UC is found by utilizing the linear SOC-OCV relationship [186, 187].

Closed-loop control simulations were performed for an UDDS drive cycle with torque and speed references driving an IPM. The switching frequency of the MSI is chosen at 10 kHz. One can notice that the mode control needs to be slower than the PWM control of the switches. Hence, the control frequency f_c must be lower than f_{sw}. On the other hand, the discharge duty cycle d_c varies between 0% and 100%. In this simulation, f_c is selected at 10 Hz and d_c is equal to 50%. Table 7.1 summarizes the simulation parameters of the DC sources in the HESS. As mentioned earlier, the first order equivalent circuit model and parametrization were performed at the cell level. The number of cells in series and parallel in the battery and UC packs are scaled according to the power requested at the DC bus. Unlike in power-split hybrid powertrain applications, both DC source voltages are equal

Table 7.1: Simulation parameters of the DC sources in the HESS.

Source	Cells in series & parallel	DC voltage (V)	Maximum power density (kW/kg)	Energy density (Wh/kg)
Battery	81 & 6	300	3.13	173.9
UC	105 & 1	300	13.7	7.7

to ensure similar power capability and limit the DC-link voltage variation while the mode control is applied.

Simulation results are shown in Figs. 7.3 and 7.4. From Figs. 7.3a and 7.3b , it can be seen that the rotor speed and torque converge to the references. This verifies that the additional mode control strategy does not hinder the performance of the system. Figs. 7.3c and 7.3d show the voltages of the two sources and their SOC. Even if a discharge duty cycle of 50% does not bias one source to another, the UC voltage and SOC drops are larger compared to those of the battery pack. This can be explained by the fact that the UC energy density is much lower than for the battery, which means that the UC will discharge faster for a similar load current. Thus, an effective choice of the discharge duty cycle needs to consider the energy density of the sources to avoid their full discharge in a short period of time. Fig. 7.4a shows the current distribution according to the operating mode during the DC/AC conversion. In Fig. 7.4b, the reference current corresponds to the input current when the mode control is not applied and only one source drives the EM. The battery and UC currents have been obtained when the mode control is used with a discharge duty cycle of 50% and f_c equal to 10 Hz. When one of the sources supplies power to the EM, its input current is equal to the reference current while it remains null when the source is not used. This leads to discontinuous currents with high ripples, which is not suitable for the battery lifetime. This discontinuity is due to the choice of a low control frequency f_c that prevents the currents from being filtered by the input capacitors. Further details will be provided in Section 7.3.

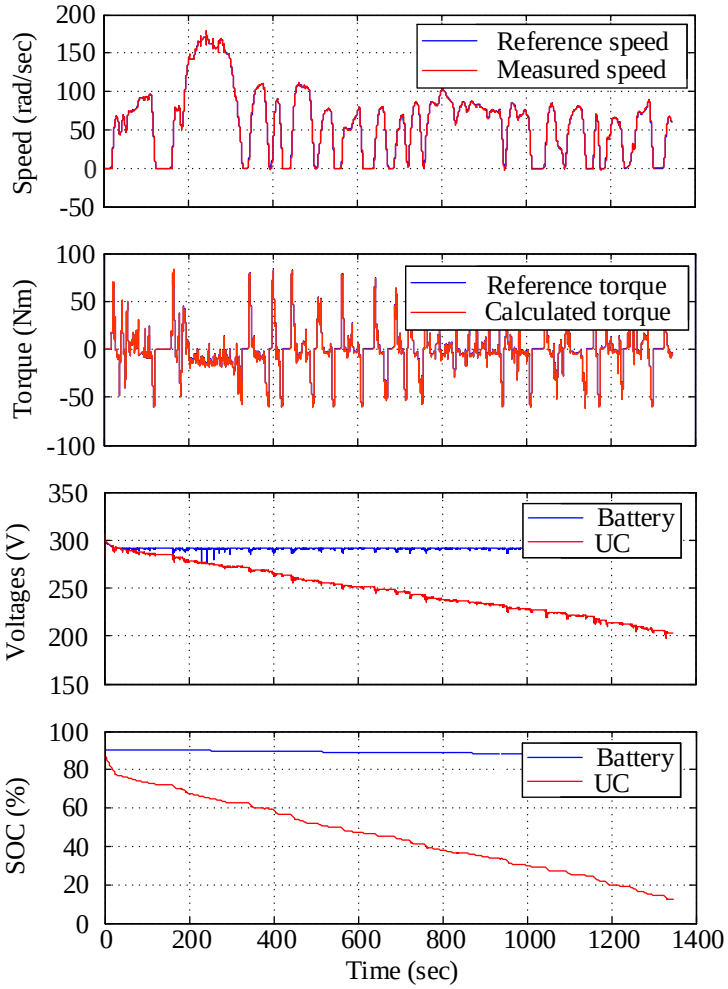

(a) Rotor speed.

(b) Torque load.

(c) Input DC voltages.

(d) SOC of the sources.

Figure 7.3: Simulation results of the HESS with the MSI.

7.3 Influence of the mode control parameters

From the previous part, it has been shown that the additional mode control does not impede the performance of the speed and torque controls. However, a low control frequency f_c leads to discontinuous currents, which is not suitable for the lifetime of the battery. Moreover, choosing a discharge duty cycle of 50% pointed out the lower energy density of the UC. This will affect the choice of the discharge duty cycle since it can impact on the discharge rate of the sources. The influence of the control frequency f_c and the discharge duty cycle

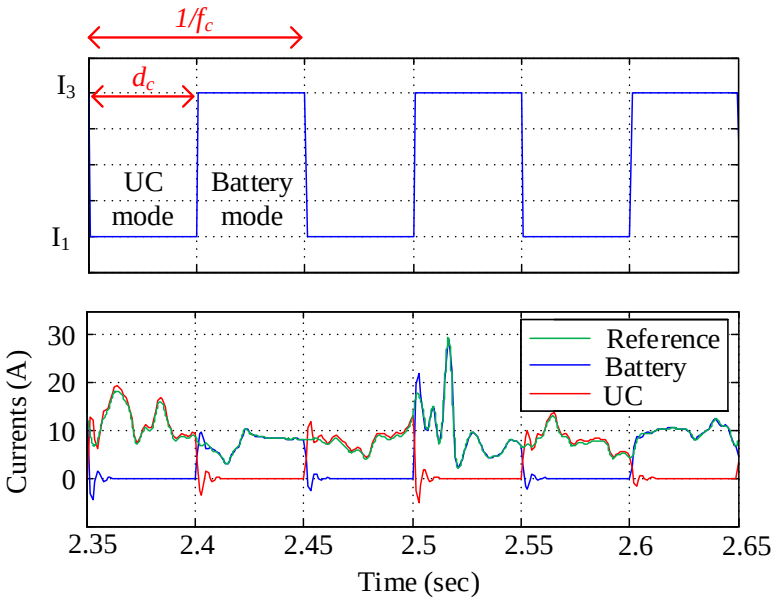

(a) Operating modes.

(b) Reference, battery and UC currents.

Figure 7.4: Simulation of the mode control.

d_c on the input currents and the SOC of the sources are discussed in the following section.

7.3.1 Influence of the control frequency f_c

Input capacitor banks are used to protect the DC-link voltage from transient spikes and minimize ripple currents caused by the switching actions of the semiconductors. They act as low-pass filters and allow the low frequency signals while blocking those with high frequencies. The new control scheme for the proposed active HESS topology with the MSI aims to take advantage of these input filters to smooth the source currents. Indeed, by an appropriate choice of f_c, high frequency source currents can be generated to be filtered by the input capacitors. As a result, the source currents will be continuous, and their ripple will be reduced.

Closed-loop control simulations for three different values of f_c with a constant discharge duty cycle of 50% were performed for a shorted time UDDS drive cycle with torque and speed references driving an IPM. In the simulation model, input capacitor banks of 3 mF have

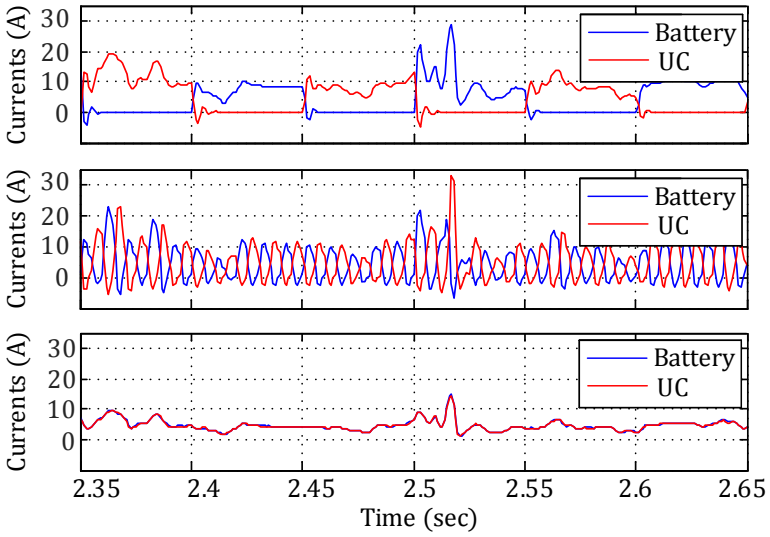

(a) $f_c = 10$ Hz.

(b) $f_c = 100$ Hz.

(c) $f_c = 5$ kHz.

Figure 7.5: Influence of f_c on i_{bat} and i_{uc} with a constant $d_c = 50\%$.

been selected and a parasitic resistance of 0.1 Ω is considered. Thus, the cut-off frequency of these input filters is equal to 530 Hz. The battery and the UC current waveforms are shown in Fig. 7.5. As expected, it can be seen that increasing f_c smooths the input currents. Since the cut-off frequency is equal to 530 Hz, input currents for f_c equal to 10 Hz are not filtered and thus discontinuous, as shown in Fig. 7.5a. Fig. 7.5b displays currents with a medium frequency of 100 Hz. The signals start being filtered which is characterized by continuous waveforms with large oscillations. Finally, Fig. 7.5c presents the current waveforms for f_c equal to 5 kHz. The high frequency signals are completely filtered by the input capacitors which can be seen by the low current ripple.

From these simulation results, it can be concluded that choosing a high f_c smooths the input currents, which is particularly beneficial for the battery lifetime.

7.3.2 Influence of the discharge duty cycle d_c

Since the discharge duty cycle biases one source to another, it is intuitively expected that it will impact on the average currents and the SOC of the sources.

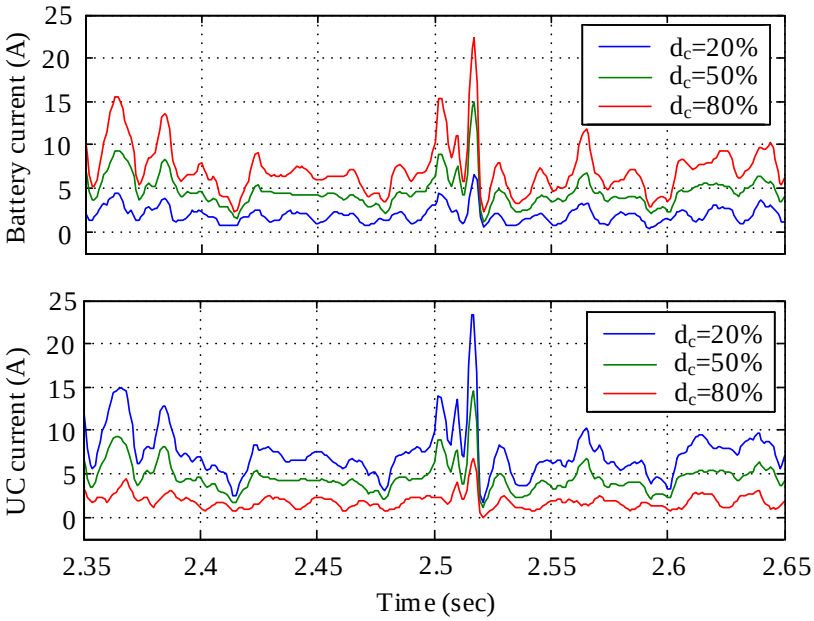

(a) Battery current.

(b) UC current.

Figure 7.6: Influence of d_c on i_{bat} and i_{uc} with f_c = 5kHz.

Closed-loop control simulations for several discharge duty cycles with a constant control frequency f_c of 5 kHz were performed for a shorted time UDDS drive cycle with torque and speed references driving an IPM. The influence of d_c on the source currents is shown in Fig. 7.6. From Fig 7.6a, it can be seen that the average current and ripple of the battery become smaller when the discharge duty cycle decreases. On the other hand, a low discharge duty cycle increases the UC average current and its ripple, as shown in Fig. 7.6b. This is due to the fact that decreasing the discharge duty cycle reduces the conduction time of the battery while the UC is used for a longer time during one mode control period. Fig. 7.7 shows the SOC of the battery and the UC for a control frequency f_c of 5 kHz at different discharge duty cycles. Increasing the discharge duty cycle leads to larger SOC drop for the battery and lower SOC drop for the UC. Since the SOC is calculated as a function of the current, these results are consistent with those from Fig. 7.6.

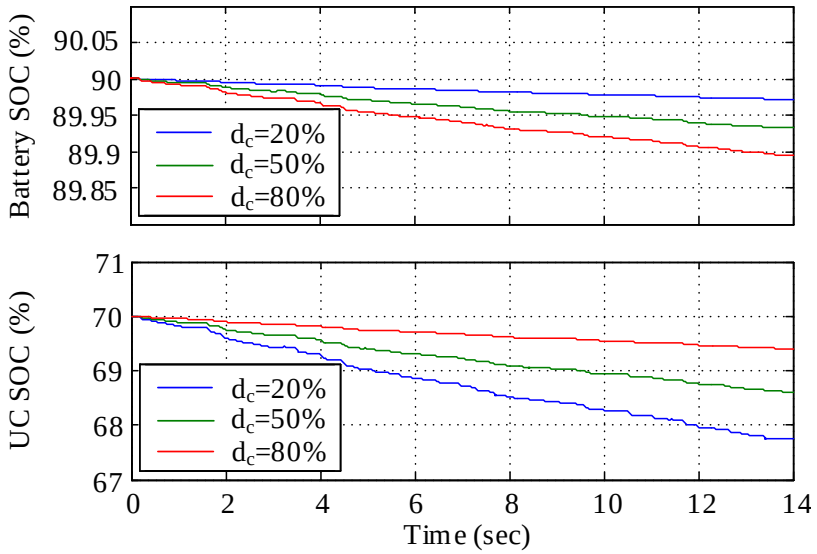

(a) Battery SOC.

(b) UC SOC.

Figure 7.7: Influence of d_c on the SOC rates with $f_c = 5$ kHz.

Table 7.2: Experimental parameters for the HESS with the MSI.

Parameters	Value
Battery and UC voltages	150 V
Switching frequency	10 kHz
R-L load	5Ω and 256μH

7.3.3 Experimental results

The influence of the new control parameters f_c and d_c on the input DC currents were experimentally tested with the prototype of the MSI_1, previously presented in Fig. 4.11. Experiments with an R-L load were performed, and the battery and UC voltages were provided by two power supplies. The parameters are presented in Table 7.2. In the following results, the same operating point has been tested for different f_c and d_c.

In Figs. 7.8 to 7.10, the currents i_{bat}, i_{uc}, and i_a are shown for a discharged duty cycle fixed at 50% and a control frequency f_c of 10 Hz, 100 Hz and 5 kHz respectively. For each figure, simulation and experimental waveforms are displayed to provide a one-to-one comparison. It can be seen that, as the frequency increases, both input currents become

continuous and their ripple is also reduced. Indeed, in Figs. 7.8 and Fig. 7.9, i_{bat} and i_{uc} are discontinuous and their ripple is high. On the other hand, smooth current sharing is achieved for a high frequency f_c of 5 kHz thanks to the input capacitor banks that act as low-pass filters, as shown in Fig. 7.10.

In Figs. 7.11 and 7.12, the currents i_{bat}, i_{uc} and i_a are displayed for a constant control frequency f_c of 5 kHz and a discharge duty cycle of 20% and 80% respectively. By choosing a discharge duty cycle lower than 50%, the UC provides more power than the battery which can be seen by a higher average current in Fig. 7.11. On the contrary, the average battery current will be greater than the average UC current if d_c is greater than 50%, as shown in Fig. 7.12.

Finally, one can note that the phase current i_a is sinusoidal with a constant amplitude and frequency, regardless of the variation of f_c or d_c. This validates the fact that the additional mode control does not interfere with the control of the load.

In conclusion, the experimental results are consistent with the theoretical operations of the new control strategy of the active HESS with the MSI. Furthermore, the influence of both parameters f_c and d_c on the source currents is validated.

7.3.4 Influence of the mode control parameters on the battery

One solution to extend the battery lifetime is to control its average current and reduce its current ripple. The following graphs summarize the effects of the control mode parameters on these two battery current variables.

The absolute value of the battery current has been averaged in order to consider positive and negative currents since they both adversely affect the battery lifetime. A ratio of the time-average value R_{ave} is calculated as in (7.2).

$$R_{ave} = \frac{\langle i_{bat} \rangle}{\langle i_{ref} \rangle} \tag{7.2}$$

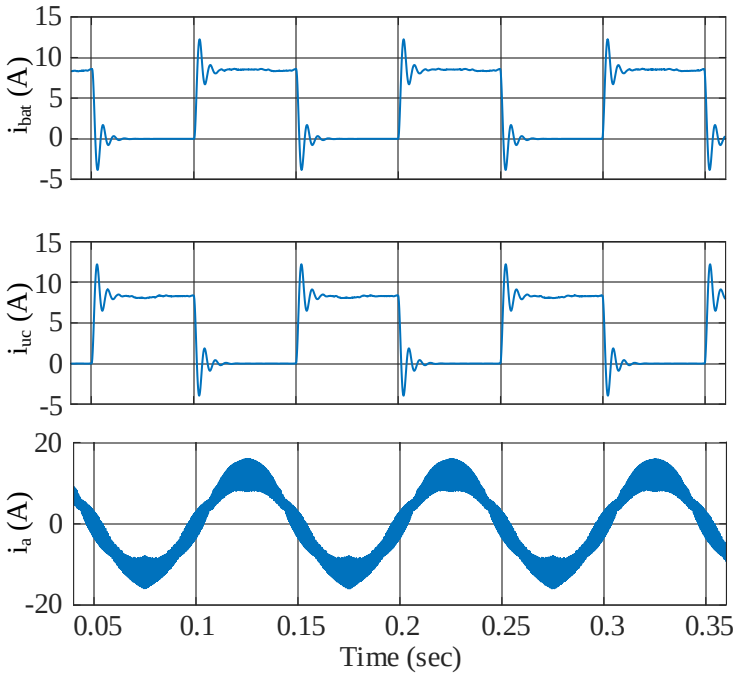

(a) Simulation waveforms.

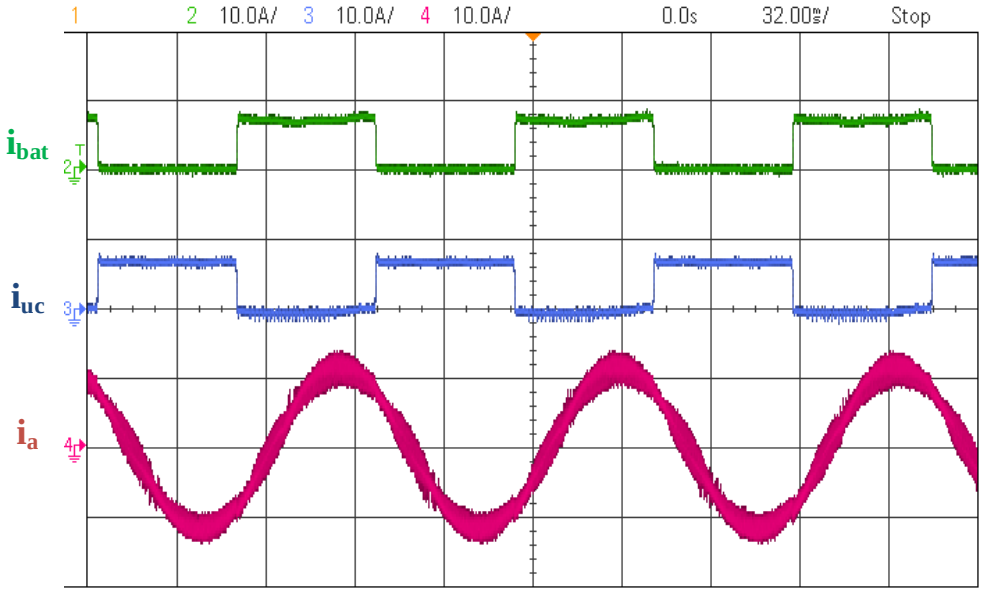

(b) Experimental results.

Figure 7.8: Waveforms of i_{bat}, i_{uc}, and i_a for $d_c = 50\%$ and $f_c = 10Hz$.

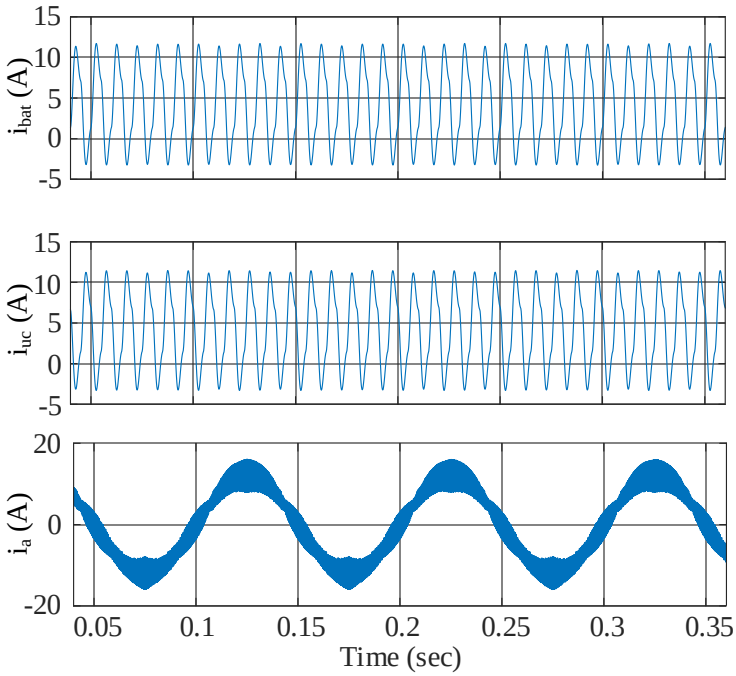

(a) Simulation waveforms.

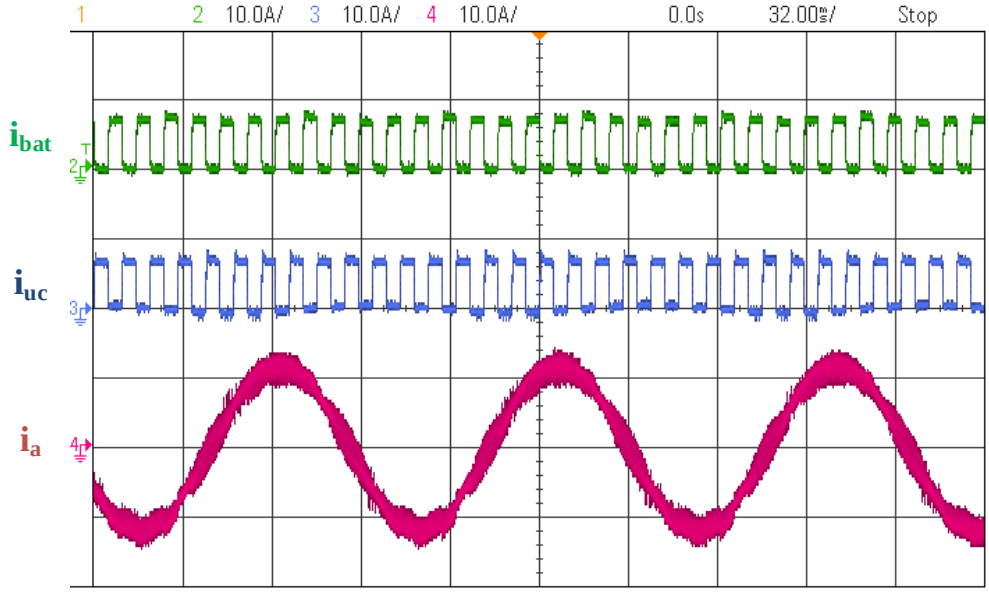

(b) Experimental results.

Figure 7.9: Waveforms of i_{bat}, i_{uc}, and i_a for $d_c = 50\%$ and $f_c = 100Hz$.

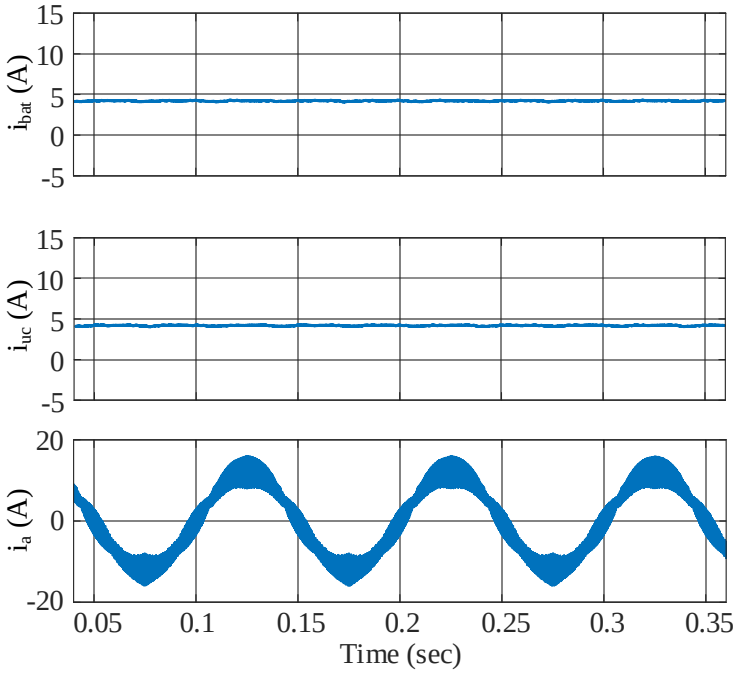

(a) Simulation waveforms.

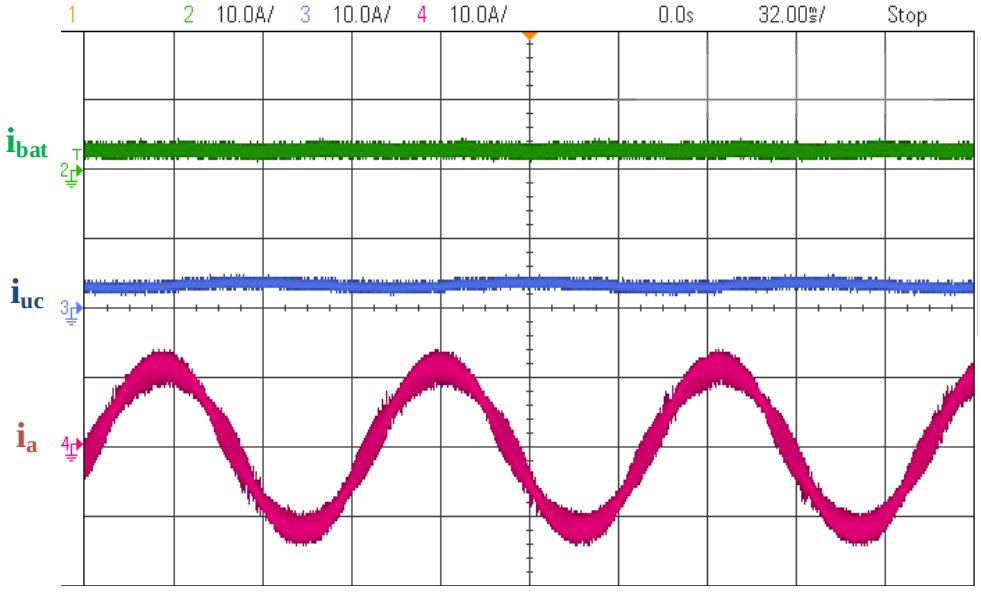

(b) Experimental results.

Figure 7.10: Waveforms of i_{bat}, i_{uc}, and i_a for $d_c = 50\%$ and $f_c = 5kHz$.

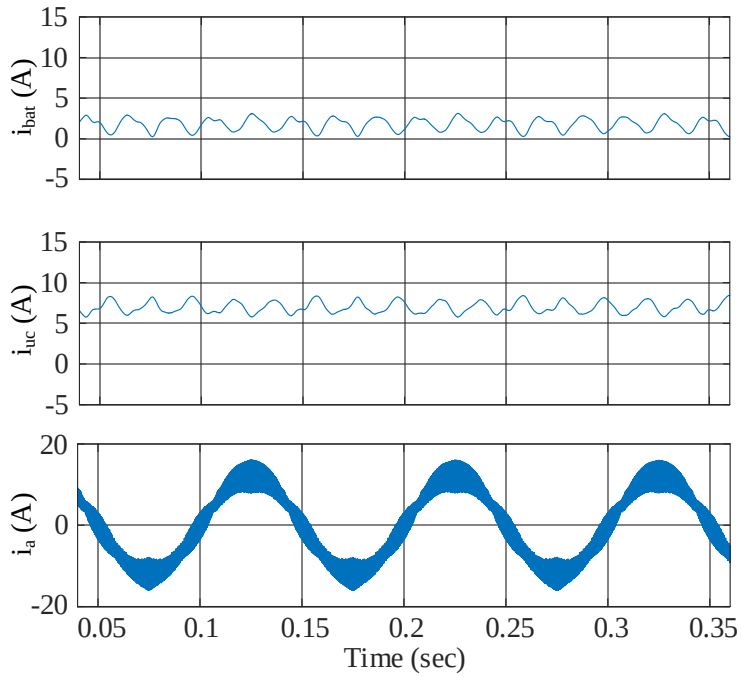

(a) Simulation waveforms.

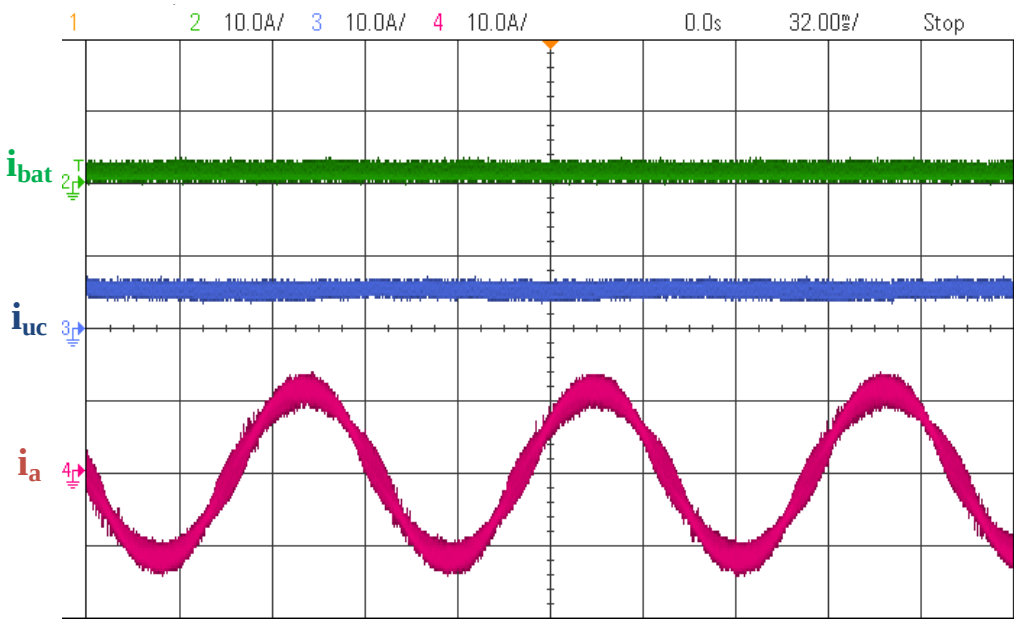

(b) Experimental results.

Figure 7.11: Waveforms of i_{bat}, i_{uc}, and i_a for $f_c = 5kHz$ and $d_c = 20\%$.

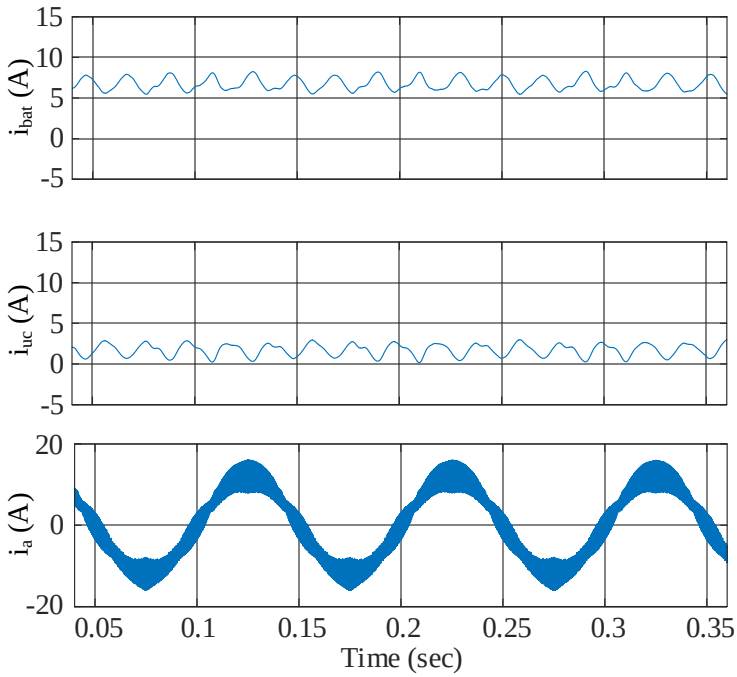

(a) Simulation waveforms.

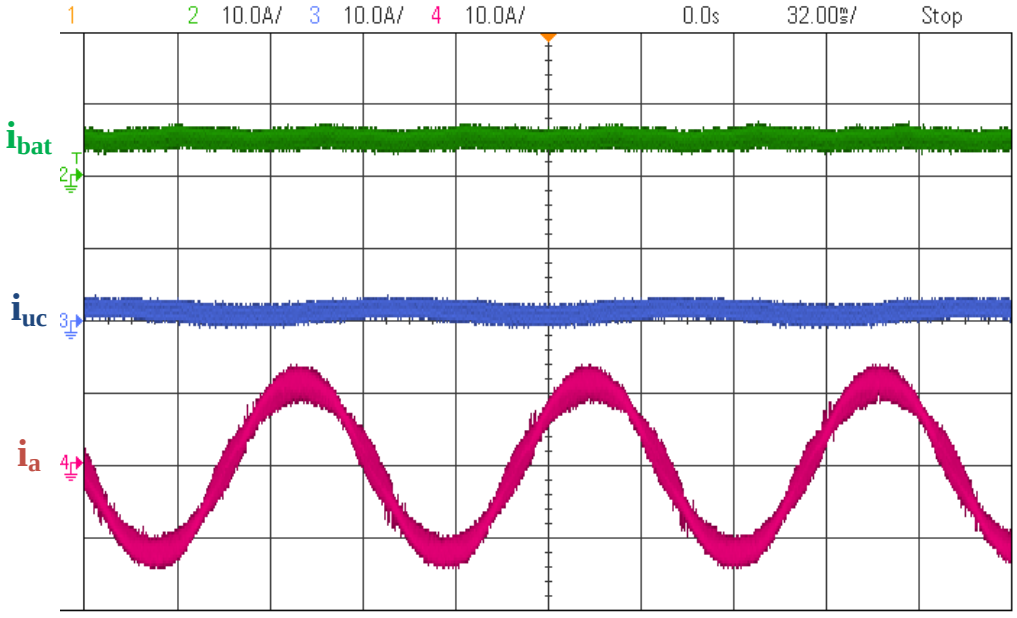

(b) Experimental results.

Figure 7.12: Waveforms of i_{bat}, i_{uc}, and i_a for $f_c = 5kHz$ and $d_c = 80\%$.

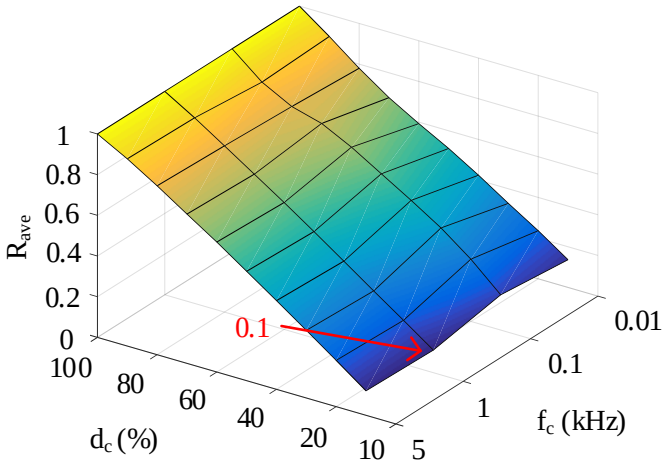

Figure 7.13: Ratio R_{ave} depending on f_c and d_c.

where $\langle i_{ref} \rangle$ is the average reference current. The reference current has been previously introduced in Fig. 7.4 and corresponds to the case where the mode control is not applied and only one source drives the EM. Hence, the ratio R_{ave} points out the average battery current reduction that can be achieved compared to the reference case for a specific control frequency f_c and discharge duty cycle d_c.

In Fig. 7.13, it can be seen that a low discharge duty cycle leads to a low ratio R_{ave}. In other terms, decreasing the discharge duty cycle reduces the average battery current, which is consistent since the battery is less used. Moreover, it can be seen that the control frequency f_c has a moderate impact on R_{ave}.

The current ripple can be calculated as the difference between the maximum and the minimum current values. A ratio of the battery current ripple $R_{\Delta I}$ is given by (7.3).

$$R_{\Delta I} = \frac{\Delta i_{bat}}{\Delta i_{ref}} \tag{7.3}$$

where Δi_{bat} and Δi_{ref} are the battery and reference current ripples, respectively.

The ratio $R_{\Delta I}$ is also a function of f_c and d_c and indicates the battery current ripple reduction that can be achieved compared to the reference case. It can be seen in Fig. 7.14

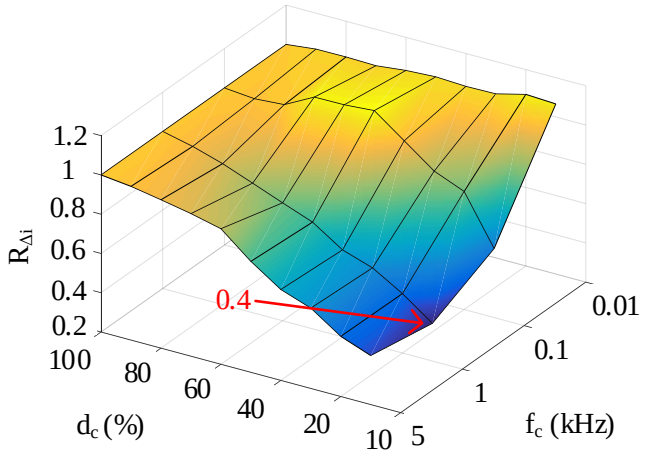

Figure 7.14: Ratio $R_{\Delta I}$ depending on f_c and d_c.

that increasing the control frequency f_c significantly reduces the battery current ripple. A low discharge duty cycle also leads to larger reduction of the battery current ripple which is due to the power sharing with the UC.

Finally, one can note that R_{ave} and $R_{\Delta I}$ reach the values 0.1 and 0.4 respectively for a discharge duty cycle d_c of 10% and a control frequency f_c of 1 kHz. In other terms, the average battery current and the battery current ripple can be reduced by up to 90% and 60% respectively, compared to traditional electrified powertrains that only uses a single energy source. However, it should be kept in mind that, even if a low discharge duty cycle and high control frequency seem more suitable to preserve the battery lifetime, it also leads to a faster discharge of the UC. Therefore, a trade-off needs to be made to minimize the ripple and average battery current, while ensuring sufficient SOC rates for both sources. The optimization of the new control parameters has been investigated in [18].

7.4 Conclusion

In this chapter, a new active HESS topology which couples a battery to an UC through the MSI was presented. An innovative control scheme has been developed to actively control the

operating mode of the inverter and aims to achieve similar performance than a typical HESS architecture with the additional benefit of not using a DC/DC converter. Indeed, thanks to the input capacitors that act as low-pass filters, smooth current sharing is accomplished by periodically switching the operating mode at high frequency. Moreover, a duty cycle can also be selected to bias the use of one energy storage device over another, which enables controlling the discharge rate of the two sources. Closed-loop control simulations have been performed to verify that the additional mode control strategy does not hinder the performance of the system. Moreover, the influence of the mode control parameters has been analyzed and validated through experiments with a scaled-down prototype and an R-L load. Finally, the influence of the new control on the battery has been studied. The average battery current and the battery current ripple can be reduced by up to 90% and 60% respectively, for a discharge duty cycle d_c of 10% and a control frequency f_c of 1 kHz, compared to traditional electrified powertrains that only uses a single energy source.

Chapter 8

Conclusions and future work

8.1 Conclusions

This thesis focused on the concept, analytical design, efficiency analysis, and implementation of the MSI for EVs.

The fundamentals of power electronics in EVs and their characteristics were first introduced. Vehicle-level modeling methods and simulation tools for power electronics were reviewed. It has been found that Autonomie enables rapid architecture comparisons and high-level performance assessment. However, this simulation tool shows some limitations regarding the customization of powertrains with unconventional converters.

A review of traction inverters implemented in EVs was realized. Despite the wide array of inverter topologies, nearly all contemporary EVs integrate the renowned VSI. Either used by itself or in combination with an additional DC/DC boost converter, this topology offers a good trade-off between performance, control complexity, cost, and size of the electrified powertrain. Practical inverter design considerations, including a review of the inverter components, were presented. For any topology to be seriously considered by the automotive industry, it must be able to compete on cost, reliability, efficiency, and power density.

The concept of the MSI was introduced, and two circuits, MSI_1 and MSI_2, were presented. When two voltages V_{dc1} and V_{dc2} are applied on the DC side, both topologies can operate in three operating modes during the DC/AC conversion. Indeed, the EM can be driven by either one source or a series combination of both, allowing for three distinct DC voltage levels, namely V_{dc2}, $V_{dc1} - V_{dc2}$, and V_{dc1}. When it operates as a rectifier, two operating modes are achievable where the power generated by the EM is supplied to one DC voltage or another. Due to the uniqueness of the MSI_1 and MSI_2 circuits, new PWM control strategies were developed for both inverter and rectifier operations of the MSI. Closed-loop control simulations and experiments with a scale-down prototype of the MSI_1 were performed with multiple speed and torque references. Results in both DC/AC and AC/DC operations are consistent with the theory, which validate the effectiveness of the proposed topology and concept.

A comprehensive design analysis and efficiency model for both the MSI_1 and MSI_2 were developed. The switch configuration of the MSI has been compared with that of the VSI through the VA rating. Although the MSI_1 and the MSI_2 have respectively three times and twice more switches than the VSI, their VA ratings relatively increase by 55.6% and 27.8% respectively. Analytical calculations of the RMS capacitor ripple current and capacitance were suggested to select the proper capacitor banks for the MSI. Whereas both MSI topologies have a second DC input source V_{dc2}, the overall volume of their capacitor banks is not doubled compared to the VSI but is enlarged by 50%. An analytical efficiency model based on the average and RMS currents in the switches was developed. Experiments with the MSI_1 and MSI_2 prototypes validated the theoretical analysis with a error of less than 2 % at maximum efficiency. An efficiency comparison between the MSI_1, the MSI_2, and the VSI was also conducted. The MSI_1 is less efficient than the MSI_2 due to the additional switches, regardless of the operating modes. Furthermore, the MSI_2 is slightly less efficient than the VSI when a DC voltage of V_{dc2} or $V_{dc1} - V_{dc2}$ is applied to the load. On the other hand, the MSI_2 is as efficient as the VSI if a high voltage V_{dc1} is applied.

The control and simulation model of a new power-split hybrid electric powertrain with the MSI were investigated. The Toyota Prius was taken as a case study and the control strategies of the power split device composed of the ICE and both EMs were first reviewed. The Prius powertrain was simulated in Autonomie and the simulation models of the battery and the ETDS were examined. A vehicle-level simulation model of the battery and the new ETDS with the MSI was developed in Matlab/Simulink to estimate the potential benefits of the proposed powertrain. Due to the additional DC-link connection between the battery and the MSI, new control strategies based on the operating modes of the MSI were proposed. The power transferred through the DC/DC converter in the Prius and the suggested powertrain was compared for four drive cycles. Although the power rating of this converter cannot be decreased, up to 25% of the averaged power transferred by the DC/DC converter can be reduced in most drive cycles tested. Furthermore, the MSI allows for more battery charging opportunities. These are encouraging results since the control has not been optimized for the suggested powertrain. It is believed that the power rating of the DC/DC converter can be reduced by revising the powertrain control and taking advantage of the additional DC connection between the battery and the MSI. Moreover, the SOC balancing can be improved by developing an optimized control for the suggested powertrain that mainly uses Mode I_2 to charge the battery.

A novel active HESS topology with the MSI that couples a battery and an UC directly to the EM, without the use of any additional power electronic converters, was suggested. Like every active HESS structure, the proposed topology with the MSI needs to efficiently control the source currents to take advantage of the high energy density of the batteries and the large specific power and cycle life of the UCs, while minimizing battery degradation. Hence, a new control strategy has been developed to manage the current distribution between the two sources. Closed-loop control simulations for a drive cycle have been performed to verify the operating principle of this novel HESS topology. The influence of the additional control parameters on the source currents and their SOC has been further investigated through

simulations. Moreover, experiments with the MSI_1 prototype and an R-L load have been carried out and validated the theoretical influence of the new control on the input DC currents. By an appropriate choice of the new control parameters, the average battery current and the battery current ripple can be reduced by up to 90% and 60% respectively compared to traditional electrified powertrains that only uses a single energy source.

8.2 Future work

In regard to future work on the MSI, the following directions are suggested.

Numerous PWM techniques, besides SPWM and SVPWM, have been developed in the literature and could be adapted for the MSI. For example, the selected harmonic elimination PWM technique can be considered to reduce the harmonic distortion of the line voltage by eliminating the low-order harmonics [120]. Furthermore, it has been reported in [126, 127] that General Motors employs the SVPWM for the linear modulation region, and then applies the six-step modulation in the over modulation region. By doing so, the DC link voltage utilization is maximized, and the EM performance is improved.

The analytical design of the DC-link capacitor in Chapter 5 has been developed for the adapted SPWM technique, but other modulation strategies would lead to different results. Moreover, the peak efficiency in each operating mode depends on the DC input voltage applied to the MSI. Hence, a design optimization could be performed to maximize the power density along with the efficiency while considering the switching frequency, the modulation strategy, the DC voltage levels, and the switch configuration as variables.

The efficiency model can be further improved with advanced methods to estimate the power losses. For instance, more accurate results would be obtained by using experimental measurements of the switching energy losses instead of using the values from the datasheet. The forward voltage drop of the switch can also be measured for several currents to improve the conduction loss model. Finally, it has been shown that the temperature impacts the

losses and should also be considered in the average models.

In a direct continuation of the work from Chapter 6, a new powertrain control developed specifically for the suggested power-split powertrain with the MSI can be investigated. First, every powertrain component, including the mechanical systems such as the power split device and the ICE, needs to be incorporated in the vehicle-level simulation model. A driver model is also required to supervise the overall control of the vehicle. Then, powertrain control strategies should be optimized to take advantage of the additional DC connection between the battery and the MSI, as well as the different operating modes. The optimization problem could be defined based on multi-objective functions that minimize the use of the DC/DC converter, while considering the ICE efficiency and SOC balancing. Finally, from the optimal power distribution obtained with the control optimization, the whole powertrain could be redesigned, and power rating reductions of the DC/DC converter are expected. Furthermore, it would be interesting to compare the design of the suggested powertrain with the MSI with other powertrains in terms of cost, power density, and efficiency. The vehicle-level simulation model could also be used for several drive cycles to estimate the fuel economy of the suggested architecture.

In Chapter 7, the HESS topology with the MSI has been simulated and the influence of the mode control parameters were analyzed. In [18], an optimization problem using dynamic programming and neural networks has been investigated to minimize the battery wear by controlling the discharge duty cycle d_c. As a next step, the optimal control should be experimentally implemented in real-time for different drive cycles to validate the proposed topology. The control frequency could also be added as a variable in the optimization problem. Furthermore, the battery ripple and SOC of the sources could be compared with those obtained in a conventional active HESS topology using a DC/DC converter. It is expected that the suggested topology with the MSI will achieve similar performance, without the use of any additional power converter. A design comparison of both architectures can also be conducted regarding the cost and power density.

Appendices

A.1 Commutation paths of the MSI_1

The commutation paths of the operating areas during the interval $[\frac{\pi}{6}; \frac{\pi}{2}]$ of Fig. 4.4a are detailed in Figs. A.1 and A.2 for Modes I_2 and I_3 respectively. It is assumed that the phase currents $i_a(t)$ and $i_c(t)$ are positive while $i_b(t)$ is negative. As expected from the theory, it can be seen that the DC-link voltage $V_{dc1} - V_{dc2}$ is supplied through (P_1) and (P_2) in Mode I_2 while the DC-link voltage V_{dc1} is supplied through (P_1) and (O) when the MSI runs in Mode I_3.

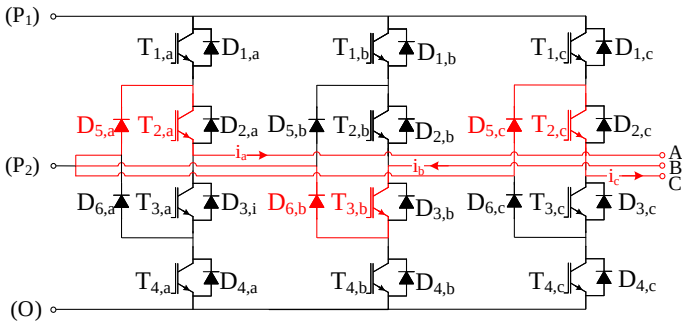

(a) Operating area I.

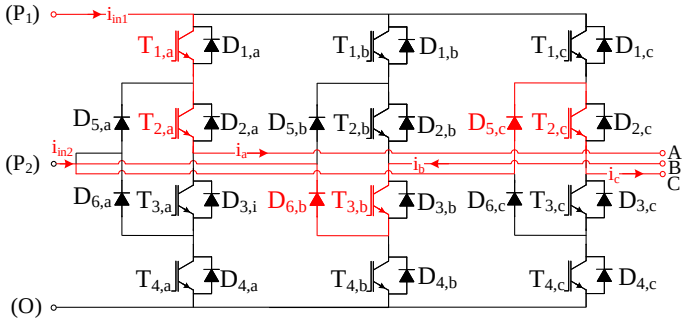

(b) Operating area II.

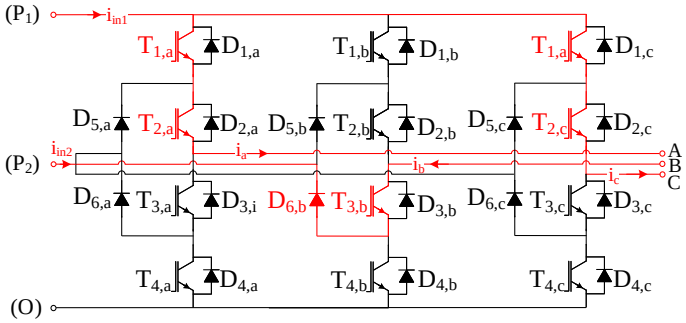

(c) Operating area III.

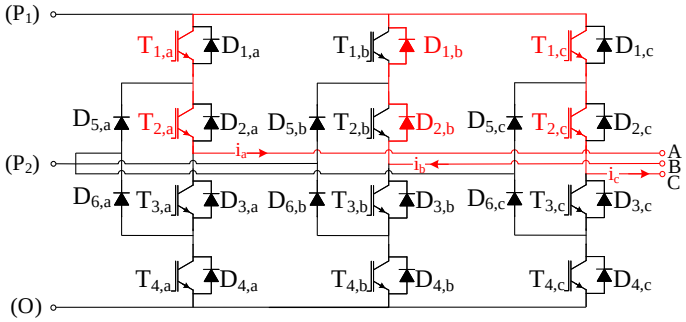

(d) Operating area IV.

Figure A.1: Commutation paths of the MSI_1 in Mode I_2.

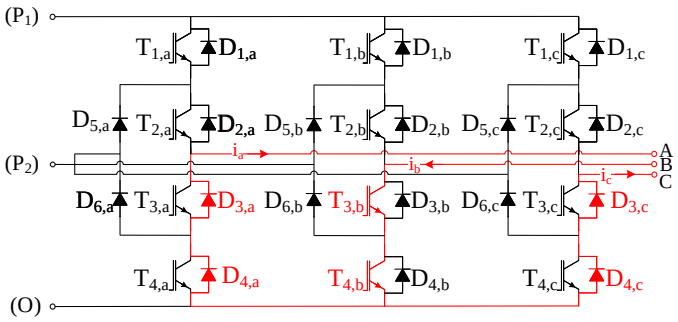

(a) Operating area I.

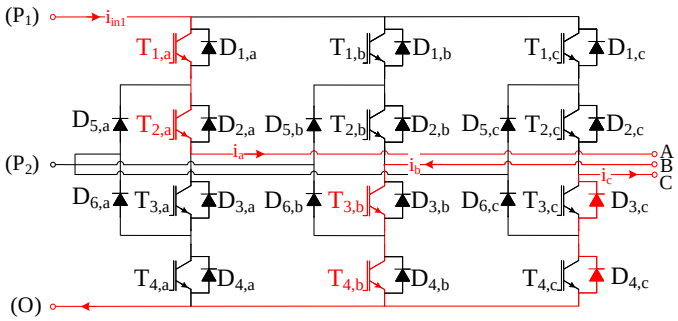

(b) Operating area II.

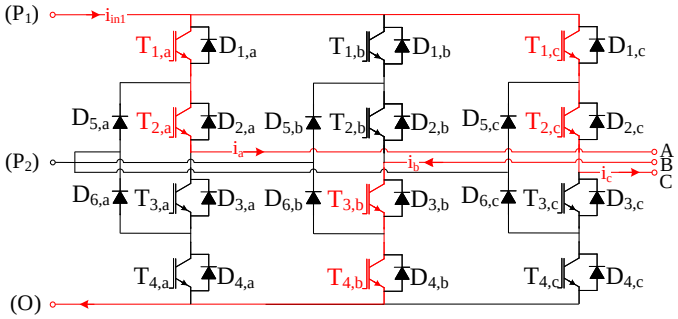

(c) Operating area III.

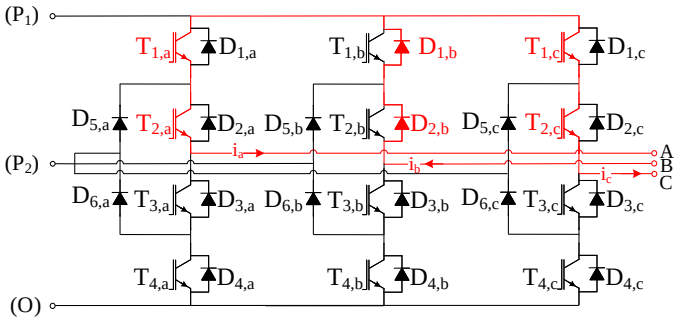

(d) Operating area IV.

Figure A.2: Commutation paths of the MSI_1 in Mode I_3.

A.2 Commutation paths of the MSI_2

The commutation paths of the operating areas during the interval $[\frac{\pi}{6}; \frac{\pi}{2}]$ of Fig. 4.4a are detailed in Figs. A.3 to A.5 for the MSI_2. It is assumed that the phase currents $i_a(t)$ and $i_c(t)$ are positive while $i_b(t)$ is negative.

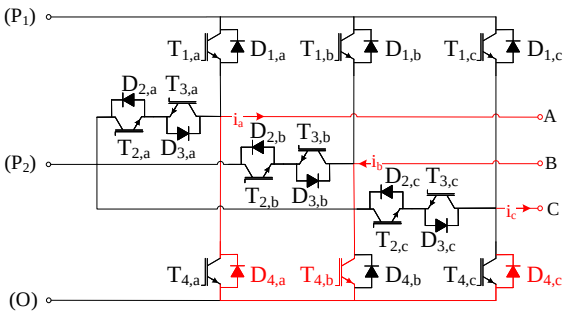

(a) Operating area I.

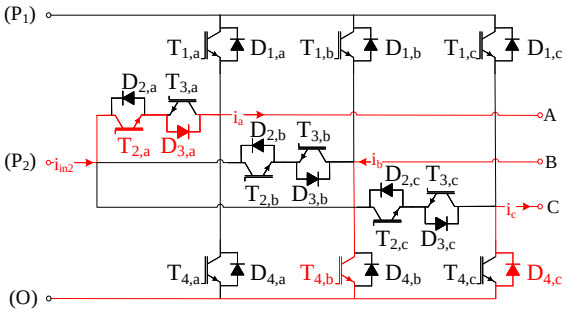

(b) Operating area II.

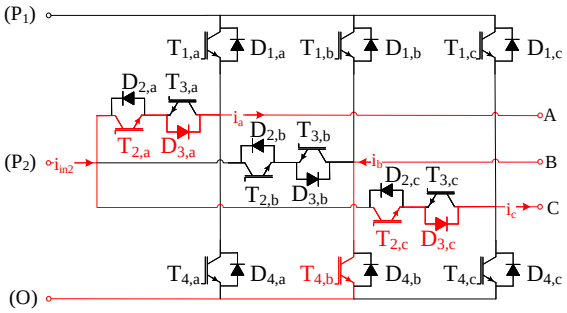

(c) Operating area III.

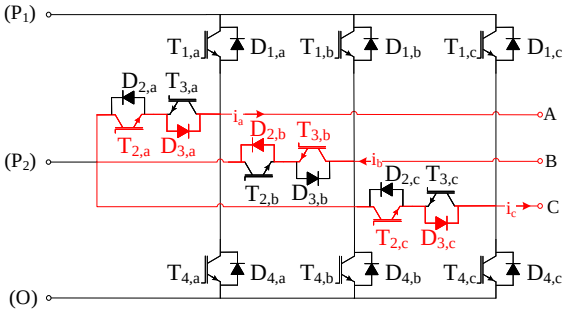

(d) Operating area IV.

Figure A.3: Commutation paths of the MSI_2 operating in Mode I_1.

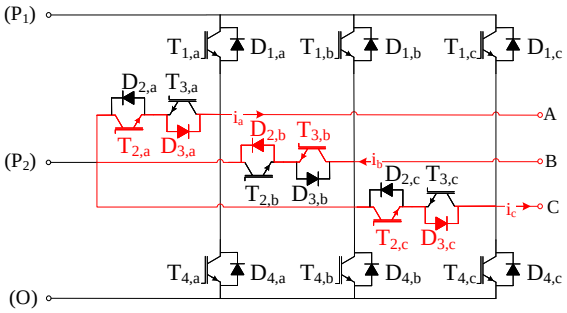

(a) Operating area I.

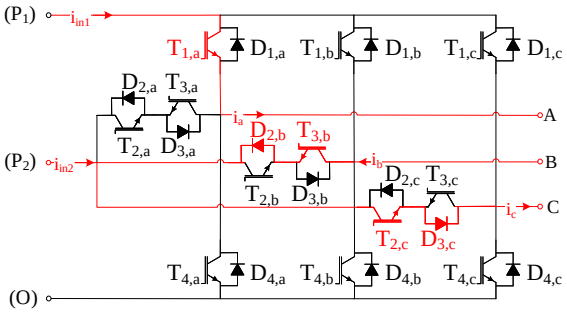

(b) Operating area II.

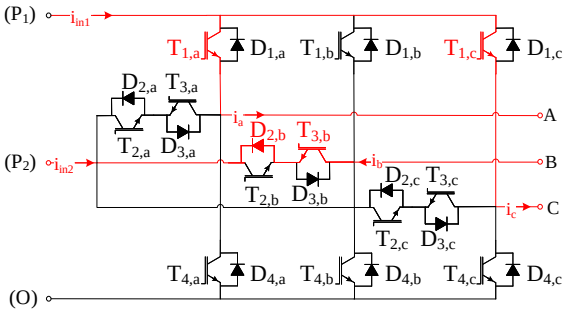

(c) Operating area III.

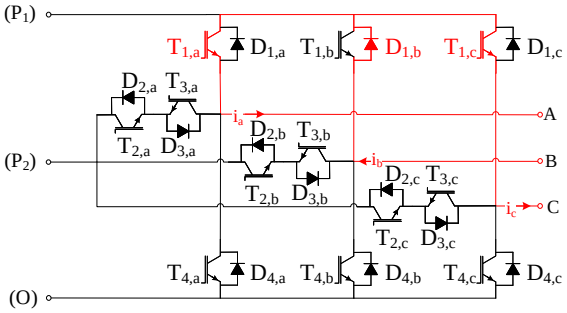

(d) Operating area IV.

Figure A.4: Commutation paths of the MSI_2 operating in Mode I_2.

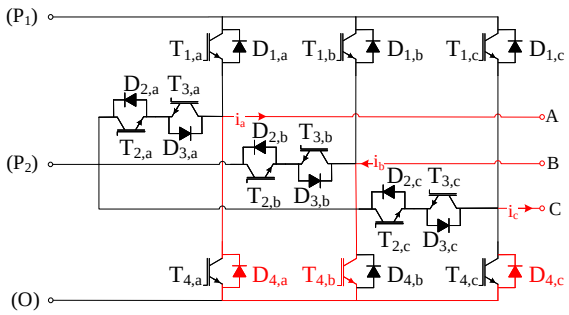

(a) Operating area I.

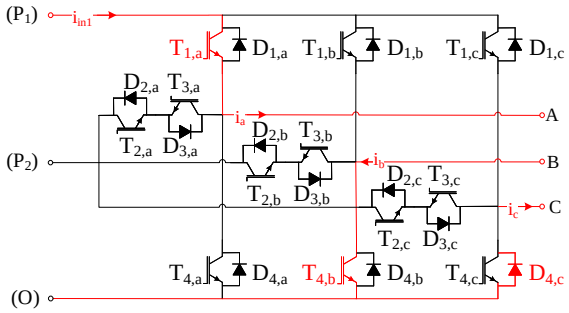

(b) Operating area II.

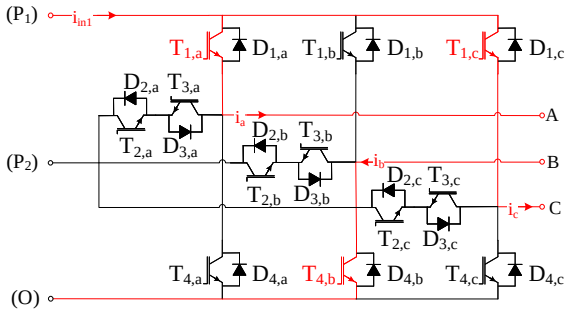

(c) Operating area III.

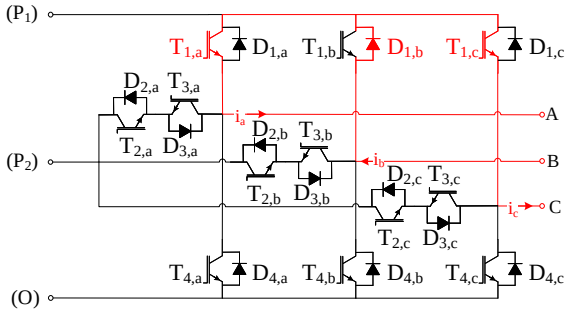

(d) Operating area IV.

Figure A.5: Commutation paths of the MSI_2 operating in Mode I_3.

References

[1] BP Energy Outlook 2018 edition. [Online]. Available: https://www.bp.com/en/global/corporate/energy-economics/energy-outlook.html

[2] Greenhouse gas emissions: drivers and impacts. [Online]. Available: https://www.canada.ca/en/environment-climate-change/services/environmental-indicators/greenhouse-gas-emissions-drivers-impacts.html

[3] "Light-duty automotive technology, carbon dioxide emissions, and fuel economy trends: 1975 through 2017," U.S. Environmental Protection Agency, Tech. Rep. EPA-420-S-18-001, Jan. 2018.

[4] Global EV outlook 2018 - Towards Cross-Modal Electrification. [Online]. Available: www.iea.org

[5] S. C. Davis, S. E. Williams, R. G. Boundy, and S. Moore, "2016 vehicle technologies market report," Oak Ridge National Laboratory (ORNL), Tech. Rep. ORNL/TM-2017/238, 2017.

[6] Actions by countries to phase out internal combustion engines. [Online]. Available: https://climateprotection.org/actions-by-countries-phase-out-gas/

[7] B. Bilgin, P. Magne, P. Malysz, Y. Yang, V. Pantelic, M. Preindl, A. Korobkine, W. Jiang, M. Lawford, and A. Emadi, "Making the case for electrified transportation,"

IEEE Transactions on Transportation Electrification, vol. 1, no. 1, pp. 4–17, May 2015.

[8] "U.S. DRIVE Electrical and Electronics Technical Team Roadmap," U.S. Department of Energy, Oct. 2017.

[9] A. Emadi and P. Magne, "Power Converter," Patent U.S. 0 117 770 A1, May 1, 2014.

[10] R. Hou, J. Guo, L. Dorn-Gomba, and A. Emadi, *Control of Power Electronic Converters and Systems*, 2nd ed. Elsevier, 2018, ch. 23: Power Electronics Systems and Control in Automobiles.

[11] L. Dorn-Gomba, J. Guo, J. Reimers, R. Hou, D. Wang, and A. Emadi, "Modeling and simulation of power electronics in electrified vehicles," *for submission to IEEE Transactions on Power Electronics.*

[12] J. Reimers, L. Dorn-Gomba, C. Mak, and A. Emadi, "Automotive traction inverters: Current status and future trends," *Accepted with minor revisions to IEEE Transactions on Vehicular Technology.*

[13] L. Dorn-Gomba, P. Magne, B. Danen, and A. Emadi, "On the concept of the multi-source inverter for hybrid electric vehicle powertrains," *IEEE Transactions on Power Electronics*, vol. 33, no. 9, pp. 7376–7386, Oct. 2018.

[14] L. Dorn-Gomba, P. Magne, C. Barthelmebs, and A. Emadi, "On the concept of the multi-source inverter," in *2016 IEEE Applied Power Electronics Conference and Exposition (APEC)*, Long Beach, CA, Mar. 2016, pp. 453–459.

[15] L. Dorn-Gomba, J. Guo, and A. Emadi, "Comparison of multi-source inverter and voltage source inverter for electrified vehicles," *for submission to IEEE Transactions on Power Electronics.*

[16] ——, "Multi-source inverter for power-split hybrid electric powertrains," *Submitted to IEEE Transactions on Vehicular Technology.*

[17] L. Dorn-Gomba, E. Chemali, and A. Emadi, "A novel hybrid energy storage system using the multi-source inverter," in *2018 IEEE Applied Power Electronics Conference and Exposition (APEC)*, San Antonio, TX, Mar. 2018, pp. 684–691.

[18] J. Ramoul, E. Chemali, L. Dorn-Gomba, and A. Emadi, "A neural network energy management controller applied to a hybrid energy storage system using the multi-source inverter," in *2018 IEEE Energy Conversion Congress and Exposition (ECCE)*, Portland, OR, Sep. 2018.

[19] "U.S. DRIVE Electrical and Electronics Technical Team Roadmap," U.S. Department of Energy, Jun. 2013.

[20] N. R. Council *et al.*, *Cost, effectiveness, and deployment of fuel economy technologies for light-duty vehicles.* National Academies Press, Jun. 2015.

[21] P. R. Windover, R. J. Owens, T. M. Levinson, and M. D. Laughlin, "Stop and restart effects on modern vehicle starting system components: Longevity and economic factors," Argonne National Laboratory (ANL), Tech. Rep. ANL-15/04, Apr. 2015.

[22] A. Emadi, *Advanced Electric Drive Vehicles.* CRC Press Taylor and Francis Group, Oct. 2014.

[23] "Midterm evaluation of light-duty vehicle greenhouse gas emission standards and corporate average fuel economy standards for model years 2022-2025," Office of Transportation and Air Quality, U.S. Environmental Protection Agency, National Highway Traffic Safety Administration, U.S. Department of Transportation And California Air Resources Board, Tech. Rep. EPA-420-D-16-900, Jul. 2016.

[24] S. Schiffer, A. Kain, P. Wilde, M. Helbing, and B. Baeker, "Improving longitudinal dynamics of conventional vehicles in comparison to electrified vehicles to meet customer behavior," in *2017 Twelfth International Conference on Ecological Vehicles and Renewable Energies (EVER)*, Jun. 2017, pp. 1–11.

[25] M. Kuypers, "Application of 48 volt for mild hybrid vehicles and high power loads," in *SAE Technical Paper*, no. 2014-01-1790, 2014.

[26] F. Atzler, M. Wegerer, F. Mehne, S. Rohrer, C. Rathgeber, and S. Fischer, "Fuel consumption and emissions effects in passenger car diesel engines through the use of a belt starter generator," in *SAE Technical Paper*, no. 2015-01-1162, 2015.

[27] D. Cottrell, M. Miller, A. Oury, E. Staley *et al.*, "Development of general motors eAssist Gen3 propulsion system," in *SAE Technical Paper*, no. 2018-01-0422, 2018.

[28] T. A. Staunton, R. H. Burress and M. L. D., "Evaluation of the 2005 Honda Accord hybrid electric drive system," Oak Ridge National Laboratory, Tech. Rep. ORNL/TM-2006/535, Sep. 2006.

[29] T. Fukui and T. Saito, "Development of hybrid system for 2011 compact sedan," in *SAE Technical Paper*, no. 2011-01-0865, 2011.

[30] C. Mi and M. A. Masrur, *Hybrid electric vehicles: principles and applications with practical perspectives*. John Wiley & Sons, 2017.

[31] I. N. L. (INL). Advanced Vehicles - Vehicle Testing. [Online]. Available: https://avt.inl.gov/vehicle-type/all-powertrain-architecture

[32] P. Nelson, R. Vijayagopal, K. Gallagher, and A. Rousseau, "Sizing the battery power for phevs based on battery efficiency, cost and operational cost savings," *World Electric Vehicle Journal*, vol. 6, no. 3, pp. 514–522, Sep. 2013.

[33] D. Santini, M. Rood, Y. Zhou, T. Stephens, J. Miller, and L. Bluestein, "Implications of successes and failures of bev-focused incentive support for pevs in the us, canada and europe," *World Electric Vehicle Journal*, vol. 8, no. 4, pp. 831–841, Dec. 2016.

[34] G. Wu, X. Zhang, and Z. Dong, "Powertrain architectures of electrified vehicles: Review, classification and comparison," *Journal of the Franklin Institute*, vol. 352, no. 2, pp. 425–448, Feb. 2015.

[35] N. Higuchi, Y. Sunaga, M. Tanaka, and H. Shimada, "Development of a new two-motor plug-in hybrid system," *SAE International Journal of Alternative Powertrains*, vol. 2, no. 1, pp. 135–145, May 2013.

[36] A. Steier and A. Munday, "Advanced strong hybrid and plug-in hybrid engineering evaluation and cost analysis," Apr. 2017.

[37] T. A. Burress, S. L. Campbell, C. L. Coomer, C. W. Ayers, A. A. Wereszczak, J. P. Cunningham, L. D. Marlino, L. E. Seiber, and H. T. Lin, "Evaluation of the 2010 Toyota Prius hybrid synergy drive system," Oak Ridge National Laboratory, Tech. Rep. ORNL/TM-2010/253, Jan. 2008.

[38] X. Zhang, C.-T. Li, D. Kum, and H. Peng, "Prius+ and Volt: Configuration analysis of power-split hybrid vehicles with a single planetary gear," *IEEE Transactions on Vehicular Technology*, vol. 61, no. 8, pp. 3544–3552, Jul. 2012.

[39] Gm provides technical details of the gen 2 Voltec propulsion system used in the 2016 volt. [Online]. Available: http://www.greencarcongress.com/2015/04/20150423-voltec.html

[40] A. N. Duhon, K. S. Sevel, S. A. Tarnowsky, and P. J. Savagian, "Chevrolet volt electric utilization," *SAE International Journal of Alternative Powertrains*, vol. 4, no. 2, pp. 269–276, Jul. 2015.

[41] E. Chemali, M. Preindl, P. Malysz, and A. Emadi, "Electrochemical and electrostatic energy storage and management systems for electric drive vehicles: State-of-the-art review and future trends," *IEEE Journal of Emerging and Selected Topics in Power Electronics*, vol. 4, no. 3, pp. 1117–1134, May 2016.

[42] A. Khaligh, Z. Li *et al.*, "Battery, ultracapacitor, fuel cell, and hybrid energy storage systems for electric, hybrid electric, fuel cell, and plug-in hybrid electric vehicles: State of the art," *IEEE Transactions on Vehicular Technology*, vol. 59, no. 6, pp. 2806–2814, Apr. 2010.

[43] M. Yamauchi. Led by Volt, LEAF and Tesla Model S, EV drivers in the U.S. have racked up well over 10 billion e-miles driven. [Online]. Available: https://www.pluglesspower.com/learn/led-volt-leaf-tesla-model-s-ev-drivers-u-s-racked-well-10-billion-e-miles-driven/

[44] D. Gohlke and Y. Zhou, "Impacts of electrification of light-duty vehicles in the united states, 2010-2017," Argonne National Lab.(ANL), Argonne, IL, Tech. Rep. ANL/ESD-18/1, Jan. 2018.

[45] N. Qin, R. P. Brooker, A. Raissi *et al.*, "Fuel cell vehicle technologies, infrastructure and requirements," Electric Vehicle Transportation Center (EVTC), University of Central Florida, Tech. Rep. FSEC-CR-2059-17, Apr. 2017.

[46] May 2018 sales dashboard. [Online]. Available: https://www.hybridcars.com/may-2018-sales-dashboard/

[47] 2018 Toyota Mirai fuel cell vehicle. [Online]. Available: https://ssl.toyota.com/mirai/fcv.html

[48] 2017 Hyundai Tucson fuel cell. [Online]. Available: http://www.hyundainews.com/models/hyundai-tucson-fuel-cell-2017/specifications

[49] 2018 Honda Clarity fuel cell specifications and features. [Online]. Available: https://automobiles.honda.com/clarity-fuel-cell

[50] J. Kim and S. Kim, "Obstacles to the success of fuel-cell electric vehicles: Are they truly impossible to overcome?" *IEEE Electrification Magazine*, vol. 6, no. 1, pp. 48–54, Feb. 2018.

[51] J. De Santiago, H. Bernhoff, B. Ekergård, S. Eriksson, S. Ferhatovic, R. Waters, and M. Leijon, "Electrical motor drivelines in commercial all-electric vehicles: A review," *IEEE Transactions on Vehicular Technology*, vol. 61, no. 2, pp. 475–484, Dec. 2012.

[52] J. O. Estima and A. J. M. Cardoso, "Efficiency analysis of drive train topologies applied to electric/hybrid vehicles," *IEEE Transactions on Vehicular Technology*, vol. 61, no. 3, pp. 1021–1031, Feb. 2012.

[53] M. Yilmaz and P. T. Krein, "Review of battery charger topologies, charging power levels, and infrastructure for plug-in electric and hybrid vehicles," *IEEE Transactions on Power Electronics*, vol. 28, no. 5, pp. 2151–2169, Aug. 2013.

[54] C. Liu, K. Chau, D. Wu, and S. Gao, "Opportunities and challenges of vehicle-to-home, vehicle-to-vehicle, and vehicle-to-grid technologies," *Proceedings of the IEEE*, vol. 101, no. 11, pp. 2409–2427, Jul. 2013.

[55] R. Hou, P. Magne, B. Bilgin, and A. Emadi, "A topological evaluation of isolated dc/dc converters for auxiliary power modules in electrified vehicle applications," in *2015 IEEE Applied Power Electronics Conference and Exposition (APEC)*, Charlotte, NC, Mar. 2015, pp. 1360–1366.

[56] R. Hou and A. Emadi, "Applied integrated active filter auxiliary power module for electrified vehicles with single-phase onboard chargers," *IEEE Transactions on Power Electronics*, vol. 32, no. 3, pp. 1860–1871, May 2017.

[57] R. H. Staunton, C. W. Ayers, L. D. Marlino, J. N. Chiasson, and T. A. Burress, "Evaluation of the 2004 Toyota Prius hybrid synergy drive system," Oak Ridge National Laboratory, Tech. Rep. ORNL/TM-2006/423, May 2006.

[58] O. Kitazawa, T. Kikuchi, M. Nakashima, Y. Tomita, H. Kosugi, and T. Kaneko, "Development of power control unit for compact-class vehicle," *SAE International Journal of Alternative Powertrains*, vol. 5, pp. 278–285, Apr. 2016.

[59] T. Kimura, R. Saitou, K. Kubo, K. Nakatsu, H. Ishikawa, and K. Sasaki, "High-power-density inverter technology for hybrid and electric vehicle applications," *Hitachi Review*, vol. 63, no. 2, pp. 96–102, 2014.

[60] M. Anwar, S. N. Hasan, M. Teimor, M. Korich, and M. B. Hayes, "Development of a power dense and environmentally robust traction power inverter for the second-generation Chevrolet VOLT extended-range EV," in *2015 IEEE Energy Conversion Congress and Exposition (ECCE)*, Montreal,QC, Canada, Sep. 2015, pp. 6006–6013.

[61] T. Geinzer, A. Schwarz, and M. Gleich, "Innovations for IGBT based power modules in HEV drivetrain applications," in *PCIM Europe 2017; International Exhibition and Conference for Power Electronics, Intelligent Motion, Renewable Energy and Energy Management*, Nuremberg, Germany, May 2017, pp. 1–3.

[62] M. Brubaker, D. El Hage, T. Hosking, E. Sawyer, and W. T. Franke, "Integrated DC link capacitor/bus enables a 20% increase in inverter efficiency," in *PCIM Europe 2014; International Exhibition and Conference for Power Electronics, Intelligent Motion, Renewable Energy and Energy Management*, Nuremberg, Germany, May 2014, pp. 501–508.

[63] E. Sawyer, M. Brubaker, and T. Hosking, "Understanding the contribution of switch input connection geometry to overall DC link inductance," in *2015 17th European*

Conference on Power Electronics and Applications (EPE'15 ECCE-Europe), Geneva, Switzerland, Sep. 2015, pp. 1–8.

[64] M. A. Brubaker, T. A. Hosking, T. Reiter, L. D. Marlino, and M. S. Chinthavali, "Optimized DC link for next generation power modules," in *PCIM Europe 2016; International Exhibition and Conference for Power Electronics, Intelligent Motion, Renewable Energy and Energy Management*, Nuremberg, Germany, May 2016, pp. 1–9.

[65] M. Pourabdollah, N. Murgovski, A. Grauers, and B. Egardt, "Optimal sizing of a parallel phev powertrain," *IEEE Transactions on Vehicular Technology*, vol. 62, no. 6, pp. 2469–2480, Jan. 2013.

[66] E. Silvas, T. Hofman, N. Murgovski, L. P. Etman, and M. Steinbuch, "Review of optimization strategies for system-level design in hybrid electric vehicles," *IEEE Transactions on Vehicular Technology*, vol. 66, no. 1, pp. 57–70, Mar. 2017.

[67] L. Xu, C. D. Mueller, J. Li, M. Ouyang, and Z. Hu, "Multi-objective component sizing based on optimal energy management strategy of fuel cell electric vehicles," *Applied Energy*, vol. 157, pp. 664–674, Nov. 2015.

[68] M. Pourabdollah, B. Egardt, N. Murgovski, and A. Grauers, "Convex optimization methods for powertrain sizing of electrified vehicles by using different levels of modeling details," *IEEE Transactions on Vehicular Technology*, vol. 67, no. 3, pp. 1881–1893, Oct. 2018.

[69] X. Wang, H. Bai, Z. Zhao, and L. Yuan, "Mathematical models of the system-level safe operational areas of power electronic converters in plug-in hybrid electric vehicles," *IEEE Transactions on Vehicular Technology*, vol. 60, no. 9, pp. 4288–4298, Sep. 2011.

[70] M. Riera-Guasp, J. A. Antonino-Daviu, G.-A. Capolino *et al.*, "Advances in electrical machine, power electronic, and drive condition monitoring and fault detection: State of the art," *IEEE Transactions on Industrial Electronics*, vol. 62, no. 3, pp. 1746–1759, Dec. 2015.

[71] J. Poon, P. Jain, I. C. Konstantakopoulos, C. Spanos, S. K. Panda, and S. R. Sanders, "Model-based fault detection and identification for switching power converters," *IEEE Transactions on Power Electronics*, vol. 32, no. 2, pp. 1419–1430, Mar. 2017.

[72] A. Rousseau and A. Moawad, "Impact of control strategies on fuel efficiency of different phevs using real world driving conditions," *IAMF 2010*, 2010.

[73] M. Zandi, A. Payman, J.-P. Martin, S. Pierfederici, B. Davat, and F. Meibody-Tabar, "Energy management of a fuel cell/supercapacitor/battery power source for electric vehicular applications," *IEEE Transactions on Vehicular Technology*, vol. 60, no. 2, pp. 433–443, Nov. 2011.

[74] A. M. Ali and D. Söffker, "Towards optimal power management of hybrid electric vehicles in real-time: A review on methods, challenges, and state-of-the-art solutions," *Energies*, vol. 11, no. 3, pp. 476–500, Feb. 2018.

[75] C. M. Martinez, X. Hu, D. Cao, E. Velenis, B. Gao, and M. Wellers, "Energy management in plug-in hybrid electric vehicles: Recent progress and a connected vehicles perspective," *IEEE Transactions on Vehicular Technology*, vol. 66, no. 6, pp. 4534–4549, Jun. 2017.

[76] A. A. Malikopoulos, "Supervisory power management control algorithms for hybrid electric vehicles: A survey," *IEEE Transactions on Intelligent Transportation Systems*, vol. 15, no. 5, pp. 1869–1885, Mar. 2014.

[77] R. M. Patil, Z. Filipi, and H. K. Fathy, "Comparison of supervisory control strategies for series plug-in hybrid electric vehicle powertrains through dynamic programming," *IEEE Transactions on Control Systems Technology*, vol. 22, no. 2, pp. 502–509, May 2014.

[78] D. F. Opila, X. Wang, R. McGee, R. B. Gillespie, J. A. Cook, and J. W. Grizzle, "An energy management controller to optimally trade off fuel economy and drivability for hybrid vehicles," *IEEE Transactions on Control Systems Technology*, vol. 20, no. 6, pp. 1490–1505, Oct. 2012.

[79] Z. Chen, C. C. Mi, J. Xu, X. Gong, and C. You, "Energy management for a power-split plug-in hybrid electric vehicle based on dynamic programming and neural networks," *IEEE Transactions on Vehicular Technology*, vol. 63, no. 4, pp. 1567–1580, Nov. 2014.

[80] J. Shen, A. Khaligh *et al.*, "A supervisory energy management control strategy in a battery/ultracapacitor hybrid energy storage system," *IEEE Transactions on Transportation Electrification*, vol. 1, no. 3, pp. 223–231, Oct. 2015.

[81] F. U. Syed, M. L. Kuang, J. Czubay, and H. Ying, "Derivation and experimental validation of a power-split hybrid electric vehicle model," *IEEE Transactions on Vehicular Technology*, vol. 55, no. 6, pp. 1731–1747, Nov. 2006.

[82] Z. Asus, E.-H. Aglzim, D. Chrenko, Z.-H. C. Daud, and L. Le Moyne, "Dynamic modeling and driving cycle prediction for a racing series hybrid car," *IEEE Journal of Emerging and Selected Topics in Power Electronics*, vol. 2, no. 3, pp. 541–551, Feb. 2014.

[83] C. Yi, B. I. Epureanu, S.-K. Hong, T. Ge, and X. G. Yang, "Modeling, control, and performance of a novel architecture of hybrid electric powertrain system," *Applied Energy*, vol. 178, pp. 454–467, Sep. 2016.

[84] C. C. Chan, A. Bouscayrol, and K. Chen, "Electric, hybrid, and fuel-cell vehicles: Architectures and modeling," *IEEE Transactions on Vehicular Technology*, vol. 59, no. 2, pp. 589–598, Oct. 2010.

[85] D. Maksimovic, A. M. Stankovic, V. J. Thottuvelil, and G. C. Verghese, "Modeling and simulation of power electronic converters," *Proceedings of the IEEE*, vol. 89, no. 6, pp. 898–912, Jun. 2001.

[86] A. Davoudi, J. Jatskevich, and T. De Rybel, "Numerical state-space average-value modeling of pwm dc-dc converters operating in dcm and ccm," *IEEE Transactions on Power Electronics*, vol. 21, no. 4, pp. 1003–1012, Jul. 2006.

[87] A. Yazdani and R. Iravani, "A unified dynamic model and control for the voltage-sourced converter under unbalanced grid conditions," *IEEE Transactions on Power Delivery*, vol. 21, no. 3, pp. 1620–1629, Jun. 2006.

[88] Y. Xu, Y. Chen, C.-C. Liu, and H. Gao, "Piecewise average-value model of pwm converters with applications to large-signal transient simulations," *IEEE Transactions on Power Electronics*, vol. 31, no. 2, pp. 1304–1321, Apr. 2016.

[89] S. R. Sanders and G. C. Verghese, "Synthesis of averaged circuit models for switched power converters," *IEEE Transactions on Circuits and Systems*, vol. 38, no. 8, pp. 905–915, Aug. 1991.

[90] A. Davoudi, J. Jatskevich, P. L. Chapman, and A. Khaligh, "Averaged-switch modeling of fourth-order pwm dc–dc converters considering conduction losses in discontinuous mode," *IEEE Transactions on Power Electronics*, vol. 22, no. 6, pp. 2410–2415, Nov. 2007.

[91] S. Chiniforoosh, J. Jatskevich, A. Yazdani, V. Sood, V. Dinavahi, J. Martinez, and A. Ramirez, "Definitions and applications of dynamic average models for analysis of

power systems," *IEEE Transactions on Power Delivery*, vol. 25, no. 4, pp. 2655–2669, Jul. 2010.

[92] E. Tara, S. Filizadeh, J. Jatskevich, E. Dirks, A. Davoudi, M. Saeedifard, K. Strunz, and V. Sood, "Dynamic average-value modeling of hybrid-electric vehicular power systems," *IEEE Transactions on Power Delivery*, vol. 27, no. 1, pp. 430–438, Oct. 2012.

[93] M. Amrhein and P. T. Krein, "Dynamic simulation for analysis of hybrid electric vehicle system and subsystem interactions, including power electronics," *IEEE Transactions on Vehicular Technology*, vol. 54, no. 3, pp. 825–836, May 2005.

[94] F. L. Mapelli, D. Tarsitano, and M. Mauri, "Plug-in hybrid electric vehicle: Modeling, prototype realization, and inverter losses reduction analysis," *IEEE Transactions on Industrial Electronics*, vol. 57, no. 2, pp. 598–607, Aug. 2010.

[95] T. A. Burress, C. L. Coomer, S. L. Campbell, L. E. Seiber, L. D. Marlino, R. Staunton, and J. P. Cunningham, "Evaluation of the 2007 Toyota Camry hybrid synergy drive system," Oak Ridge National Laboratory, Tech. Rep. ORNL/TM-2007/190, May 2011.

[96] T. A. Burress, C. Coomer, S. Campbell, A. Wereszczak, J. Cunningham, L. Marlino, L. Seiber, and H.-T. Lin, "Evaluation of the 2008 Lexus LS 600H hybrid synergy drive system," Oak Ridge National Laboratory, Tech. Rep. ORNL/TM-2008/185, Jan. 2009.

[97] Green vehicles. [Online]. Available: https://www.mathworks.com/solutions/automotive/green-vehicles.html

[98] GM standardizes on model-based design for hybrid powertrain development. [Online]. Available: https://www.mathworks.com/company/user-stories/gm-standardizes-on-model-based-design-for-hybrid-powertrain-development.html

[99] D. W. Gao, C. Mi, and A. Emadi, "Modeling and simulation of electric and hybrid vehicles," *Proceedings of the IEEE*, vol. 95, no. 4, pp. 729–745, Apr. 2007.

[100] Vehicle technology simulation and analysis tools. [Online]. Available: https://www.nrel.gov/transportation/systems-analysis-tools.html

[101] A. Hardin. Argonne launches new tool to help auto industry reduce costs. [Online]. Available: http://www.anl.gov/articles/argonne-launches-new-tool-help-auto-industry-reduce-costs

[102] Autonomie. [Online]. Available: https://www.autonomie.net/

[103] A. Moawad, N. Kim, N. Shidore, and A. Rousseau, "Assessment of vehicle sizing, energy consumption, and cost through large-scale simulation of advanced vehicle technologies," Argonne National Laboratory (ANL), Tech. Rep. ANL/ESD-15/28, Mar. 2016.

[104] S. A. Rogers, "Annual progress report for the advanced power electronics and electric motors program," U.S. Department of Energy, Tech. Rep. DOE/EE-1040, Dec. 2013.

[105] M. H. Rashid, *Power Electronics Handbook: devices, circuits, and applications*, 3rd ed. Elsevier Inc, 2011.

[106] H. Wen, W. Xiao, X. Wen, and P. Armstrong, "Analysis and evaluation of DC-link capacitors for high-power-density electric vehicle drive systems," *IEEE Transactions on Vehicular Technology*, vol. 61, no. 7, pp. 2950–2964, Jun. 2012.

[107] W. Deng, Y. Zhao, and J. Wu, "Energy efficiency improvement via bus voltage control of inverter for electric vehicles," *IEEE Transactions on Vehicular Technology*, vol. 66, no. 2, pp. 1063–1073, Apr. 2017.

[108] Z. Wu and G.-J. Su, "High-performance permanent magnet machine drive for electric vehicle applications using a current source inverter," in *2008 34th Annual Conference of IEEE Industrial Electronics*, Orlando, FL, Jan. 2008, pp. 2812–2817.

[109] E. P. Wiechmann, P. Aqueveque, R. Burgos, and J. Rodríguez, "On the efficiency of voltage source and current source inverters for high-power drives," *IEEE Transactions on Industrial Electronics*, vol. 55, no. 4, pp. 1771–1782, Apr. 2008.

[110] F. Z. Peng, "Z-source inverter," *IEEE Transactions on Industry Applications*, vol. 39, no. 2, pp. 504–510, Mar. 2003.

[111] F. Z. Peng, A. Joseph, J. Wang, M. Shen, L. Chen, Z. Pan, E. Ortiz-Rivera, and Y. Huang, "Z-source inverter for motor drives," *IEEE Transactions on Power Electronics*, vol. 20, no. 4, pp. 857–863, Jul. 2005.

[112] F. Z. Peng, M. Shen, and K. Holland, "Application of Z-source inverter for traction drive of fuel cell in battery hybrid electric vehicles," *IEEE Transactions on Power Electronics*, vol. 22, no. 3, pp. 1054–1061, May 2007.

[113] M. Shen, A. Joseph, J. Wang, F. Z. Peng, and D. J. Adams, "Comparison of traditional inverters and Z-source inverter for fuel cell vehicles," *IEEE Transactions on Power Electronics*, vol. 22, no. 4, pp. 1453–1463, Jul. 2007.

[114] A. Nabae, I. Takahashi, and H. Akagi, "A new neutral-point-clamped pwm inverter," *IEEE Transactions on Industry Applications*, vol. IA-17, no. 5, pp. 518–523, Sep. 1981.

[115] J. Rodriguez, J.-S. Lai, and F. Z. Peng, "Multilevel inverters: a survey of topologies, controls, and applications," *IEEE Transactions on Industrial Electronics*, vol. 49, no. 4, pp. 724–738, Nov. 2002.

[116] J. Rodriguez, S. Bernet, P. K. Steimer, and I. E. Lizama, "A survey on neutral-point-clamped inverters," *IEEE Transactions on Industrial Electronics*, vol. 57, no. 7, pp. 2219–2230, Sep. 2010.

[117] M. Schweizer and J. W. Kolar, "Design and implementation of a highly efficient three-level T-type converter for low-voltage applications," *IEEE Transactions on Power Electronics*, vol. 28, no. 2, pp. 899–907, Jun. 2013.

[118] R. Teichmann and S. Bernet, "A comparison of three-level converters versus two-level converters for low-voltage drives, traction, and utility applications," *IEEE Transactions on Industry Applications*, vol. 41, no. 3, pp. 855–865, May 2005.

[119] M. Schweizer, T. Friedli, and J. W. Kolar, "Comparative evaluation of advanced three-phase three-level inverter/converter topologies against two-level systems," *IEEE Transactions on Industrial Electronics*, vol. 60, no. 12, pp. 5515–5527, Dec. 2013.

[120] D. G. Holmes and T. A. Lipo, *Pulse width modulation for power converters: principles and practice*. John Wiley & Sons, 2003.

[121] A. Andersson, D. Lennström, and A. Nykänen, "Influence of inverter modulation strategy on electric drive efficiency and perceived sound quality," *IEEE Transactions on Transportation Electrification*, vol. 2, no. 1, pp. 24–35, Jan. 2016.

[122] I. P. Tsoumas and H. Tischmacher, "Influence of the inverter's modulation technique on the audible noise of electric motors," *IEEE Transactions on Industry Applications*, vol. 50, no. 1, pp. 269–278, Jun. 2014.

[123] A. Mehrizi-Sani and S. Filizadeh, "An optimized space vector modulation sequence for improved harmonic performance," *IEEE Transactions on Industrial Electronics*, vol. 56, no. 8, pp. 2894–2903, Nov. 2009.

[124] H. W. Van Der Broeck, H.-C. Skudelny, and G. V. Stanke, "Analysis and realization of a pulsewidth modulator based on voltage space vectors," *IEEE Transactions on Industry Applications*, vol. 24, no. 1, pp. 142–150, Jan./Feb. 1988.

[125] A. Cataliotti, F. Genduso, A. Raciti, and G. R. Galluzzo, "Generalized PWM-VSI control algorithm based on a universal duty-cycle expression: Theoretical analysis, simulation results, and experimental validations," *IEEE Transactions on Industrial Electronics*, vol. 54, no. 3, pp. 1569–1580, Apr. 2007.

[126] S. Jurkovic, K. Rahman, B. Bae, N. Patel, and P. Savagian, "Next generation chevy volt electric machines; design, optimization and control for performance and rare-earth mitigation," in *2015 IEEE Energy Conversion Congress and Exposition (ECCE)*, Montreal, QC, Canada, Sep. 2015, pp. 5219–5226.

[127] F. Momen, K. Rahman, Y. Son, and P. Savagian, "Electrical propulsion system design of chevrolet bolt battery electric vehicle," in *2016 IEEE Energy Conversion Congress and Exposition (ECCE)*, Milwaukee, WI, Sep. 2016, pp. 1–8.

[128] D. Ward, I. Husain, C. Castro, A. Volke, and M. Hornkamp, *Fundamentals of Semiconductors for Hybrid-Electric Powertrain*, 1st ed. Infineon Technologies North America Corp, 2013.

[129] Y. Lobsiger and J. W. Kolar, "Closed-loop di/ dt and dv/dt IGBT gate driver," *IEEE Transactions on Power Electronics*, vol. 30, no. 6, pp. 3402–3417, Jun. 2015.

[130] X. Pei, W. Zhou, and Y. Kang, "Analysis and calculation of DC-link current and voltage ripples for three-phase inverter with unbalanced load," *IEEE Transactions on Power Electronics*, vol. 30, no. 10, pp. 5401–5412, Dec. 2015.

[131] J. Guo, J. Ye, and A. Emadi, "DC-link current and voltage ripple analysis considering antiparallel diode reverse recovery in voltage source inverters," *IEEE Transactions on Power Electronics*, vol. 33, no. 6, pp. 5171–5180, Aug. 2018.

[132] M. A. Vogelsberger, T. Wiesinger, and H. Ertl, "Life-cycle monitoring and voltage-managing unit for DC-link electrolytic capacitors in pwm converters," *IEEE Transactions on Power Electronics*, vol. 26, no. 2, pp. 493–503, Jul. 2011.

[133] V. Smet, F. Forest, J.-J. Huselstein, F. Richardeau, Z. Khatir, S. Lefebvre, and M. Berkani, "Ageing and failure modes of igbt modules in high-temperature power cycling," *IEEE Transactions on Industrial Electronics*, vol. 58, no. 10, pp. 4931–4941, Feb. 2011.

[134] Y. Yamada, Y. Takaku, Y. Yagi, I. Nakagawa, T. Atsumi, M. Shirai, I. Ohnuma, and K. Ishida, "Reliability of wire-bonding and solder joint for high temperature operation of power semiconductor device," *Microelectronics Reliability*, vol. 47, no. 12, pp. 2147–2151, Dec. 2007.

[135] J. Ye, K. Yang, H. Ye, and A. Emadi, "A fast electro-thermal model of traction inverters for electrified vehicles," *IEEE Transactions on Power Electronics*, vol. 32, no. 5, pp. 3920–3934, Jun. 2017.

[136] K. Ma, A. S. Bahman, S. Beczkowski, and F. Blaabjerg, "Complete loss and thermal model of power semiconductors including device rating information," *IEEE Transactions on Power Electronics*, vol. 30, no. 5, pp. 2556–2569, Aug. 2015.

[137] A. S. Bahman, K. Ma, and F. Blaabjerg, "A lumped thermal model including thermal coupling and thermal boundary conditions for high-power IGBT modules," *IEEE Transactions on Power Electronics*, vol. 33, no. 3, pp. 2518–2530, Apr. 2018.

[138] Z. Luo, H. Ahn, and M. Nokali, "A thermal model for insulated gate bipolar transistor module," *IEEE Transactions on Power Electronics*, vol. 19, no. 4, pp. 902–907, Jul. 2004.

[139] E. Laloya, O. Lucia, H. Sarnago, and J. M. Burdio, "Heat management in power converters: From state of the art to future ultrahigh efficiency systems," *IEEE Transactions on Power Electronics*, vol. 31, no. 11, pp. 7896–7908, Dec. 2016.

[140] A. D. Callegaro, J. Guo, M. Eull, B. Danen, J. Gibson, M. Preindl, B. Bilgin, and A. Emadi, "Bus bar design for high-power inverters," *IEEE Transactions on Power Electronics*, vol. 33, no. 3, pp. 2354–2367, Apr. 2018.

[141] P. Hummel, D. Lesne, J. Radlinger, C. Golbaz, C. Langan, K. Takahashi, D. Mulholland, A. Stott, G. Haire, M. Mittermaier, N. Gaudois, and L. Shaw, "UBS evidence lab electric car teardown disruption ahead?" *UBS report, Basel*, 2017.

[142] G. L. Grant, "Low-cost U.S. manufacturing of power electronics for electric drive vehicles," Delphi Automotive Systems, LLC, Tech. Rep. ARRAVT022, May 2013.

[143] S. Yang, A. Bryant, P. Mawby, D. Xiang, L. Ran, and P. Tavner, "An industry-based survey of reliability in power electronic converters," *IEEE Transactions on Industry Applications*, vol. 47, no. 3, pp. 1441–1451, Mar. 2011.

[144] S. Yang, D. Xiang, A. Bryant, P. Mawby, L. Ran, and P. Tavner, "Condition monitoring for device reliability in power electronic converters: A review," *IEEE Transactions on Power Electronics*, vol. 25, no. 11, pp. 2734–2752, May 2010.

[145] H. Wang, M. Liserre, and F. Blaabjerg, "Toward reliable power electronics: Challenges, design tools, and opportunities," *IEEE Industrial Electronics Magazine*, vol. 7, no. 2, pp. 17–26, Jun. 2013.

[146] K. B. Pedersen and K. Pedersen, "Dynamic modeling method of electro-thermo-mechanical degradation in IGBT modules," *IEEE Transactions on Power Electronics*, vol. 31, no. 2, pp. 975–986, Apr. 2016.

[147] K. B. Pedersen, P. K. Kristensen, V. Popok, and K. Pedersen, "Degradation assessment in IGBT modules using four-point probing approach," *IEEE Transactions on Power Electronics*, vol. 30, no. 5, pp. 2405–2412, Aug. 2015.

[148] A. S. Bahman, F. Iannuzzo, C. Uhrenfeldt, F. Blaabjerg, and S. Munk-Nielsen, "Modeling of short-circuit-related thermal stress in aged IGBT modules," *IEEE Transactions on Industry Applications*, vol. 53, no. 5, pp. 4788–4795, May 2017.

[149] U.-M. Choi, F. Blaabjerg, and K.-B. Lee, "Study and handling methods of power IGBT module failures in power electronic converter systems," *IEEE Transactions on Power Electronics*, vol. 30, no. 5, pp. 2517–2533, Dec. 2015.

[150] H. Wang and F. Blaabjerg, "Reliability of capacitors for DC-link applications in power electronic converters:an overview," *IEEE Transactions on Industry Applications*, vol. 50, no. 5, pp. 3569–3578, Feb. 2014.

[151] D. Hirschmann, D. Tissen, S. Schroder, and R. W. De Doncker, "Reliability prediction for inverters in hybrid electrical vehicles," *IEEE Transactions on Power Electronics*, vol. 22, no. 6, pp. 2511–2517, Nov. 2007.

[152] H. Huang and P. Mawby, "A lifetime estimation technique for voltage source inverters," *IEEE Transactions on Power Electronics*, vol. 28, no. 8, pp. 4113–4119, Dec. 2013.

[153] B. A. Welchko, T. A. Lipo, T. M. Jahns, and S. E. Schulz, "Fault tolerant three-phase ac motor drive topologies: a comparison of features, cost, and limitations," *IEEE Transactions on Power Electronics*, vol. 19, no. 4, pp. 1108–1116, Jul. 2004.

[154] Y. Sato, S. Ishikawa, T. Okubo, M. Abe, and K. Tamai, "Development of high response motor and inverter system for the Nissan LEAF electric vehicle," in *SAE Technical Paper*, no. 2011-01-0350, 2011.

[155] Viper: The small inverter power switch that packs a big punch. [Online]. Available: https://www.delphi.com/innovations/viper-inverter-power-switch

[156] J. R. Rodriguez, J. W. Dixon, J. R. Espinoza, J. Pontt, and P. Lezana, "Pwm regenerative rectifiers: State of the art," *IEEE Transactions on Industrial Electronics*, vol. 52, no. 1, pp. 5–22, Feb. 2005.

[157] D. Y. Ohm, "Dynamic model of induction motors for vector control," *Drivetech, Inc., Blacksburg, Virginia*, pp. 1–10, 2001.

[158] P. A. Dahono, Y. Sato, and T. Kataoka, "Analysis and minimization of ripple components of input current and voltage of pwm inverters," *IEEE Transactions on Industry Applications*, vol. 32, no. 4, pp. 945–950, Jul./Aug. 1996.

[159] J. W. Kolar and S. D. Round, "Analytical calculation of the rms current stress on the dc-link capacitor of voltage-pwm converter systems," *IEEE Proceedings-Electric Power Applications*, vol. 153, no. 4, pp. 535–543, Jul. 2006.

[160] M. Qing-yun, M. Wei-Ming, S. Chi, J. Gui-sheng, and Q. Wei, "Analytical calculation of the average and rms currents in three-level npc inverter with spwm," in *2009 IEEE 35th Annual Conference of Industrial Electronics (IECON)*, Porto, Portugal, Nov. 2009, pp. 243–248.

[161] Y. Firouz, M. T. Bina, and B. Eskandari, "Efficiency of three-level neutral-point clamped converters: analysis and experimental validation of power losses, thermal modelling and lifetime prediction," *IET Power Electronics*, vol. 7, no. 1, pp. 209–219, Jan. 2014.

[162] F. Blaabjerg and J. K. Pedersen, "Optimized design of a complete three-phase PWM-VS inverter," *IEEE Transactions on Power Electronics*, vol. 12, no. 3, pp. 567–577, May 1997.

[163] H. Uemura, F. Krismer, and J. W. Kolar, "Comparative evaluation of T-type topologies comprising standard and reverse-blocking igbts," in *2013 IEEE Energy Conversion Congress and Exposition (ECCE)*, Denver, CO, Sep. 2013, pp. 1288–1295.

[164] P. Dushan, "Igbt power losses calculation using the data-sheet parameters," *Infineon, Appl. Note, V1. 1*, 2009.

[165] A. Wintrich, U. Nicolai, T. Reimann, and W. Tursky, "Application manual power semiconductors," 2011.

[166] *Printed Circuit Board Mount Power Film Capacitors C4AE*, KEMET.

[167] L. Sejpal, "Comparison of two-level and three-level neutral-point clamped inverters in automotive applications," Ph.D. dissertation, Concordia University, 2013.

[168] N. Kim, A. Rousseau, and E. Rask, "Autonomie model validation with test data for 2010 toyota prius," in *SAE Technical Paper*, no. 2012-01-1040, 2012.

[169] G. Mohan, F. Assadian, and S. Longo, "Comparative analysis of forward-facing models vs backward-facing models in powertrain component sizing," in *2013 IET 4th Hybrid and Electric Vehicles Conference 2013 (HEVC13)*, London, UK, Nov. 2013.

[170] R. Ahmed, M. E. Sayed, I. Arasaratnam, J. Tjong, and S. Habibi, "Reduced-order electrochemical model parameters identification and soc estimation for healthy and

aged li-ion batteries. part ii: Aged battery model and state of charge estimation," *IEEE Journal of Emerging and Selected Topics in Power Electronics*, vol. 2, no. 3, pp. 678–690, Jun. 2014.

[171] ——, "Reduced-order electrochemical model parameters identification and soc estimation for healthy and aged li-ion batteries. part i: Aged battery model and state of charge estimation," *IEEE Journal of Emerging and Selected Topics in Power Electronics*, vol. 2, no. 3, pp. 659–677, Jun. 2014.

[172] I. J. Fernandez, C. F. Calvillo, A. Sanchez-Miralles, and J. Boal, "Capacity fade and aging models for electric batteries and optimal charging strategy for electric vehicles," *Energy Journal*, vol. 60, pp. 35–43, Oct. 2013.

[173] L. Lam and P. Bauer, "Practical capacity fading model for li-ion battery cells in electric vehicles," *IEEE Transactions on Power Electronics*, vol. 28, no. 12, pp. 5910–5918, Dec. 2013.

[174] S. Pay and Y. Baghzouz, "Effectiveness of battery-supercapacitor combination in electric vehicles," in *2003 IEEE Bologna Power Tech Conference Proceedings*, Bologna, Italy, Jun. 2003, pp. 728–733.

[175] A. Kuperman, I. Aharon, S. Malki, and A. Kara, "Design of a semiactive battery-ultracapacitor hybrid energy source," *IEEE Transactions on Power Electronics*, vol. 28, no. 2, pp. 806–815, Jun. 2013.

[176] B. Hredzak, V. Agelidis, and M. Jang, "A model predictive control system for a hybrid," *IEEE Transactions on Power Electronics*, vol. 29, no. 3, pp. 1469–1479, May 2014.

[177] S. M. Lukic, S. G. Wirasingha, F. Rodriguez, J. Cao, and A. Emadi, "Power management of an ultracapacitor/battery hybrid energy storage system in an hev," in *2006*

IEEE Vehicle Power and Propulsion Conference (VPPC'06), Windsor, UK, Sep. 2006, pp. 1–6.

[178] J. Cao and A. Emadi, "A new battery/ultracapacitor hybrid energy storage system for electric, hybrid, and plug-in hybrid electric vehicles," *IEEE Transactions on Power Electronics*, vol. 27, no. 1, pp. 122–132, May 2012.

[179] A. Ostadi, M. Kazerani, and S. K. Chen, "Hybrid energy storage system (HESS) in vehicular applications: A review on interfacing battery and ultra-capacitor units," in *2013 IEEE Transportation Electrification Conference and Expo (ITEC)*, Detroit, MI, Jun. 2013, pp. 1–7.

[180] A. Kuperman, I. Aharon, S. Malki, and A. Kara, "Design of a semiactive battery-ultracapacitor hybrid energy source," *IEEE Transactions on Power Electronics*, vol. 28, no. 2, pp. 806–815, Jun. 2013.

[181] J. Cao and A. Emadi, "A new battery/ultracapacitor hybrid energy storage system for electric, hybrid, and plug-in hybrid electric vehicles," *IEEE Transactions on Power Electronics*, vol. 27, no. 1, pp. 122–132, May 2012.

[182] E. Chemali, L. McCurlie, B. Howey, T. Stiene, M. M. Rahman, M. Preindl, R. Ahmed, and A. Emadi, "Minimizing battery wear in a hybrid energy storage system using a linear quadratic regulator," in *41st Annual Conference of the IEEE Industrial Electronics Society (IECON)*, Yokohama, Japan, Nov. 2015, pp. 3265–3270.

[183] Y. Fuyuan, L. Languang, Y. Yuping, and Y. He, "Characterization , analysis and modeling of an ultracapacitor," *World Eletric Vehicle Journal*, vol. 4, no. 2, pp. 358–369, Jun. 2010.

[184] C. Farcas, D. Petreus, I. Ciocan, and N. Palaghita, "Modeling and simulation of supercapacitors," in *2009 15th International Symposium for Design and Technology of Electronics Packages (SIITME)*, Gyula, Hungary, Sept 2009, pp. 195–200.

[185] Maxwell, "Datasheet - k2 ultracapacitors - 2.85v/3400f," Tech. Rep., 2014.

[186] S. E. Samadani, R. Fraser, and M. Fowler, "A review study of methods for lithium-ion battery health monitoring and remaining life estimation in hybrid electric vehicles," in *SAE Technical Paper*, no. 2012-01-0125, 2012.

[187] S. S. Lee, H. J. Kim, G. J. Han, D. Cho, and G. Deok, "A study on the dynamic SOC compensation of an ultracapacitor module for the hybrid energy storage system," in *INTELEC 2009 - 31st International Telecommunications Energy Conference*, Incheon, South Korea, Oct 2009, pp. 1–7.